Defect Chemistry and Ion Transport in Perovskite Oxides Probed by Atomistic Simulations

Von der Fakultät für Mathematik und Naturwissenschaften der RWTH Aachen University zur Erlangung des akademischen Grades eines Doktors der Naturwissenschaften genehmigte Dissertation

vorgelegt von Alexander Bonkowski, M.Sc.
aus Düsseldorf

Berichter:
Prof. Dr. Roger A. De Souza
Prof. Dr. Arne Lüchow

Tag der mündlichen Prüfung: 23. Oktober 2025

Diese Dissertation ist auf den Internetseiten der Universitätsbibliothek online verfügbar.

Eidesstattliche Erklärung

Alexander Bonkowski erklärt hiermit, dass diese Dissertation und die darin dargelegten Inhalte die eigenen sind und selbstständig, als Ergebnis der eigenen originären Forschung, generiert wurden.

Hiermit erkläre ich an Eides statt

1. Diese Arbeit wurde vollständig oder größtenteils in der Phase als Doktorand dieser Fakultät und Universität angefertigt;
2. Sofern irgendein Bestandteil dieser Dissertation zuvor für einen akademischen Abschluss oder eine andere Qualifikation an dieser oder einer anderen Institution verwendet wurde, wurde dies klar angezeigt;
3. Wenn immer andere eigene- oder Veröffentlichungen Dritter herangezogen wurden, wurden diese klar benannt;
4. Wenn aus anderen eigenen- oder Veröffentlichungen Dritter zitiert wurde, wurde stets die Quelle hierfür angegeben. Diese Dissertation ist vollständig meine eigene Arbeit, mit der Ausnahme solcher Zitate;
5. Alle wesentlichen Quellen von Unterstützung wurden benannt;
6. Wenn immer ein Teil dieser Dissertation auf der Zusammenarbeit mit anderen basiert, wurde von mir klar gekennzeichnet, was von anderen und was von mir selbst erarbeitet wurde;
7. Ein Teil oder Teile dieser Arbeit wurden zuvor veröffentlicht und zwar in:
    - A. Bonkowski, C. Perkampus, R. A. De Souza, *J. Mater. Chem. A* **2023**, *11*, 10231–10262
    - A. Bonkowski, J. A. Kilner, R. A. De Souza, *RSC Appl. Interfaces* **2024**, *1*, 699–710
    - A. Bonkowski, M. J. Wolf, J. Wu, S. C. Parker, A. Klein, R. A. De Souza, *J. Am. Chem. Soc.* **2024**, *146*, 23012–23021

Aachen, Juni 2025

Alexander Bonkowski

Abstract

Energy storage and conversion devices have become essential to modern society and play a crucial role in the transition toward a more sustainable energy supply. Solid-state ionic conductors, such as perovskite oxides, are key materials in these devices. Despite significant progress in recent decades, many fundamental questions about ion transport in solids remain unanswered. In particular, the interplay between chemical composition, defect chemistry, lattice symmetry, and external conditions (e.g., temperature, oxygen partial pressure), and how these factors influence ion diffusion, is still not fully understood. This thesis addresses some of these open questions using atomistic simulations to study ion diffusion in perovskite oxides, with an emphasis on practical implications for energy storage and conversion applications.

A compact guide for performing molecular dynamics simulations of ion transport in solids is presented, including practical advice on simulation setup and analysis, as well as a discussion of common pitfalls and how to avoid them.

The poor stability of the superlative oxide-ion conductor $Ba_{0.5}Sr_{0.5}Co_{0.8}Fe_{0.2}O_{2.5}$ (BSCF) severely limits its applicability. An alternative composition, in which Ba is replaced by Ca, was investigated with respect to structural properties and oxygen-vacancy diffusion using molecular dynamics simulations. The resulting material, $Ca_{0.5}Sr_{0.5}Co_{0.8}Fe_{0.2}O_{2.5}$ (CSCF), is predicted to exhibit improved stability while maintaining similar oxygen-vacancy diffusivity, making it a promising candidate for experimental validation.

Exsolution is a strategy for generating catalytically active nanoparticles on the surfaces of oxide host materials, yet the mechanisms underlying this process are not fully understood. A new model for the thermodynamics and kinetics of metal exsolution from perovskite oxides is proposed, based on the reduction of the transition-metal ion within the host lattice rather than at the surface. This model accounts for a wider range of experimental observations than previous approaches.

The diffusion of oxygen in polycrystalline (La,Sr)$FeO_{3-\delta}$ (LSF) was investigated using molecular dynamics simulations. The results show that at lower temperatures, faster grain-boundary diffusion of oxide ions occurs due to the near-complete depletion of oxygen vacancies in the bulk regions.

Zusammenfassung

Energiespeicher und -umwandlungsvorrichtungen sind für die moderne Gesellschaft unverzichtbar geworden und spielen eine entscheidende Rolle beim Übergang zu einer nachhaltigeren Energieversorgung. Festkörper-Ionenleiter, wie Perowskit-Oxide, sind wichtige Materialien in diesen Geräten. Trotz erheblicher Fortschritte in den letzten Jahrzehnten bleiben viele grundlegende Fragen zum Ionen-Transport in Festkörpern unbeantwortet. Insbesondere das Zusammenspiel von chemischer Zusammensetzung, Defektchemie, Gitter-Symmetrie und äußeren Bedingungen (z.B. Temperatur, Sauerstoff-Partialdruck), und wie diese Faktoren die Ionen-Diffusion beeinflussen, ist noch nicht vollständig aufgeklärt. Diese Dissertation befasst sich mit einigen dieser offenen Fragen unter Verwendung atomistischer Simulationen zur Untersuchung des Ionen-Transports in Perowskit-Oxiden, mit einem Schwerpunkt auf praktischen Implikationen für Anwendungen in der Energiespeicherung und -umwandlung.

Ein kompakter Leitfaden für die Durchführung von Molekulardynamik-Simulationen des Ionen-Transports in Festkörpern wird vorgestellt, einschließlich praktischer Ratschläge zur Simulationseinrichtung und -analyse sowie einer Diskussion häufiger Fallstricke und wie diese vermieden werden können.

Die schlechte Stabilität des herausragenden Oxid-Ionenleiters $Ba_{0.5}Sr_{0.5}Co_{0.8}Fe_{0.2}O_{2.5}$ (BSCF) schränkt seine Anwendbarkeit erheblich ein. Eine alternative Zusammensetzung, bei der Ba durch Ca ersetzt wird, wurde hinsichtlich der strukturellen Eigenschaften und der Diffusion von Sauerstoff-Leerstellen mittels Molekulardynamik-Simulationen untersucht. Das resultierende Material, $Ca_{0.5}Sr_{0.5}Co_{0.8}Fe_{0.2}O_{2.5}$ (CSCF), weist eine verbesserte Stabilität auf und behält gleichzeitig eine ähnliche Sauerstoff-Leerstellen-Diffusivität bei, was es zu einem vielversprechenden Kandidaten für experimentelle Validierung macht.

Exsolution ist eine Strategie zur Erzeugung katalytisch aktiver Nanopartikel auf den Oberflächen von Oxid-Wirtsmaterialien, doch die Mechanismen, die diesem Prozess zugrunde liegen, sind nicht vollständig aufgeklärt. Ein neues Modell für die Thermodynamik und Kinetik der Metall-Exsolution aus Perowskit-Oxiden wird vorgeschlagen, das auf der Reduktion des Übergangsmetall-Ions innerhalb des Wirtsgitters und nicht an der Oberfläche basiert. Dieses Modell berücksichtigt ein breiteres Spektrum experimenteller Beobachtungen als frühere Ansätze.

Die Diffusion von Sauerstoff in polykristallinem (La,Sr)$FeO_{3-\delta}$ (LSF) wurde mittels Molekulardynamik-Simulationen untersucht. Die Ergebnisse zeigen, dass bei niedrigeren Temperaturen eine schnellere Korngrenz-Diffusion von Oxid-Ionen aufgrund der nahezu vollständigen Entleerung von Sauerstoff-Leerstellen in den Korninnenbereichen auftritt.

Preface

The work presented in this thesis was conducted at the Institute of Physical Chemistry, RWTH Aachen University, under the supervision of Prof. Dr. Roger A. De Souza.

The research presented in this thesis was supported by funding from the European Union's Horizon 2020 research and innovation programme under grant agreement No 101017709 (EPISTORE). Simulations were performed with computing resources granted by RWTH Aachen University.

Parts of this thesis are based on data obtained from student's research projects supervised during this time. I would like to thank

- Caitlin Perkampus

  Oxygen diffusion in the perovskite system $(Ba,Ca)_{0.5}Sr_{0.5}Co_{0.8}Fe_{0.2}O_{2.5}$ (student assistant project, 2022)

  Computational study of oxygen diffusion in the perovskite families (Ca,Sr,Ba)(Ti,Fe)O_3 and (Bi,Ca)FeO_3 (Bachelor thesis, 2022)

- Alexei Torgashov

  Oxygen diffusion in vertically aligned nanocomposites (VANs) consisting of $SrTiO_3$ and Gd-doped CeO_2 (student research project, 2022)

- Kathrin Rübartsch

  MD simulations of oxygen transport in crystalline and amorphous (La,Sr)(Ga,Fe)O_3 (Bachelor thesis, 2023)

- Jonas Jacoby

  Metropolis–Monte Carlo Modelling of the defect structure in $La_{0.6}Sr_{0.4}Co_{0.2}Fe_{0.8}O_{3-\delta}$ (student research project, 2024)

for their contributions to this thesis.

Acknowledgements

First and foremost, I would like to thank my supervisor, Prof. Dr. Roger A. De Souza, for the opportunity to work in his group and for his continuous support, guidance, and encouragement throughout my PhD. His enthusiasm and persistence led me to many (sometimes unexpected) discoveries, and his willingness to discuss my work at any time made this thesis possible. I am grateful for the freedom to explore my own ideas, as well as for his guidance in keeping me on the right track whenever I needed it. I learned a lot from him, especially from his outstanding presentation skills.

I would like to thank Prof. Dr. Arne Lüchow for serving as the second examiner of this thesis.

I am grateful to my colleagues in the group, with whom I have shared many discussions, ideas, laughs, cakes, and coffee breaks. I will miss the time we spent together, especially at conferences. I always felt welcome and supported. I would also like to thank the (former) group of Prof. Dr. Manfred Martin for creating a friendly and welcoming atmosphere in the institute.

Special thanks go to Dr. Matthew J. Wolf, Adrian L. Usler, and Sonja Ambaum for proofreading parts of this thesis and for their valuable comments.

I would like to thank Caitlin Perkampus, Alexei Torgashov, Kathrin Rübartsch, and Jonas Jacoby for their contributions to this thesis. It has been a pleasure to work with you, and I am grateful for your enthusiasm and dedication.

Funding for my PhD was provided by the European Union's Horizon 2020 research and innovation programme under grant agreement No 101017709 (EPISTORE). I would like to thank the EPISTORE team for their support and collaboration. I also thank the NHR Center NHR4CES at RWTH Aachen University for providing computing resources and support for my simulations.

Finally, I would like to thank my family and friends for their support and encouragement throughout my PhD. It was a long and challenging journey with many ups and downs, but you helped me through it all.

Publications

Parts of this thesis have previously been published or have been prepared for publication:

- **Alexander Bonkowski**, Caitlin Perkampus, Roger A. De Souza, High oxygen-vacancy diffusivity predicted for perovskite oxide $Ca_{0.5}Sr_{0.5}Co_{0.8}Fe_{0.2}O_{2.5}$, *J. Mater. Chem. A* **2023**, *11*, 10551–10555.
  doi:10.1039/D2TA09897K

- **Alexander Bonkowski**, John A. Kilner, Roger A. De Souza, Oxygen grain-boundary diffusion in (La,Sr)$FeO_{3-\delta}$ perovskite-oxides probed by molecular-dynamics simulations, *RSC Appl. Interfaces* **2024**, *1*, 699–710.
  doi:10.1039/D3LF00263B

- **Alexander Bonkowski**, Matthew J. Wolf, Ji Wu, Stephen C. Parker, Andreas Klein, Roger A. De Souza, A single model for the thermodynamics and kinetics of metal exsolution from perovskite-oxides, *J. Am. Chem. Soc.* **2024**, *146(33)*, 23012–23021.
  doi:10.1021/jacs.4c03412

- **Alexander Bonkowski**, Roger A. De Souza, From Setup to Analysis: A Compact Guide to Performing Molecular Dynamics Simulations of Ion Transport in Solids, *submitted*.

The following collaborative work has been published or prepared for publication and is not part of this thesis:

- Sylvia Körfer, **Alexander Bonkowski**, Joe Kler, Peter Hatton, Blas Pedro Uberuaga, Roger A. De Souza, The Sluggish Diffusion of Cations in CeO_2 Probed through Molecular Dynamics and Metadynamics Simulations, *Adv. Eng. Mater.* **2023**, *25*, 2201788.
  doi:10.1002/adem.202201788

- Adrian L. Usler, Dennis Kemp, **Alexander Bonkowski**, Roger A. De Souza, A general expression for the statistical error in a diffusion coefficient obtained from a solid-state molecular-dynamics simulation, *J. Comput. Chem.* **2023**, *44(14)*, 1347-1359.
  doi:10.1002/jcc.27090

- Haley B. Buckner, Joshua Simpson-Gomez, **Alexander Bonkowski**, Kathrin Rübartsch, Hua Zhou, Roger A. De Souza, Nicola H. Perry, Transforming an Ionic Conductor into an ElectronicConductor via Crystallization: In Situ Evolution of Transference Numbers and Structure in (La,Sr)(Ga,Fe)O_{3-x} Perovskite Thin Films, *Adv. Funct. Mater.* **2024**, *34(41)*, 2401854.
  doi:10.1002/adfm.202401854

- Alex M. Ganose, Hrushikesh Sahasrabuddhe, Mark Asta, Kevin Beck, Tathagata Biswas, **Alexander Bonkowski**, Joana Bustamante, Xin Chen, Yuan Chiang, Daryl Chrzan, Jacob Clary, Orion Cohen, Christina Ertural, Max Gallant, Janine George, Sophie Gerits, Rhys Goodall, Rishabh Guha, Geoffroy Hautier, Matthew Horton, Aaron Kaplan, Ryan Kingsbury, Matthew Kuner, Bryant Li, Xavier Linn, Matthew McDermott, Rohith Srinivaas Mohanakrishnan, Aakash Naik, Jeffrey Neaton, Kristin Persson, Guido Petretto, Thomas Purcell, Francesco Ricci, Benjamin Rich, Janosh Riebesell, Gian-Marco Rignanese, Andrew Rosen, Matthias Scheffler, Jonathan Schmidt, Jimmy-Xuan Shen, Andrei Sobolev, Ravishankar Sundararaman, Cooper Tezak, Victor Trinquet, Joel Varley, Derek Vigil-Fowler, Duo Wang, David Waroquiers, Mingjian Wen, Han Yang, Hui Zheng, Jiongzhi Zheng, Zhuoying Zhu, Anubhav Jain, Atomate2: Modular Workflows for Materials Science, *submitted*.
  10.26434/chemrxiv-2025-tcr5h

Contents

1 Introduction **3**

2 Theoretical Background **7**

2.1 Defects in Solids 7

2.1.1 Point Defects 8

2.1.2 Planar Defects 10

2.2 Diffusion and Conductivity in Solids 11

2.2.1 Introduction 12

2.2.2 Diffusion Mechanisms in Solids 13

2.3 Perovskite-type Oxides 14

2.3.1 Crystal Structure 14

2.3.2 Oxide-Ion Conductivity 16

2.3.3 Defect Chemistry 16

2.4 Reaction Rates 18

2.4.1 Arrhenius Equation 19

2.4.2 Transition State Theory 19

3 Computational Methods **21**

3.1 Classical Molecular Dynamics 21

3.1.1 Basic Principles of Classical Molecular Dynamics 21

3.1.2 Classical Force Fields 22

3.1.3 Integration Algorithms 24

3.1.4 Ensembles 26

3.1.5 Thermostats and Barostats 29

3.2 Density Functional Theory 31

3.2.1 Introduction to DFT 31

3.2.2 Periodicity and the Bloch Theorem 32

3.2.3 HARTREE–FOCK Theory . . . 33
3.2.4 Hohenberg-Kohn Theorems . . . 34
3.2.5 Kohn–Sham Equations . . . 35
3.2.6 Exchange-Correlation Functionals . . . 36
3.2.7 Basis Sets and Pseudopotentials . . . 40
3.3 Defect and Transition State Calculations . . . 41
3.3.1 Defect Formation Energies . . . 41
3.3.2 Nudged Elastic Band . . . 42
3.4 Monte Carlo Simulations . . . 44
3.4.1 Basic Principles of Monte Carlo Simulations . . . 45
3.4.2 METROPOLIS Algorithm . . . 45
3.4.3 Applications of Monte Carlo Simulations . . . 46
3.5 Codes . . . 47
3.5.1 Structure Creation, Manipulation, and Analysis . . . 47
3.5.2 Force Field Simulations . . . 47
3.5.3 Density Functional Theory Calculations . . . 47
3.6 Computational Details . . . 48
3.6.1 Force Field Simulations . . . 48
3.6.2 Density Functional Theory Calculations . . . 48

4 Best Practices for Molecular Dynamics Simulations of Ion Diffusion in Solids 51
4.1 Introduction . . . 51
4.1.1 Accuracy and Uncertainty . . . 53
4.2 Force Fields . . . 54
4.3 Setup of the Simulation . . . 54
4.3.1 Equilibration . . . 54
4.3.2 Fluctuations of Thermodynamic Quantities . . . 58
4.3.3 Diffusive Regime and Diffusion Coefficient . . . 60
4.3.4 Simulations with a Fixed Lattice Volume . . . 62
4.3.5 Cell-Size Effects . . . 64
4.4 Evaluation of the Diffusion Data . . . 66
4.4.1 The Error in the Diffusion Coefficient . . . 66
4.4.2 Linear vs Non-Linear Fitting . . . 67
4.4.3 Extrapolation to Other Temperatures . . . 71
4.4.4 Conductivity from MD Simulations . . . 72
4.5 Concluding Remarks . . . 77

5 Substitution of Ba by Ca in BSCF5582 **79**
5.1 Introduction . . . 79
5.2 Results and Discussion . . . 80
5.2.1 Lattice Symmetry . . . 80
5.2.2 Oxygen-Vacancy Diffusion . . . 81
5.3 Comparison with Experimental Data . . . 84
5.4 Concluding Remarks . . . 87

6 Transition-Metal Exsolution from Perovskite Oxides **89**
6.1 Introduction . . . 89
6.2 Results and Discussion . . . 93
6.2.1 Charge-Transition Levels of Ni in $SrTiO_3$ . . . 93
6.2.2 Thermodynamics of Exsolution . . . 96
6.2.3 Kinetics of Exsolution . . . 99
6.2.4 Perovskites as Exsolution Hosts . . . 103
6.3 Concluding Remarks . . . 103

7 Oxygen Grain-Boundary Diffusion in LSF **105**
7.1 Introduction . . . 105
7.2 Simulation Methods . . . 106
7.2.1 Bulk Simulation Cells . . . 106
7.2.2 Polycrystal Creation . . . 107
7.2.3 MMC Simulations . . . 108
7.2.4 Compositional Analysis . . . 108
7.3 Results . . . 111
7.3.1 LSF Lattices . . . 111
7.3.2 Polycrystalline LSF . . . 114
7.3.3 Oxygen Diffusion in Polycrystalline Cells . . . 117
7.4 Discussion . . . 125
7.5 Concluding Remarks . . . 126

8 Conclusions **129**

9 Bibliography **137**

Appendix **161**

1 Introduction

Many state-of-the-art technological devices utilise solid-state materials. Over the past decades, the development of new materials and the improvement of existing ones has driven technological advancements. This includes the miniaturisation of electronic components, the development of novel energy storage systems, and the creation of new sensors and heterogeneous catalysts. Within the solid-state field, ion-conducting materials are a key subset of materials. They enable the transport of ions, a property typically associated with liquids, through their lattice.

On the microscopic level, diffusion in any state of matter is explained by the random motion of particles due to thermal energy. In solids, diffusion is strongly influenced by the presence of well-defined lattice sites, which restrict the positions of particles much more than in fluids (liquids or gases), where particles move more freely. This inherent constraint typically results in slower diffusion rates compared to fluids; however, it also allows for a greater degree of control over transport properties, opening up a wide range of applications. The interaction with the lattice also makes the understanding of ion transport in solids more complex.

An industrially relevant class of ion-conducting materials is oxide-ion conductors. They are used particularly, but not exclusively, in solid oxide fuel cells, oxygen sensors, catalysts, membranes for gas separation, and resistive switching devices. Depending on the application, it may be that only the oxide ion transport rates are supposed to be high, while in other applications, additional ionic species should also be mobile. There are even cases in which the transport rates must be adjustable, i.e. controlled by external stimuli. Lastly, there are materials with an additional requirement of high electronic conductivity, so-called mixed ionic–electronic conductors.

Over the years, many different oxide-ion conductors have been developed and studied. Some of the most prominent are the perovskite-type oxides. These materials, with the general formula ABO_3, are used because of their high versatility. There are countless possibilities for modifications of the

structure, from partial or total substitution of the *A*- or *B*-site cations and the oxygen anions, to deviations from nominal ABO_3 stoichiometry on both the cation and anion sub-lattices.

From the different factors that control ion migration, to the role of defects and of external stimuli, many fundamental questions about ion transport in solids remain unanswered to this day. External conditions such as temperature, oxygen partial pressure, and mechanical stress strongly influence material properties such as defect concentrations, (electronic/ionic) conductivity, and density, which in turn affect ion transport. The mechanisms by which these external factors influence transport properties are often difficult to disentangle by experimental means alone.

The research field of solid-state ionics has undergone a profound revolution with the emergence of high-performance computers. The ability to simulate materials at the atomic level complements experimental work by elucidating complex phenomena and allowing for predictions to be made. Transport properties can be studied by means of molecular dynamics simulations, by allowing the simulated system to evolve in time. These simulations are carried out utilising Newton's laws of motion and principles of statistical thermodynamics. Compared to real-world experiments, systems simulated with computational methods can be controlled more rigorously, but they are only as good as the models on which they are based. Although molecular dynamics simulations have been used for over 40 years, their transferability to the real world is still constantly being worked on.

This thesis first introduces the theoretical background of defects and ion transport in solids. It then deals in more detail with perovskite-like oxides as well as reaction rates. In the subsequent chapter, the computational methods used in this work are explained. After the fundamentals are covered, guidelines for conducting molecular dynamics simulations of ion transport in solids are derived, demonstrated for an exemplary system, and validated. Attention is paid to the proper setup of the simulation, a mathematically sound analysis of the results, and the transfer of the results to the experimental domain.

In the following, three different systems are studied in detail to showcase the influence of various factors on ion transport. The first system is the exceptional mixed ionic-electronic conductor $Ba_{0.5}Sr_{0.5}Co_{0.8}Fe_{0.2}O_{3-\delta}$ (BSCF5582), which suffers from poor stability under certain operating conditions. It is shown that, with a simple modification of the material composition, a new material can be obtained that promises to be more stable. All that is required is the substitution of Ba with Ca, which likely inhibits an unwanted phase transition while maintaining the high ionic conductivity.

The second case study concerns the emerging field of exsolution catalysts. These materials are prepared as solid solutions of a transition-metal oxide and a host oxide material. Upon heating in a reducing atmosphere, the metal oxide exsolves from the host material, forming nanoparticles with outstanding catalytic properties. This phenomenon has been demonstrated in many systems, most of which are composed of a perovskite-type oxide host. The underlying mechanisms, however, are not yet well understood. In this work, the exsolution of Ni from a $SrTiO_3$ host, a well-known model system, is studied by means of high-fidelity electronic structure calculations. A new unified exsolution model is proposed that covers both the thermodynamics and the kinetics of the exsolution process by considering the reduction of exsolving metal cations within the host material, unlike previous models, which have proposed the reduction step to occur at the surface.

Lastly, the observation of faster grain-boundary diffusion in polycrystalline (La,Sr)FeO_3 (LSF) at low temperatures is studied by means of molecular dynamics simulations. The complexity of the model is gradually increased, starting with the bulk material, subsequently introducing grain boundaries, then allowing for dopant segregation to the grain boundaries, and finally modifying the oxygen stoichiometry. It is shown that the grain-boundary diffusivity does not decrease as strongly as bulk diffusivity with decreasing temperature. This is attributed to the oxidation of the material at low temperatures, which strongly depletes oxygen vacancies from the bulk but not as strongly from the grain boundaries. Further analysis is performed to clarify the role of grain-boundary space-charge layers on the grain-boundary diffusivity.

2 Theoretical Background

This chapter provides a brief overview of the theoretical background relevant to the work presented in this thesis. All information presented here has been taken from a few textbooks or book chapters (see Refs [4–8]) unless otherwise stated.

2.1 Defects in Solids

Compared to their idealised counterparts, real crystalline materials contain defects. There are different reasons for the existence of defects — entropy-driven disorder at finite temperatures, non-stoichiometry during synthesis, doping, irradiation, mechanical stress, thermal fabrication history, etc. — and they can have a significant, if not dominant, influence on the material's properties.

The presence of defects reduces the translational symmetry of the crystal lattice, making the theoretical description of defective lattices more complex than that of perfect crystals. In ionic compounds, defect formation increases the lattice energy. For point defects (Sec. 2.1.1), this increase is offset by the rise in configurational entropy, especially at elevated temperatures. Due to slow ion transport in many solids, defects can be kinetically trapped at low temperatures, resulting in metastable states. These defects may be removed by thermal treatment at elevated temperatures over a certain period of time.

There are different types of defects, which can be classified by their dimensionality. In the following, point defects (zero-dimensional) and planar defects (two-dimensional) are introduced in more detail.

2.1.1 Point Defects

Point defects are the conceptually simplest type of defect and are also referred to as zero-dimensional defects since they do not extend periodically in any direction. *Intrinsic* point defects form spontaneously as a result of free energy minimisation of the system, driven by an increase of the configurational entropy. *Extrinsic* point defects, on the other hand, are introduced from external sources by doping or substitution of ions, and directly alter the stoichiometry of a material. There are different types of point defects, of which the most important ones (in the context of solid-state ionics) are shown in Fig. 2.1 and described in the following.

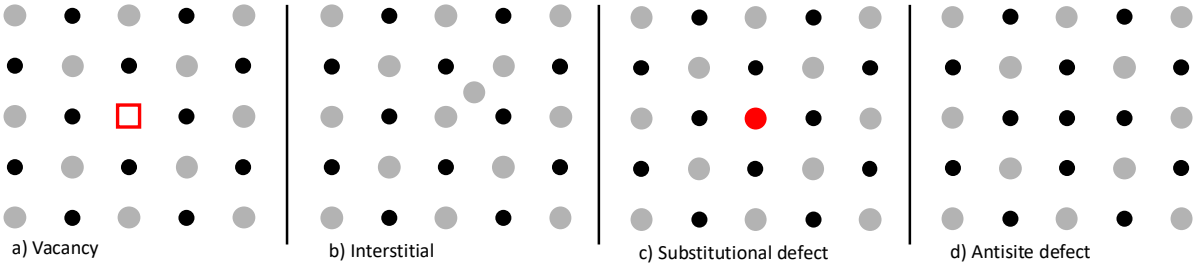


Figure 2.1 Schematic depiction of defects in a binary compound. The atoms are represented by circles of different colours and size. The square box represents a vacancy Shown are (a) vacancies, (b) interstitials, (c) substitutional defects, and (d) antisite defects.

- **Vacancies:** These defects are characterised by a vacant site that would be occupied in the perfect lattice. Vacancies are mostly created during crystal growth, through non-stoichiometric processing conditions, or by thermal activation. Some materials possess vacant sites as part of their perfect lattice structure. Although these sites are termed "structural vacancies", they are not considered defects in the same sense as they are part of the perfect lattice. A SCHOTTKY defect consists of vacant cation and anion sites of a full formula unit of the compound, preserving the overall stoichiometry of the crystal.

- **Interstitials:** Interstitials are atoms that occupy a site in the lattice that would be unoccupied in the perfect lattice. Only if interstitial sites in the lattice offer enough space for an interstitial atom to be accommodated, are interstitials formed with a reasonable formation energy. Accordingly, interstitial atoms are usually small.

- **Substitutional defects:** In this case, a site is occupied by a different species than in the perfect lattice. Substitutional defects can be generated by impurities in the precursor materials or by introducing them intentionally.

- **Antisite defects:** These defects occur when a species occupies a crystallographic site normally reserved for a different species. Unlike substitutional defects, the occupying species is part of the host compound but is not located on its native site. Antisite defects do not necessarily require a direct exchange ("swap") between two species; a single species can occupy an incorrect site without a corresponding exchange.

KRÖGER–VINK Notation

Ordinary chemical notation is not well suited to describing defects in a crystal lattice. One of the problems is the charge of a defect: a vacancy itself, for example, does not carry a charge, but there is missing charge on one of the regular lattice sites. More important in this context is the difference between the charge present at the defect site and the charge present at the site in the host lattice. This relative charge then depends on the lattice site on which the defect is located and the (quasi-)particle that occupies it.

The KRÖGER–VINK notation[9] is a widely used convention to describe defects in a crystal lattice. A defect is described by the symbol X_Y^Z, where X is the defect species, Y is the lattice site, and Z is the relative charge. Defect species and lattice site are expressed by the chemical symbol or by lowercase letters v (vacancy), e (electron), h (hole), or i (interstitial).[10] The relative charge can either be neutral ($\times$), positive ($\bullet$), or negative ($'$), where a multiple charge is expressed by repeating the symbols. As examples, the symbol for an oxygen vacancy in an oxide is $\mathrm{v}_\mathrm{O}^{\bullet\bullet}$, and the symbol for a Sr^{2+} ion on a La^{3+} site is Sr'_La.

Defect Concentrations

The defect concentration c in a system (without any additional constraints) is given by a BOLTZMANN expression

$$c = N \exp\left(-\frac{\Delta_f G}{k_\mathrm{B} T}\right), \tag{2.1}$$

where N is the number of lattice sites (per unit volume). The relevant energetic quantity is the

GIBBS free energy of formation $\Delta_f G = \Delta_f H - T\Delta_f S$, where $\Delta_f S$ relates to changes of phonon properties. $\Delta_f G$ is the free energy required to create a defect in the lattice and is by definition positive. Thus, it must be compensated by the gain in configurational entropy, $-T\Delta S_{\text{config}}$, for the defect to be thermodynamically stable. The defect concentration is a function of the temperature, with the defect concentration increasing with increasing temperature. Typical defect reactions for ionic solids are presented in Sec. 2.3.3.

2.1.2 Planar Defects

Planar defects are characterised by a plane within the crystal where the atomic arrangement deviates from that of the perfect lattice. Common examples of such interfaces include grain boundaries, stacking faults, and twin boundaries, as well as surfaces and interfaces with other materials.

Grain Boundaries

If a material is polycrystalline, it consists of many small crystallites, or grains, that are separated by grain boundaries. The interior of those grains is identical to that of a single crystal, but the grain boundaries disrupt the periodic arrangement of atoms. The properties of a grain boundary are determined by the orientation of the grains relative to each other. One of these properties is the grain-boundary energy per surface, which is the energy cost associated with the creation of that grain boundary. All grain boundaries are metastable. In practice, the number of grain boundaries in a sample can be decreased by treating the material at elevated temperatures.

Grain boundaries are generally classified by their misorientation angle into low-angle grain boundaries ($\lesssim 15°$) and high-angle grain boundaries ($\gtrsim 15°$). Additionally, there are special types of grain boundaries, most importantly twin boundaries, where the two grains are related by a mirror plane. Twin boundaries often have a lower energy than random grain boundaries.[11]

A grain boundary can be uniquely characterised by five independent macroscopic degrees of freedom: the mutual misorientation of adjoining grains, described by the rotation axis (two parameters) and the rotation angle (one parameter), and the orientation of the boundary plane, described by the MILLER indices of the plane normal (two parameters). Additionally, three microscopic

parameters define the translational vector, which describes the relative translation of the grains. While independent of the five macroscopic parameters, these microscopic values influence the grain boundary energy.[11]

Grain boundaries have a significant impact on ion transport in polycrystalline materials. In many ceramics, high bulk ionic conductivity is accompanied by significantly lower ionic conductivity across grain boundaries. In contrast, some materials with poor bulk ionic transport exhibit enhanced ionic conductivity along grain boundaries (often described as *faster* grain-boundary diffusion in a comparative sense). While some aspects about faster ion transport along grain boundaries are not yet fully understood, it is generally accepted that the higher ionic conductivity is due to different concentrations of defects at the grain boundaries compared to the bulk, as well as the different local structure of the grain boundaries that can facilitate alternative diffusion pathways. The kinetics of ion transport across grain boundaries can be studied by, i.a., impedance spectroscopy, and information about transport along grain boundaries can be inferred with this method if bulk transport properties are known.[4] The theoretical description of faster ion transport along grain boundaries is often done with the model by HARRISON.[12] More details on ion diffusion in solids are given in the following section.

2.2 Diffusion and Conductivity in Solids

At a given temperature, solid-state mass transport is typically significantly slower than in liquids or gases because atoms or ions are constrained to fixed lattice positions. For diffusion to occur in solids, a particle must not only acquire enough thermal energy to overcome the migration barrier but also require an available neighbouring site (such as a vacancy or an interstitial position or, in the case of the interstitialcy mechanism, displace another atom into an interstitial site). Atoms vibrate around their equilibrium positions and only occasionally, with sufficient thermal activation and the presence of an accessible site, jump to neighbouring positions. While most ionic solids are slow ion conductors, some exhibit high ionic conductivity and are termed fast ion or superionic conductors. Several factors influence the ionic conductivity of a material and they are discussed in the following sections.[7]

2.2.1 Introduction

Diffusion is phenomenologically described by FICK's laws.[13] FICK's first law (2.2) defines a diffusion coefficient D_i for each species i and relates the flux J_i, of species i, to the (location-dependent) concentration gradient ∇c_i:

$$J_i = -D_i \nabla c_i, \tag{2.2}$$

FICK's second law (2.3) describes the time dependence of the concentration $\frac{\partial c_i}{\partial t}$.

$$\frac{\partial c_i}{\partial t} = D_i \nabla^2 c_i \tag{2.3}$$

The mathematical description of diffusion at the atomic level was pioneered by EINSTEIN and SMOLUCHOWSKI.[14,15] It is based on the random walk of particles and the probability of finding a particle at a certain position and time. The diffusion coefficient D_i for diffusive transport in d dimensions is related to the mean squared displacement $\langle r_i^2(t) \rangle$ by the EINSTEIN–SMOLUCHOWSKI relation[14,15]

$$\langle r_i^2(t) \rangle = 2dD_i t, \tag{2.4}$$

with the mean squared displacement given for N particles as

$$\langle r_i^2(t) \rangle = \frac{1}{N} \sum_{i=1}^{N} \left(||\mathbf{r}_i(t) - \mathbf{r}_i(0)|| \right)^2 . \tag{2.5}$$

For a 3-dimensional (isotropic and homogeneous) system, the relationship between the diffusion coefficient and the mean squared displacement is then $\langle r_i^2(t) \rangle = 6D_i t$.

A distinction is often made between diffusion driven by a concentration gradient and self-diffusion. Diffusion along a concentration gradient results in a net flux of particles, moving the system towards

a homogeneous distribution. Once this homogeneous state is reached, the net diffusive flux vanishes. Even in the absence of this concentration gradient, the particles within a system move randomly. This inherent random motion of particles in a system at equilibrium, driven by the kinetic energy, is termed self-diffusion.

Self-diffusion in a homogeneous bulk phase is not accessible experimentally, as the concentration of particles remains spatially uniform and no net flux exists. It is often studied experimentally by introducing chemically similar but distinguishable particles into the system. These may be different isotopes of the same element or different elements with similar chemical properties. This is referred to as tracer diffusion, characterised by the tracer diffusion coefficient, D^*.

2.2.2 Diffusion Mechanisms in Solids

Essentially, three distinct mechanisms can be observed for ion transport in crystalline solids (Fig. 2.2).[4] Their occurrence depends on a materials ability to form vacancies and interstitials, respectively.

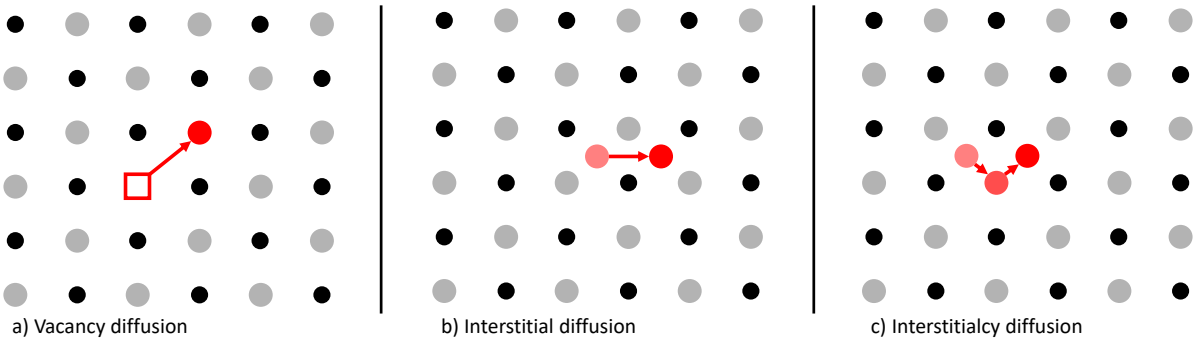


Figure 2.2 Schematic depiction of the different mechanisms of ion migration in a binary compound. The ions are represented by circles of different colours and size. The arrows indicate the direction in which the ions have migrated. The square box represents an existing vacancy. Shown are the mechanisms for (a) vacancy diffusion, (b) interstitial diffusion, and (c) interstitialcy diffusion.

Vacancy diffusion

Ions on regular lattice sites migrate to unoccupied lattice sites.

Interstitial diffusion

Ions on interstitial sites migrate to regularly unoccupied interstitial sites.

Interstitialcy diffusion

Ions displace other ions from regularly occupied to regularly unoccupied interstitial sites and occupy the vacated sites.

Vacancy diffusion can be described by a vacancy diffusion coefficient D_v. In case of a diluted vacancy concentration, the tracer diffusion coefficient can be related to the vacancy diffusion coefficient through the tracer correlation factor f^* and the vacancy site fraction x_v.[16]

$$D_V = \frac{D^*}{f^* \cdot x_v} \tag{2.6}$$

2.3 Perovskite-type Oxides

The archetypal perovskite structure type derives its name from the mineral $CaTiO_3$, first discovered in the Ural Mountains in 1839 by GUSTAV ROSE. He named it after the Russian mineralogist LEV PEROVSKI.[17] Nowadays, the group of perovskites comprises a large number of compounds that are characterised not only by different chemical elements, but also by different symmetries and properties, thus offering a wide range of possible applications. There are a few hundred experimentally known perovskites[8], and around 250 000 theoretically predicted perovskites[18]. Most notably, Bridgmanite $(Mg,Fe)SiO_3$ is the most abundant mineral in the Earth's mantle (ca. 38% of the solid phase).[8] Perovskite-structured materials have achieved widespread use in various applications, such as solid oxide fuel cells (SOFCs), solid oxide electrolysis cells (SOECs), photovoltaic cells, catalysts, and gas sensors, as well as subsidiary interest in the field of superconductivity, magnetoresistance, and multiferroicity. Depending on the scope of the application, the properties of the materials can be tailored to achieve high ionic conductivity, catalytic activity, and thermal stability by adjusting the composition and synthesis conditions.

2.3.1 Crystal Structure

Perovskite-type oxides are described by the general formula ABO_3. The idealised cubic form of the crystal structure can be understood as a cubic close packing of oxygen and A cations, with the B

cations occupying interstitial sites. The larger A cations have a coordination number of 12, the smaller B cations have an octahedral coordination (with a coordination number of 6).

The cubic perovskite structure is the aristotype (the structure type with the highest symmetry), distorted structure types with lower symmetry are called hettotypes.[19] Only a few perovskite-type materials exhibit the cubic symmetry structure at room temperature and instead show symmetry-lowering distortions. These can be categorised as distortions of the anion octahedra, rotation or tilting of the octahedra, and off-centering of the B-site cations from the center of the octahedra. The relative stability of a perovskite phase can be quantified by the semi-empirical GOLDSCHMIDT tolerance factor,[20]

$$t_{\mathrm{G}} = \frac{r_A + r_{\mathrm{X}}}{\sqrt{2}(r_B + r_{\mathrm{X}})} \tag{2.7}$$

where r_A, r_B and r_X are the radii of the A-site and B-site cations and anions (X), respectively. Generally, a tolerance factor of $t_{\mathrm{G}} > 1$ results in a hexagonal structure, while $0.8 \leq t_{\mathrm{G}} \leq 1$ form corner-sharing octahedra either in cubic (around $0.9 \leq t_{\mathrm{G}} \leq 1$) or orthorhombic (around $0.8 \leq t_{\mathrm{G}} \leq 0.9$) symmetry. Conclusions drawn from the tolerance factor are a rule of thumb; real materials typically do not follow these strict boundaries precisely.[21–23]

The ions in the perovskite structure can have different charges, but must satisfy the charge neutrality of the compound, i.e. $q_A + q_B + 3q_X = 0$. For oxides ($q_X = q_{\mathrm{O}} = -2$) and other doubly charged anions, there are three possible combinations of cations that satisfy the charge neutrality: $(q_A, q_B) = (+1, +5)$ (e.g. $NaNbO_3$), $(+2, +4)$ (e.g. $SrTiO_3$), and $(+3, +3)$ (e.g. $LaFeO_3$). A special case is the derived ReO_3 structure type, where the A-site is unoccupied and the B-site cations have a charge of $+6$.

In addition to the simple primitive perovskite structure, there are many perovskite-related structures, including inverse perovskites, double perovskites, the brownmillerite structure, RUDDLESDEN–POPPER (interlayer) phases, DION–JACOBSON phases, and AURIVILLIUS phases. Inverse perovskites have the A and B cations swapped, double perovskites have two B cations. The brownmillerite structure can be understood as an oxygen-deficient perovskite superstructure with an ordering of the oxygen vacancies ($A_2B_2O_5$). RUDDLESDEN–POPPER phases have a general formula $A_{\mathrm{n+1}}B_{\mathrm{n}}O_{3n+1}$ and consist of n perovskite-like layers separated by a rock-salt layer. These structures

can be used to tune the properties of the resulting materials for specific applications.[24]

2.3.2 Oxide-Ion Conductivity

One of the most important properties of perovskite-type oxides is their high oxide-ion conductivity. Oxygen transport is generally accepted to occur by a vacancy mechanism. Factors such as the size and charge of the A and B cations and the metal–oxygen bond strength influence the oxide-ion conductivity.[25]

Several design strategies have been employed to enhance oxide-ion conductivity in perovskite-type oxides by increasing the oxygen-vacancy concentration. Among the most widely used is the adjustment of the composition by substitution of cations. Reducing conditions during operation can also increase the oxygen-vacancy concentration. Structural modifications induced by cation engineering or by the introduction of defects can also influence the oxide-ion diffusion pathway and activation energy.[26,27] Corresponding chemical reactions are discussed in the following section.

2.3.3 Defect Chemistry

Perovskite-type oxides can accommodate a variety of defects. A fundamental condition for any defect to form is the maintenance of charge neutrality:

$$\sum_{i=1}^{N} q_i c_i = 0 \tag{2.8}$$

Eq. (2.8) is called the charge neutrality condition or electroneutrality condition. An important defect reaction is the SCHOTTKY reaction, where a whole formula unit of the perovskite (ABO_3) is removed from the lattice. For a $A^{II}B^{IV}O_3$ perovskite, the SCHOTTKY reaction is given by

$$\varnothing \rightleftharpoons v''_A + v''''_B + 3\,v^{\bullet\bullet}_O \tag{2.9}$$

Partial SCHOTTKY reactions are also possible, where only $A\mathrm{O}$ or $B\mathrm{O}_2$ formula units are removed. The concentration of oxygen vacancies is additionally influenced by an equilibrium with the atmosphere:

$$\mathrm{O}_\mathrm{O}^\times \rightleftharpoons \mathrm{v}_\mathrm{O}^{\bullet\bullet} + 2\,\mathrm{e}' + \frac{1}{2}\,\mathrm{O}_2 \tag{2.10}$$

Reaction (2.10) shows how perovskites can become mixed conducting under reducing conditions. Oxygen vacancies can also be introduced extrinsically by doping of the perovskite with aliovalent cations. A common example is the substitution of the A-site cation in an $A^{\mathrm{II}}B^{\mathrm{IV}}\mathrm{O}_3$ perovskite by a trivalent cation C during synthesis:

$$2\,A\mathrm{O} + C_2\mathrm{O}_3 \xrightarrow{A B \mathrm{O}_3} 2\,A_A^\times + 2\,C_A' + 5\,\mathrm{O}_\mathrm{O}^\times + \mathrm{v}_\mathrm{O}^{\bullet\bullet} \tag{2.11}$$

There are essentially two types of electronic defects in perovskite-type oxides: electron holes and electrons. Reaction (2.10), for example, yields electrons that can be trapped at specific sites in the lattice. In order for an electron to become trapped at such a site, there must be a corresponding state, localised at that site, within the band gap. In an $A^{\mathrm{II}}B^{\mathrm{IV}}\mathrm{O}_3$ perovskite, an electron may be trapped at a B^{IV} site, forming a B^{III} cation. On the other hand, electron holes may also localise at specific sites such that an ion is oxidised. For example, in SrTiO_3, small hole polarons localise at an oxygen atom.[28]

Defect Chemistry in LS(C)F

Lanthanum strontium cobalt ferrite (LSCF)[29–31] is a well-known class of mixed ionic–electronic conductors (MIEC) with the general formula $\mathrm{La}_{1-x}\mathrm{Sr}_x\mathrm{Co}_{1-y}\mathrm{Fe}_y\mathrm{O}_{3-\delta}$ (LSCF). The oxygen-ion conductivity of LSCF is tailored by the substitution of La^{3+} with Sr^{2+} in the host compound $\mathrm{LaCo}_{1-y}\mathrm{Fe}_y\mathrm{O}_3$. Variation in the B-site cations, Co^{3+} and Fe^{3+}, is employed to control the electronic conductivity of the material. For simplicity, the defect reactions are presented here for the case of $y = 1$. The main defect reaction for Sr substitution, similar to reaction (2.11), thus reads:

$$2\,\mathrm{SrO} \xrightarrow{\mathrm{LaFeO_3}} 2\,\mathrm{Sr'_{La}} + 2\,\mathrm{O_O^\times} + \mathrm{v_O^{\bullet\bullet}}. \tag{2.12}$$

Alternatively, and depending on the exact composition, temperature, and oxygen partial pressure, the Sr substitution can also be compensated by the formation of electron holes. The material can also lose or gain oxygen from the atmosphere, depending on the temperature and the oxygen partial pressure p_{O2}, according to the oxidation reaction

$$\frac{1}{2}\,\mathrm{O_2} + \mathrm{v_O^{\bullet\bullet}} \rightleftharpoons \mathrm{O_O^\times} + 2\,\mathrm{h^\bullet}. \tag{2.13}$$

As a result, the material will have increased oxygen non-stoichiometry δ under reducing conditions. The oxygen-vacancy concentration can be further increased by the introduction of A-site vacancies (e.g., $\mathrm{La_{0.98}FeO_{3-\delta}}$).

The mixed-valence B-site cations, Co and Fe, are able to accommodate the additional electrons or holes, respectively. LS(C)F is prone to phase stability issues, most prominently by Sr segregation to the surface.

2.4 Reaction Rates

Since chemical reactions are fundamentally stochastic processes, there are two main factors that influence the rate of a reaction: the frequency to attempt a reaction and the probability (per attempt) that the reaction will occur. This probability is determined by the activation energy of the reaction, i.e., the energy barrier that must be overcome to proceed from the reactant state to the product state.

2.4.1 Arrhenius Equation

The temperature dependence of reaction rates is described empirically by the ARRHENIUS equation:[32]

$$k = A \exp\left(-\frac{E_\mathrm{a}}{k_\mathrm{B}T}\right), \tag{2.14}$$

with the activation energy E_a. Most diffusion processes are found to obey the ARRHENIUS equation. The diffusion coefficient D can be related to the rate constant k by $D = a^2k$, where a is the jump distance, and the pre-exponential factor $A = gf\nu^0$ is expressed in terms of a geometric factor g, the correlation factor f, and the attempt frequency ν^0. The relationship is then written as

$$D = D_0 \exp\left(-\frac{\Delta_\mathrm{mig}H}{k_\mathrm{B}T}\right) \tag{2.15}$$

where $D_0 = gf\nu^0 a^2 \exp\left(-\frac{\Delta_\mathrm{mig}S}{k_\mathrm{B}}\right)$ is the pre-exponential factor.[4]

2.4.2 Transition State Theory

The temperature dependence of reaction rates can be studied in the framework of transition state theory (TST), which was first formulated by EYRING in 1935.[33] It postulates that a system must overcome an energy barrier $\Delta G^\ddagger$ to proceed from the reactant state to the product state. The rate constant k of the reaction is then given by an exponential dependence on the activation energy $\Delta G^\ddagger$ through the EYRING(–POLANYI) equation:[33,34]

$$k = \frac{\kappa k_\mathrm{B}T}{h} \exp\left(-\frac{\Delta G^\ddagger}{k_\mathrm{B}T}\right) \tag{2.16}$$

The transmission coefficient κ is a dimensionless factor that accounts for the fraction of the flux through the transition state that leads to the product without returning to the transition state, and

it is usually assumed to be (close to) unity. Expanding the GIBBS free energy $\Delta G^{\ddagger} = \Delta H^{\ddagger} - T\Delta S^{\ddagger}$, Eq. (2.16) can be rewritten as

$$k = \frac{\kappa k_{\mathrm{B}} T}{h} \exp\left(-\frac{\Delta H^{\ddagger}}{k_{\mathrm{B}} T}\right) \exp\left(\frac{\Delta S^{\ddagger}}{k_{\mathrm{B}}}\right). \tag{2.17}$$

The quantity of interest for diffusion processes is mostly the activation enthalpy $\Delta H^{\ddagger}$. It's determination requires to identify saddle point(s) on the free energy surface, i.e. the transition state(s). The activation enthalpy is then calculated from the energy difference between the transition state and the initial state, which is a local minimum of the free energy.

3 Computational Methods

This chapter provides an overview of the computational methods used in this work. It covers both the theoretical background of simulation techniques and practical aspects of their implementation. All information presented here has been taken from a few textbooks or book chapters (see Refs [6, 35–38]) unless otherwise stated.

3.1 Classical Molecular Dynamics

Molecular dynamics (MD) simulations are widely used in materials science to study the time-dependent behaviour of atoms and molecules. They allow for the simulation of system properties at finite temperatures, including diffusion, phase transitions, and mechanical properties. The "classical" designation of the method refers to both the use of classical mechanics to describe the motion of particles and the use of (semi-)empirical force fields to evaluate interatomic forces. The following sections provide an overview of the basic principles of classical MD simulations, including force fields, integration algorithms, and ensembles.

3.1.1 Basic Principles of Classical Molecular Dynamics

MD simulations are based on numerically solving the equations of motion for a system of interacting particles. These particles must be assigned masses, initial positions and velocities, and forces that act between them. For simple classical MD simulations, these forces are derived from a force field represented by analytical potential energy functions. Parameters for these functions are typically fitted to experimental data or high-level quantum mechanical calculations for a specific material.

This can be an effective way to include quantum mechanics, but the classification as *classical* becomes ambiguous.

For solid-state systems, it is often useful to assume periodic boundary conditions. This means that the simulation cell is replicated infinitely in all directions, which eliminates edge effects and allows for the simulation of bulk properties without the need for a large system size. It is also possible to simulate surfaces by applying periodic boundary conditions in two directions and a vacuum in the third direction.

The fundamentals of molecular dynamics simulations are rather simple, since the particle motion is governed by NEWTON's second law of motion, combined with forces derived from the applied force field. A major factor for the computational expense and complexity of a simulation is thus the level of theory of the force field.

In addition, simulations can be subject to external conditions or forces that interact with the particles or the simulation cell. These include thermostats and barostats, which regulate the temperature and pressure by exchanging energy with the system, as well as external fields such as electric or magnetic fields that influence particle dynamics. The choice and implementation of such external controls allow MD simulations to realistically model a wide range of physical environments and phenomena.

3.1.2 Classical Force Fields

Classical force fields provide a computationally efficient approach to modelling the potential energy surface of atoms and molecules in condensed-phase systems. In contrast to *ab initio* methods, which explicitly solve the SCHRÖDINGER equation, classical force fields rely on simplified, effective potential energy functions to describe the interactions between particles. These functions are typically parametrised to reproduce experimental data (then they are called Empirical Pair Potentials or EPP) or high-level quantum mechanical calculations.

For ionic solids, most established potentials of force fields $V(r)$ are composed of a COULOMB term[39] (for long range interactions) and a non-COULOMB term $\phi(r)$ (for short range interactions):

$$V(r) = \sum_{i=1}^{N-1} \sum_{j=i+1}^{N} \frac{q_i q_j}{4\pi\epsilon_0 r_{ij}} + \phi(r) \tag{3.1}$$

The charges q_i and q_j are *effective* charges of the ions i and j, respectively. Some potential models do not use full ionic charges to account for shielding effects. The term $\phi(r_{ij})$ can take several forms, depending on the specific material and the desired properties to be modelled. They may include terms for covalent, ionic, and van der Waals interactions, can be pairwise or many-body, and may include explicit angular and dihedral terms. The following overview is restricted to two-body potentials, the simplest and computationally most efficient form.

Common forms are LENNARD-JONES[40,41] (3.2), BUCKINGHAM[42] (3.3) or MORSE[43] (3.4) potentials and combinations thereof:

$$\phi_{\mathrm{LJ}}(r_{ij}) = 4\epsilon\left[\left(\frac{\sigma}{r_{ij}}\right)^{12} - \left(\frac{\sigma}{r_{ij}}^{6}\right)\right] \tag{3.2}$$

$$\phi_{\mathrm{Buck}}(r_{ij}) = A\exp\left(-\frac{r_{ij}}{\rho}\right) - \frac{C}{r_{ij}^6} \tag{3.3}$$

$$\phi_{\mathrm{Morse}}(r_{ij}) = D_{\mathrm{e}}\left(1 - \exp\left(-a\left(r_{ij} - r_{\mathrm{e}}\right)\right)\right)^2 \tag{3.4}$$

The LENNARD-JONES potential contains the depth of the potential well, ϵ, and the finite distance of $\phi_{\mathrm{LJ}}(r_{ij}) = 0$, σ, as parameters. In the BUCKINGHAM expression, A and ρ together describe PAULI repulsion, while C is part of an attractive dispersion term. The MORSE potential equals $-D_{\mathrm{e}}$ as the global minimum at $r_{ij} = r_{\mathrm{e}}$. The parameter $a = \sqrt{k_{\mathrm{e}}/2D_{\mathrm{e}}}$ determines the width of the potential and is a function of the force constant of the bond k_{e}. All aforementioned parameters are specific to each pair of species.

In most cases a set of parameters is fitted for a narrow set of particle types and must be validated for use cases beyond the fitting range. Due to their simple, analytical form, they exhibit lower transferability than *ab initio* methods, but are computationally much more efficient. In contrast, *ab initio* methods provide a more accurate description of the potential energy surface, but those simulations can exhibit poor statistics due to the limited system size. More recently, machine learning methods have been developed to close the gap between the accuracy of *ab initio* methods

and the efficiency of classical force fields.[44]

3.1.3 Integration Algorithms

Molecular dynamics simulations are based on NEWTON's second law of motion:

$$\mathbf{F}_i := -\frac{\partial V_i}{\partial \mathbf{r}_i} = m_i \frac{\partial^2 \mathbf{r}_i}{\partial t^2} \tag{3.5}$$

This second-order nonlinear ordinary differential equation can only be solved analytically for trivial systems. Instead, numerical integration schemes are used to approximate the solution. There are two main types of integration schemes: explicit schemes only require the properties at the current timestep, while implicit schemes require the properties at the current and the next timestep. Implicit integration schemes are numerically more stable and available for these tasks, but they are generally unpopular due to the complexity of the potential energy surface. Instead, explicit integration schemes are generally used. In classical molecular dynamics, the most commonly used algorithm is the VERLET algorithm[45] (or the velocity VERLET variant[46]). The integration scheme is obtained by starting from a TAYLOR expansion of the position $\mathbf{r}_i$ around the current time t for the forward ($+\Delta t$) and backward ($-\Delta t$) timestep:

$$\mathbf{r}_i(t+\Delta t) = \mathbf{r}_i(t) + \Delta t \mathbf{v}_i(t) + \frac{1}{2}\Delta t^2 \mathbf{a}_i(t) - \frac{1}{6}\Delta t^3 \frac{\partial^3 \mathbf{r}_i}{\partial t^3} + \mathcal{O}(\Delta t^4) \tag{3.6}$$

$$\mathbf{r}_i(t-\Delta t) = \mathbf{r}_i(t) - \Delta t \mathbf{v}_i(t) + \frac{1}{2}\Delta t^2 \mathbf{a}_i(t) + \frac{1}{6}\Delta t^3 \frac{\partial^3 \mathbf{r}_i}{\partial t^3} + \mathcal{O}(\Delta t^4) \tag{3.7}$$

The first and second derivatives of the position $\mathbf{r}_i$ are the velocity $\mathbf{v}_i$ and the acceleration $\mathbf{a}_i$, respectively. All terms beyond third order are included in $\mathcal{O}(\Delta t^4)$. Summation of Eq. (3.6) and (3.7) leads to a simplified expression for the position at the time $t + \Delta t$, where all terms of uneven order cancel out:

$$\mathbf{r}_i(t+\Delta t) = 2\mathbf{r}_i(t) - \mathbf{r}_i(t-\Delta t) + \mathbf{a}_i(t)(\Delta t)^2 + \mathcal{O}(\Delta t^4) \tag{3.8}$$

The velocity is one of the terms of uneven order that is not present in Eq. (3.8) any more, but required for system properties such as temperature and pressure. It can be calculated by subtracting Eq. (3.7) from Eq. (3.6), dividing by $2\Delta t$, and neglecting terms of order $\mathcal{O}(\Delta t^2)$:

$$\mathbf{v}_i(t+\Delta t) = \frac{\mathbf{r}_i(t+\Delta t) - \mathbf{r}_i(t-\Delta t)}{2\Delta t} + \mathcal{O}(\Delta t^2) \tag{3.9}$$

This is not ideal, since the errors in position and velocity are not of the same order. In addition, the algorithm is not self-starting, as the position at the time $t - \Delta t$ is unknown for the first timestep.[1] The velocity variant of the VERLET algorithm uses a more elegant approach by shifting Eq. (3.7) by Δt:

$$\mathbf{r}_i(t) = \mathbf{r}_i(t+\Delta t) - \Delta t\mathbf{v}_i(t+\Delta t) + \frac{1}{2}\Delta t^2\mathbf{a}_i(t+\Delta t) + \frac{1}{6}\Delta t^3\frac{\partial^3\mathbf{r}_i}{\partial t^3} + \mathcal{O}(\Delta t^4) \tag{3.10}$$

Now, summation of Eq. (3.6) and (3.10) leads to an expression for the velocity update instead of the position update:

$$\mathbf{v}_i(t+\Delta t) = \mathbf{v}_i(t) + \frac{1}{2}\Delta t\left[\mathbf{a}_i(t) + \mathbf{a}_i(t+\Delta t)\right] + \mathcal{O}(\Delta t^3) \tag{3.11}$$

The position update is then obtained by inserting Eq. (3.11) into Eq. (3.6):

$$\mathbf{r}_i(t+\Delta t) = \mathbf{r}_i(t) + \Delta t\mathbf{v}_i(t) + \frac{1}{2}\Delta t^2\mathbf{a}_i(t) + \mathcal{O}(\Delta t^3) \tag{3.12}$$

Neglecting the terms of order $\mathcal{O}(\Delta t^3)$, the velocity VERLET algorithm is obtained by introducing half-timestep velocity update $\mathbf{v}_i\left(t + \frac{1}{2}\Delta t\right) := \mathbf{v}_i(t) + \frac{1}{2}\Delta t\mathbf{a}_i(t)$:

[1] The position at the time $t - \Delta t$ can be estimated by calculating $\mathbf{r}_i(-\Delta t) = \mathbf{r}_i(0) - \mathbf{v}_i(0)\Delta t$, which requires an initial guess for the velocity. This initial guess is also required for evaluation of the velocity variant and cannot be avoided.

$$\mathbf{r}_i(t+\Delta t) = \mathbf{r}_i(t) + \Delta t \mathbf{v}_i\left(t+\frac{1}{2}\Delta t\right) \tag{3.13}$$

$$\mathbf{v}_i(t+\Delta t) = \mathbf{v}_i\left(t+\frac{1}{2}\Delta t\right) + \frac{1}{2}\Delta t \mathbf{a}_i(t+\Delta t) \tag{3.14}$$

The implementation of the velocity VERLET algorithm can be done in a four-step process:

1. $\mathbf{v}_i(t+\frac{1}{2}\Delta t) = \mathbf{v}_i(t) + \frac{1}{2}\Delta t \mathbf{a}_i(t)$
2. $\mathbf{r}_i(t+\Delta t) = \mathbf{r}_i(t) + \Delta t \mathbf{v}_i\left(t+\frac{1}{2}\Delta t\right)$
3. Calculate $\mathbf{a}_i(t+\Delta t)$ from the forces
4. $\mathbf{v}_i(t+\Delta t) = \mathbf{v}_i\left(t+\frac{1}{2}\Delta t\right) + \frac{1}{2}\Delta t \mathbf{a}_i(t+\Delta t)$

The VERLET algorithm is a symplectic integrator, conserving phase space volume and energy. This is especially relevant for long-term simulations, where accumulation of errors can lead to unphysical results. Its time-reversibility enables running trajectories backwards by changing the sign of Δt, which can simplify, i.a., error checking and time-averaged property calculations. The choice of a value for the timestep Δt is critical. A large Δt can accelerate simulations accompanied by a decrease in accuracy, while a small Δt generally improves accuracy but may lead to numerical instabilities due to the accumulation of round-off errors. The timestep should ideally resolve the fastest vibrational modes (e.g. 20 THz $\rightarrow$ 50 fs[47]), thus it is typically in the single-digit femtosecond range.[37]

3.1.4 Ensembles

A single configuration of a system is not sufficient to describe its properties. Even at absolute zero temperature, due to zero-point vibrational modes, a system can explore multiple configurations. The complexity of these configurations increases with system size.

At non-zero, finite temperatures, systems in equilibrium sample numerous distinct microstates. These systems fluctuate around one or more minima of the potential energy surface, and their

equilibrium state is best described by a probability distribution in phase space. Statistical thermodynamics imply that the probability of each structure is a function of the temperature and some form of energy, depending on the external conditions. Fixed variables define the ensemble, e.g. the NpT ensemble is characterized by a constant number of particles N, constant pressure p and constant temperature T. Caution must be taken as most simulations do not have fixed values for some of these variables, but rather apply various techniques to ensure convergence of the time averages to given values.

In three-dimensional space, a classical system without external forces is represented by $6N$ coordinates. This $6N$-dimensional space is called phase space, and one point in phase space corresponds to one (micro)state of the system. The $6N$ coordinates are distributed over position $\mathbf{r}_i$ and momentum $\mathbf{p}_i$ (where both are three-dimensional vectors). The total momentum and position are then given by the sum of the individual momenta and positions:

$$\mathbf{r} = \sum_i^N \mathbf{r}_i = \sum_i^N (x_i, y_i, z_i) \tag{3.15}$$

$$\mathbf{p} = \sum_i^N \mathbf{p}_i = \sum_i^N \left(p_{x,i}, p_{y,i}, p_{z,i}\right) \tag{3.16}$$

The total energy E is the sum of the kinetic and potential energy of the system. The potential energy E_{pot} of the system is simply the sum of the potential energies of all particles, as determined by the force field. The total kinetic energy E_{kin} is defined as the sum of the kinetic energies of all particles:[37]

$$E_{\text{kin}} := \frac{1}{2} \sum_i m_i \mathbf{v}_i^T \mathbf{v}_i \tag{3.17}$$

According to the equipartition theorem, the average kinetic energy of a particle in a system at temperature T is $\frac{1}{2} k_{\text{B}} T$ per degree of freedom. For a three-dimensional system with N particles, this results in an expression for the "kinetic temperature" T_{kin}:

$$T_{\text{kin}} = \frac{2E_{\text{kin}}}{3Nk_{\text{B}}} = \frac{1}{3Nk_{\text{B}}} \sum_{i}^{N} m_i \mathbf{v}_i^T \mathbf{v}_i. \tag{3.18}$$

It is important to note that the kinetic temperature is not the same as the thermodynamic temperature T of the system, as the latter is obtained as the time average of the kinetic temperature. More details are provided in Sec. 4.

The pressure P is given as the sum[2] of a kinetic and a potential energy part:[48,49]

$$P = \frac{2}{V}(E_{\text{kin}} - W) = \frac{Nk_{\text{B}}T}{V} + \frac{1}{3V} \sum_{i}^{N} \mathbf{r}_i^T \mathbf{F}_i \tag{3.19}$$

Here, $\mathbf{F}_i$ is the total force acting on particle i. The second term is the virial contribution,[50,51] equal to $-\frac{\mathrm{d}U}{\mathrm{d}V}$ (where $U = E_{\text{pot}}$):

$$W := -\frac{1}{2} \sum_{i}^{N} \mathbf{r}_i^T \mathbf{F}_i \tag{3.20}$$

Microcanonical Ensemble

The conceptually simplest ensemble is the microcanonical ensemble (NVE), in which the total energy E is strictly conserved. The velocity VERLET algorithm is straightforward to implement for this ensemble, as all particles experience an undamped motion. Forces are evaluated as the time derivative of the momentum vectors ($\mathbf{F}_i = \frac{\mathrm{d}\mathbf{p}_i}{\mathrm{d}t}$). This ensemble is rarely used for simulations of diffusion processes, because one is usually interested in the dynamics of the system at a temperature rather than a fixed energy.[46]

[2] Strictly speaking, it is necessary to introduce the kinetic energy and the virial as tensors to obtain a pressure tensor rather than a scalar. This is done by replacing the dot products $\mathbf{v}_i^T \mathbf{v}_i$ and $\mathbf{r}_i^T \mathbf{F}_i$ with the dyadic products $\mathbf{v}_i \otimes \mathbf{v}_i$ and $\mathbf{r}_i \otimes \mathbf{F}_i$, respectively. Since only the scalar pressure is of interest here, this can be omitted for simplicity.

Canonical Ensemble

Instead of fixing the energy, the canonical ensemble (NVT) attempts to keep the temperature of a system constant. This is achieved by application of a thermostat, which modifies the velocities of particles (see Sec. 3.1.5). It is important to understand that the temperature is not constrained to a certain value as it is the case for the energy in the microcanonical ensemble, since this would require the kinetic energy to be fixed, or rather, rescaled to the target temperature at each timestep.[52] Such a strict constraint would lead to an unphysical trajectory of the system. In fact, the fluctuation (variance) of the kinetic temperature (3.18) around the target temperature is a function of the number of particles N, as described in Sec. 4.[35,53–55]

Isothermal-isobaric Ensemble

The isothermal-isobaric ensemble (NpT) combines thermostating with additional barostating. This allows the system to fluctuate around its equilibrium volume at a given temperature and pressure. The barostat modifies the lattice vectors of the simulation cell and thus the particle positions according to its specific implementation (see Sec. 3.1.5). Similar to the temperature, the pressure is not strictly constant, but fluctuates around the target value with a variance that is a function of the isothermal compressibility (see Sec. 4).

3.1.5 Thermostats and Barostats

In order to maintain a constant temperature in a molecular dynamics simulation, a thermostat is applied to the system. There are three main types of thermostats used in classical molecular dynamics simulations: stochastic, velocity rescaling, and extended system thermostats. Appling a barostat and/or thermostat to the system is done by appropriate modification of the velocity VERLET algorithm.[35,37,49,56]

Stochastic Thermostats

Stochastic thermostats are based on the idea of mimicking the coupling of the system to a heat bath. In the ANDERSEN thermostat,[57] a number of particles are selected at random at each timestep and their velocities (and thus their momenta) are resampled from a GAUSSian distribution at the target temperature. The LANGEVIN thermostat[58] adds a random force and a friction term to the equations of motion for all particles. The magnitudes are determined such that the fluctuation-dissipation theorem is satisfied. These stochastic thermostats (unless modified) are not suitable for simulations of diffusion processes, as they destroy the momentum transfer between particles.

Velocity Rescaling Thermostats

While exact velocity rescaling ("strong coupling") can force the system to a certain temperature at each timestep,[52] it lacks a physical basis. The BERENDSEN thermostat[59] thus introduces a "weak coupling" to exponentially rescale the velocities of all particles to the target temperature:

$$\frac{\mathrm{d}T}{\mathrm{d}t} = \frac{T_0 - T}{\tau} \tag{3.21}$$

The coupling parameter τ controls the strength at which the system is coupled to the heat bath, and the target temperature T_0 is the desired temperature. Due to this coupling, the thermostat does not produce a correct canonical ensemble: it disproportionally samples temperatures (and thus velocities and kinetic energies) close to the target temperature, which does not reproduce the true MAXWELL–BOLTZMANN distribution.[60] Furthermore, one commonly observed undesirable phenomenon with this type of thermostat is the so-called *flying ice cube* effect, where rescaling leads to all kinetic energy being transferred to translational of (and rotation around) the center of mass.[61,62]

Extended System Thermostats

The third type of thermostat is the extended system thermostat, which is based on the idea of adding an additional degree of freedom to the system that acts as a heat bath. The widely used

NOSÉ[53]–HOOVER[54] thermostat introduces a fictitious particle with a mass Q and temperature T_0 that interacts with the system by modifications of the equations of motion. It thus applies an indirect rescaling of the velocities, which is more physical than the direct rescaling. In principle, the resulting ensemble can be considered canonical. However, the temperature will exhibit periodic oscillations with a frequency depending on Q, and only large systems will behave ergodically.[55] It is, despite its limitations, one of the most widely used thermostats in molecular dynamics simulations.

3.2 Density Functional Theory

3.2.1 Introduction to DFT

Density functional theory (DFT) has become a widely used tool in computational materials science to study the electronic structure of solid-state materials. Historically, DFT emerged as a more exact alternative to traditional electronic structure methods like HARTREE–FOCK (section 3.2.3), which rely on complex many-electron wavefunctions. By focusing on the electron density as the fundamental quantity, DFT cuts the problem down to a (semi-)local single-particle description.[3] This reduces the computational cost significantly, while maintaining accuracy for many practical cases.

DFT aims to solve the time-independent, non-relativistic form of the SCHRÖDINGER equation, given as

$$\mathcal{H}\Psi = E\Psi. \tag{3.22}$$

The operator $\mathcal{H}$ is the HAMILTONian, and can be written as the sum of the kinetic ($\hat{T}$) and potential energy operators ($\hat{V}$). The energy E is associated with the wave function Ψ of the quantum chemical system. Exact solutions in closed form are available only for one-electron systems; many-electron systems require approximations.

According to the BORN–OPPENHEIMER approximation,[63] equations for the ionic dynamics are

[3] HARTREE–FOCK also employs a single-particle description, but includes non-local exchange.

decoupled from equations for the electronic state, as the nuclei are much heavier than the electrons. The electronic SCHRÖDINGER equation is then given as:

$$\mathcal{H}_{\mathrm{el}}\Psi_{\mathrm{el}} = E_{\mathrm{el}}\Psi_{\mathrm{el}}, \tag{3.23}$$

with the electronic HAMILTONian $\mathcal{H}_{\mathrm{el}} = \hat{T}_{\mathrm{el}} + \hat{V}_{\mathrm{ee}} + \hat{V}_{\mathrm{ne}}$, where $\hat{T}_{\mathrm{el}}$ is the kinetic energy operator, $\hat{V}_{\mathrm{ee}}$ is the electron-electron interaction operator, and $\hat{V}_{\mathrm{ne}}$ is the electron-nucleus interaction operator. Here, the nuclei coordinates are considered fixed and are used as parameters. The total energy of the system is then given as the sum of the electronic and (constant) nuclear energy.

The wavefunction Ψ itself is not an observable quantity, but its square modulus, $|\Psi|^2$, can be interpreted as the probability density of finding an electron in a certain volume element, according to the BORN rule.[64]

3.2.2 Periodicity and the Bloch Theorem

The theoretical description of a finite-sized, molecular (gas-phase) system involves a finite number of atoms. A molecule's atomic positions are represented by real-space vectors, $\mathbf{r}$:

$$\mathbf{r} = n_1\mathbf{e}_1 + n_2\mathbf{e}_2 + n_3\mathbf{e}_3, \tag{3.24}$$

where $\mathbf{e}_i$ are the unit vectors of the coordinate system. A 3-dimensional solid-state system, on the other hand, shows (effectively) infinite periodicity in space. By exploiting the translational symmetry of the crystal lattice, the description can be greatly simplified, as all information about the system is contained in the unit cell. Instead of using real space, it is then more convenient to use reciprocal space, where the reciprocal vector $\mathbf{K}$ is defined as:

$$\mathbf{K} = m_1\mathbf{g}_1 + m_2\mathbf{g}_2 + m_3\mathbf{g}_3 \tag{3.25}$$

where $\mathbf{g}_i$ are the reciprocal lattice vectors. The reciprocal lattice is the FOURIER transform of the real-space lattice, such that a large cell vector in real space corresponds to a small cell vector in reciprocal space ($\exp(i\mathbf{K}^T\mathbf{r}) = 1$). The BLOCH theorem states that the wave function of an electron in a periodic potential can be written as a product of a plane wave and a periodic function:

$$\psi_{n\mathbf{k}}(\mathbf{r}) = e^{i\mathbf{k}\cdot\mathbf{r}} u_{n\mathbf{k}}(\mathbf{r}) \tag{3.26}$$

The wave vector $\mathbf{k}$ is a quantum number that describes the periodicity of the wave function, and $u_{n\mathbf{k}}(\mathbf{r})$ is a periodic function with the same periodicity as the crystal lattice. The BLOCH theorem allows the wave function to be described in terms of a small number of wave vectors in the first BRILLOUIN zone, which may be understood as the unit cell of the reciprocal lattice. The density of the mesh wave vectors required to properly describe the wave function is system-dependent.

One way of constructing the wave vectors is the MONKHORST–PACK scheme.[65] For a given mesh of $N_1 \times N_2 \times N_3$ mesh points, the wave vectors are constructed as follows:

$$\mathbf{k}_\alpha = \mathbf{g}_1 \frac{k_1 + \frac{1}{2}}{N_1} + \mathbf{g}_2 \frac{k_2 + \frac{1}{2}}{N_2} + \mathbf{g}_3 \frac{k_3 + \frac{1}{2}}{N_3} \tag{3.27}$$

where $0 \leq k_i < N_i$ are integers. The MONKHORST–PACK scheme ensures that the mesh points are distributed evenly in the BRILLOUIN zone. The number of mesh points required for a calculation can be significantly reduced by exploiting the crystal lattice's symmetry. Furthermore, larger real-space unit cells often necessitate fewer mesh points in their corresponding smaller reciprocal space cells to achieve convergence.

3.2.3 HARTREE–FOCK Theory

The HARTREE–FOCK (HF)[66,67] method is one of the first approaches to solve the many-electron problem in quantum mechanics. It is based on the idea of expressing the many-electron wave function as a SLATER determinant of single-electron wave functions or spin orbitals. The strength of this method is that the PAULI exclusion principle is automatically satisfied, as the wave function

(the SLATER determinant) is antisymmetric with respect to the exchange of two electrons.

The spin orbitals can be obtained by using the RAYLEIGH[68]–RITZ[69] variational principle, which states that the energy of any trial wave function is always greater than or equal to the true ground state energy, E_0:

$$E_0 \leq E_{\text{trial}} = \frac{\langle \Psi_{\text{trial}} | \, \mathcal{H} \, | \Psi_{\text{trial}} \rangle}{\langle \Psi_{\text{trial}} | \Psi_{\text{trial}} \rangle} \tag{3.28}$$

By variation of Ψ_{trial} and minimisation of E_{trial}, the ground state energy and wave function can be obtained.

The HF method includes a full treatment of the exchange interaction (due to the antisymmetry of the SLATER determinant), but it fails to account for electron correlation. The reason for this is a limitation to only one SLATER determinant, which causes the electrons to only experience the mean field of the other electrons. Another problem with the HF method, specifically for periodic solids, is the high computational cost, and the poor scaling with system size [$\mathcal{O}(N^4)$]. While *post-HF* methods like *Configuration Interaction* (CI) and *Coupled Cluster* (CC) can account for electron correlation, they are even more computationally expensive.[38]

3.2.4 Hohenberg-Kohn Theorems

The first idea of using the electron density as the central quantity in quantum mechanics was proposed by THOMAS and FERMI in 1927.[70,71] In their theory, the energy $E[\rho(\mathbf{r})]$ of a system is a functional of the spatial electron density $\rho(\mathbf{r})$. The THOMAS–FERMI model never gained widespread acceptance, as it failed to explain the electronic shell structure and chemical bonding. The reason for this failure was the approximation of the kinetic energy based on a homogeneous electron gas.

The breakthrough in the development of modern DFT came with the work of HOHENBERG and KOHN in 1964[72] by proving two theorems:[73,74]

1. The external potential $V(\mathbf{r})$ can be determined, except for a trivial additive constant, using

only the electron density $\rho(\mathbf{r})$. Thus, it follows:[6]

$$\Psi \equiv \Psi[\rho(\mathbf{r})] \tag{3.29}$$

2. By variation of the energy functional $E[\rho(\mathbf{r})]$, the exact ground state energy can be obtained and the electron density $\rho(\mathbf{r})$, that minimises the energy, is the exact ground state density:

$$E_0 = \min_{\rho(\mathbf{r})} E[\rho(\mathbf{r})] \tag{3.30}$$

The HOHENBERG–KOHN theorems provide the theoretical foundation for DFT, but they do not include a direct method for calculating the electron density.

3.2.5 Kohn–Sham Equations

The KOHN–SHAM approach introduces a fictitious system of non-interacting electrons that has the same ground-state density as the real interacting system. The electron density of this auxiliary system is described as

$$\rho(\mathbf{r}) = \sum_i^N \rho_i(\mathbf{r}) = \sum_i^N |\psi_i(\mathbf{r})|^2 , \tag{3.31}$$

where $\psi_i(\mathbf{r})$ are the KOHN–SHAM orbitals. This auxiliary system is described by single-particle HAMILTONians, which includes the external potential, the classical COULOMB interaction, and an additional term, the exchange-correlation potential, to account for the effects of electron-electron interactions (including kinetic energy corrections). These SCHRÖDINGER-like equations or KOHN–SHAM equations are given by:

$$\left[-\frac{\hbar^2}{2m}\nabla^2 + V_{\text{ext}}(\mathbf{r}) + V_{\text{H}}(\mathbf{r}) + V_{\text{XC}}(\mathbf{r})\right]\psi_i(\mathbf{r}) = \epsilon_i\psi_i(\mathbf{r}). \tag{3.32}$$

Solving these equations yields the KOHN–SHAM orbitals and their corresponding eigenvalues, as well

as the actual electron density according to Eq. (3.31). KOHN–SHAM DFT provides, in principle, an exact description of the electronic structure in the ground state in terms of electronic e**x**change and **c**orrelation (XC). While the KOHN–SHAM equations provide a computationally efficient way to solve the many-electron problem, the exact form of the exchange-correlation potential is unknown except for a few trivial cases (assuming a reasonable amount of calculation time).[75,76] Approximations to this term are discussed the following section.

3.2.6 Exchange-Correlation Functionals

The exchange-correlation energy is generally only a small part of the total energy of a system, but it contributes significantly to the binding energy between atoms. Since the exact form of the exchange-correlation energy is unknown, approximations are required to solve the KOHN–SHAM equations. The different flavours of these exchange-correlation functionals determine the accuracy of the DFT calculations. The order of the four main types of functionals below is known as the JACOB's ladder,[77] where a higher rung indicates a higher level of sophistication, but at the cost of increased computational expense.

Local (Spin) Density Approximation (LSDA)[78] The simplest form of exchange-correlation functional is the local density approximation (LDA), which is based only on the spatially varying electron density $\rho(\mathbf{r})$. It was, similar to THOMAS–FERMI theory, originally derived for the uniform electron gas.[72] It yields reasonable results for many solid-state systems, but performs poorly for atomisation energies of molecules by overestimating the binding energy.

Generalized Gradient Approximation (GGA)[79–82] By including the gradient of the electron density, the generalized gradient approximation (GGA) accounts for the inhomogeneity of the electron density. This leads to similar or often improved results for solids, while greatly improving the description of molecular systems compared to LDA. Still, GGA functionals violate many exact constraints of the exchange-correlation energy, and, more problematically, their variants either predict accurate energies or geometries, but rarely both.

Table 3.1 Overview of different types of exchange-correlation functionals.

Functional type	**Description**
Local (spin) density approximation (LDA)	$\epsilon_{\mathrm{XC}}^{\mathrm{LDA}}(\rho(\mathbf{r}))$
Generalized gradient approximation (GGA)	$\epsilon_{\mathrm{XC}}^{\mathrm{GGA}}(\rho(\mathbf{r}), \nabla\rho(\mathbf{r}))$
Meta-GGA	$\epsilon_{\mathrm{XC}}^{\mathrm{GGA}}(\rho(\mathbf{r}), \nabla\rho(\mathbf{r}), \tau(\mathbf{r}))$
Hybrid methods	$\alpha E_{\mathrm{X}}^{\mathrm{HF}} + (1-\alpha)E_{\mathrm{X}}^{\mathrm{DFT}} + E_{\mathrm{C}}^{\mathrm{DFT}}$

Meta-GGA[83–87] A comparatively easy way to circumvent the dilemma of either accurate energies or geometries is the inclusion of the KOHN–SHAM kinetic energy density in the functional. These types of functionals (meta-GGA) are only slightly more computationally expensive than GGA functionals because the kinetic energy density is readily available from the occupied KOHN–SHAM orbitals.

Hybrid methods[88,89] Hybrid methods replace a fraction of the exchange and correlation energy in a standard DFT functional with exact exchange energy, taken from HARTREE–FOCK theory. The mixing parameter α determines the fraction of exact exchange energy included in the hybrid functional. The tendency of HARTREE–FOCK to over-localise electrons alleviates the over-delocalisation of GGA functionals. Hybrid functionals significantly increase the computational cost compared to (meta-)GGA functionals, often by more than one order of magnitude.

Practical Considerations

Typically, LDA tends to underestimate bond lengths and lattice parameters (a phenomenon known as "overbinding"), whereas GGA usually overestimates them.[6,90–92] In come cases, more accurate results can come from a supposedly less accurate functional due to favourable error cancellation (e.g., phonon frequencies are sometimes better described by LDA than GGA functionals).

One of the most widely used GGA functionals is PBE, developed by PERDEW, BURKE, and ERNZERHOF.[93,94] The revised version PBEsol[95,96] specifically designed for solids yields more accurate lattice parameters, with the drawback of less accurate (cohesive) energies.[97]

The major strength of meta-GGA functionals over GGA (and LDA) is their ability to differentiate between single-orbital and overlap regions. This allows for a more accurate description of

both molecules and solids. One of the most widely used meta-GGA functionals is the Strongly Constrained and Appropriately Normed (SCAN) functional developed by SUN, RUZSINSZKY, and PERDEW,[98] which satisfies all 17 known physical constraints[4] of the exact exchange-correlation functional. SCAN has been shown to provide improved accuracy for the prediction of bulk properties from semiconducting oxides.[99–102] The lower numerical stability of the SCAN functional compared to GGA and LDA has prompted the development of the more stable, regularised rSCAN[103] and restored-regularised r^{2}SCAN[104–106] functionals. This improvement of numerical stability is achieved by relaxing one of the 17 constraints (specifically the fourth order gradient expansion constraint for exchange GE4X).[104–106] The r^{2}SCAN functional converges on average faster than the SCAN functional (but slower than the PBEsol functional).[107]

While the aforementioned (semi-local) functionals produce accurate results for many properties, especially for materials with slowly varying electron densities (for which the electron gas is a good starting point), they still suffer from a poor description of the band gap. Semi-local functionals lack the discontinuity of the derivate of the functional with respect to the number of electrons that is present in exact KOHN–SHAM DFT.[108] The description is worse in systems with rapidly varying electron densities, such as systems with localised electronic states or magnetic effects. Hybrid functionals have been developed to mitigate these issues while maintaining the single-particle reference (and thus avoiding the high computational cost of many-body methods). These functionals combine the semi-local exchange-correlation functional with a fraction of exact exchange from HARTREE–FOCK theory, which includes the exact exchange energy but neglects the correlation energy (see section 3.2.3). Thus, HARTREE–FOCK theory alone overly localises electronic states, but a specific fraction of it (typically 0.1 to 0.5) can greatly improve the description of band gaps. The downside is the increased computational cost of more than an order of magnitude.

There are two important categories of hybrid functionals for solids: Global (or unscreened) hybrid functionals include a fixed fraction of exact exchange for all pair-separation distances. One established variant is the PBE0 functional,[109,110] which includes 25 % exact exchange and 75 % standard PBE exchange. This specific fraction was determined by perturbation theory.[109] In solids, especially those with small or no band gaps, these functionals are extremely computationally costly because the long-range part of the HARTREE–FOCK exchange decays slowly. There are essentially two ways to address this issue, either by artificial truncation or by acceleration of the spatial decay. Since truncation schemes lead to problems in delocalised systems,[111] a more promising approach is the screening of the COULOMB interaction for a faster decay. One aspect to consider is the compen-

[4] PBE, on the other hand, only satisfies 11 of the constraints.

sation of the neglected interactions arising from this approach. To address this, range-separated (or screened) hybrid functionals have been developed.[112] They employ a partition of the electron repulsion operator into short-range and long-range components, which are treated separately only for the exchange interaction but not in the Hartree and correlation terms. The short-range exchange is then mixed, but the long-range exchange is fully DFT. The popular HEYD–SCUSERIA–ERNZERHOF (HSE) functional[113–115] uses the expression

$$\frac{1}{|\mathbf{r}|} = \frac{\operatorname{erfc}(\omega|\mathbf{r}|)}{|\mathbf{r}|} + \frac{\operatorname{erf}(\omega|\mathbf{r}|)}{|\mathbf{r}|} \tag{3.33}$$

with the error function erf for the long-range and the complementary error function erfc $= 1 -$ erf for the short-range part. The adjustable parameter ω ($= 0.207\,\text{Å}^{-1}$ for HSE06) determines the range separation; at $|\mathbf{r}| \geq 2/\omega$, the short-range interactions become negligible. The choice of the error function is purely for practical reasons.[113] For $\omega \to 0$, it transforms into the PBE0 functional, while for $\omega \to \infty$, it becomes the PBE functional.

In molecular computational chemistry, screened hybrid functionals with HARTREE–FOCK exchange for the long range part are more popular (e.g. B3LYP[89,116–118]), since the correct long-range decay of the exchange interaction far from the nuclei may be important. In this case, the incorrect asymptotic behaviour of the exchange as $-\alpha|\mathbf{r}|^{-1}$ is replaced by the correct $-1|\mathbf{r}|^{-1}$.[119]

HUBBARD *U* Correction

As described above, non-hybrid exchange-correlation functionals perform especially poorly for systems with localised electronic states. A computationally cheaper alternative than employing hybrid functionals is to use a HUBBARD U repulsion parameter. The idea of DFT+U[120] is to correct the strong on-site COULOMB repulsion by adding a HUBBARD-like term to the HAMILTONian. This correction is mostly used for the d and f orbitals of transition metals and rare earth elements, but it can also be applied to p orbitals.[121–123]

There are two established variants of DFT+U corrections in DFT. LIECHTENSTEIN *et al.*[124] use the parameters U (on-site COULOMB repulsion) and J (on-site exchange), whereas DUDAREV *et al.*[125] use the parameters U and J as a single parameter $U_{\text{eff}} = U - J$. The major challenge of this method

is to determine an appropriate HUBBARD U parameter for a given element, since no single true value exists. Methods to determine U include linear response theory,[126] fitting to experimental reaction energies,[127] or adjustment for target properties (e.g., band gaps, magnetic moments, lattice parameters etc.).

3.2.7 Basis Sets and Pseudopotentials

To solve the KOHN–SHAM equations, the KOHN–SHAM orbitals must be expanded in a basis set, either atomic orbitals or plane waves. Atomic orbital basis sets are centred on the atomic nuclei and can be represented by SLATER-type orbitals (STOs) or GAUSSian-type orbitals (GTOs). They are mostly used for the description of molecules, where the atomic orbitals are well-localised. Plane wave basis sets, delocalized functions periodic within the simulation cell, are particularly effective for describing solids. The **k**-dependent wave functions follows BLOCH's theorem Eq. (3.26):

$$\psi_n(\mathbf{k}, \mathbf{r}) = \sum_{\mathbf{G}} c_{n\mathbf{k}}(\mathbf{G}) e^{i(\mathbf{k}+\mathbf{G})^T \mathbf{r}}, \tag{3.34}$$

where **G** are the reciprocal lattice vectors and $c_{n\mathbf{k}}(\mathbf{G})$ are the expansion coefficients. The choice of basis set can significantly affect the accuracy and computational cost of DFT calculations: Larger basis sets generally provide higher accuracy but also require more computational resources. Two key quantities for Plane Wave Basis sets are the kinetic energy cutoff and the number of valence electrons. The kinetic energy cutoff determines the number of plane waves used to expand the wave functions:

$$\frac{\hbar^2}{2m} |\mathbf{k} + \mathbf{G}|^2 \leq E_{\text{cut}} \tag{3.35}$$

It follows from Eq. (3.35) that the number of plane waves is **k**-dependent, such that the number of plane waves changes smoothly with the cell volume (a criterion using G_{cut} would have a constant number of plane waves for each **k**-point, but would converge more slowly).

The second key quantity is the number of valence electrons. The high potential energy in the core region leads to strong oscillations in the valence wavefunctions for that region, which requires

a large number of plane waves to converge. Since core electrons minimally influence valence properties anyway, pseudopotentials replace them with an effective potential that reproduces the core electrons' scattering behaviour. This approach is known as the frozen-core approximation.

There are different types of pseudopotentials. Norm-Conserving Pseudopotentials ensure that the wavefunction and its derivative are continuous at the core radius. Ultrasoft Pseudopotentials allow for a smoother cutoff of the core wavefunction, which can lead to a reduction in the number of plane waves required, but are more expensive to generate. The Projector Augmented Wave (PAW)[128] method is a more convenient approach to handling core electrons. Here, the wavefunction is divided into a smooth part and a localized part. The localized part is confined to the core region and is treated using atomic-like functions. The smooth part is treated using plane waves or other basis sets. The connection between the smooth and localized parts is established using projection operators.

3.3 Defect and Transition State Calculations

3.3.1 Defect Formation Energies

Isolated defects are more difficult to model than perfect lattice structures. Since they are not periodic (unless a system of ordered defects is considered), using just a single unit cell is rarely sufficient to describe them, because the self-interaction between periodic images of the defect can be significant and lead to substantial errors in the calculated properties. The most straightforward way to improve the description is to use a supercell approach, where the defect is embedded in a large supercell of the host structure.

In the supercell approach, the defect formation energy E_f is calculated as the difference between the total energy of the supercell with the defect and the total energy of the perfect supercell, complemented by the chemical potentials of the species added or removed to create the defect:

$$E_f = E_{\text{def}} - E_{\text{host}} + \sum_i n_i \mu_i + q E_{\text{Fermi}}. \tag{3.36}$$

In this equation, E_{def} is the total energy of the supercell with the defect, E_{host} is the total energy

of the perfect supercell (with the same number of atoms except the defect), n_i is the number of atoms of species i added to or removed from the supercell to create the defect, and μ_i is the chemical potential of species i. For charged defects, the FERMI level must also be taken into account by adding the term qE_{Fermi}, where q is the charge of the defect (including its sign) and E_{Fermi} is the FERMI level. Additionally, the formation energy should be corrected for finite-size effects (see below in Section 3.3.1). Since the FERMI level depends on external conditions, defect formation energies are often reported as a function of the FERMI level.

Finite-size Corrections

Since the earliest attempts, calculations of charged defects have been a challenge. The long-range COULOMB interaction between charged defects and their periodic images can lead to significant errors in the calculated defect formation energies. To correct for these errors, several methods have been developed to account for the finite-size effects in supercell calculations.[129] They are based on a classical model of a charge distribution in a dielectric medium. Historically, the LESLIE–GILLAN method[130] (modelling point charge in an isotropic dielectric medium), the MAKOV–PAYNE method[131] (additionally considering higher-order multipoles) and the LANY–ZUNGER method[132] (additionally calculating the quadrupole moment and aligning the electrostatic potential) have been predecessors to the popular FREYSOLDT–NEUGEBAUER–VAN DE WALLE (FNV) method[133]. In the FNV method, the defect charge is described as a GAUSSian distribution, and the difference in the electrostatic potential between the defective cell (far away from the defect) and the bulk cell is aligned with the defect model potential. It is widely used in DFT calculations. More recently, the KUMAGAI–OBA method[134] was developed to extend the FNV method to anisotropic dielectric systems.

3.3.2 Nudged Elastic Band

Knowledge of the energy barrier of a chemical reaction is crucial for understanding the kinetics of the process. While it is comparatively easy to calculate the energy of the initial and final states, which are both local (and possibly even global) minima of the potential energy surface, the transition state between these states is more challenging to determine. Geometry optimisation methods are designed to find a minimum, whereas the transition state is a saddle point, a maximum along the

reaction coordinate but a minimum along all other degrees of freedom. Since the exact geometry of the minimum energy path is generally not known *a priori*, several methods have been developed to find the transition state and its energy barrier.

The original plain elastic band (PEB) method is intended to gather information about the minimum energy path (MEP) and to determine saddle points of minimum energy paths. A given number of successive intermediate configurations between initial and final state, termed *images*, represent the trajectory between those two states. In order to ensure equidistant images, additional spring forces between each pair of adjacent images along the path are introduced. This kind of "elastic band" will tighten during energy minimisation. Therefore, the PEB will yield an inaccurate MEP except for the special case of a collinear path. This lead to the development of the nudged elastic band (NEB) method. In this technique, both the real and the spring force are split into their components parallel and perpendicular to the path. During the energy minimisation, only the perpendicular part of the real force and the parallel part of the spring force are considered.[135,136] This way, the images are "nudged" towards the MEP and represent minima in respect to all degrees of freedom except the reaction coordinate.

In an NEB calculation, the $N+1$ images are denoted as $[\mathbf{r}_0, \mathbf{r}_1, \mathbf{r}_2, \dots, \mathbf{r}_N]$, whereat $\mathbf{r}_0$ and $\mathbf{r}_N$ are minima corresponding to the initial and final state. The algorithm optimises all $N-1$ intermediate states.

To split the forces into their components, the direction of the path must be determined first. It is considered to be the tangent τ_i at the point i along the path. It is approximated by both of the circumjacent images:

$$\tau_i = \frac{\mathbf{r}_i - \mathbf{r}_{i-1}}{|\mathbf{r}_i - \mathbf{r}_{i-1}|} + \frac{\mathbf{r}_{i+1} - \mathbf{r}_i}{|\mathbf{r}_{i+1} - \mathbf{r}_i|} \tag{3.37}$$

After normalisation of the tangent $\hat{\tau} = \frac{\tau}{|\tau|}$, the force $\mathbf{F}_i$ is calculated by evaluation of the perpendicular part of the real force $\nabla V(\mathbf{r}_i)|_\perp$ and the parallel part of the spring force $\mathbf{F}_i^s|_\parallel$ with the spring constant k:

$$\mathbf{F}_i = \mathbf{F}_i^s|_\parallel - \nabla V(\mathbf{r}_i)|_\perp \tag{3.38}$$

$$\nabla V(\mathbf{r}_i)|_\perp = \nabla V(\mathbf{r}_i) - \nabla V(\mathbf{r}_i) \cdot \hat{\tau}_i \tag{3.39}$$

$$\mathbf{F}_i^s|_\parallel = k[(\mathbf{r}_{i+1} - \mathbf{r}_i) - (\mathbf{r}_i - \mathbf{r}_{i-1})] \cdot \hat{\tau}_i \hat{\tau}_i$$

Except for mirror-symmetric energy barriers, the NEB method is not able to find the exact transition state.[135,136] To overcome this limitation, the *climbing image* (CI-NEB) variant has been developed. The transition state[33,137] corresponds to a saddle point of the energy hypersurface, i.e. a maximum regarding one degree of freedom (and still a minimum regarding all the other degrees of freedom). Within the unmodified NEB method, a energy minimisation to every degree of freedom would be performed so that the images move away from the MEP. After a few iterations of the standard NEB protocol, the image with the highest energy is selected and, only at this configuration, the real force parallel to the tangent τ_i is inverted, and the spring force is disregarded:[135,136]

$$\mathbf{F}_{i,\max} = -\nabla V(\mathbf{r}_{i,\max}) + 2\nabla V(\mathbf{r}_{i,\max})|_\parallel \tag{3.40}$$

The convergence of CI-NEB calculations depends, among other factors, on the choice of the spring constant k, the number of images N, the initial guess of the path, and the optimisation algorithm.

3.4 Monte Carlo Simulations

Relationships between atomistic structure and macroscopic properties can be investigated by means of MD simulations (see Sec. 3.1). However, the exploration of configurational space in MD is fundamentally limited by the timescales accessible to the simulation: rare events or transitions that occur infrequently may not be sampled within feasible simulation times. Monte Carlo simulations, on the other hand, are based on stochastic sampling of the phase space, which generally allows for a more efficient exploration of the relevant configuration space. Fundamentally, Monte Carlo simulations consider the probability of a system to be in a certain state, which is determined by the Boltzmann probability distribution:[138]

$$P(\mathbf{r},\mathbf{p}) = \frac{1}{Z}\exp\left(-\frac{\mathcal{H}(\mathbf{r},\mathbf{p})}{k_\mathrm{B}T}\right) \tag{3.41}$$

Here, Z is the partition function $Z = \int \exp\left(-\frac{\mathcal{H}(\mathbf{r},\mathbf{p})}{k_\mathrm{B}T}\right) \mathrm{d}\mathbf{r}\,\mathrm{d}\mathbf{p}$. The probability of a system to be in a certain state thus depends on the energy of this state and the temperature of the system.

3.4.1 Basic Principles of Monte Carlo Simulations

The basic idea of Monte Carlo simulations is to sample the phase space of a system by generating (pseudo-)random configurations and determining their energy. This stochastic trajectory is in contrast to the deterministic trajectory of MD simulations. Since the way in which the configurations are generated is controlled by the user setup, certain irrelevant degrees of freedom can be neglected, while others can be sampled more efficiently. For example, lattice defects or phase transitions may be explicitly included or excluded from the generation of configurations, while MD simulations would require them to be introduced by the dynamics of the system.

The thermal average of a property A can be calculated by sampling the phase space and weighting the values of A by the BOLTZMANN probability distribution:

$$\langle A\rangle = \int P(\mathbf{r},\mathbf{p})\,A(\mathbf{r},\mathbf{p})\;\mathrm{d}\mathbf{r}\,\mathrm{d}\mathbf{p} \tag{3.42}$$

Here, $\langle A\rangle$ is accessible without explicitly letting the positions and momenta of the particles evolve in time. In practice, the integral in Eq. 3.42 is approximated by a sum over a finite number of sampled configurations for $\mathbf{r}_i$ and $\mathbf{p}_i$, and these variables may be transformed into a set of variables that are more convenient for the system of interest.

3.4.2 METROPOLIS Algorithm

Instead of random sampling of configurations and weighting them consequently by their BOLTZMANN factor, METROPOLIS *et al.*[139] suggested to choose configurations according to their BOLTZ-

MANN factor and weighting them equally. The algorithm was later generalised by HASTINGS[140][5] and is composed of the following steps:[36]

1. A configuration $(\mathbf{r}_{i+1}, \mathbf{p}_{i+1})$ is generated by a random but controlled perturbation of the current configuration $(\mathbf{r}_i, \mathbf{p}_i)$.

2. The energy difference $\Delta\mathcal{H} = \mathcal{H}(\mathbf{r}_{i+1}, \mathbf{p}_{i+1}) - \mathcal{H}(\mathbf{r}_i, \mathbf{p}_i)$ is calculated. The probability of accepting the new configuration is given by:

$$P(\mathbf{r}_i, \mathbf{p}_i \to \mathbf{r}_{i+1}, \mathbf{p}_{i+1}) = \min\left[1, \frac{\exp\left(-\frac{\mathcal{H}(\mathbf{r}_{i+1}, \mathbf{p}_{i+1})}{k_\mathrm{B}T}\right)}{\exp\left(-\frac{\mathcal{H}(\mathbf{r}_i, \mathbf{p}_i)}{k_\mathrm{B}T}\right)}\right] = \begin{cases} 1 & \text{if } \Delta\mathcal{H} \leq 0 \\ \exp\left(-\frac{\Delta\mathcal{H}}{k_\mathrm{B}T}\right) & \text{if } \Delta\mathcal{H} > 0 \end{cases} \tag{3.43}$$

   In other words, the new configuration is always accepted if the energy is lower than the previous configuration. If the energy is higher, the new configuration is accepted with a probability that depends on the energy difference and the temperature of the system. In this case, a random number $z \in [0, 1]$ is generated, and the new configuration is accepted if $z \leq P$.

The value of $\langle A \rangle$ is then calculated by averaging over the accepted configurations.

3.4.3 Applications of Monte Carlo Simulations

Common types of perturbations in atomistic Monte Carlo simulations include the insertion, deletion, and displacement of single or groups of atoms, as well as the exchange of atoms between different sites, and lattice volume changes. Monte Carlo simulations can be employed to obtain thermodynamic properties of a system, but they may also be used to find minimum energy configurations that are not realistically accessible by MD simulations. For example, sluggish diffusion processes may restrict the phase space to be close to the initial state, while Monte Carlo simulations can reach more distant configurations.

[5] The original METROPOLIS algorithm is a special case of the METROPOLIS–HASTINGS algorithm for a symmetric proposal distribution.

3.5 Codes

3.5.1 Structure Creation, Manipulation, and Analysis

Structures were created, manipulated, and analysed using the `pymatgen` (Python Materials Genomics)[141] and `ASE` (Atomic Simulation Environment)[142,143] packages. Polycrystalline structures were generated using the `atomsk`[144] software.

Visualisation of structures as well as further analysis was performed using `VESTA`[145] and `OVITO`[146].

3.5.2 Force Field Simulations

MD simulations were conducted in `LAMMPS` (Large-scale Atomic/Molecular Massively Parallel Simulator)[147,148]. Some static simulations were conducted in `GULP`[149–152] (General Utility Lattice Program).

3.5.3 Density Functional Theory Calculations

All DFT calculations were performed using the Vienna *ab initio* Simulation Package (`VASP`).[153–156] Finite size corrections were calculated using the `sxdefectalign` code.[157] Charge partitioning was performed using the BADER analysis[158] and DDEC6 analysis.[159,160]

3.6 Computational Details

3.6.1 Force Field Simulations

The interactions in the molecular dynamics (MD) calculations are described with a short-range potential of the BUCKINGHAM form [Eq. (3.3)] and a long-range COULOMBic term [Eq. (3.1)]. The BALDUCCI potential[161] was used for simulations of CeO_2 (chapter 4), which is known to yield a migration barrier of 0.638 eV for oxygen in ceria.[162] For BSCF/CSCF materials (chapter 5), a set of parameters previously used in the literature was employed,[163,164] and the model was expanded to include Ca^{2+} using parameters derived for the same oxygen–oxygen potential. For (La,Sr)FeO_3 (chapter 7), parameters derived by ISLAM *et al.*[165] for (La,Sr)MnO_3 were used, with the model expanded to include Fe using parameters from CHERRY *et al.*[166] as applied in a static study of $LaFeO_3$.[167] The potential parameters for all systems are given in Tables S1, S2 and S3.

All MD calculations were carried out using the `LAMMPS` (Large-scale Atomic/Molecular Massively Parallel Simulator) code,[147,148] employing the velocity Verlet algorithm[45] with periodic boundary conditions. Simulations were performed in the isothermal–isobaric (NpT) ensemble at $p = 1013.25$ mbar, using a NOSÉ[53]–HOOVER[54] thermostat and barostat (damping times $t_p = 1$ ps, $t_T = 0.1$ ps) and a timestep of $\delta t = 1$ fs. METROPOLIS Monte Carlo calculations[139] were also performed as implemented in `LAMMPS`.

3.6.2 Density Functional Theory Calculations

DFT calculations were performed in the context of chapter 6. Core electrons were treated with PAW pseudopotentials[128] from the `VASP` 5.4 PERDEW–BURKE–ERNZERHOF (PBE)[93,94] potential set, as provided by the `VASP` developers (see Table 3.2).

In order to accurately describe the band gap, the hybrid HSE06 exchange-correlation functional is used.[113–115] The default value of 25% HARTREE–FOCK exchange was left unchanged to ensure compatibility with other HSE06 calculations[168–171] and because the (direct/indirect) computational band gap (3.33 eV/3.73 eV) is sufficiently close to the experimental band gap (3.25 eV/3.75 eV).[172,173]

Table 3.2 Pseudopotentials used in the calculations.

Atom	Name of potential	Electrons
Sr	Sr_sv	$4s^2 4p^6 5s^2$
Ti	Ti_sv	$3s^2 3p^6 3d^2 4s^2$
O	O	$2s^2 2p^4$
Ni	Ni	$3d^8 4s^2$

Collinear spin polarisation as well as aspherical contributions to the gradient corrections inside the PAW spheres were included. Calculations were initialised with high-spin and low-spin configurations and then continued only from the lower-energy state. If the initial calculation revealed the system to have equal spin up/spin down (e.g. all calculations with Ni^0 or without an Ni in the system), it was continued as a non-spin-polarised calculation to reduce the computational cost.

All calculations were performed under periodic boundary conditions. The plane-wave kinetic energies were truncated at 520 eV for the initial relaxation of the unit cell, yielding a lattice parameter of 3.899 Å. For subsequent calculations, the lattice parameters were kept fixed at a multiple of this value (i.e. 15.596 Å for the $4 \times 4 \times 4$ cell) and the plane-wave cutoff was reduced to 400 eV to reduce computational demand. For all supercell calculations with a $4 \times 4 \times 4$ expansion of the cubic unit cell, the **k**-point sampling was performed only at the Gamma point (the initial unit cell optimisation used a $7 \times 7 \times 7$ **k**-point sampling grid). Atomic positions were optimised until the residual force were below 0.02 eV $Å^{-1}$ (0.04 eV $Å^{-1}$ for NEB images). Climbing image (CI) NEB calculations were performed using the implementation by HENKELMAN *et al.*[135,136]

All calculations were carried out in an expansion of the cubic unit cell. This introduces a methodological error,[174] because tetragonal $SrTiO_3$ is the ground state at 0 K, but this error is negligible in the present case because of the low energy difference of the two polymorphs ($\Delta E < 0.001$ eV per atom with the HSE functional).

For the calculations of the charge-transition levels, corrections accounting for the periodic self-interaction of the charge were applied according to the FNV (FREYSOLDT, NEUGEBAUER, and VAN DE WALLE) scheme[133] as implemented in the sxdefectalign package.[157] The energy of an electron was calculated as the sum of VBM (Valence Band Maximum, obtained from a bandstructure calculation) and the band gap. The energy corrections were calculated for a total dielectric constant of 6.9, as obtained from a present DFT calculation. It is noted that this value differs from that

measured in experiments, but this is attributed to the imaginary soft TO1 phonon frequency present with both PBE and HSE functionals.[170] It is contended that the computational value of the dielectric constant should be used to obtain the correction term rather than the much higher experimental value, since this is consistent with the actual dielectric response of the material in the calculation.

For the thermodynamic energy calculations, the same corrections as mentioned above were applied. In addition, a HSE-specific correction[127,175] of +0.85 eV for the energy of a O_2 molecule to account for oxygen over-binding was applied. The procedure to include the effect of the oxygen chemical potential as a function of temperature and pressure is given in the main text.

For all CI-NEB calculations, no charge corrections were applied to obtain the energy barriers.

4 Best Practices for Molecular Dynamics Simulations of Ion Diffusion in Solids

Parts of this chapter have been submitted for publication:[1]

A. Bonkowski, R. A. De Souza, From Setup to Analysis: A Compact Guide to Performing Molecular Dynamics Simulations of Ion Transport in Solids, *submitted*.

4.1 Introduction

Before presenting results from molecular dynamics (MD) simulations, it is crucial to ensure that both the simulation setup and the subsequent data analysis are performed with care and rigour. In this chapter, best practices for molecular dynamics (MD) simulations, specifically for the study of ion diffusion in solids, are outlined.

Molecular dynamics (MD) simulations have become a powerful tool for investigating the finite-temperature properties of condensed-matter systems. By numerically solving Newton's equations of motion for all particles, MD simulations can provide insights into a wide range of phenomena, including diffusion[163,176–178], radiation effects[179–182], heat transfer[183–185], and chemical reactions[186–188]. In the field of energy materials, MD simulations have been particularly valuable for studying ion transport in solids, a process that plays a crucial role in applications such as Li batteries, solid oxide fuel cells, and solar-thermal devices.[189–195] By simulating the transport of ions within a crystal lattice, MD simulations can provide not only diffusion coefficients, and subsequently from simula-

[1] All simulations were prepared, carried out, and analysed by the author of this thesis. The submitted manuscript was written by the author of this thesis, with contributions from the co-author.

tions as a function of temperature, activation energies, but also atomic-scale insights into migration mechanisms.

The primary objective of many MD studies of ion transport is to determine the diffusion coefficient of that ion, generally as a function of temperature. Subsequently, an ARRHENIUS-type expression can be used to obtain the activation energy of the diffusion process. Such work has been carried out since the 1950s,[196] albeit with varying degrees of accuracy. Early MD simulations were limited by the computational resources available at the time, such that only fast diffusion processes could be studied, and even then, for only limited time periods, and mostly in small simulation cells containing low numbers of particles. For these reasons, the statistics of the data were often poor, and the results often had large uncertainties. Increases in computational power and the development of more sophisticated algorithms have allowed slower processes to be studied, for longer times, and in larger systems. It has also made even *ab initio* simulations of ion transport possible. More recently, the rise of machine learning (ML) approaches has allowed for relatively large systems to be investigated with close to *ab-initio* accuracy (although off-the-shelf ML potentials are not necessarily suitable for MD studies of ion transport).

An MD simulation, performed with no concentration gradient and without an external driving force, yields the tracer diffusion coefficient D_i^* of ion i from the evolution as a function of time of the ions' mean square displacement, $\langle \Delta\mathbf{r}_i(t)^2 \rangle = \langle ||\mathbf{r}_i(t) - \mathbf{r}_i(0)||^2 \rangle$:[37]

$$D_i^* = \frac{1}{2n_{\mathrm{dim}}} \lim_{t\to\infty} \frac{\mathrm{d}}{\mathrm{d}t} \langle \Delta\mathbf{r}_i(t)^2 \rangle, \tag{4.1}$$

where n_{dim} is the number of dimensions in which diffusion occurs. In most studies, however, D_i^* is obtained by fitting a linear function to a plot of $\langle \Delta\mathbf{r}_i(t)^2 \rangle$ vs. t, rather than by determining a limiting value, as indicated in Eq. (4.1).

While fitting a linear function to $\langle \Delta\mathbf{r}_i(t)^2 \rangle$ gives a reliable value of D_i^*, calculating the uncertainty of D_i^* solely from the regression error of the linear fit substantially underestimates the true uncertainty.[197] This is because the regression error assumes that each data point is an independent measurement, even though the data points show strong autocorrelation, $\langle \Delta\mathbf{r}_i(t + \Delta t)^2 \rangle$ being highly correlated with $\langle \Delta\mathbf{r}_i(t)^2 \rangle$ for small Δt. It is only recently that more sophisticated statistical methods[197,198] have made the true uncertainty accessible without performing a statistically significant number of independent MD simulations.

In this chapter, key practices to be kept in mind when performing MD simulations of ion diffusion in solids are examined. To begin with, the importance of ensuring proper equilibration of the simulation cell prior to collecting transport data is discussed. Subsequently, the inherent fluctuations of thermodynamic quantities are considered, and the relationship between these fluctuations and system properties is explained. The impact of properly accounting for thermal lattice expansion on the results is also examined. The improvement of ARRHENIUS fits by considering the statistical uncertainty of diffusion coefficients is demonstrated (because this is often underestimated and especially high for low temperatures). Finally, the conversion of tracer diffusion coefficients to ionic conductivities is discussed. These points are illustrated with a range of different MD simulations of oxygen tracer diffusion in oxygen-deficient ceria.

This is by no means an exhaustive list. Rather, it is a selection of important issues that are regarded as receiving insufficient attention in the literature. Other issues may be considered by other researchers to be equally worthy of examination.

4.1.1 Accuracy and Uncertainty

Uncertainty was mentioned above, but it is useful to define exactly what is meant, and to draw attention to the difference between uncertainty and accuracy. *Accuracy*[2] refers to how close a measurement (or the mean of multiple measurements) is to the true value, while *uncertainty* quantifies the range within which the true value is expected to lie. Simulations, being mathematical operations performed with a certain machine precision, typically exhibit high accuracy in replicating their model. When carried out again on the same platform, the simulation, being entirely deterministic, should yield exactly the same result. The accuracy of a simulation in reproducing the behaviour of a real-world system, however, depends on the quality of the underlying model.

The primary source of uncertainty in simulations stems from the finite number of particles and the limited simulation time. In contrast, real-world experiments, even when conducted under identical conditions (and assuming that they lead to identical systems), yield varying results due to inherent measurement uncertainties.

[2]Contrary to the common use in scientific literature, ISO defines accuracy as the combination of trueness and precision. In this work, the term accuracy is used only in the sense of trueness.

4.2 Force Fields

One model system was used for illustration purposes: oxygen-deficient ceria (that is CeO_2 containing oxygen vacancies and no charge compensating defects but a background charge). The force field[161] was chosen because it is robust and efficient, and because it has been successfully applied to ion transport in ceria.[162,199–201]

The choice of force field[202,203] is, of course, crucial for the accuracy and speed of the simulation. Some force fields may, for ion transport, give quantitative agreement with experiment, both in terms of absolute magnitude of D_i^* and its activation enthalpy; others may only allow comparisons of ion transport between different materials. It is evidently not necessary that ion transport data is required in the derivation of the force fields (see, e.g., Refs [204–207], in which force fields derived for glasses and binary oxides quantitatively describe diffusion data for titanate perovskites). Further discussion of this topic is beyond the scope of this chapter, since it strongly depends on the system under investigation.

4.3 Setup of the Simulation

4.3.1 Equilibration

To determine a tracer diffusion coefficient D_i^* accurately, the system must be in a well-defined thermodynamic state, characterized by thermodynamic variables that fluctuate around their respective equilibrium values. Depending on the thermodynamic ensemble used, some variables are allowed to fluctuate, either freely or under external control (e.g. by a thermostat or barostat), while others are kept constant. For example, in the NpT ensemble, the particle number (N) is fixed; temperature (T) and pressure (p) are controlled; and volume (V) and energy (E) adapt to these conditions [with all variables (other than N) fluctuating around their equilibrium values]. In the NVT ensemble, the volume is fixed and the temperature is controlled, while pressure and energy adapt to these conditions. In the NVE ensemble, energy and volume are fixed, and the temperature adapts to these conditions.

The problem is that the system needs to be given time to reach equilibrium from its initial state,

otherwise it will exhibit initialisation bias, that is, the result obtained depends on the system's initial state. Such a bias can be excluded by giving the system sufficient time, but too much time is a waste of computational resources. The key issue, then, is one of identifying the time from which equilibrium has been reached. Various schemes have been proposed to tackle the equilibration problem.[208–213] The relevant quantity is the optimal truncation time t_{eq}, which cuts off the initial transient but retains as much data as possible for accurate determination of properties. Ideally, the scheme should be robust, accurate, computationally cheap, applicable to any observable, not require manual intervention or inspection, and not rely on empirical or arbitrary parameters.[214] If these criteria are met, equilibration time detection can be carried out not only during post-processing, but also on-the-fly for, e.g., high-throughput simulations.

Several studies[214–217] have reviewed methods for determination of the equilibration time (sometimes called warm-up length or burn-in time) and concluded that the Marginal Standard Error Rule (MSER) is a well-suited metric.[218–221] This rule is based on the concept of minimising the uncertainty in the mean (it selects a truncation point that minimises the width of the confidence interval of the truncated mean). This is achieved by calculating the marginal standard error of the mean as a function of the truncation time and selecting the time at which it is minimal.[221] Importantly, the determined equilibration time t_{eq} is unlikely to increase with further simulation time, assuming equilibrium has already been reached.[216] Modified variants of this method have been proposed[213,215] to speed up the calculation or to retain more data points.

As an example, the MSER was applied to the equilibration of oxygen-deficient CeO_2 at $T = 2000\,\mathrm{K}$ and $p = 0\,\mathrm{bar}$ in Fig. 4.3 (grey data points; a more detailed overview is provided in Fig. 4.1). All considered quantities (T, p, E_{pot}, V) were found to be converged after about $t \approx 5\,\mathrm{ps}$. E_{pot} was chosen for consideration instead of $E_{total}(= E_{pot} + E_{kin})$, as E_{kin} is proportional to T and thus has the same equilibration time.

Not in all cases is the equilibration time similar for all quantities. While temperature and pressure often equilibrate faster (they are directly controlled by thermostat or barostat in an NpT simulation), energy and volume may take long to reach equilibrium. Likewise, the temperature in a NVT simulation may equilibrate faster than the energy. In addition to automatic quantification, visual inspection is recommended to confirm that equilibrium has been reached. Another equilibration problem is specific to ion-conducting solids with many energetically similar configurations of the mobile ions. For such systems, it is not widely appreciated that the ions also have to achieve an equilibrium distribution, which may deviate substantially from a random distribution. Consequently,

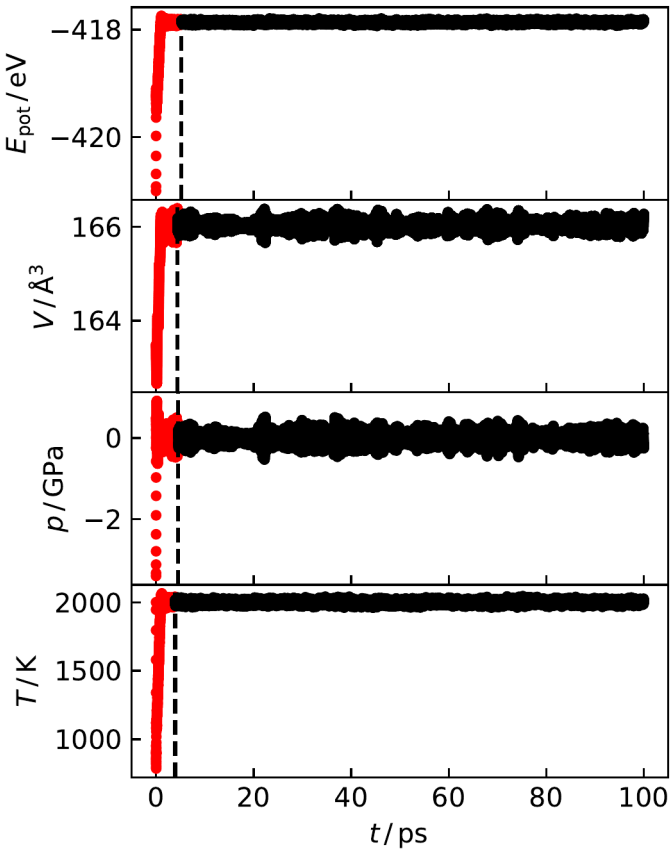


Figure 4.1 Equilibration of $CeO_{2-\delta}$ at $T = 2000$ K and $p = 0$ bar using the MSER method. E_{pot} and V normalised per unit cell. Minima of MSER determined using `pyMSER`[222]

.

taking a random distribution as the starting point for an MD simulation of ion transport may not be appropriate. The equilibration time for the ion distribution will generally be substantially longer than that for the thermodynamic variables. MSER may give a consistent value in such cases, but it is clear that the system is not yet equilibrated (see, e.g., Fig. 4.2). A different type of case is the distribution of mobile ions in systems with extended defects (e.g. grain boundaries, dislocations)[2,223,224] or restricted equilibria in systems with immobile ions (e.g. dopants on sublattices without vacancies)[225].

A more efficient way to tackle the equilibration problem for such systems can be a METROPOLIS Monte Carlo[139] (MMC) simulation. This method allows the system to access more stable configurations by applying system modifications, including, but not limited to, random particle displacements, particle swaps, or lattice volume changes.[3] This allows the system to minimise its

[3]The acceptance of these modifications is based on the METROPOLIS criterion, which compares the energy of the

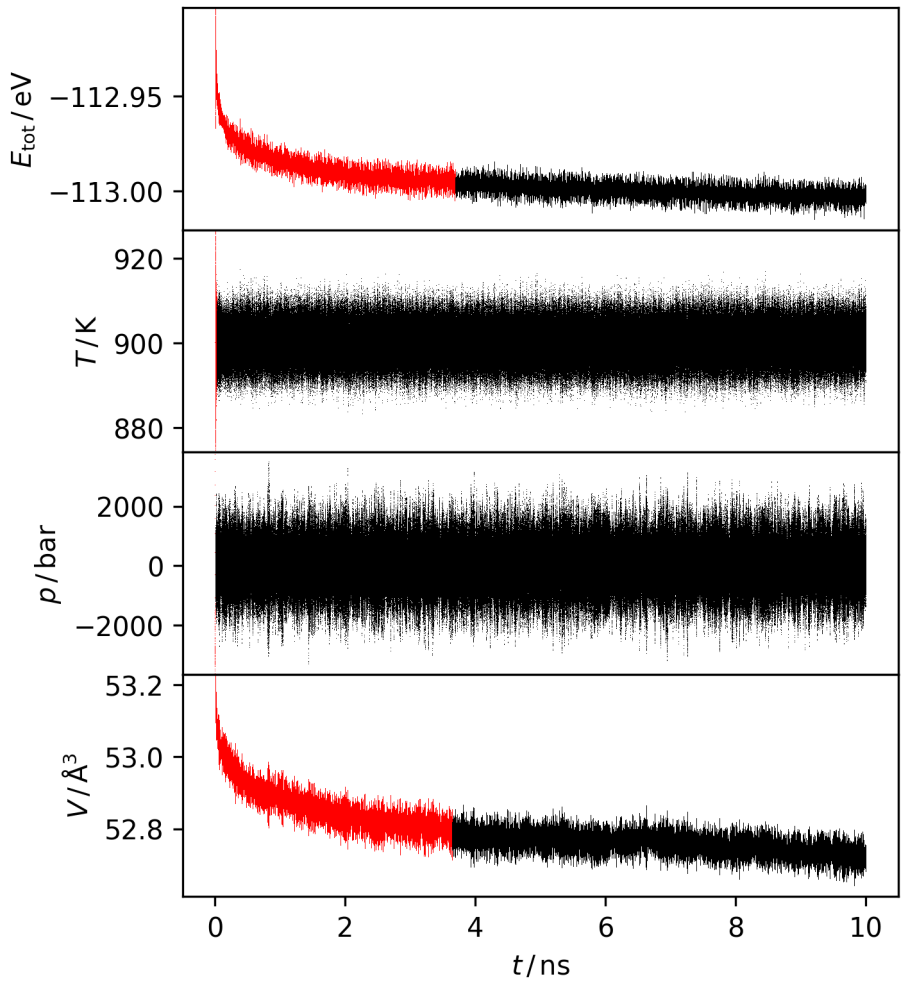


Figure 4.2 Temperature T, total energy E, pressure p, and volume V in a simulation of $Ca_{0.5}Sr_{0.5}Co_{0.8}Fe_{0.2}O_{2.5}$ at $T_{target} = 900\,K$ and $p_{target} = 0$ during the first 10 ns of the simulation. Energy and volume are normalised per unit cell. Much longer simulation times are required for their equilibration (as determined with `pyMSER`[222]), and even in the supposedly equilibrated region, a slow decrease in both of these quantities is still observed.

energy while escaping local minima.[35,37] MMC simulations may be applied alone or in combination with MD simulations in a hybrid scheme.[226–230] The MMC temperature (for the probability factor) is a parameter that controls the acceptance rate of the modifications, where a higher temperature leads to a higher acceptance rate of energy-increasing modifications.

4.3.2 Fluctuations of Thermodynamic Quantities

Experiments on macroscopic systems typically probe the behaviour of systems with particle numbers of the order of a mole ($N \approx 10^{23}$) and thus refer to the thermodynamic limit. Under these conditions, thermodynamic quantities, such as temperature, volume, and energy, are well-defined and effectively constant, albeit subject to measurement errors. In contrast, MD simulations often involve vastly fewer particles ($N \sim 10^3$ to 10^6), and thus are far from the thermodynamic limit. Consequently, the fluctuations of these quantities about their mean values become non-negligible; to the beginner, they may appear unusually large. Some key points are outlined below to show that, large as these fluctuations may be, they have to exhibit large values because N is so small. Furthermore, examination of the fluctuations can be useful.

In MD simulations it is important to note that the temperature $\bar{T}$ is only well defined as an average over the simulation time (once the system has reached equilibrium). The instantaneous temperature $\hat{T}$, calculated from the instantaneous kinetic energy, should not be considered as the temperature of the system, as discussed in Ref. [231], even though it is often denoted as such in the literature and in the output of molecular dynamics software. In an NpT simulation, this kinetic temperature, given by

$$\hat{T} = \frac{2\hat{E}_{\mathrm{kin}}}{3N_{\mathrm{Particles}}k_{\mathrm{B}}} \tag{4.2}$$

(with $\hat{E}_{\mathrm{kin}}$ as the kinetic energy); the instantaneous pressure $\hat{p}$; and instantaneous energy, $\hat{E}_{\mathrm{total}} = \hat{E}_{\mathrm{kin}} + \hat{E}_{\mathrm{pot}}$; fluctuate around their mean values $\langle\hat{T}\rangle$, $\langle\hat{p}\rangle$ and $\langle\hat{E}_{\mathrm{total}}\rangle$. The fluctuations can be quantified by the variance $\mathrm{Var}[Y] = \sigma_Y^2 = \langle Y^2\rangle - \langle Y\rangle^2$ of the quantity Y. For the temperature, the standard deviation is given as[231]

system before and after the modification. If the energy is lower after the modification, the change is accepted, otherwise it is accepted with a probability of $\exp\left(-\frac{\Delta E}{k_{\mathrm{B}}T}\right)$.

$$\sigma_T^2 = \frac{2T^2}{3N_{\text{Particles}}}. \tag{4.3}$$

It is apparent that, the smaller the number of particles, the more the instantaneous temperature must vary during a simulation. This is not a problem with the simulation: rather, it is a thermodynamic necessity if the simulation is running correctly. For the energy, the standard deviation is related to the heat capacity C through

$$\sigma_E^2 = k_\mathrm{B} T^2 C. \tag{4.4}$$

That is, given a non-zero heat capacity, the system's energy must fluctuate around its mean value. Depending on the ensemble, the heat capacity at constant volume C_V ($E_{\text{total}} = U$) or the heat capacity at constant pressure C_p ($U + pV = H$) must be considered.

For simulations in the NpT ensemble, pressure p and volume V fluctuations can be extracted from the simulation. For the pressure, the standard deviation is given as

$$\sigma_p^2 = \frac{k_\mathrm{B} T}{V \beta_T}, \tag{4.5}$$

where $\beta_T = -\frac{1}{V}\left(\frac{\partial V}{\partial p}\right)_T$ is the isothermal compressibility, equal to the inverse of the bulk modulus K. For the volume in a NpT simulation, the standard deviation is given as[232]

$$\sigma_V^2 = V k_\mathrm{B} T \beta_T. \tag{4.6}$$

Another relationship concerns not the variance of a quantity, but the covariance between energy and volume:[37]

$$\mathrm{Cov}[E, V] = V k_\mathrm{B} T^2 \alpha_V \tag{4.7}$$

with the thermal expansion coefficient α_V. Fig. 4.3 shows the quantities from Fig. 4.1 without the equilibration period as well as their distributions and derived properties. A significant number of data points is required, so that good estimates of the standard deviations can be extracted. Once they reach constant values, these expressions can support validation of the simulation setup (and the force fields) by comparison with experimental data. If good agreement is found for a variety of properties, it is far more likely that the diffusion coefficients refer to the real system.

Fig. 4.3 shows an excellent agreement between the expected [calculated from Eq. (4.3)] and actual standard deviations [obtained from the simulation] for the instantaneous temperature (11.44 K vs. 11.34 K), indicating proper temperature equilibration. The heat capacity of $c_p = 82.70\,\mathrm{J\,mol^{-1}K^{-1}}$ is physically reasonable,[233–236] but a direct comparison is not possible, since no experimental data are available at this high temperature (for comparison $c_p \approx 78\,\mathrm{J\,mol^{-1}K^{-1}}$ at $T = 800\,\mathrm{K}$[234]).

The bulk modulus K was determined from pressure fluctuations as $K = 235.2\,\mathrm{GPa}$ and from volume fluctuations as $K = 217.1\,\mathrm{GPa}$. Both values are in excellent agreement with experimental values of 204 GPa[237], 220 GPa[238], 230 GPa[239], and 236 GPa[240].

4.3.3 Diffusive Regime and Diffusion Coefficient

The use of Eq. (4.1) to obtain D_i^* is only valid when the system behaves diffusively, $\langle r_i(t)^2\rangle \propto D_i^* t$. Some systems exhibit sub-diffusive or super-diffusive behaviour,[241] i.e. $\langle r_i(t)^2\rangle \propto t^\alpha$, with $\alpha \neq 1$. In other words, the mean square displacement does not exhibit a linear increase with time but a weaker ($\alpha < 1$) or a stronger ($\alpha > 1$) development. Even though systems of mobile ions generally show diffusive behaviour in the long-term limit, they often show sub-diffusive behaviour at the beginning of a simulation. For an ARRHENIUS plot of the diffusion coefficient, it is crucial to ensure that data for all temperatures refer to the diffusive regime.

Fig. 4.4 shows data obtained as a function of temperature for oxygen-deficient ceria, a system that should behave diffusively in the long term limit. Fig. 4.4(a) is the standard plot of $\langle r_i(t)^2\rangle$ vs. t; Fig. 4.4(b) is a double-logarithmic plot of the same data, and hence clearly reveals the nature of the diffusive behaviour. For these data, α only becomes unity (indicating diffusive behaviour) after increasingly longer times for increasing lower temperatures. At $T = 800\,\mathrm{K}$, α does not reach unity even after $t = 5\,\mathrm{ns}$, showing that the system does not yet exhibit diffusive behaviour. It is apparent that simulations at lower temperatures should be run longer to reach $\alpha = 1$ or should be discarded

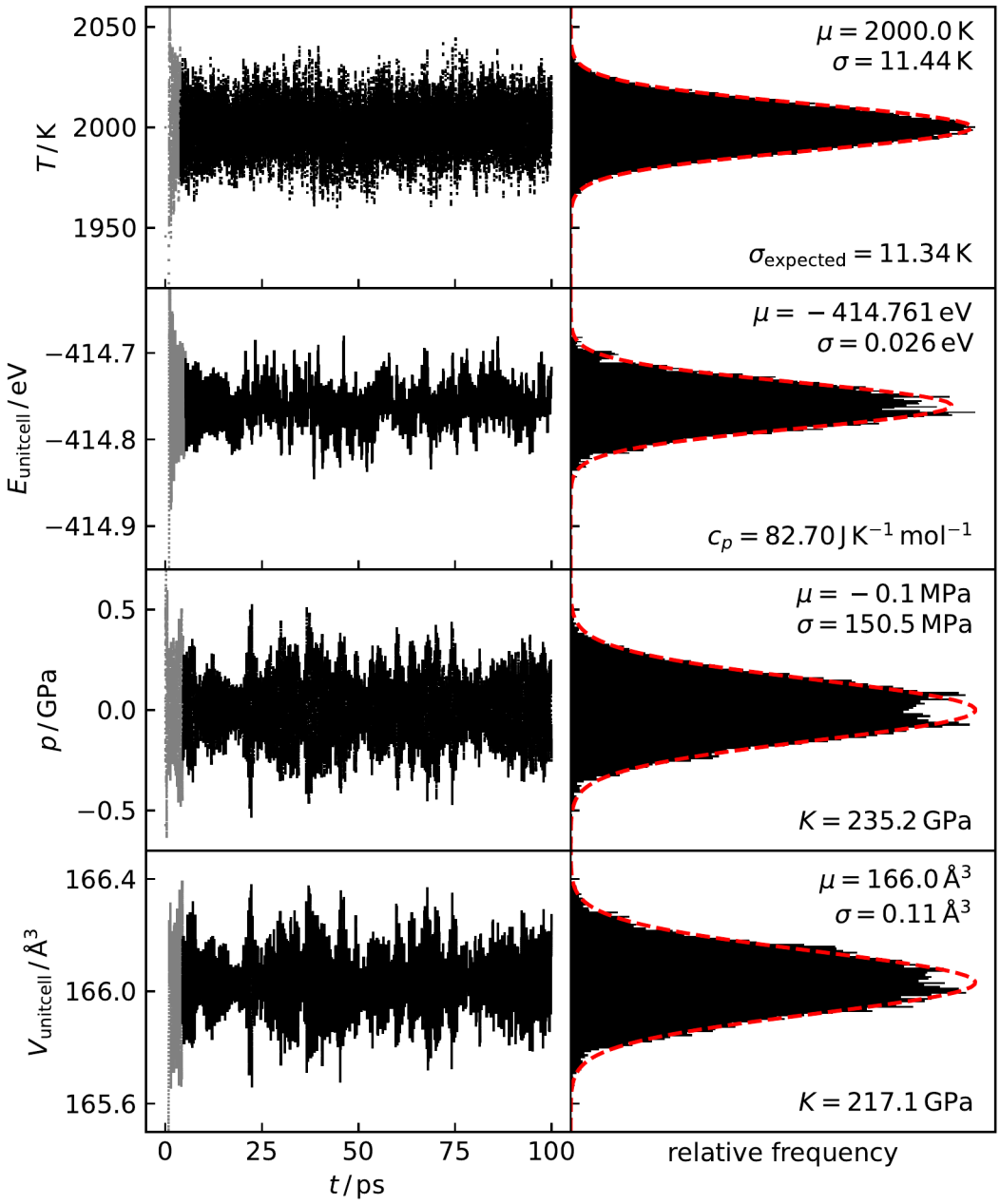


Figure 4.3 Temperature T, energy E, pressure p, and volume V in a simulation of oxygen-deficient CeO_2 at $T_{target} = 2000\,K$ and $p_{target} = 0$ during the first 100 ps of the simulation (the equilibration period for each variable is shown in grey); left: as a function of time, right: relative frequency (grey equilibration period excluded) of the values with normal distribution fit (dotted red line) and fit parameters.

from the determination of ΔH_{mig}. As mentioned before, some systems might not reach the diffusive regime at all, such as systems with different barriers for short- and long-range diffusion.[242]

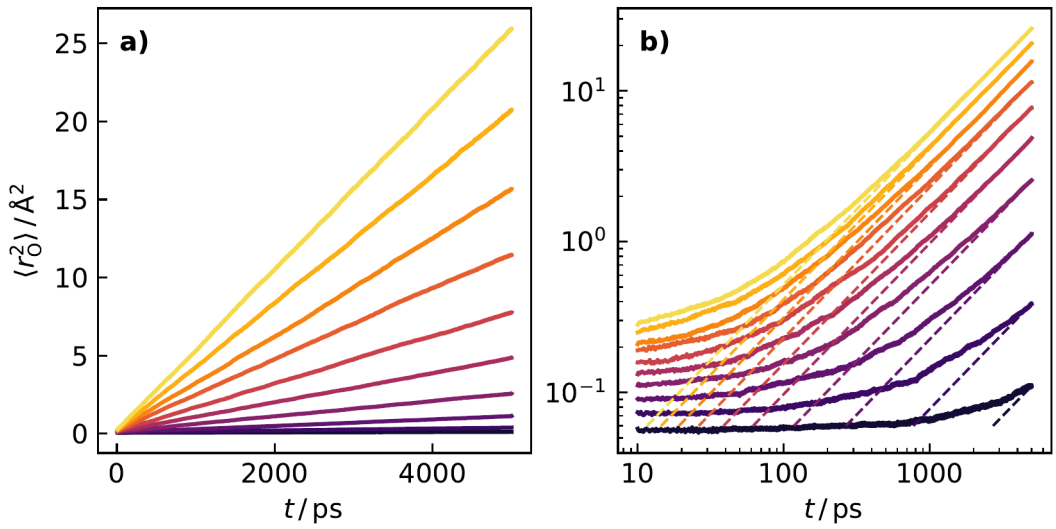


Figure 4.4 Mean square displacement of oxide ions in oxygen-deficient CeO_2 at $800 \leq T\,/\,\mathrm{K} \leq 2600$ (a) on a linear scale, (b) on a double-logarithmic scale, where dotted lines indicate $\alpha = 1$. The colour gradient indicates the temperature.

4.3.4 Simulations with a Fixed Lattice Volume

Production runs for diffusion simulations can be carried out in the isothermal-isobaric ensemble (NpT) or the canonical ensemble (NVT). There are two aspects to consider when choosing the ensemble for the simulation: the activation volume of migration $\Delta^{\ddagger}V$ and the thermal expansion of the lattice.

The second effect will have a more significant impact on the ARRHENIUS parameters. Upon heating, generally materials' lattices expand. This effect can be observed in simulations of the isothermal-isobaric ensemble (NpT), where the pressure is controlled by a barostat and the cell volume is allowed to change. The equilibration of the cell volume in this ensemble can take a long time, especially for disordered systems. In some computational studies, thermal expansion is ignored and the cell volume is fixed at the initial value from a static (0 K) geometry optimisation. This approach will lead to a non-zero stress in the system that increases with increasing temperature. The consequence of this stress are changes in the activation barrier of migration of the ions.[243] In addition, the attempt frequency of the ions will be affected by the stress,[47] which will also affect the

diffusion coefficient. Since this effect will increase with temperature, diffusion coefficients will be affected more strongly at higher temperatures and the slope (and therefore the activation enthalpy) of the ARRHENIUS plot will be incorrect.

To this end, MD simulations of oxygen diffusion in ceria were carried out with the lattice parameter fixed to the value obtained from a static minimisation (i.e. at $T = 0\,\mathrm{K}$) ($a = 5.4286\,\text{Å}$). Assuming an activation volume of migration on the order of $\Delta_{\mathrm{mig}}V \approx 2\,\mathrm{cm^3\,mol^{-1}}$,[244] and an effective pressure of $p \approx 8\,\mathrm{GPa}$ (see Fig. 4.6), the energy difference between the two simulations should be close to $p\Delta_{\mathrm{mig}}V \approx 0.16\,\mathrm{eV}$. The actual value will deviate from this estimate because the pressure is not constant but increases with temperature.

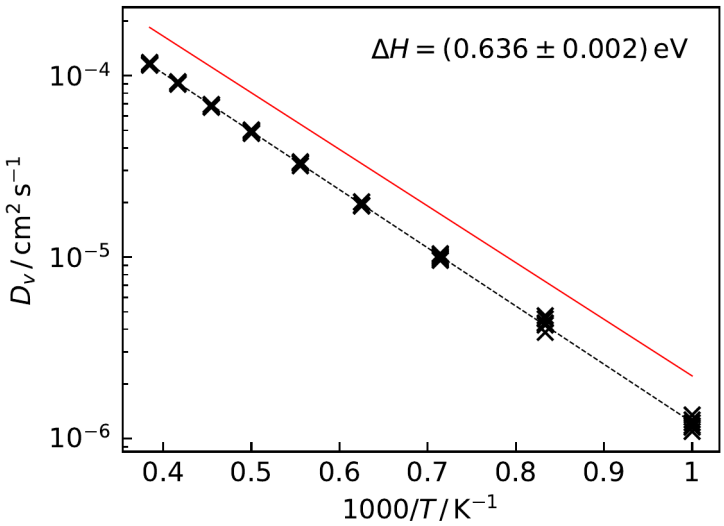


Figure 4.5 Vacancy diffusion coefficients and migration barrier of oxygen in ceria as a function of temperature for a system with 13814 oxygen ions and 10 oxygen vacancies (six random seeds). The lattice parameter was fixed at $a = 5.4286\,\text{Å}$. As a comparison, the vacancy diffusion coefficients for simulations at equilibrium volume are shown as a red solid line.

The results are shown in Fig. 4.5. Vacancy diffusion coefficients are underestimated by a factor of just under 2 for the whole temperature range of $1000 \leq T/\mathrm{K} \leq 2600$. An ARRHENIUS fit yields a slightly overestimated migration barrier (0.638 eV for the fixed volume compared with 0.619 eV for simulations with NpT equilibration), and an underestimated effective jump frequency $\nu^0 \exp\left(\Delta_{\mathrm{mig}}S/k_{\mathrm{B}}\right)$ (2.86 THz compared with 3.89 THz). For other materials and migrating species, the magnitude (and even the sign) of this error will depend on the thermal expansion coefficient and the strain-dependence of migration enthalpy, entropy, and attempt frequency.

Hence, a requirement for obtaining the correct migration energy (or entropy) is to perform simula-

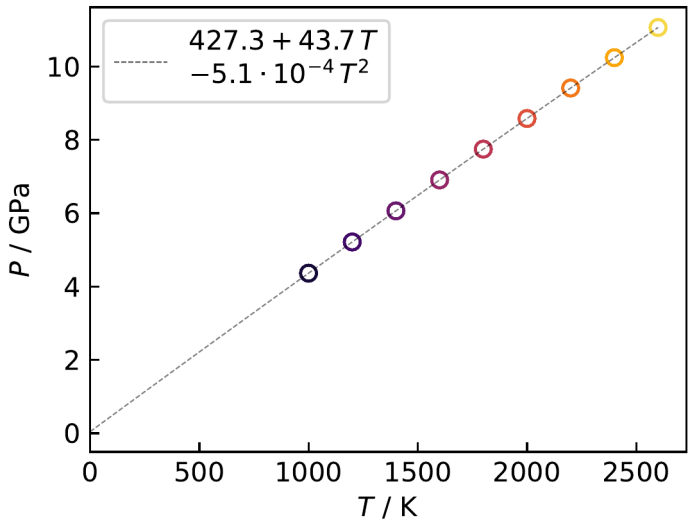


Figure 4.6 Average pressure as a function of temperature for the same simulation as in Fig. 4.5. With increasing temperature, the pressure increases, indicating the suppression of the volume expansion.

tions with the appropriate volume for that temperature. This can be achieved by performing an equilibration in the isothermal-isobaric ensemble (NpT) and allowing the cell volume to change, or by using static calculations to determine the thermal expansion coefficient of the material and adjusting the cell volume accordingly.

4.3.5 Cell-Size Effects

To evaluate the impact of the supercell size on the diffusion coefficients, MD simulations of oxygen tracer diffusion in oxygen-deficient ceria at $1000 \leq T\,/\,\mathrm{K} \leq 2600$ (intervals of 200 K) with one vacancy for $t = 5$ ns were performed. Different supercell sizes ($2 \leq N_{\mathrm{cell}} \leq 8$) of Ce_4O_8 were used. In order to obtain a good estimate of the true values of $\Delta_{\mathrm{mig}}H$ and $\nu^0 \exp(\Delta_{\mathrm{mig}}S/k_{\mathrm{B}})$, additional simulations were carried out with an $N_{\mathrm{cell}} = 12$ supercell with 10 vacancies. Instead of obtaining a large number of data points for each temperature, five simulations with different random seeds were performed for each supercell size. By using nine temperatures and carrying out the ARRHENIUS fits with each possible combination, $5^9 = 1953125$ fits per supercell size were obtained. Non-linear weighted least-squares (WLS) fits were used to obtain the activation energies and effective attempt frequencies (for details on the fitting procedure, see Sec. 4.4.2). The results are shown in Fig. 4.7.

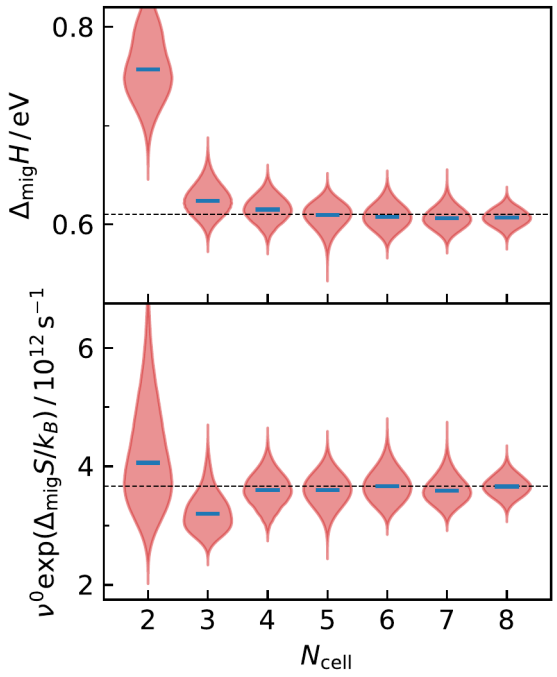


Figure 4.7 Migration barriers and effective attempt frequencies obtained from non-linear WLS fits of oxygen diffusion in ceria. Vertical lines indicate the large-cell values as obtained from a $12 \times 12 \times 12$ supercell with 10 vacancies. Bars represent median values.

First, it is important to understand that MD simulations are most often carried out with only one data point per temperature; this means that the fit will yield one draw from the relevant distribution in Fig. 4.7, without information on the spread. Even if the distribution is somewhat close to the true value, as is the case for $N = 3$, a single data point, as obtained from MD simulations, is likely to deviate from the true value.

Second, from the data in Fig. 4.7, it appears that both migration barrier and the effective attempt frequency are reliably determined for supercell sizes of $N_{\text{cell}} = 4$ and larger, with standard deviations of $\sigma_{\Delta_{\text{mig}}H} \leq 0.02\,\text{eV}$ and $\sigma_{\nu^0 \exp(\Delta_{\text{mig}}S)} \leq 0.28\,\text{THz}$, respectively. For the smaller supercell size of $N_{\text{cell}} = 3$, deviations of the mean from the true (estimated) values are observed. The migration barrier is overestimated, as evidenced by the deviation of the mean value. For the smallest cells ($N_{\text{cell}} = 2$), the spread of the data is much larger.

These conclusions are valid for simulations in the limit of long times (here: $t = 5\,\text{ns}$). Even for these untypically long times, small cells will not converge to the large-cell distributions and thus are not reliable. For shorter, typical AIMD times, the spread of the data will be larger, especially for

small cells. For these cases, Eq. (4.11) can reveal more information about the reliability of the data. One method to estimate the expected number of jumps is to multiply the simulation time with the jump rate, Γ_v, given as[197]

$$\Gamma_\mathrm{v} = \nu^0 \exp\left(-\frac{\Delta_\mathrm{mig}H}{k_\mathrm{B}T}\right). \tag{4.8}$$

If this number is in the single-digit range, the data will not have sufficient statistical significance.[197]

4.4 Evaluation of the Diffusion Data

4.4.1 The Error in the Diffusion Coefficient

The tracer diffusion coefficient D_i^* of tracer particles i is calculated from the mean square displacement $\langle r_i(t)^2\rangle$ of the ions using the EINSTEIN relation [Eq. (4.1)]. Conventionally, one of two methods is used to calculate $\langle r_i(t)^2\rangle$ from the mean square displacement: Either with an ensemble average over the displacements of all ions in the system with respect to their initial positions,

$$\langle r_i(t)^2\rangle = \frac{1}{N_i}\sum_{i=1}^{N_i} ||\mathbf{r}_i(t) - \mathbf{r}_i(0)||^2, \tag{4.9}$$

or with the ensemble average over a time average,

$$\langle r_i^2(\Delta t)\rangle = \frac{1}{N_i}\sum_{i=1}^{N_i}\frac{1}{N_t}\sum_{t<t_\mathrm{sim}} ||\mathbf{r}_i(t+\Delta t) - \mathbf{r}_i(t)||^2. \tag{4.10}$$

In the second case, $\langle r_i^2(\Delta t)\rangle$ is then a function of the time lag Δt rather than the absolute time t. This variant is especially common for the analysis of *ab initio* molecular dynamics simulations, in combination with a weighted least-squares fit (data points weighted by the reciprocal of their

variance $1/\sigma^2(\langle r_i^2(\Delta t)\rangle)$).[198,245] The problem with this approach is that the data appears much smoother than with the first method, but the determined D_i^* has no substantially lower error.[197] In fact, any scheme that uses the regression error as an estimate of the error in the diffusion coefficient is flawed and will underestimate it significantly because of the autocorrelation of the data.

USLER et al.[197] examined the statistics of the diffusion coefficient D_i^*. They found that the uncertainty can be estimated from a single MD simulation using the expression[197]

$$u_{\mathrm{rel}} = \sqrt{\frac{2}{n_{\mathrm{dim}} N_i \cdot \left[1 - \exp\left(-\frac{\langle r_i^2\rangle}{s_i^2}\right)\right]}}, \tag{4.11}$$

with s_i as the jump distance of the tracer particle and $\langle r_i^2\rangle$ as the final mean square displacement. Eq. (4.11) shows that the relative error in the diffusion coefficient — assuming no large changes in tracer concentration and jump distance — decreases with increasing temperature (since $\langle r_i^2\rangle$ increases with temperature) given constant simulation time.

There are other methods to estimate the error in the diffusion coefficient, notably by BAYESian regression.[198] This method requires data from the whole simulation (i.e., the full trajectory), whereas Eq. (4.11) can be calculated from the slope of the ensemble average of the mean square displacement, which may be calculated on-the-fly during the simulation or even post-simulation from only a small fraction of structures of the trajectory. (It can also be used beforehand if $\langle r_i^2\rangle$ can be estimated.)

4.4.2 Linear vs Non-Linear Fitting

To obtain the activation enthalpy and the pre-exponential factor of tracer diffusion, the ARRHENIUS expression

$$D^* = D_0^* \exp\left(-\frac{\Delta H_{D^*}}{k_{\mathrm{B}} T}\right) \tag{4.12}$$

is fitted to data obtained at a variety of temperatures. This equation is most often fitted to the data $D^*(T)$ in its linearised form:

$$\ln D^* = \ln D_0^* - \frac{\Delta H_{D^*}}{k_\mathrm{B}} \frac{1}{T}. \tag{4.13}$$

Generally, a linear fit is used as it constitutes a robust and straightforward method to determine the targeted parameters. Linear least-squares fitting, however, can be imprecise if the uncertainties in the data are not identical (an identical uncertainty would mean that every datapoint has the same absolute uncertainty).[246] The assumptions of the ordinary least-squares (OLS) method are that the errors in the dependent variable are homoscedastic (i.e., the variance of the errors is constant for all values of the independent variable) and that the errors are normally distributed.

It can be assumed that, for MD simulations with long simulation times and thus a large number of jumps, the *relative* error in the diffusion coefficient approaches a constant value [see. Eq. (4.11)], say, 5 %.[197] For a linearised plot of D^* vs. $1/T$, uncertainty propagation must be considered, where the uncertainty in $\ln(D^*)$ is given by $u_{\ln(D^*)} = u_{D^*}/D^* = u_\mathrm{rel} = 0.05$. This means that the error in the diffusion coefficient is homoscedastic [it is constant for all values of $\ln(D^*)$]. Consequently, the ordinary least-squares fit will yield very similar results to a weighted least-squares fit for the linearised data. Since the errors in D^* are heteroscedastic in the exponential form of the ARRHENIUS equation (they are then proportional to D^*), the ordinary least-squares fit for this type of fit will perform poorly.

For shorter simulation times (or equally for lower temperatures) where the number of successful jumps is low, the relative error in the diffusion coefficient will be higher [cf. Eq. (4.12)]. Thus, the approximation of a constant relative error in the diffusion coefficient does not hold and ordinary least-squares fitting of the linearised form of the ARRHENIUS equation yields biased results. In this case, a weighted least-squares fit must be used, but even then the results are biased for the linearised form of the fit. This is because the normal distribution of the errors of D_i^* leads to a non-normal distribution of the errors in $\ln(D_i^*)$.[247] The non-linear weighted least-squares fit yields the correct results in this case.

The performance of different fitting methods is difficult to assess for actual MD data alone: True values of relevant parameters ($\Delta H_{D_i^*}$, D_0^*) are generally not known and can only be estimated from large-scale simulations, and a vast number of data points is required to obtain smooth distributions for D_i^* at each temperature. An alternative approach is to generate synthetic data points with known parameters and uncertainties. To this end, a set of data points was generated by drawing 2^{16} random numbers from a normal distribution of $D_i^*(T)$, for which the mean at temperature T,

$\bar{D}_i^*$, was calculated according to Eq. 4.12. The standard deviation for $\bar{D}_i^*$ was calculated according to Eq. (4.11). This procedure was carried out for the temperature range $600 \leq T\,/\,\mathrm{K} \leq 1400$ with intervals of 200 K. The obtained activation energies are shown in Fig. 4.8. The linear ordinary least-squares fit yields a biased mean and an asymmetric distribution of the activation energies. The weighted least-squares fit yields a slightly biased mean, and only the non-linear weighted least-squares fit yields the correct mean. The non-linear ordinary least-squares fit exhibits a broad distribution, indicating that this method should never be used.

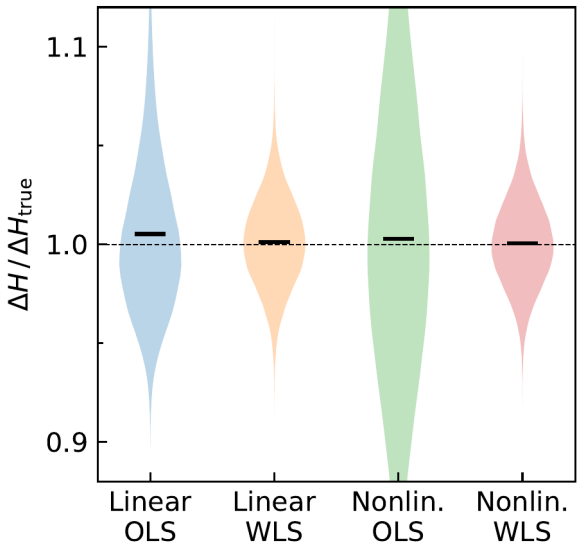


Figure 4.8 Migration barriers obtained from linear and non-linear OLS and WLS fits of randomly generated data points for the temperature range $600 \leq T\,/\,\mathrm{K} \leq 1400$. The obtained activation energies are normalised to the true value.

The analysis above shows the performance for idealised data with many draws from the distribution of the diffusion coefficient at each temperature. In practice, the number of available diffusion coefficients per temperature is limited and is usually only one (or a few). It is essentially just one (or a few) random draw(s) from the distribution of the diffusion coefficient at that temperature. Without the knowledge of the true diffusion coefficient, the error according to Eq. (4.11) will be only an estimate. If the drawn value of $D_i^*(T)$ is higher than the true value, the error will be overestimated, and vice versa. In small systems, some finite-size effects of different origins (e.g. variations of the tracer correlation factor f^*, charge-compensation effects, etc.) can occur. These effects can lead to a systematic error in the diffusion coefficient (see Sec. 4.3.5). The analysis of real data (see Sec. 4.3.5) is shown in Fig. 4.9.

As in the ideal case [Fig. 4.8], the linear ordinary least-squares fit (OLS) exhibits a broad distribution

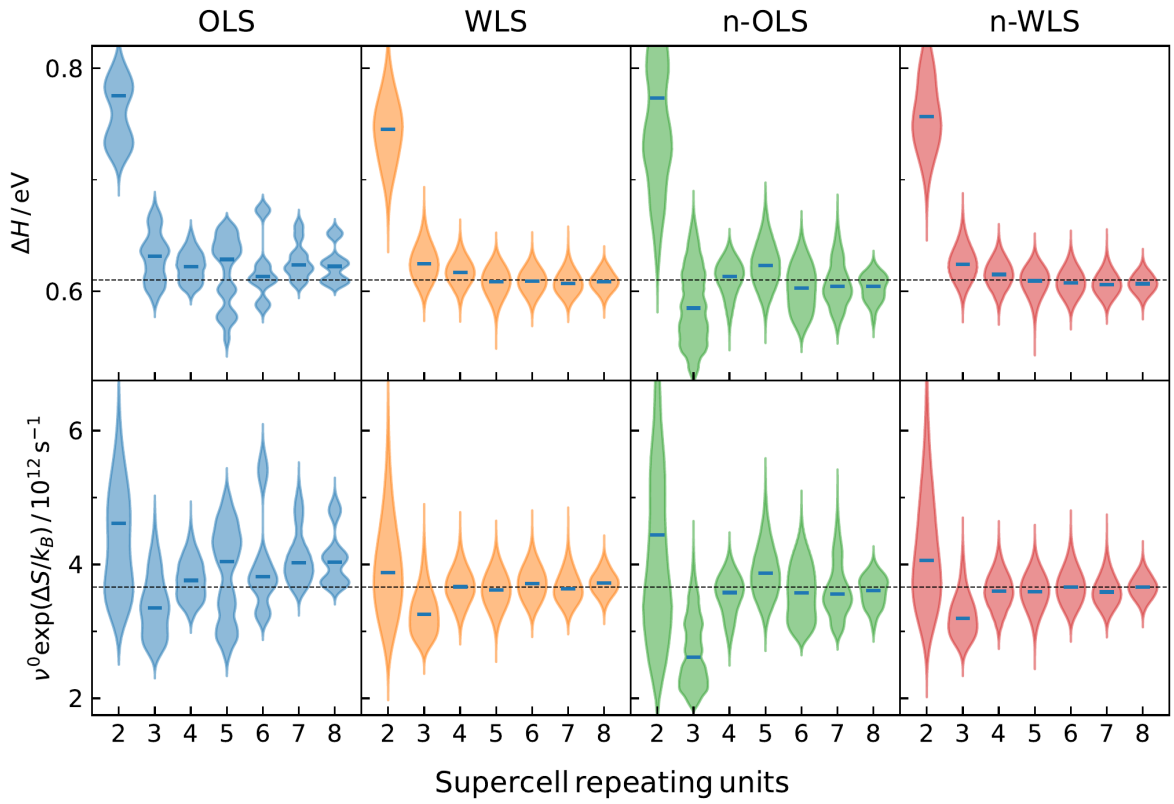


Figure 4.9 Migration barriers and entropy terms obtained from linear and non-linear OLS and WLS fits of oxygen diffusion in ceria. Vertical lines indicate the large-cell values as obtained from a $12 \times 12 \times 12$ supercell with 10 vacancies. Bars represent median values.

of the fitted values. In addition, the respective means of activation enthalpy and the entropy term do not converge to their (estimated) true values as the system size increases. The formation of satellite peaks is observed. This effect can be explained by the limited number of data points per temperature and cell size (only five). The non-linear ordinary least-squares fit (n-OLS) exhibits similar behaviour, but satellite peaks are not observed. In contrast, both types of weighted least-squares fits (linear and non-linear) yield a much narrower distribution of the fitted values, and the arithmetic mean of the fitted values is much closer to the true values.

Fig. 4.9 also reveals information about the convergence of these fit values with cell size. For both WLS fits, median and spread of the entropy term do not change significantly for $N \geq 4$, but the spread of $\Delta_{\mathrm{mig}}H$ slightly decreases. Values for $N = 3$ differ from the larger cell sizes, indicating that the finite-size effects are not yet converged, and the data series for $N = 2$ appear completely unreliable. The OLS fits show a somewhat similar trend, but the spread of the values and the deviations of the medians are much stronger even for $N \geq 4$, suggesting that weighted fitting should

be used even when finite-size effects are negligible.

The important points can be summarised as follows:

- When the system exhibits a large number of jumps ($\langle r_i^2 \rangle / s_i^2 \gg 1$), the relative error in the diffusion coefficient will be constant and OLS fitting or the linearised form of the ARRHENIUS equation will yield sufficiently accurate results.

- With a small number of jumps, a weighted least-squares fit should be employed. The linearised fit will yield a biased mean, whereas the non-linear fit will yield the correct mean.

- An ordinary least-squares fit of the non-linear form should never be used.

4.4.3 Extrapolation to Other Temperatures

MD simulations of ion transport are often performed at elevated temperatures where diffusion coefficients are high enough to yield reliable data (see Sec. 4.3.3). In contrast, temperatures of interest are often much lower, e.g., the operating temperature of the material (typically in the range of $300 \leq T\,/\,\mathrm{K} \leq 1000$). After fitting the high-temperature data to an ARRHENIUS equation, the diffusion coefficient is extrapolated to the temperature of interest.

As discussed above, Eq. (4.11) provides a closed-form expression for the uncertainty in the diffusion coefficient from the simulation at a given temperature. With diffusion coefficients and their uncertainty known for each temperature, the uncertainty of the extrapolated diffusion coefficient can be assessed. USLER *et al.*[197] have shown how a reasonably sized uncertainty at the simulation temperatures can lead to a large uncertainty at the extrapolated temperature. One contributing factor is the large distance over which the extrapolation is performed, as reciprocal distances become larger at low (temperature) values, i.e. $|T_1^{-1} - T_2^{-1}|$ is larger if T_1 and T_2 are low.

One approach to estimate the uncertainty of the extrapolated diffusion coefficient is to use the uncertainties of $D(T)$ for obtaining maximum/minimum slopes for the fitting. This can yield an estimate of the uncertainty of the extrapolated diffusion coefficient. More information on the actual distribution of the extrapolated data can be obtained from a BAYESian approach.

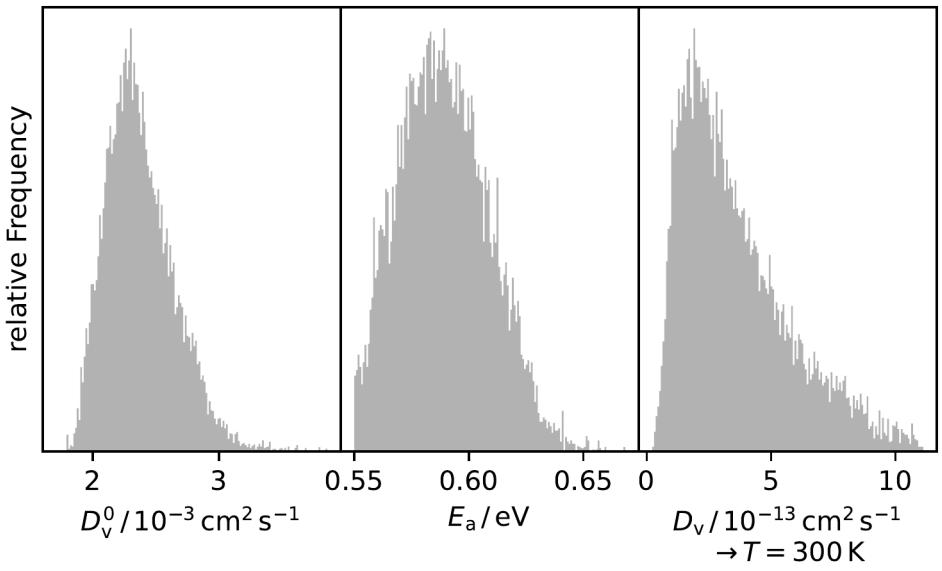


Figure 4.10 The distribution of the prefactor D_0 (left), the activation energy ΔH (middle), and the diffusion coefficient D at 300 K (right) for oxygen diffusion in $CeO_{2-\delta}$. The data were obtained from a BAYESian non-linear fit to the ARRHENIUS equation for one random seed per temperature. The corresponding ARRHENIUS plot is shown in Fig. 4.11.

The procedure does not differ significantly from the usual maximum likelihood estimation. Various implementations are available that allow for BAYESian data fitting.[248–250] Data for oxygen diffusion in $CeO_{2-\delta}$ (Fig. 4.9) for a $3 \times 3 \times 3$ supercell, using only 100 ps for fitting to mimic typical MD simulations, were used to extrapolate the diffusion coefficient to $T = 300\,K$. The distribution of the prefactor D_v^0, the activation energy $\Delta_{mig}H$, and the diffusion coefficient D_v at 300 K are shown in Fig. 4.11. From the data, the extrapolated diffusion coefficient can be given as $D_v(\rightarrow 300\,K) = 3.06 \cdot 10^{-13}\,cm^2s^{-1}$ with 95% confidence intervals of $[0.82, 8.94] \cdot 10^{-13}\,cm^2s^{-1}$, a span of more than an order of magnitude.

4.4.4 Conductivity from MD Simulations

Although a tracer diffusion coefficient is the ion transport parameter most easily obtained from simulations, an ionic conductivity is the parameter most easily measured experimentally. In order to convert from one to the other, the NERNST–EINSTEIN relation and knowledge of the HAVEN ratio are required.

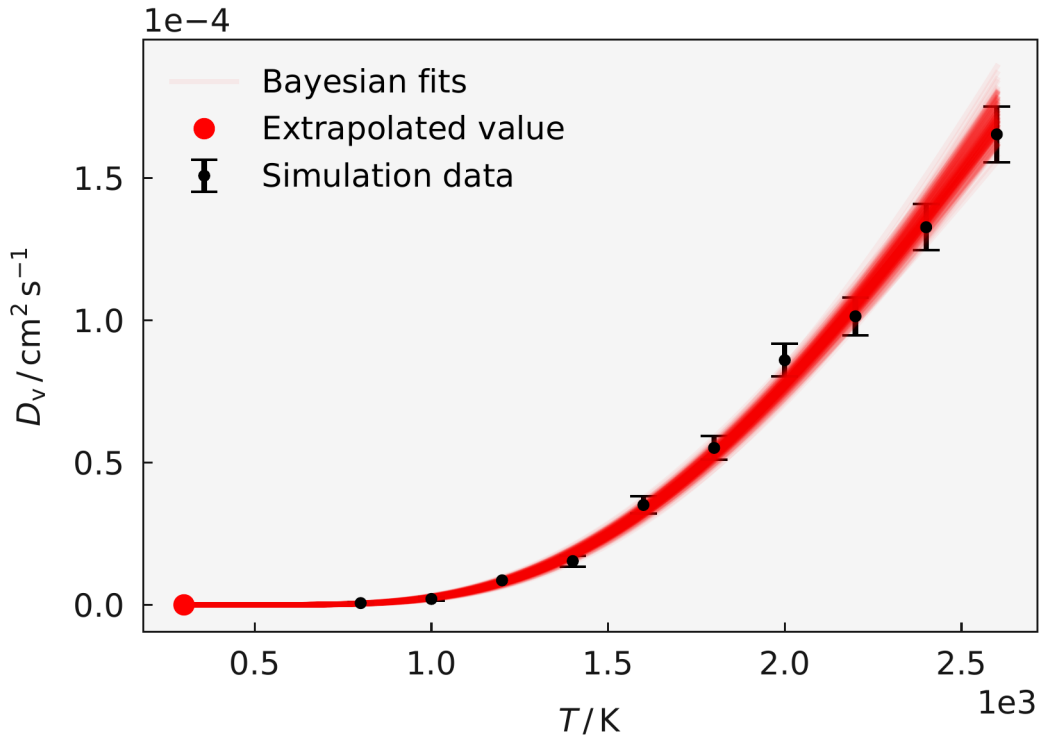


Figure 4.11 ARRHENIUS plot of the diffusion coefficient of oxygen in $CeO_{2-\delta}$. The data was obtained from a BAYESian non-linear fit to the ARRHENIUS equation for one random seed per temperature. The errorbars were calculated with Eq. (4.11). The red lines represent 0.8% of the whole data set. Fitted using the `uravu` package[249].

The definition of the ionic conductivity σ_i is given by

$$\sigma_i = |q_i| c_i u_i, \tag{4.14}$$

where q_i is the charge, c_i is the concentration, and u_i is the electrochemical mobility of the ion. The NERNST–EINSTEIN relation[14,15] allows the definition of a conductivity diffusion coefficient D_i^σ as

$$D_i^\sigma = \frac{\sigma_i}{|q_i|^2 c_i} k_\mathrm{B} T. \tag{4.15}$$

In MD simulations, since all particles are effectively labelled, the tracer diffusion coefficient D_i^* is obtained. The relationship between D_i^* and D_i^σ is expressed by the HAVEN ratio H_r,[251,252]

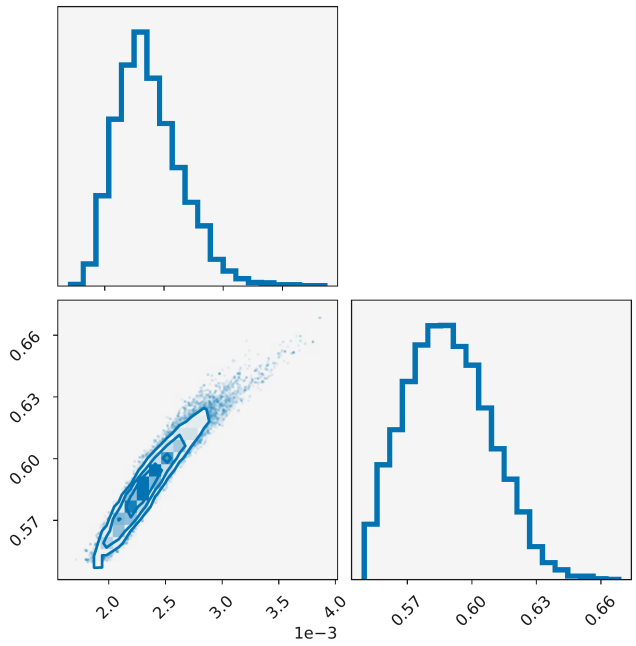


Figure 4.12 Corner plot of the prefactor D_{v}^{0} and the activation energy ΔH_{v} for oxygen diffusion in $CeO_{2-\delta}$. The data was obtained from a BAYESian non-linear fit to the ARRHENIUS equation for one random seed per temperature. See Fig. 4.11 for the corresponding ARRHENIUS plot.

$$H_{\mathrm{r}} = \frac{D_i^*}{D_i^\sigma}. \tag{4.16}$$

Instead of the ratio of diffusion coefficients, the HAVEN ratio can also be expressed as the ratio of correlation factors, $H_{\mathrm{r}} = f^*/f^\sigma$. The tracer correlation factor f^* depends on the diffusion mechanism and lattice geometry and is known analytically only for a few cases. For a dilute solution of non-interacting defects, ions as the charge carriers, and the same jump distance for charge carriers and tracer ions, $f^\sigma = 1$.[253]

An expression for σ_i as a function of the computationally available D_i^* can be obtained by combining Eq. (4.15) and Eq. (4.16), yielding

$$\sigma_i = \frac{|q_i|^2 c_i}{k_{\mathrm{B}} T} \frac{D_i^*}{H_{\mathrm{r}}}. \tag{4.17}$$

Since the HAVEN ratio is required to calculate σ_i from D_i^* but is often not known, it is usually assumed

to be unity, implying a system without correlation effects. This approximation is, in many cases, inaccurate. The value of H_r may not only deviate strongly from unity, but may also, in principle, be temperature dependent.

Alternatively, there are two main methods for obtaining a conductivity from MD simulations. The first is to examine the velocity autocorrelation function to obtain the ONSAGER transport coefficient L_{ii} from which the conductivity can be calculated. The second is to perform MD simulations with an applied field (within the linear response regime), and the steady-state drift velocity is used to calculate the electrochemical mobility u_i, and subsequently, the conductivity.

In the first method, the ONSAGER coefficient L_{ii} is obtained from the velocity autocorrelation function.[254,255]

$$L_{ii} = \frac{1}{3Vk_\mathrm{B}T}\int_0^\infty \langle v_i(t)v_i(0)\rangle \mathrm{d}t. \tag{4.18}$$

The conductivity is then obtained from the ONSAGER coefficient as[256]

$$\sigma_i = |q_i|^2 L_{ii} \tag{4.19}$$

In the second method, the conductivity is obtained from simulations with an applied field. When a field E is used under steady state conditions, a drift of the ions in the direction of the field is observed, expressed by the drift velocity $v_{\mathrm{drift},i}$. The electrochemical mobility u_i is then defined as the ratio of the drift velocity to the field strength:

$$u_i = \frac{v_{\mathrm{drift},i}}{E}. \tag{4.20}$$

For small fields, the mobility is independent of the field strength, as the increase in drift velocity is linear with the field strength.[162] In practice, calculations should be performed as a function of field strength in order to allow exclusion of data from the non-linear regime.[225,257]

The use of Eq. (4.1) to analyse the results of MD simulations with an applied field is inconsistent

with irreversible thermodynamics, in the sense of thermodynamic driving forces and resultant fluxes. Its use will lead to errors. For example, ABDALLAH and YOUSSEF,[258] used Eq. (4.1) and they consequently obtain negative activation enthalpies in ARRHENIUS plots. When a drift is present, the one-dimensional probability density function of particles is no longer GAUSSian, but rather a displaced GAUSSian:

$$p(x,t) = \frac{1}{\sqrt{4\pi D_i^* t}} \exp\left[-\frac{(x - v_{\mathrm{drift},k}t)^2}{4D_i^* t}\right]. \tag{4.21}$$

The mean-squared displacement is then given as the second moment of the probability density function:

$$\langle x_i^2 \rangle = \int_{-\infty}^{\infty} x^2 p(x,t)\mathrm{d}x = 2D_i^* t + (v_{\mathrm{drift},k}t)^2. \tag{4.22}$$

The additional term $(v_{\mathrm{drift},k}t)^2$ constitutes the additional drift term. While it can be obtained by analysing the second time derivative of $\langle x_i^2 \rangle$, this analysis can result in large uncertainties. Instead of analysing the second moment, the mean displacement $\langle x_i \rangle$ can be considered, which is given as

$$\langle x_i \rangle = \int_{-\infty}^{\infty} x p(x,t)\mathrm{d}x = v_{\mathrm{drift},k}t. \tag{4.23}$$

The slope of the mean displacement thus yields the drift velocity. With Eq. (4.20), the electrochemical mobility can be obtained from the mean displacement. Lastly, the conductivity can be obtained by combining the expression with Eq. (4.14):

$$\sigma = \frac{q_i c_i}{E} \frac{\mathrm{d}\langle x_i \rangle}{\mathrm{d}t} \tag{4.24}$$

The HAVEN ratio H_r can be obtained by determining the conductivity, either from Eq. (4.19) or Eq. (4.24), and independently the tracer diffusion coefficient D_i^*, and then combining these with Eq. (4.17).

4.5 Concluding Remarks

As a beginner, it may be tempting to treat the result of a computer simulation of ion transport as unimpeachable. The computer has done exactly as instructed: Carry out an MD simulation and yield a tracer diffusion coefficient. If the simulation is repeated, the same result is obtained. Unimpeachability is, however, a misconception. As detailed in this chapter, a number of issues need to be kept in mind, and a number of pitfalls should be avoided.

First and foremost, a sufficient equilibration period is required. This is not only to ensure that the system is in a well-defined and thermodynamically stable state, but also to have an equilibrium distribution of the tracer ions, a crucial factor for the determination of tracer diffusion coefficients. A reliable method to determine the equilibration time is the Marginal Standard Error Rule (MSER), but visual inspection of the data is still required. Equilibration does not require quantities to be constant, since inherent fluctuations are a feature of (small) systems. The system size must be large enough to yield statistically meaningful results and to avoid finite-size effects.

Diffusion coefficients are determined from ARRHENIUS fits. The fitting procedure is not trivial, as both linearisation and the omission of proper weighting will lead to biased results. The most accurate method is thus a non-linear weighted least-squares fit. Extrapolating the diffusion coefficient to other (lower) temperatures is a common exercise, but the uncertainty of the extrapolated value can be large. BAYESian methods can be used to obtain the uncertainty of the extrapolated value.

5 Substitution of Ba by Ca in BSCF5582

Parts of this chapter have been published in:[1]

A. Bonkowski, C. Perkampus, R. A. De Souza, *J. Mater. Chem. A* **2023**, *11*, 10231–10262.

5.1 Introduction

First introduced into the field in the early 2000s,[259] the perovskite-type oxide $Ba_{0.5}Sr_{0.5}Co_{0.8}Fe_{0.2}O_{3-\delta}$ (BSCF5582) is a superlative mixed ionic–electronic conductor. It shows exceptionally high rates of oxygen diffusion and oxygen surface exchange, and thus outstanding performance as an oxygen permeation membrane[260] and as a solid oxide fuel cell cathode.[261,262] In addition, it is also a candidate for use as an anode material in solid oxide electrolysis cells.[263]

BSFC5582 stands out as a mixed ionic–electronic conductor because it exhibits the highest oxygen nonstoichiometry δ observed to date within the family of cubic $ABO_{3-\delta}$ perovskite-type oxides ($\delta < 0.8$);[264,265] and in contrast to the related material $SrCo_{0.8}Fe_{0.2}O_{3-\delta}$, it does this without forming (at $\delta = 0.5$) an $A_2B_2O_5$ brownmillerite-type phase.[266] On the other hand, BSCF5582 displays very limited thermodynamic stability,[267–270] decomposing at temperatures below 1173 K into a 2*H* hexagonal $(Ba,Sr)CoO_{3-\delta}$ perovskite phase (with face-sharing octahedra) and a Ba- and Co-deficient cubic perovskite phase (with corner-sharing octahedra).[268] Although the kinetics of the decomposition become sluggish on the timescale of hours at temperatures below 800 K,[265]

[1] All simulations were prepared, carried out, and analysed by the author of this thesis, with preliminary simulations prepared, carried out, and analysed by Caitlin Perkampus. The published manuscript was written by the author of this thesis, with contributions from the co-authors.

a preferable approach, especially for material stability in operational devices on the timescale of years, would be to find an acceptable alternative. BSCF5582 also deteriorates rapidly in the presence of even small amounts of CO_2, and a higher chemical stability in this respect would also be welcome.[271–273]

Considering the GOLDSCHMIDT tolerance factor t_G [Eq. (2.7)],[20] corner-sharing perovskite structures generally form for the range $0.8 \leq t_G \leq 1$; hexagonal structures are generally preferred for $t_G > 1$.[274] Of the four ABO_3 parent compounds of BSCF5582, $BaCoO_3$ constitutes the major problem in this regard, for its tolerance factor is the largest at $t_G = 1.2$. If the *B*-site composition is kept unchanged, the tendency of BSCF5582 to decompose to a hexagonal phase could be reduced by lowering t_G, and this can be achieved by isovalent substitution of Ba^{2+} with smaller cations. Sr^{2+} can be discarded immediately as a possibility (on account of SCF forming a brownmillerite-type phase at $\delta = 0.5$).[275] Ca^{2+} is a possibility, but perovskites containing Ca^{2+} tend to exhibit orthorhombic structures, rather than the cubic structure that is favoured by researchers in looking for high-diffusivity compositions.[276] Mg^{2+} can be ignored, since it is too small a cation to form a perovskite phase with Fe/Co on the *B*-site. It appears, therefore, that there is no easy solution to the stability problem.

A computational study[207] has shown that oxygen-vacancy diffusion in orthorhombic $CaTiO_3$ ($t_G = 0.964$) is faster than in cubic $SrTiO_3$ ($t_G = 1$). This result suggests that, contrary to common expectations, the Ca analogue of BSCF5582, i.e. $Ca_{0.5}Sr_{0.5}Co_{0.8}Fe_{0.2}O_{3-\delta}$ (CSCF5582), may display high rates of oxygen-vacancy diffusion, even in a distorted perovskite symmetry.

5.2 Results and Discussion

5.2.1 Lattice Symmetry

In investigating CSCF5582, the first major question is the lattice symmetry. The simulations in the isobaric–isothermal ensemble (NpT) were initialised with orthorhombic symmetry (space group *Pnma*) and showed that the cell is cubic above $T = 1100$ K for the two different Ca^{2+}–O^{2-} empirical pair potentials[277,278] (Fig. 5.1). The predicted transition temperature should be regarded with caution for two reasons. First, simulation cells did not appear to reach equilibrium at lower temperatures; and second, MD simulations on other low-symmetry perovskite systems[207,279] considerably

overestimate phase transition temperatures to the cubic form. If the temperature is also overestimated for CSCF5582, the material may well show cubic symmetry at much lower temperatures, i.e. those of interest for application as an SOFC cathode or as an oxygen permeation membrane. It is not inconceivable, though, that the transition temperature is underestimated in our simulations. Regardless of whether over- or underestimated, this result is advantageous because it allows us to examine oxygen tracer diffusion in cubic CSCF5582, and to compare its behaviour with that of cubic BSCF5582.

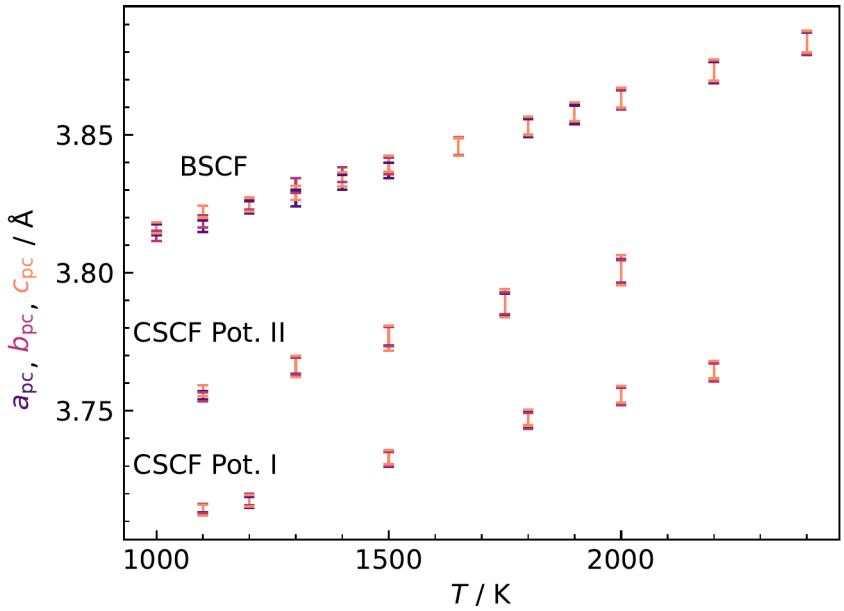


Figure 5.1 Pseudocubic lattice parameters in CSCF5582, starting from orthorhombic CSCF5582, shown for two different potential sets with their standard deviation as error bars. For comparison, the cubic lattice parameters of BSCF5582 are given, where simulations were initialised from the cubic structure. The lattice parameter of CSCF5582 is smaller than that of BSCF5582 due to the smaller cation radius of Ca^{2+} relative to Ba^{2+}.

Simulations at 500 K show a cubic cell parameter of $a(\text{BSCF}) = 3.799$ Å, exactly the same as Shiiba *et al.*[164], and $a(\text{CSCF}) = 3.744$ Å, slightly lower due to $r_{Ca^{2+}} < r_{Ba^{2+}}$.

5.2.2 Oxygen-Vacancy Diffusion

To study the oxygen transport properties of the materials, simulation cells containing 40 000 ions with random distributions of cations and oxygen vacancies were first subjected to an equilibration

period $t_{eq,1} \geq 1.0$ ns (longer runs were necessary for low temperatures) in the isobaric–isothermal ensemble (NpT), until the cell parameters converged to constant values. Thereafter, a further equilibration in the isochoric–isothermal (NVT) ensemble was carried out ($t_{eq,2} \geq 3.0$ ns), until the energy converged to a constant value. In the production runs (NVT ensemble), the mean-squared-displacement of the oxide ions, $\langle r_O^2 \rangle$, was monitored for a period of $t_{run} \geq 1.0$ ns. The standard Einstein relation was applied to $\langle r_O^2 \rangle(t)$ in order to obtain the tracer diffusion coefficient of oxygen,

$$D_O^* = \frac{1}{6} \frac{\mathrm{d}\langle r_O^2 \rangle}{\mathrm{d}t}.$$

Relative errors in D_O^* values were calculated with the formula of Usler *et al.*[197]; only those values with a relative error of 1% or lower are plotted in Fig. 5.2. The results for the known system BSCF5582 are examined first, and the obtained D_O^* values are compared with data from Shiiba *et al.*[164] For the temperature range for which diffusion data was obtained, good agreement was found between the two datasets, but this is not surprising, since the same set of potentials was used in both cases. Extrapolating the present data to lower temperatures, it is discerned that the diffusion coefficients determined by Shiiba *et al.* at the three lowest temperatures appear to be

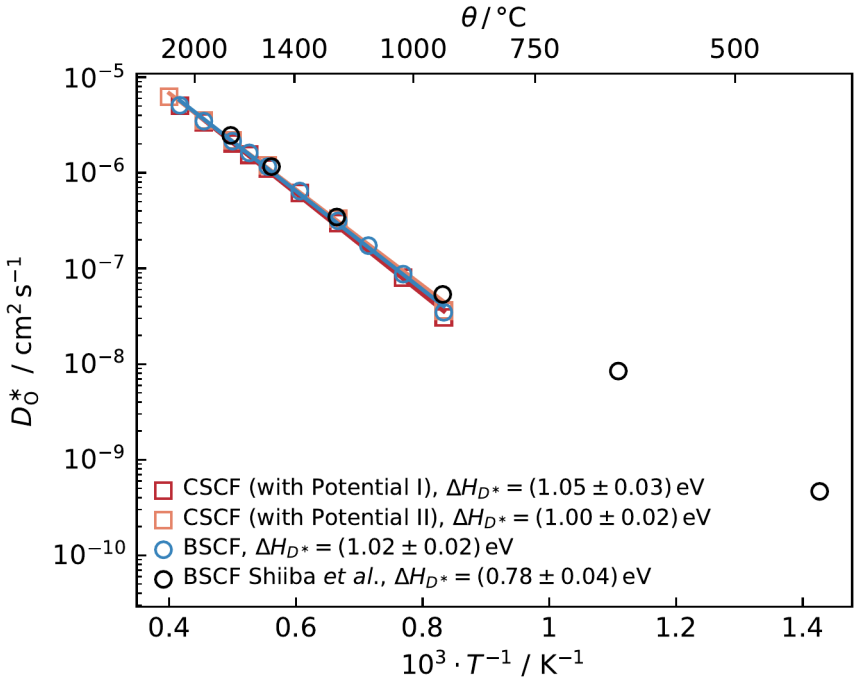


Figure 5.2 Oxygen tracer diffusion coefficients versus inverse temperature for cubic $Ba_{0.5}Sr_{0.5}Co_{0.8}Fe_{0.2}O_{2.5}$ (circles) and cubic $Ca_{0.5}Sr_{0.5}Co_{0.8}Fe_{0.2}O_{2.5}$ (squares), obtained from MD simulations. Also plotted are literature data from MD simulations reported by Shiiba *et al.*[164]

overestimated. This overestimation is attributed to the simulation cells at these temperatures not having reached equilibrium. SHIIBA *et al.* used equilibration times of only $t_{eq} \leq 100$ ps, whereas in the present simulations slow changes in cell energy and volume were observed, even at $T = 1173$ K, on a nanosecond timescale.

Since the equilibration of the oxygen sublattice is evidently the problem — oxygen ions being the only species whose distribution could change during equilibration —, METROPOLIS Monte Carlo (MMC) simulations were performed on the initial simulation cells, swapping oxygen ions and oxygen vacancies for each temperature of interest. Subsequent MD simulations at the respective temperatures yielded tracer diffusion coefficients similar those obtained at the end of a long equilibration run (see Fig. 5.3), with comparable activation enthalpies of diffusion.

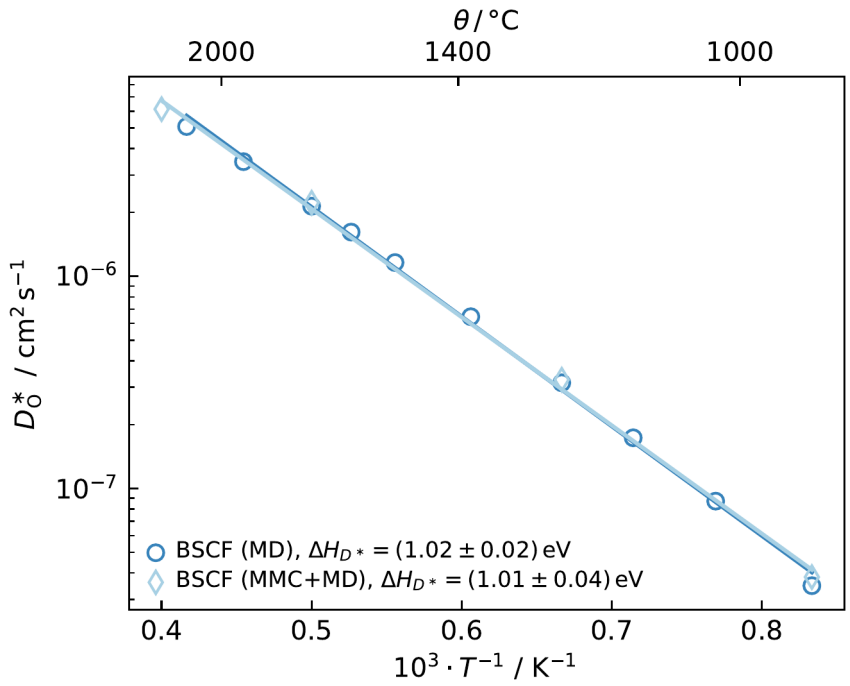


Figure 5.3 Oxygen tracer diffusion coefficients versus inverse temperature for cubic $Ba_{0.5}Sr_{0.5}Co_{0.8}Fe_{0.2}O_{2.5}$, obtained from MD simulations, with and without preceding MMC simulations.

An analogous set of MD simulations was performed for CSCF5582 with both empirical pair potentials[277,278] for the Ca^{2+}–O^{2-}. Surprisingly, both sets of potentials yield similar oxygen diffusivities for cubic CSCF5582, as can be seen in Fig. 5.2. No data is shown for orthorhombic CSCF, since the temperatures were too low to allow reliable tracer diffusion coefficients to be obtained in accessible simulation times. Even more surprising (Fig. 5.2) is that there is little difference between the D_O^*

values obtained for CSCF5582 and for BSCF5582.

5.3 Comparison with Experimental Data

In the remainder of this chapter three questions are considered that the results of Fig. 5.2 raise: Are the predictions reasonable? Why is the difference in oxygen diffusion rates in BSCF5582 and CSCF5582 so small? And why does the equilibration take so much time, considering the fast oxygen diffusion rates?

To examine the first question, finite-temperature data obtained for BSCF5582 is compared with experimental data. Fig. 5.4 is a comparison of the thermal expansion behaviour. It is important to note that data from the present MD simulations were obtained at constant non-stoichiometry δ. The experimental data can be divided into two regimes, with only the data at lower temperatures referring to constant δ. Above $T \approx 770\,\mathrm{K}$, the thermal expansion is accompanied by chemical expansion, caused by an increase in δ with increasing temperature. To make a strict comparison, therefore, the present data needs to be extrapolated down to lower temperatures. Good agreement,

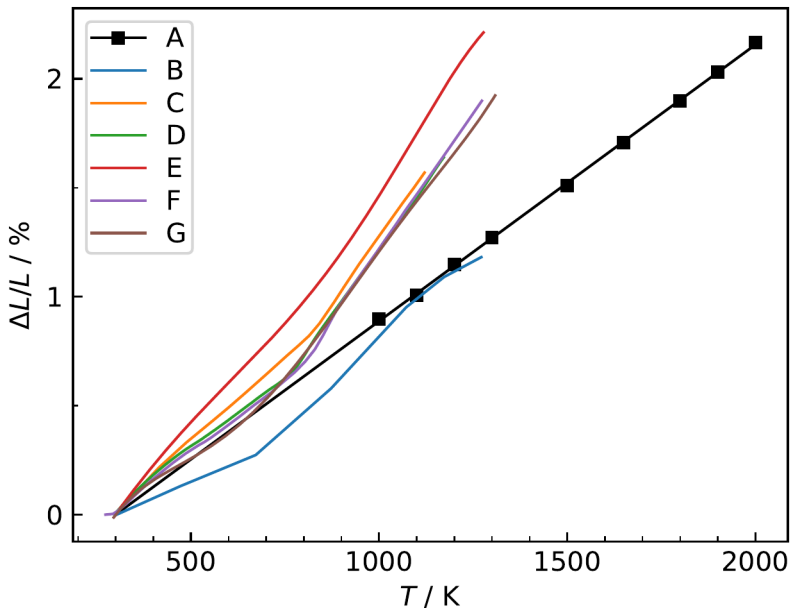


Figure 5.4 Lattice expansion of BSCF5582. A (MD, this work, linear fit), B,[280] C,[281] D,[282] E,[283] F,[284] G.[285]

as seen in Fig. 5.4, is found on a qualitative level.

On a quantitative level, the thermal expansion coefficient

$$\alpha = \frac{1}{L_0(298\,\mathrm{K})}\frac{\mathrm{d}L}{\mathrm{d}T} \tag{5.1}$$

is examined. From the present data, a value of $10^6 \cdot (\alpha\,/\,\mathrm{K}^{-1}) = 12.7 \pm 0.1$ is obtained, which compares very well with experimental values obtained from a linear fit for the temperature range of $473 \leq T/\mathrm{K} \leq 773$ (where no chemical expansion is observed) of 14.9 ± 0.2,[281] 12.5 ± 0.1,[282] 17.6 ± 0.2,[283] 12.7 ± 0.2,[284] 12.0 ± 0.4,[285] and 10 ± 4.[286] That is, with one exception,[283] there is very good agreement between simulation and experiment, providing some support for the reasonableness of the MD results.

As a further test of the MD results, the data for BSCF5582 is compared with experimental data.[284,287–291] To do this, the different oxygen nonstoichiometries first need to be corrected. As noted above, a constant value of $\delta = 0.5$ is used in the simulations, whereas experiments are generally performed at constant oxygen partial pressure, which means that the nonstoichiometry varies with temperature (and oxygen partial pressure). The $\delta(T)$ values obtained by Mueller *et al.*[265] for BSCF5582 (at $p\mathrm{O}_2 = 0.2\,\mathrm{bar}$) were used to correct the $D_\mathrm{O}^{*,\mathrm{sim}}$ data according to:

$$D_\mathrm{O}^{*,\mathrm{pred}} = D_\mathrm{O}^{*,\mathrm{sim}} \frac{\delta(T)}{3-\delta(T)} \frac{3-0.5}{0.5}.$$

The resulting values of $D_\mathrm{O}^{*,\mathrm{pred}}$, extrapolated to the experimental temperature range of $773 \leq T\,/\,\mathrm{K} \leq 1123$, are compared with experimental data in Fig. 5.5. Dataset D[288] was obtained from D_O data and converted according to $D_\mathrm{O}^* = f^* D_\mathrm{O}$, with $f^* = 0.69$.[292] Datasets E[289] and H[284] were obtained from D_chem data and converted according to $D_\mathrm{chem} = \gamma_\mathrm{O} D_\mathrm{O}$, with γ_O taken from Mueller *et al.*[265] for each temperature.

The data appear to fall into two groups. Data from the first group (datasets B,[287] D[288] and F[290] at lower temperatures) agree well in terms of activation enthalpy with the present value, corrected for oxygen nonstoichiometry [$\Delta H_\mathrm{mig}^\mathrm{J} = (0.92 \pm 0.11)\,\mathrm{eV}$] vs. [$\Delta H_\mathrm{mig}^\mathrm{A} = (1.07 \pm 0.02)\,\mathrm{eV}$], while the absolute magnitude is underestimated by one order of magnitude. Given that this set of

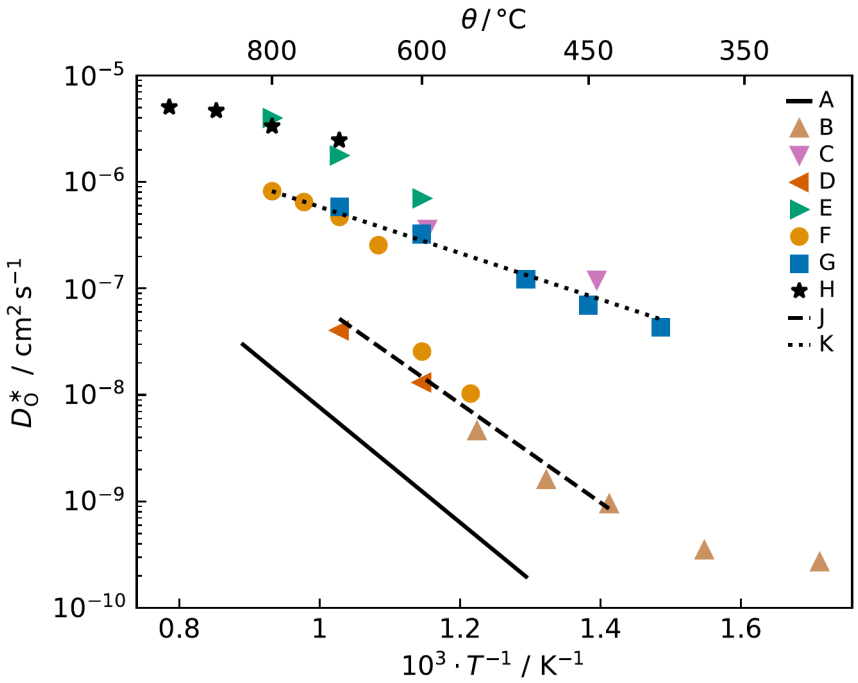


Figure 5.5 Comparison of oxygen tracer diffusion coefficients obtained for $Ba_{0.5}Sr_{0.5}Co_{0.8}Fe_{0.2}O_{3-\delta}$. MD data obtained in this work were corrected for experimental nonstoichiometry (see text). A (MD, this work), B and C,[287] D,[288] E,[289] F,[290] G,[291] H.[284] Line J [$\Delta H_{mig} = (0.92 \pm 0.11)$ eV] and line K ($\Delta H_{mig} = (0.43 \pm 0.04)$ eV) are fits to the two groups of data (see text).

potentials was not fitted to diffusion data, the degree of agreement, and in particular, the agreement regarding the activation enthalpy, is more than satisfactory. The second group (datasets C,[287] E,[289] G[291] and F[290] at higher temperatures) agree well with one another, but are substantially higher than the present results in absolute magnitude, with a much lower activation enthalpy [of $\Delta H^K_{mig} = (0.43 \pm 0.04)$ eV]. Datasets E[289] and H[284] were excluded from the fit, in order to obtain a good description of as many data points as possible.

In their oxygen tracer diffusion studies, BERENOV *et al.*[287] obtained datasets B and C, and they concluded (i) that dataset B is the more reliable, and (ii) that dataset C was affected, possibly, by faster diffusion along pores or grain boundaries. Our MD data (dataset A) is certainly consistent with this interpretation. Nevertheless, it is unclear why dataset F[290] exhibits a jump from the lower to the upper group, and why the data for the upper group fall so closely together, although the density of pores and/or grain boundaries was likely to have varied substantially between the various studies (C,E,F,G).

A previous DFT study[293] yielded migration barriers of ≈ 0.5 eV, depending on the exact *B*-site environment, values that are in better agreement with regime K. However, the calculations were carried out with rather small supercells ($2 \times 2 \times 2$ ABO_3 perovskite unit cells) and with strictly alternating *A*-site Ba/Sr occupation, severely limiting the transferability to experimental structures.

Having established that the MD diffusion data for BSCF5582 are consistent with certain experimental studies (i.e. the D_O^* values are not physically unreasonable), it is concluded that the predictions for CSCF5582 shown in Fig. 5.2 are reasonable, too, at least according to the present simulations. Consequently, it is rather surprising (i) that the two sets of diffusion data for CSCF5582 are so similar and (ii) that they are so similar to those for BSCF5582. It is contended that these similarities are not an artefact. The lattice parameters of the two systems are different (see Fig. 5.1). Ion migration is a complex many-body process, and many factors play a role in determining the rate at which it occurs. In the present case, it appears, therefore, that the various factors are combining in different ways to produce roughly the same oxygen-vacancy diffusion coefficients.

Coming to the third question—why the equilibration takes so long—it is found that during the MMC calculation, both the O–O and the $v_O^{\bullet\bullet}$–$v_O^{\bullet\bullet}$ coordination numbers decrease. The initial random distribution of oxygen vacancies is characterised by an average coordination number of 6.67 for O coordinated by O and 1.33 for a vacancy coordinated by a vacancy. These values decrease to 6.54 and 0.70, respectively. In other words, the initial random distribution lead to regions in the supercell with too many oxygen ions and regions with too many vacancies, relative to the thermodynamic equilibrium distribution. The need to get vacancies into the oxygen-rich regions, and the oxygen ions into the vacancy-rich regions is evidently what causes the long equilibration times.

5.4 Concluding Remarks

In conclusion, it is predicted that oxygen-vacancy diffusion in cubic CSCF5582 occurs at the same rate as in cubic BSCF5582. The respective rates of oxide-ion diffusion [$\propto D_v\delta/(3-\delta)$] are expected to be different, since the oxygen nonstoichiometry $\delta(T, pO_2)$ will certainly differ between the two compounds. It does remain to be seen whether CSCF5582 adopts cubic symmetry at the temperatures of interest for fuel cells and permeation membranes, but even if this is not the case, oxygen-vacancy diffusion in orthorhombic CSCF5582 will probably[207] only be slightly slower than in the cubic form with a slightly higher activation enthalpy of diffusion. The expected increased chemical stability

of CSCF5582 over BSCF5582, on account of its lower GOLDSCHMIDT factor, also remains to be confirmed. Furthermore, it needs to be determined whether the increased stability is sufficient for applications.

Lastly, this chapter is considered as drawing attention not only to a new promising mixed ionic–electronic conductor, CSCF5582, but also more generally, to other Ca-containing perovskites that may have been overlooked as possible mixed ionic–electronic conductors on account of their lower symmetry.

6 Transition-Metal Exsolution from Perovskite Oxides

Parts of this chapter have been published in:[1]

A. Bonkowski, M. J. Wolf, J. Wu, S. C. Parker, A. Klein, R. A. De Souza, *J. Am. Chem. Soc.* **2024**, *146*, 23012–23021.

6.1 Introduction

Nanoparticles of transition metals, finely distributed on oxide supports, constitute established catalytic systems. In recent years, exsolution has become a key method for producing such metal nanoparticles anchored at the surfaces of ABO_3 perovskite-oxide hosts.[294,295] These systems provide a range of benefits over those produced by conventional methods — enhanced catalytic activity, high resistance to agglomeration, homogeneous size distribution, high tunability, and efficient use of precious metals. An enormous variety of host ABO_3 perovskite compositions has been studied,[296–304] with the exsolving metal residing initially on the perovskite's B-site and with a high concentration of A-site vacancies.[305] One representative composition[294,295,306] is thus $Sr_{1-3x/2}La_xTi_{1-y}Ni_yO_{3-y}$, with Sr as the host A-site cation, La as the donor species that compensates the A-site deficiency, Ti as the host B-site cation and Ni as the B-site substituent (that will exsolve). Treatment of such systems at elevated, but not very high, temperatures in moderately reducing conditions results in the exsolution of the B-site substituent as stable, embedded, well-distributed metal nanoparticles.

[1] All simulations were prepared, carried out, and analysed by the author of this thesis. Thermodynamic modelling was carried out by the author of this thesis. The published manuscript was written by the author of this thesis, with contributions from the co-authors.

Although, or perhaps even because, exsolution has been observed for such an enormous variety of ABO_3 perovskite systems,[296–304] the thermodynamic origin of exsolution remains unclear. It has been proposed that the combination of A-site deficiency from the starting composition and oxygen deficiency introduced by reduction is responsible for B-site exsolution. This combination produces a surfeit of B-site cations, and to ameliorate the situation, the perovskite lattice expels these B-site cations.[294,297,306,307] This proposal is inconsistent, however, with the general observation that only the substituent B-site cations are exsolved and not the host B-site cations. The proposed instability of the perovskite lattice cannot explain, therefore, the exsolution of B-site substituent cations. An alternative proposal considers exsolution to occur when the GIBBS energy of reduction of the transition-metal oxide becomes negative.[294,308,309] Support for this proposal has been drawn from the good agreement found between those transition-metal cations that so far have been observed experimentally to exsolve from perovskites (and also those that have not) and their respective GIBBS energies of reduction. Nonetheless, this approach is flawed: the exsolution process is implicitly separated into two (physically reasonable) steps, the transition-metal oxide's removal from the perovskite-oxide host and its subsequent reduction, but then the first step is ignored. Furthermore, the first step has to be unfavourable (because its reverse is highly favourable), and its GIBBS energy may be larger in magnitude than the GIBBS energy of reduction. This approach is, therefore, incomplete, in addition to being empirical, and thus does not provide a fundamental explanation of exsolution. A third proposal involves the segregation energy of the substituent B-site cations to the surface. According to DFT calculations,[310,311] the energy for the co-segregation of the B-site substituent and an oxygen vacancy is predicted to be much higher than the segregation energy of the B-site substituent alone, and hence, a substantial increase in oxygen-vacancy concentration leads to exsolution. The first problem with this proposal is that segregation to the surface is not exsolution. If some moiety segregates to a surface, it resides in the first atomic layer(s) of the solid and hence it is still part of the host lattice. It has not yet been exsolved as a second phase. A second problem with the segregation proposal is that it requires the oxygen-vacancy concentration to be very low in the oxidised state (which is not the case, for instance, for the representative composition $Sr_{1-3x/2}La_xTi_{1-y}Ni_yO_{3-y}$) and to increase strongly when the system is reduced. Indeed, almost all exsolving perovskites contain abundant amounts of oxygen vacancies to compensate the net concentration of acceptor species. The larger problem with this proposal is that the segregation energy of Ni alone is already negative, meaning that reducing conditions are not necessary: already under oxidising conditions, Ni should segregate to the surface. And lastly, as a fourth problem of this proposal, metal nanoparticles[312] submerged in the bulk should not be present in the samples, as without a surface, there can be no segregation to a surface. Thus, co-segregation of B-site substituents and oxygen vacancies to the surface is also evidently unable to explain exsolution.

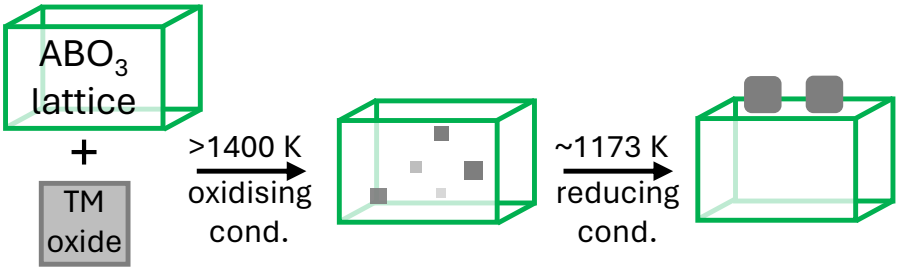


Figure 6.1 Schematic illustration of the preparation and exsolution processes. A transition-metal oxide is incorporated into a perovskite host lattice at high temperatures under oxidising conditions. Subsequently, it is exsolved at much lower temperatures under reducing conditions.

In addition to the thermodynamic origin of exsolution being unclear, the reasons for the relatively fast kinetics remain unknown. Exsolution has been found to take place, for instance, at temperatures of $T = 1173\,\mathrm{K}$ within hundreds of seconds[313] (although much longer times are generally used to produce catalytic systems). The characteristic temperature–time window for cation transport processes in titanate perovskites,[314–316] however, is substantially different, as evidenced by the typical synthesis conditions for the starting solid solutions, of $T > 1400\,\mathrm{K}$ for tens of hours[294,295,305,313,317,318] (see Fig. 6.1). Curiously, the kinetics of re-incorporation of the exsolved component under oxidising conditions[319] are consistent with the standard (high) temperature–(long) time window. It is the discrepancy between exsolution conditions, on the one hand, and synthesis and re-incorporation conditions, on the other, that remains as yet unexplained.

Lastly, it is remarkable that perovskite oxides constitute the vast majority of host materials that undergo exsolution.[320] It is suspected that many other oxide systems have been examined experimentally, but the comparatively poor performance of such systems has resulted in these negative results remaining unpublished. If the combination of factors that makes the perovskites such excellent exsolution systems could be understood, this knowledge could be exploited to facilitate property optimisation and to accelerate the development of new systems.

In this way, three critical questions to be addressed in this chapter are arrived at: Why does the transition-metal substituent exsolve but not the host *B*-site cation? How can exsolution take place so fast at such low temperatures in such short times? And why does the ABO_3 perovskite structure constitute such a good host material? Herein, a single model is proposed that provides answers to these three main questions, and to some secondary questions as well. The core of the model is that the transition-metal substituents change their valence within the perovskite matrix, as the FERMI level shifts upwards past the relevant charge-transition levels within the bandgap upon oxide reduction, Ni^{2+} in $SrTiO_3$, for example, becoming Ni^{+} and then Ni^{0}. In comparison with Ni^{2+},

the neutral species are energetically unfavoured in the perovskite lattice, and are thus expelled; and being neutral, they can migrate far more easily within the ABO_3 perovskite lattice. This new model thus stands in contrast to the standard model, in which substituent cations are reduced only once they have reached the surface, after they have left the lattice. To elucidate this model, point-defect behaviour in the model system of A -site deficient $SrTiO_3$ with Ni as the late transition-metal substituent (Ni being the most intensively studied exsolution substituent)[303] is examined, by means of hybrid density-functional-theory (DFT) calculations.

Although the term exsolution has been applied to a variety of phenomena,[300,321] in this work a narrower definition is favoured: Transition-metal species coming out of a lattice upon reduction, leaving the host composition otherwise unchanged and the host lattice otherwise intact (Fig. 6.1). Consequently, cases that involve host cations or that involve lattice decomposition do not fall under this definition. Furthermore, in such cases, alternative explanations are available. Here it will suffice to mention three examples. The first is the appearance of SrO on the surface of $SrTiO_3$ after a high-temperature anneal.[322] In this case, the host Sr cations come out of the lattice because of the active SrO partial-Schottky equilibrium (see Eq. 2.9) that produces strontium and oxygen vacancies in the bulk.[323] The second example is A -cation or B -cation based phases appearing on the surface of thin films produced, for example, by pulsed laser deposition. Such thin-film samples will generally contain concentrations of A -site and B -site cation vacancies that are far above their equilibrium values and in general not equal.[315,324,325] High-temperature treatments allow such systems to reach equilibrium by expelling excess B -site or excess A -site cations (respectively) as part of a second phase at the surface. The third example is the appearance of native B -site species from a non-substituted perovskite lattice, such as $LaNiO_3$.[326] In this case, the perovskite lattice undergoes phase decomposition to a binary oxide and a metal.

In this chapter, hybrid DFT calculations were carried out with the HSE06[113–115] functional in VASP.[153–155,327] Defect formation energies, corrected for artificial interactions between periodic images as necessary,[133] were used to obtain the charge-transition levels of Ni and defect reaction energies; the energy of the oxygen molecule was corrected for over-binding.[127,175] Activation barriers of defect migration were obtained by climbing image nudged elastic band (CI-NEB) calculations.[135,136] Further details are given in Sec. 3.6.2.

Throughout this chapter, a modified version of Kröger–Vink[9,10] notation is employed to describe point defects, using absolute (real) charges instead of relative charges.[328,329] Given the variety of Ni charge states and possible sites (A site, B site, interstitial site), the use of absolute charge is less

confusing. For example, divalent Ni cations sitting on a Ti site and in an interstice are thus Ni_{Ti}^{2+} and Ni_i^{2+}, respectively (rather than Ni_{Ti}'' and $Ni_i^{\bullet\bullet}$); and an oxygen site from which O^{2-} has been removed is thus v_O.

6.2 Results and Discussion

6.2.1 Charge-Transition Levels of Ni in $SrTiO_3$

Transition-metal cations in perovskite $SrTiO_3$ and $BaTiO_3$ have long been known to change their formal charge states upon changes in oxygen partial pressure. Particularly well-studied species include Fe^{5+}, Fe^{4+} and Fe^{3+}.[330–337] Ni has been examined experimentally to a lesser extent, but the charge states Ni^{4+}, Ni^{3+}, and Ni^{2+} have been reported.[338–344] Other transition-metal cations have received scant attention. The possibility of neutral species has been ignored. Nevertheless, trends concerning the charge-transition levels of first-row transition-metal cations in $BaTiO_3$ have been recently extracted by Klein *et al.*[345] Assuming systematic trends and extrapolating [see Fig. 14(a) of Ref. [345]], for $SrTiO_3$ (noting that charge-transition levels in $BaTiO_3$ and $SrTiO_3$ are not necessarily identical[346]) a Ni^{2+}/Ni^{+} transition at 1 eV below the conduction-band (CB) edge and a Ni^{+}/Ni^{0} transition just below the CB edge [or equivalently 2.2 eV and 3.2 eV above the valence-band (VB) edge] are tentatively predicted.

In the present DFT calculations, charge-transition levels were determined for cubic $SrTiO_3$ not only for Ni_{Ti}^{z+} but also for the defect associate with an oxygen vacancy, $(Ni_{Ti}^{z+}v_O)$; for substitutional species on the *A* site, Ni_{Sr}^{z+}; and for five species with Ni as an interstitial, Ni_i^{z+}, $(Ni_i^{z+}v_O)$, $(Ni_i^{z+}v_Ov_{Sr})$, $(Ni_i^{z+}v_O2v_{Sr})$, and $(Ni_i^{z+}v_Ov_{Ti})$. The Ni_i associates with v_{Sr} were examined, not only because of the material's *A*-site deficiency, but also because of the results of a previous DFT study;[347] those with v_{Ti}, because the formation of Ni_i from Ni_{Ti} results in the formation of v_{Ti}. The results are summarised in Fig. 6.2 for levels between VB and CB edges and around them. The value of the bandgap used in Fig. 6.2, of 3.34 eV, was taken from the hybrid DFT calculations; it compares well with the experimental value of 3.25 eV.[172,173,334]

The results of Fig. 6.2 confirm the existence of various transition levels for Ni-containing defects within the band gap of $SrTiO_3$ but show a more complicated picture than the tentative predictions.

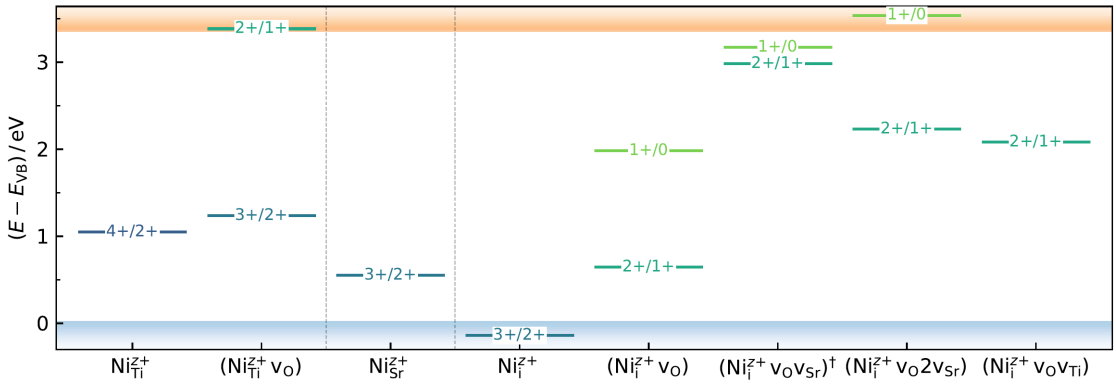


Figure 6.2 Thermodynamic charge-transition levels of different Ni-containing defects in $SrTiO_3$ obtained from hybrid DFT calculations. The six defects are divided into three groups that refer to *B* -site, *A* -site, and interstice occupation respectively. The blue region indicates the valence band; the orange region, the conduction band. †The $(Ni_i^{z+}v_Ov_{Sr})$ associate refers to a different configuration, in which the Ni^{2+} ion is displaced from the octahedral interstice towards the *A* -site vacancy.

According to the hybrid DFT calculations, not all examined Ni defects display all charge states from 4+ to 0. In particular, it was found that, for Ni residing on the *B* -site, the charge states Ni_{Ti}^{4+}, Ni_{Ti}^{3+} and Ni_{Ti}^{2+} are stable, in line with the results of an earlier DFT study.[28] As part of an associate with an oxygen vacancy,[338] Ni_{Ti}^{z+} can assume 3+ and 2+ charge states, with the 2+/1+ level being just above the CB edge. On the *A* site — or to be precise: relaxed from a slightly off-centre *A* -site symmetry position — Ni is also present as either 3+ or 2+. In other words, as a substitutional species Ni^0 is not accessible on either cation site because the relevant charge-transition levels are well above the CB minimum. Residing in an octahedral interstice as an isolated species, only Ni_i^{2+} is stable, as found in a previous DFT study of Ni_i^{2+} in perovskite $BaZrO_3$.[347] With an adjacent oxygen vacancy, however, Ni_i can take 2+, 1+ and 0 charge states; and adding one or two *A* -site vacancies to this associate shifts both transition levels, but they remain essentially accessible. The main results of Fig. 6.2, therefore, are that Ni can be reduced within the perovskite lattice to Ni^+ and even Ni^0, but only if present as an interstitial and as part of an associate with an oxygen vacancy (or with oxygen and cation vacancies); and that the reduction of Ni to Ni^+ or Ni^0 occurs at different energy levels, depending on the nature of the Ni_i-containing associate.

It is worth emphasising that the equilibrium concentration of a particular Ni species in a particular charge state on a particular site will depend on the position of the FERMI level and thus on the oxygen partial pressure and temperature. For example, Ni_{Ti}^{z+} species in Fig. 6.2 can be considered. At low FERMI levels, corresponding to oxidising conditions, Ni_{Ti}^{4+} will be the dominant charge state, with Ni_{Ti}^{3+} and Ni_{Ti}^{2+} present at non-zero, though perhaps negligible, concentrations; if the sample is

now reduced sufficiently, such that the FERMI level crosses the $Ni_{Ti}^{4+}/Ni_{Ti}^{2+}$ charge-transition level, the dominant charge state will be Ni_{Ti}^{2+}, with Ni_{Ti}^{3+} and Ni_{Ti}^{4+} present at non-zero, though perhaps negligible, concentrations. In this way, it is recognised that the absence of charge transitions involving Ni_{Ti}^{3+} in Fig. 6.2 does not mean that this charge state is not stable. It just means that it is not the dominant one: a non-zero concentration of Ni_{Ti}^{3+} will be present at all finite temperatures.[348,349] (The case of $Fe_{Ti}^{3+}/Fe_{Ti}^{4+}$ concentrations in $SrTiO_3$ is considered quantitatively, for example, in Figs. 2 and 3 of Ref. [350].) Since neither the defect chemistry of exsolution systems is known quantitatively nor has the FERMI level been determined in situ, no information is available as to the position of the FERMI level in the bandgap, neither before nor after reduction. It is noted, therefore, that at $T = 1000\,\mathrm{K}$, a change in oxygen partial pressure from 1 bar to 10^{-20} bar corresponds to the FERMI level shifting upwards by $\Delta E_F = 1\,\mathrm{eV}$.[351]

Based on these results and on the trends identified by KLEIN *et al.*,[345] it can be asserted, first, that other transition-metal substituents will have different charge-transition levels within the bandgap and hence will require more or less reducing conditions, corresponding to different FERMI-level shifts, for exsolution; and second, that accessible neutral levels will be available for the (easily reducible) late transition-metal cations, such as Ni, Cu, Pd and Rh. For early transition-metal cations, the charge-transition levels will tend to be well above the CB edge.

Good qualitative agreement is found between these results for substitutional species on the B site and those obtained in two experimental studies[338,343] of $SrTiO_3$ under oxidising conditions (i.e. FERMI levels relatively close to the VB edge). In one study,[343] Ni_{Ti}^{4+} species were found through a combination of x-ray techniques; and in a different study,[338] $(Ni_{Ti}^{3+}v_O)$ associates were detected by means of Electron Paramagnetic Resonance (EPR). However, a third study[342] reported charge-transition levels in $SrTiO_3$ for $Ni_{Ti}^{4+}/Ni_{Ti}^{3+}$ (of 0.15 eV above the VB edge) and for $Ni_{Ti}^{3+}/Ni_{Ti}^{2+}$ (of 1.2 eV above the VB edge), values that are inconsistent with the results shown in Fig. 6.2. These experimental values were not obtained directly, however, but by fitting electrical conductivity data as a function of temperature. In addition, the possibility of defect associates such as $(Ni_{Ti}^{z+}v_O)$ being present and having different charge-transition levels was not taken into account. Consequently, the values of Ref. [342] must be considered effective values, and a direct comparison with the present data is, therefore, not possible.

6.2.2 Thermodynamics of Exsolution

The thermodynamics of the exsolution reaction are now considered, assuming for simplicity that the point defects constitute a dilute solution. An overall exsolution reaction is proposed below, which is a combination of several point-defect reactions: (in no particular order) reduction of the oxide; full Schottky disorder, or rather its reverse; Ni species forming defect associates; Ni species changing their valence; Ni species being displaced from substitutional to interstitial sites; and expulsion of Ni^0 from the lattice. The first two reactions (oxide reduction and Schottky disorder) are briefly examined, since data exist against which the calculated energies can be validated. In addition, the expulsion of Ni^0 from the lattice is examined, since this defect reaction is a key part of the new model. Thereafter, the overall exsolution reaction is directly proposed. By taking this shortcut, the need to specify which defect associates in which charge states are involved (see Fig. 6.2) and in which order defect association, two valence changes and site displacement occur is avoided. In any case, all defect associates containing Ni are intermediate species and are thus eliminated in the overall reaction.

For the reduction of $SrTiO_3$ according to reaction (2.10), a value of $\Delta_{red}E = 5.7$ eV is obtained from the hybrid DFT calculations, in excellent agreement with experimental values[352–355] of (5.2 to 6.2) eV. For the full Schottky reaction (2.9) the calculations yield $\Delta_{Sch}E$ of 2.20 eV per defect, in reasonable agreement with values of 1.64 eV and 2.61 eV reported in previous DFT studies,[356,357] and values of (1.6 to 2.4) eV reported in pair-potential studies.[358–360] The good agreement for both these defect reaction energies justifies some confidence in the overall predicted reaction energy.

The expulsion of Ni^0 from an Ni_i-containing associate in the perovskite lattice according to, for example,

$$(Ni_i^0 v_O) \longrightarrow Ni^0(\text{metal}) + v_O \tag{6.1}$$

or

$$(Ni_i^0 v_O v_{Sr}) \longrightarrow Ni^0(\text{metal}) + (v_O v_{Sr}) \tag{6.2}$$

is predicted to occur with a reaction energy of $\Delta_{\text{exps}}E = -3.00\,\text{eV}$ without v_{Sr} and $\Delta_{\text{exps}}E = -1.12\,\text{eV}$ with v_{Sr}. These negative values highlight the thermodynamic reason for exsolution: the perovskite lattice permits Ni^{2+} to be reduced to Ni^0 (see Fig. 6.2), but it does not like having Ni^0 present.

The overall reaction for exsolution, starting with one Ni acceptor cation and its compensating oxygen vacancy (representing y in $Sr_{1-3x/2}La_xTi_{1-y}Ni_yO_{3-y}$), reads

$$v_{Sr} + Ni_{Ti}^{2+} + v_O + 2\,O_O^{2-} \rightleftharpoons Ni + O_2 + 2\,e^- + \varnothing\,. \tag{6.3}$$

The energy of this reaction, $\Delta_{\text{exsoln}}E$, was computed from the calculated energies of defect formation, with contributions arising from interface-specific energies being ignored (see later). Calculated in this way, $\Delta_{\text{exsoln}}E$ refers to standard conditions (1 bar O_2), and hence, a correction for exsolution occurring under reducing conditions must be applied. This correction, corresponding to a decrease in the chemical potential of oxygen, $\Delta\mu_{O_2}$, is given by

$$\Delta\mu_{O_2} = \Delta\mu_{O_2}^{\ominus} + RT\ln\frac{p_{O_2}}{p_{O_2}^{\ominus}}. \tag{6.4}$$

From thermodynamic tables,[361] $\Delta\mu_{O_2} = 2.20\,\text{eV}$ at $p_{O_2}^{\ominus} = 1\,\text{bar}$ for a typical exsolution temperature of $T = 1000\,\text{K}$ is obtained. For a pressure of $p_{O_2} = 10^{-20}\,\text{bar}$, a correction of $\Delta\mu_{O_2} = -6.17\,\text{eV}$ is then found. In this way, a — thermodynamically favourable — overall reaction energy of $\Delta_{\text{exsoln}}E = -2.33\,\text{eV}$ is obtained.

One benefit of including the reverse full Schottky reaction in Eq. (6.3) is that $\Delta_{\text{exsoln}}E$ becomes strongly favourable (see below). Another benefit is that the morphological changes in the sample needed to explain the embedding of the metal nanoparticles in the surface (socketing) and in the oxide bulk are yielded. The reverse of the full Schottky reaction corresponds to the annihilation of a full unit cell of the perovskite lattice at the surface (or an internal surface), that is, the filling of one v_{Sr}, one v_{Ti} and three v_O in the bulk with the appropriate host ions from a surface. Lastly, it is noted that including the reverse Schottky reaction provides an additional contribution (see below) to why the surface orientation (and termination) of the perovskite grains plays a role in exsolution:[295] Schottky disorder corresponds to the removal of host ions from the bulk and their attachment at a surface, and thus its energy depends on the surface orientation.

In order to emphasise the first thermodynamic benefit, as an alternative the exsolution of Ni^{2+} from the *B* site to the surface as a second phase is considered, without including the reverse Schottky reaction,

$$Ni_{Ti}^{2+} + O_O^{2-} \rightleftharpoons NiO\,(\text{phase}) + v_{Ti} + v_O, \tag{6.5}$$

combined with the subsequent reduction of NiO under exsolution conditions

$$NiO \rightleftharpoons Ni + \frac{1}{2}\,O_2. \tag{6.6}$$

Eq. (6.5) is highly unfavourable, with an energy of $\Delta E = 7.53\,\text{eV}$. In addition to emphasising the importance of the reverse Schottky reaction, this is a satisfying result, since the reverse reaction of Eq. (6.5) is evidently highly favoured, i.e., the incorporation of Ni^{2+} into the perovskite lattice. (It should be noted that segregation from the perovskite lattice to the surface does not change this energy of 7.53 eV, since the Ni^{2+} cation has to leave the perovskite lattice.) The second reaction is favourable, with an energy of $-1.54\,\text{eV}$, giving a reaction energy for

$$Ni_{Ti}^{2+} + O_O^{2-} \rightleftharpoons v_{Ti} + v_O + Ni + \frac{1}{2}\,O_2 \tag{6.7}$$

of 9.08 eV at $T = 0\,\text{K}$ and 6.00 eV under the assumed exsolution conditions ($T = 1000\,\text{K}$, $p_{O_2} = 10^{-20}$ bar). If only Eq. (6.6) is considered [this is the second explanation discussed in the Introduction (Sec. 6.1)[294,308,309]], then it is clear that exsolution is not explained.

Returning to the overall exsolution reaction of Eq. (6.3), the $\Delta\mu_{O_2}$ correction for a wide range of temperatures and oxygen partial pressures was calculated, and in this way the conditions under which exsolution is thermodynamically favourable are mapped out, i.e., the conditions under which $\Delta_{\text{exsoln}}E(T, p_{O_2})$ becomes negative. The results are plotted in Fig. 6.3. As noted above, interface-specific energetic contributions are not included in these calculations. These are (i) the increased surface energy arising from morphological changes of the oxide host, (ii) the surface energy of the nano-sized Ni particles, (iii) the interfacial energy of the perovskite|metal interface, and (iv) the variation in $\Delta_{\text{Sch}}E$ with surface orientation. Since the first two are positive, the third is negative,

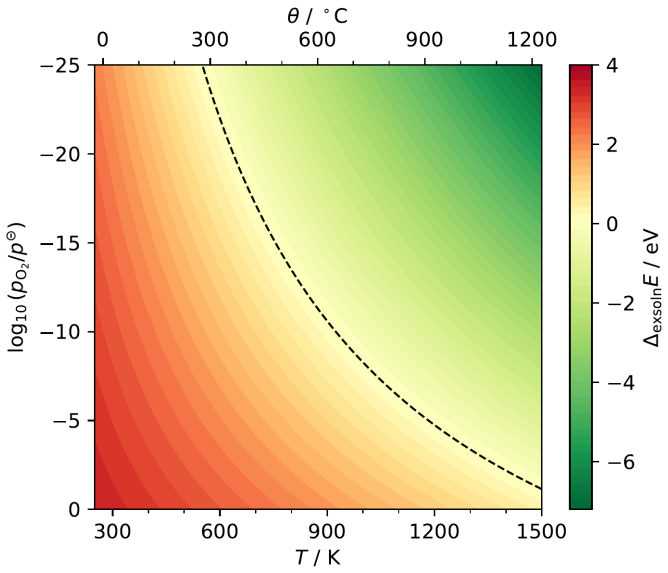


Figure 6.3 Thermodynamic prediction of conditions necessary for the exsolution of Ni from $SrTiO_3$ based on the reaction energy for the overall exsolution reaction, Eq. (6.3). The dotted line refers to $\Delta_{\text{exsoln}}E = 0$; the area above and to the right corresponds to a negative reaction energy and thus to conditions under which exsolution can take place (in the absence of kinetic hindrance). Interface-specific energies are not included (see text); dilute-solution thermodynamics are assumed.

and the fourth could be either, the boundary in Fig. 6.3 will be shifted in some non-trivial manner. The dominant contribution to the overall reaction energy, however, is given by $\Delta_{\text{exsoln}}E(T, p_{O_2})$ of Eq. (6.3), since it determines if the transition-metal substituent is expelled from the host lattice, whereas the interface-specific terms affect the shape, size and distribution of the metal nanoparticles on the surface. A shift in the line also results from moving from the dilute-solution thermodynamics of the DFT calculations to the concentrated solid-solutions of experiments, with $> 1\%$ defects. Nevertheless, it is found in Fig. 6.3 that sintering at $T = 1423\,\text{K}$ in air, for example,[317] allows nickel to be incorporated into the perovskite lattice, and that exsolution at $T = 1000\,\text{K}$ under typical exsolution conditions is possible. Importantly, the results also indicate that a critical p_{O2} is necessary at a given temperature; this may explain the observation that a critical amount of oxygen vacancies is required for exsolution.[295]

6.2.3 Kinetics of Exsolution

While the results also predict that the lower the exsolution temperature, the more strongly reducing the conditions have to be, the reaction kinetics may become too slow at lower temperatures to allow

the reaction to proceed on a reasonable timescale. Indeed, successful exsolution from titanate-based perovskites at temperatures below ca. 800 K has not been reported,[362,363] which is consistent with, but does not confirm, a kinetic limitation at these lower temperatures. This brings, then, the second critical question: Why are exsolution kinetics so fast?

Let the initial kinetics of the exsolution process be considered. Upon exposure to reducing conditions, a perovskite exsolution system will lose oxygen through ambipolar diffusion of oxygen vacancies and electronic species (electrons or holes). As a consequence, the slower of these two species will determine the overall rate of oxygen out-diffusion, and in the representative exsolution system with high electronic conductivity, this will be oxygen vacancies (and in systems with dominant ionic conductivity, this will be electronic species). As the reduction front advances into the sample, the local FERMI level shifts upwards within the bandgap, leading to changes in the populations of Ni in its various charge states and on its various lattice sites. Since perovskite-type oxides are generally excellent oxide-ion conductors but extremely poor cation conductors, attention is focused on cation migration processes. For the exsolution of Ni in perovskite $SrTiO_3$, there are, then, two processes for which the migration of Ni species is important: the individual jump of Ni from a substitutional site to an interstitial site, and the long-range out-migration of Ni_i^0, comprising multiple individual jumps. Ni also substitutes under oxidising conditions for Ti, and therefore this possibility is also considered.

First, the migration of Sr^{2+} on the *A* -site of $SrTiO_3$ by a vacancy mechanism was examined, because it is a standard case against which results can be validated. The CI-NEB calculations indicated a linear ⟨100⟩ path and an almost cosinusoidal energy profile, with an activation barrier of 4.13 eV. This value agrees well with results from experimental[314,315,364] and computational[206,365,366] studies, in which activation energies of (3.5 to 4.0) eV are reported. Interestingly, and of relevance below, it is found that the presence of a neighbouring v_{Ti} lowers the barrier for the migration of Sr^{2+} to only 1.48 eV.

Next, the migration of *B* -site cations on the *B* -site sublattice by a vacancy mechanism was examined. It is noted that the migration of *B* -site cations along ⟨110⟩ in perovskites is energetically unfavourable because of the strong electrostatic repulsion between the migrating cation and the two *A* -site cations in the saddle-point configuration.[367] As a consequence, migration along ⟨100⟩ will be preferred (only one *A* -site cation in the saddle-point configuration), and it will be further assisted by an *A* -site vacancy (no *A* -site cations in the saddle-point configuration). Indeed, CI-NEB calculations yielded an activation barrier for the migration of Ti^{4+} by a vacancy mechanism along ⟨100⟩ of

Table 6.1 Activation energies of migration for B-site cations in $SrTiO_3$ along ⟨100⟩, in the presence of v_{Sr}.[a]

Species	Ti^{4+}	Ni^{4+}	Ni^{3+}	Ni^{2+}	Ni^{1+}
$\Delta_{mig}E$ [eV]	3.40	3.02	2.84	2.09	n.a.

[a] These barriers refer to the individual jumps for Ni_{Ti}^{z+} jumping to a neighbouring v_{Ti}, but they do not correspond to the effective barrier for long-range diffusion.

6.54 eV, a barrier that is lowered substantially to 3.40 eV when an adjacent v_{Sr} is present. For the Ni species that are stable substituting for Ti^{4+}, i.e., Ni^{4+}, Ni^{3+} and Ni^{2+}, the calculated barriers for a v_{Sr}-assisted jump to a neighbouring v_{Ti} (see Table 6.1) are smaller in comparison. Consequently, for the long-range diffusion of the entire $Ni_{Ti}^{z+}v_{Ti}v_{Sr}$ associate in an A-site-deficient composition with very few v_{Ti} present, there are three steps in series, and the rate-determining step according to these calculations will be that for v_{Ti} migration (i.e., the jump of Ti^{4+}), since the activation energies for the other migration steps of Ni_{Ti}^{z+} (with a neighbouring v_{Sr}) and v_{Sr} (with a neighbouring v_{Ti}, see above) are much lower. It will therefore be the activation energy of 3.40 eV that constitutes the effective barrier for long-range diffusion of Ni_{Ti}^{z+} species. This activation energy is similar to those found for cation diffusion in the standard temperature–time window,[314,315] and hence the discrepancy mentioned in the Introduction (Sec. 6.1) does not seem to be explained.

Coming now to the migration jump of Ni^{2+} or Ni^{+} from a Ti site to a neighbouring interstitial site, the model was kept simple by including a neighbouring oxygen vacancy and a neighbouring strontium vacancy. CI-NEB calculations indicated no barrier for the jump, that is, the system's energy increased continuously as the Ni ion moved from the Ti site to the interstitial site. Under equilibrium conditions, the energy difference between initial and final states, of ca. 2.5 eV for both species, determines the populations of the two configurations according to $p(Ni_i^{z+})/p(Ni_{Ti}^{z+}) = e^{-\Delta E/k_B T}$. During exsolution, however, the interstitial Ni cations will be quickly reduced in the subsequent step(s) to Ni_i^0, thus forcing further Ni cations from Ti sites into interstitial sites in order to re-establish the quasi-equilibrium. Two points should be noted here. First, only after Ni_i has migrated away from v_{Ti} can it be reduced to Ni_i^0 (see Fig. 6.2). Second, without v_{Sr}, the energies are ca. 1.5 eV higher, indicating that A-site vacancies, by lowering the energy of the interstitial ions, accelerate the kinetics of Ni jumping from the B sites to interstitial sites.

The migration of Ni_i^0 out of the lattice depends, of course, on the defect associate that dominates. Instead of covering all possible defect associates, only the simplest case was probed, namely the

migration of Ni_i^0 as part of the $Ni_i^0v_O$ associate. The migration energy for Ni^0 was found to be only 1.44 eV. This surprisingly low value can be attributed to the migrating species being neutral. This low value also raises the question as to the activation barrier for v_O migration as part of the $Ni_i^0v_O$ associate. Such a barrier was found to be 1.45 eV (which is much higher than the activation energy for the migration of a free oxygen vacancy, of ca. 0.6 eV[204,368–371]). The long-range diffusion of the $Ni_i^0v_O$ associate will thus be characterised by an effective activation energy of ca. 1.45 eV.

The migration analysis thus indicates that Ni_i^0 species can be produced and that they are mobile in the lattice as part of the $Ni_i^0v_O$ associate. It is tempting to conclude that the diffusion of the $Ni_i^0v_O$ associate determines the overall rate of exsolution, but such a conclusion is not drawn here because not all possibilities have been examined and only activation energies (and an energy difference), but not pre-exponential terms, are available. Conceivably, the transfer of Ni cations from substitutional sites to interstices could determine the overall rate. It is also conceivable that oxygen-vacancy diffusion in lattices containing *A* -site vacancies and Ni species[207,372] is slower than the out-diffusion of the Ni_i^0 species. Lastly, it is also conceivable that the rate-determining step may change during the course of an exsolution run.

It is worth stressing that Ni_i^0 diffusion as part of the $Ni_i^0v_O$ associate does not involve cation vacancies. In perovskite systems it can occur, therefore, much faster than the vacancy-mediated migration of the host cations. This has consequences for the kinetics of socket formation, in the form of the reverse Schottky reaction, relative to that of Ni expulsion from the perovskite. Specifically, it is supposed that sockets will initially form at those places at the surface (and in the bulk) where sufficient v_{Sr}, v_O and Ni_{Ti} species are present, such that the concomitant formation of Ni_i species (and thus v_{Ti}) and further v_O supplies all the species necessary for the reverse Schottky reaction to occur, without the need for long-range migration of host cations. At those places where not all defects for the reverse Schottky reaction are present, Ni may be expelled from the solid to form on the surface Ni_{ad} species, which through surface diffusion may join the growing Ni nanoparticle. At longer timescales, cation-vacancy migration to the nascent socket can occur, but Ni_i^0 may diffuse to the growing Ni nanoparticle from much further away, since the migration of cation vacancies is not necessary for the migration of Ni_i^0. If v_{Sr} do diffuse out of a region, however, the kinetics of Ni_i forming from Ni_{Ti} will slow down drastically, because the energy difference for Ni between Ti and interstitial sites rises substantially (see above).

An explanation is also provided for why the re-incorporation of Ni into the perovskite is sluggish:[319] nanoparticles of Ni metal quickly become nanoparticles of NiO upon oxidation, but Ni^{2+}, which is

soluble in the perovskite, diffuses in as a $Ni_{Ti}^{2+}v_{Ti}v_{Sr}$ associate, and thus with an activation energy of 3.40 eV, or without v_{Sr} mediation, as $Ni_{Ti}^{2+}v_{Ti}$ (i.e. from *B*-site to *B*-site), and thus with an activation energy of 6.54 eV.

6.2.4 Perovskites as Exsolution Hosts

Lastly, the third major question is addressed: What makes perovskites such superior exsolution systems? The vast majority of reports concern this class of host oxides; very few examine fluorites, spinels and simple binary oxides, and even fewer examine other oxides.[320] It is important to note that, without knowing exactly why other materials failed as exsolution systems, it is difficult to identify the key characteristics of perovskites. Nevertheless, it can be hypothesised that some or all of the following features are important: facile chemical diffusion of oxygen out of the lattice, as this allows for quick reduction; the ability to accommodate oxygen nonstoichiometry; the ability to accommodate high cation-vacancy concentrations on the non-substituent cation sublattice, as this allows in a structure with two cation sublattices reverse Schottky disorder and thus socketing; an electronic-band structure that provides both charged and neutral charge-transition levels within an accessible range; the possibility to accommodate transition-metal interstitials in various charge states, and the ease of migration of such transition-metal species, as this allows fast cation transport whilst maintaining stability of the host. The question may also be turned round: Why are other oxides comparatively bad exsolution host materials? Fluorite oxides, for example, are good oxygen-ion conductors, but the exsolution kinetics will be slow, if fast cation-interstitial transport does not take place. Charge-transition levels for neutral species may be too high for reduction in Ar/H_2 mixtures. Spinels do exhibit fast cation transport, but there are no additional interstitial positions available since the cations already reside in the octahedral and tetrahedral sites of the fcc anion lattice. Oxygen diffusion in spinels is also relatively slow. Systematic studies on these possibly unpromising systems are, therefore, required, in order to draw strong conclusions.

6.3 Concluding Remarks

In the standard picture of the exsolution process, transition-metal cations are first removed from a perovskite lattice upon exposure to reducing conditions, after which they are reduced to the metal

at the surface. The results of hybrid DFT calculations shown in Figs. 6.2 and 6.3 for Ni in $SrTiO_3$ support an opposite description: Ni cations can be reduced within the perovskite lattice to Ni^0, and it is these energetically unfavoured species that are expelled from the lattice to form metal nanoparticles. Specifically, the model indicates that upon reduction, which shifts the FERMI level upwards within the bandgap, certain transition-metal substituents can be reduced within the oxide host if they have suitable charge-transition levels within the bandgap. In this way, a variety of experimental observations concerning not only the thermodynamics but also the kinetics of the exsolution process can be naturally accounted for. Indeed, the model also provides an alternative definition of metal-nanoparticle exsolution from oxide hosts: the expulsion of a substituent upon valence change as charge-transition levels within the band gap are crossed.

This model is applicable to all materials that possess a bandgap, within which transition-metal substituents exhibit charge transition levels. The material does not need to be a good electronic conductor: an upwards shift in FERMI level occurs in all oxides as chemical diffusion of oxygen out of the material occurs. The model is not applicable, for example, to the appearance of Fe nanoparticles on the surface of $(La,Sr)FeO_3$, since Fe is part of the host lattice, providing electronic states that form the bandgap. The model is possibly applicable to thin-film systems, if other origins of nanoparticle appearance on the surface (e.g. a lattice containing high, non-equilibrium concentrations of v_A or v_B reaching equilibrium) can be ruled out.

It should be noted that the model is incomplete, since, for example, the rate-determining step in the exsolution process is unclear. In addition, several predictions are made that are consistent with experimental data (e.g. a critical concentration of oxygen vacancies, only late transition-metal cations having accessible neutral levels), but these need to be investigated systematically and quantitatively in experiments. Further progress, it is contended, will require a strong interplay between experiment and computation.

7 Oxygen Grain-Boundary Diffusion in LSF

Parts of this chapter have been published in:[1]

A. Bonkowski, J. A. Kilner, R. A. De Souza, *RSC Appl. Interfaces* **2024**, *1*, 699–710.

7.1 Introduction

Among oxides with high electronic and high ionic conductivity, perovskite-type oxides in the (La,Ba,Sr)(Fe,Co)$O_{3-\delta}$ system constitute many of the best performing materials currently known.[373–381] Oxide-ion conduction in these materials takes place by oxygen vacancies migrating through the perovskite lattice, and at elevated temperatures this process takes place at moderately fast to astonishingly fast rates depending on the composition. At lower temperatures, the rate of ion conduction diminishes because there are fewer vacancies (sample oxidation occurs) and because the vacancies are less mobile (migration is thermally activated).

In addition to oxide ion transport within the perovskite lattice, there is the possibility of transport along grain boundaries. Indeed, for $La_{0.6}Sr_{0.4}Fe_{0.8}Co_{0.2}O_{3-\delta}$ (LSCF6482) faster grain-boundary diffusion of oxygen has been observed, although only at lower temperatures ($T < 775$ K).[31,382] At higher temperature, lattice diffusion dominates, as generally observed for (La,Ba,Sr)(Fe,Co)$O_{3-\delta}$ compositions. The observation of fast grain-boundary diffusion of oxygen raises a number of questions. Since a general rule for oxides appears to be that ions that are relatively mobile within the lattice are slowed down by structural perturbations, such as grain boundaries,[27,383] is there

[1] All simulations were prepared, carried out, and analysed by the author of this thesis. Analysis methods were developed by the author of this thesis. Simulation cells were created and analysed by the author of this thesis. The published manuscript was written by the author of this thesis, with contributions from the co-authors.

something special about boundaries in LSFC6482 materials that makes them buck this trend? Does faster diffusion occur along the structural cores of the grain boundaries, or does it occur in adjacent space-charge zones, in which oxygen vacancies are accumulated? Is the vacancy accumulation linked to Sr accumulation?[384,385] And why is faster diffusion not observed at higher temperatures?

In this chapter, two (La,Sr)FeO_3 (LSF) compositions were taken as model systems, and molecular dynamics (MD) simulations were used to study oxygen diffusion in polycrystalline perovskite materials as a function of temperature. LSF represents the simplest of the (La,Ba,Sr)(Fe,Co)$O_{3-\delta}$ materials, since it contains only two *A*-site cations (one necessarily being an aliovalent substituent) and one *B*-site cation. Several experimental studies of oxygen diffusion in various LSF compositions exist,[292,386–391] but simulation studies so far have been restricted to static calculations of oxygen-vacancy migration barriers in the perovskite lattice.[165,167,392–399] Long-range diffusion of oxygen in (heavily substituted) LSF materials has not been simulated, and the effect of grain boundaries on the rate of oxygen diffusion has not been examined. In this chapter, oxygen tracer diffusion coefficients were computed using molecular dynamics simulations both within the perovskite lattice as well as within polycrystalline simulation cells. Rather than studying high-symmetry boundaries that are confined to a single plane, curved, general boundaries were considered. The chapter is structured in the following way. The simulation techniques and the analysis methods required for polycrystalline cells are described in Sec. 7.2. The results are divided into three subsections: oxygen diffusion in LSF lattices (7.3.1); compositional analysis of polycrystalline cells (7.3.2); and oxygen diffusion in polycrystalline cells (7.3.3). A discussion of the results is given in Sec. 4.

7.2 Simulation Methods

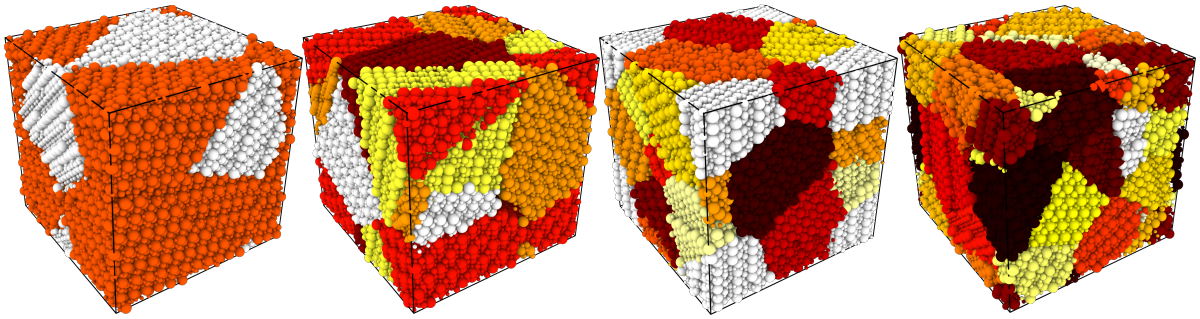
7.2.1 Bulk Simulation Cells

Bulk cells were created by a $15 \times 10 \times 15$ expansion of the orthorhombic *Pnma* unit cell and thus contained ca. 45000 ions. For each composition (LSF10 and LSF40), two cells were created by randomly replacing 10 % and 40 % of lanthanum ions with strontium ions, respectively. Oxygen vacancies were introduced, i.e. oxide ions were removed, until the total cell charge was zero.

7.2.2 Polycrystal Creation

Polycrystalline cells containing 2, 5, 10 or 20 grains were constructed with the ATOMSK code[144]. In each case, the grains were created in a cubic simulation cell with cell dimensions of 80 Å × 80 Å × 80 Å, and thus with ca. 40 000 ions. For ion pairs at the boundaries separated by less than 1.5 Å, one ion was removed at random to avoid instabilities during the minimisation. Since this leads to $A : B \neq 1$, cations at the grain boundary were removed until the numbers of A- and B-site ions were identical. Subsequently, strontium-containing cells were obtained by replacing at random the appropriate fraction of lanthanum ions with strontium ions. Oxide ions were removed at random to achieve a charge-neutral simulation cell.

In order to capture some of the variability of grain-boundary structures, three different random seeds (i.e., differently oriented grain centres, grain volumes, and $Sr'_{La}/v^{\bullet\bullet}_{O}$ configurations) were used to create cells containing 2, 5, 10 or 20 grains, resulting in a total of 12 cells for each compound (LSF10 and LSF40). Representative simulation cells are shown in Fig. 7.1, together with the average grain volume $\bar{V}$ (the cell volume being 512 nm^3) and the average grain diameters $\bar{d}$, assuming spherical grains.



(a) 2 grains. $\bar{V} = 256\,\mathrm{nm}^3$, $\bar{d} = 7.88\,\mathrm{nm}$.

(b) 5 grains. $\bar{V} = 102.4\,\mathrm{nm}^3$, $\bar{d} = 5.81\,\mathrm{nm}$.

(c) 10 grains. $\bar{V} = 51.2\,\mathrm{nm}^3$, $\bar{d} = 4.61\,\mathrm{nm}$.

(d) 20 grains. $\bar{V} = 25.6\,\mathrm{nm}^3$, $\bar{d} = 3.66\,\mathrm{nm}$.

Figure 7.1 Polycrystalline simulation cells generated and used in this chapter. Different grains are indicated with different colours. $\bar{V}$ is the average grain volume; $\bar{d}$ is the average grain diameter (assuming spherical grains).

MD simulations of polycrystalline cells were limited to $T \leq 2000$ K, since some cells appeared to undergo melting at higher temperatures. Equilibration of polycrystalline cells was performed for 2.0 ns at 2000 K. In the production run, the mean-squared displacement of oxide ions was monitored for 1.0 ns at $1200 \leq T/\mathrm{K} \leq 2000$.

7.2.3 MMC Simulations

Since cation diffusion in perovskites is generally not amenable to MD simulations,[206,400] on account of the high migration barriers and thus low ion jump rates, cations will not achieve equilibrium distributions on the timescale of an MD simulation. For real samples, high-temperature anneals for several hours at elevated temperatures lead to non-uniform cation concentrations on account of cation redistribution. In order to investigate the influence of equilibrium cation distributions on oxygen transport in polycrystalline cells, a METROPOLIS Monte Carlo[139] (MMC) approach was used to swap (quasi)particles from both the cation (Sr'_{La} and $La^{\times}_{La}$) and anion ($O^{\times}_{O}$ and $v^{\bullet\bullet}_{O}$) sublattices to simulate the high temperature sintering. NB: Through the use of general grain boundaries in three different simulation cells, cells with a distribution of grain boundaries could be used, which is a better representation of a real system.[401]

In each MMC step two particles (ions or vacancies) were swapped with each other and the energy was calculated. The swaps were accepted according to the probability $P = \exp\left[-\Delta E/(k_b T)\right]$, where $\Delta E = E_{after} - E_{before}$ is the energy difference before and after the swap. In static calculations, $La^{\times}_{La}$ were swapped with Sr'_{La}, and, simultaneously, $O^{\times}_{O}$ were swapped with $v^{\bullet\bullet}_{O}$ with 100 000 attempts each after which the total energy was observed to be constant. A hybrid approach (MMC+MD)[402] was not employed because the swapping of oxide ions and oxygen vacancies is then no longer possible (owing to the difficulties in identifying oxygen vacancies in MD simulations).

7.2.4 Compositional Analysis

As a consequence of using polycrystalline cells of the type shown in Fig. 7.1 in MD simulations, two problems are encountered when attempting to determine the compositions of the grain-boundary and bulk phases:

1. The grain boundary is not confined to a single geometric plane, which makes determining the composition normal to the grain boundary difficult.

2. Vacancies, being the absence of ions, are difficult to identify in MD simulations, on account of the ions' vibrations.

One possibility[223,403] is to consider grain boundaries at their initial positions from the creation of the cell, rather than after the MD simulation, but this method was found to be unreliable, since ions at the boundaries relax substantially within the MD equilibration (altering the nature and the position of the interfaces). A superior possibility that has been applied to metallic systems is to use structural identifier methods, such as Common Neighbour Analysis (CNA)[404–406] or Polyhedral Template Matching (PTM)[407], to differentiate between bulk and grain-boundary regions.

Owing to the highly defective and mobile oxide-ion sublattice, an indirect approach was employed, namely differentiating grain-boundary from bulk regions based solely on the cations. Specifically, all anions were removed from the initial simulation cell (for instance, in this case: Fig. 7.1c). The cations (La, Sr, Fe) form a bcc sublattice, and deviations from this bcc sublattice are thus identified as grain-boundary regions. The interval cutoff variant[407] of the CNA, as implemented in the `ovito` package[146], was used, since manual specification of a cutoff value is not required. Results obtained from the other methods (not shown) were reasonably similar. The result for the cell shown in Fig. 7.1(c) is presented in Fig. 7.2. Based only on the cations, the average grain-boundary fraction

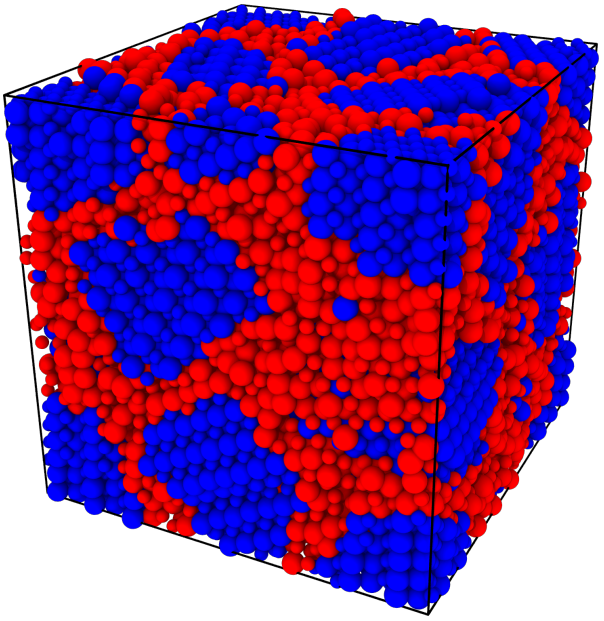


Figure 7.2 Polycrystalline cell with 10 grains (see Fig. 7.1c) after equilibration at 1800 K. Shown are only the cations (i.e. La, Sr, and Fe). The colour coding refers to the structure type identified by common-neighbour analysis of the cation sub-lattice, as implemented in the `ovito` package.[146] Blue ions are identified as bcc structured (and hence as bulk ions or grain core), whereas red ions do not have a bbc type coordination (grain boundary ions).

(number of grain-boundary cations divided by total number of cations) was calculated. It would be expected that the data for LSF10 and LSF40 are identical, since the data were derived from the same

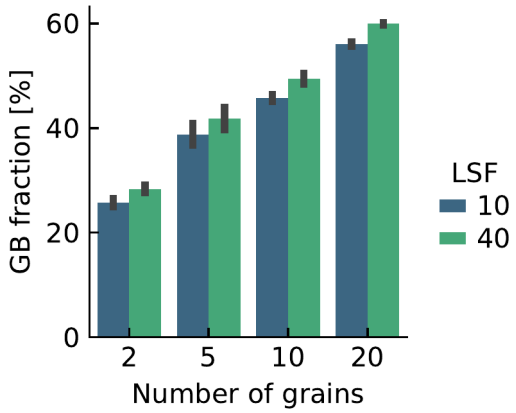


Figure 7.3 Average grain boundary fractions (cations only) for the initial structures. As the cells were subject to MD simulation, the fractions increased slightly. The fractions are higher for LSF40 than LSF10 due to the higher structural perturbation induced by the higher substitution fraction (see text). Error bars refer to the standard deviation.

initial polycrystalline cell, but as shown in Fig. 7.3, slight differences are observed. The difference is attributed to the four-times-higher concentration of both Sr'_{La} and $v_O^{\bullet\bullet}$ in LSF40, which leads to stronger structural perturbations of the bcc cation sublattice in the vicinity of the grain boundaries (in addition to the perturbation from the grain boundaries themselves) and thus to more cations being identified as belonging to this region. This plot is shown because the difference between LSF10 and LSF40 indicates the limits of this analysis method.

After analysis of the cations' bcc sublattice, the anions can be considered again. It is possible to use a nearest-neighbour or cutoff criterion to assign the anions to bulk or grain-boundary cations, but this approach is not self-consistent, since some anions can be nearest neighbours (or can be within a cutoff) of both grain boundary and bulk cations, resulting in ambiguous assignment of labels. Therefore, the criterion adopted was to count anions as grain-boundary particles if the majority of the five nearest-neighbouring cations is non-crystalline, and as bulk particles otherwise.

Another difficulty concerns vacancy concentrations. As noted above, while oxygen vacancies are considered as swappable particles in MMC calculations, they are not considered as particles in the MD simulations (in which a vacancy means that an ion is missing). In order to still extract oxygen-vacancy concentrations after MD simulations, the oxygen-vacancy fraction was calculated indirectly. To do so, the number of cations in the respective region was extracted and from that, the number of oxygen sites N_{anions} was obtained ($3 \cdot N_{\text{cations}} = 2 \cdot N_{\text{anions}}$). Subtracting the number of anions actually found with the chemical analysis in the respective region yields the number of vacancies (and thus the vacancy fraction). Corrections were applied to account for the non-planar

structure of the grain boundaries by calculating the anion-to-cation ratio in the ideal initial structure (which deviates slightly from 2 : 3 due to the way anions are assigned), where the vacancy content is known (LSF10: 1.66 %; LSF40: 6.67 %).

The analysis methods described above were bundled into a Python library (`agility`).[408]

7.3 Results

7.3.1 LSF Lattices

Lattice Structure

Lanthanum ferrite exhibits the orthorhombic *Pnma* perovskite structure at room temperature and ambient pressure. With increasing temperature, phase transitions occur, to rhombohedral $R\bar{3}c$ symmetry at $T = (1228 \pm 9)\,\mathrm{K}$ and then to cubic $Pm\bar{3}m$ symmetry at $T = (2140 \pm 30)\,\mathrm{K}$.[409] Upon substituting La with Sr, the transition temperatures are lowered substantially, according to both computational[398] and experimental studies[409,410]. In the MD simulations of LSF10 and LSF40, the orthorhombic structure was found to transform directly to the cubic phase. The transition temperatures were overestimated in both cases, although the trend towards lower transition temperatures with increasing Sr content is reproduced (see Fig. 7.4).

Although the potentials are unable to reproduce the rhombohedral phase, this is not critical, since experimental data for oxygen diffusion refer to the temperature ranges for orthorhombic LSF10 and cubic LSF40 ($1000 \leq T\,/\,\mathrm{K} \leq 1373$), i.e., phases that are reproduced in the simulations. In fact, the overestimation of transition temperatures allows tracer diffusion coefficients to be determined at elevated temperatures, where jump statistics are much better,[197] and then to be extrapolated to lower temperatures.

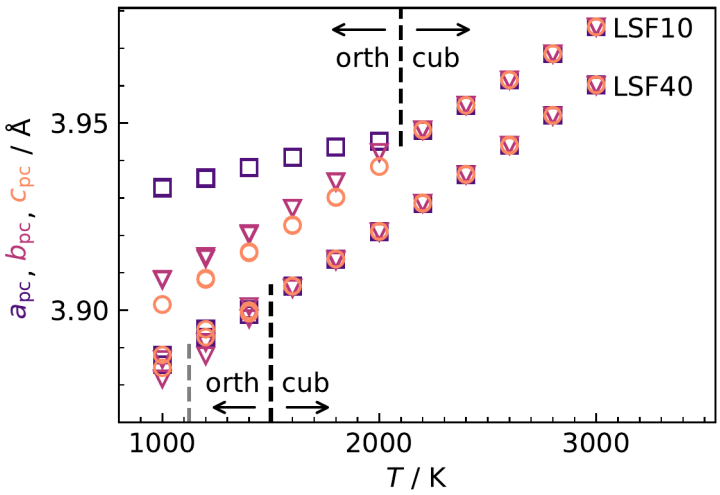


Figure 7.4 Pseudocubic cell parameters a (purple squares), b (magenta triangles), and c (orange circles) obtained for LSF10 and LSF40 from MD simulations as a function of temperature T. At each temperature, two simulations with different random Sr'_{La} distributions and different initial kinetic-energy distributions were carried out. The phase transitions from orthorhombic ($a \neq b \neq c$) to cubic ($a = b = c$) are indicated with black lines; the grey line indicates the experimental transition temperature for LSF40.[410]

Bulk Oxygen Diffusion

Oxygen tracer diffusion coefficients D^*_O were obtained by monitoring the mean-squared displacement of the oxide ions, $\langle r^2_O \rangle$, as a function of time t (see Fig. 7.5). If $\langle r^2_O \rangle$ evolves smoothly and linearly with t, D^*_O can be obtained from the EINSTEIN relation [Eq. (2.4)]. The relative error in D^*_O was calculated from the expression of USLER *et al.*[197]

In order to compare the results with literature data, the oxygen-vacancy diffusion coefficient D_v was calculated from the tracer diffusion coefficient D^*_O, since the MD simulations were performed at constant oxygen deficiency, whereas experiment refers to constant oxygen partial pressure and thus varying oxygen deficiency.

$$D_v = \frac{D^*_O}{f^*} \frac{[O^\times_O]}{[v^{\bullet\bullet}_O]} \tag{7.1}$$

The tracer correlation factor f^* for diffusion of a dilute solution of vacancies in a cubic perovskite is $f^* = 0.69$,[292] and this value is used throughout this chapter even though the site fractions of vacancies are far beyond the dilute limit and the perovskite composition may deviate from cubic symmetry.

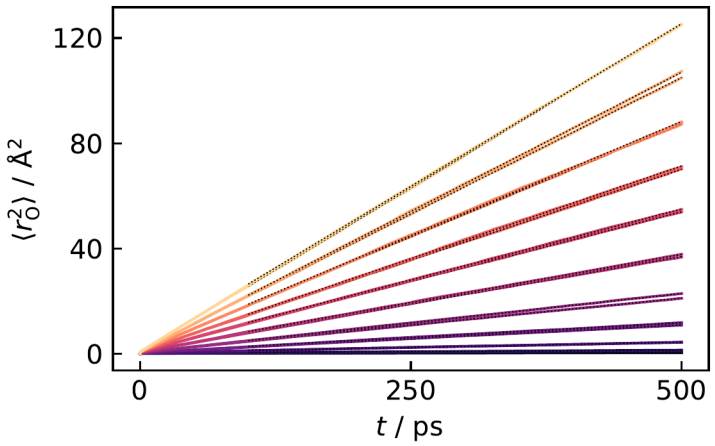


Figure 7.5 Mean-squared displacement of oxygen ions $\langle r_O^2 \rangle$ obtained as a function of time from MD simulations of LSF10, $n_v = 1.66\,\%$. Results are shown for various temperatures $1000 < T\text{K} < 3000$; at each temperature, two simulations with different random initial kinetic energy distributions were carried out.

The oxygen-vacancy diffusivities obtained are plotted in Fig. 7.6a,b for LSF10 and LSF40. Both compositions exhibit a lower activation enthalpy of oxygen-vacancy migration for the (high-temperature) cubic phase than for the (lower-temperature) orthorhombic phase (see Tab. 7.1). Similar behaviour was recently observed for oxygen tracer diffusion in the orthorhombic and cubic phases of $CaTiO_3$.[207] In other words, at constant composition, oxygen-vacancy diffusion in perovskites is evidently faster in the higher symmetry phase.

Fig. 7.6 also compares the results with experimental data. The experimental D_v data for LSF10 correspond to oxygen-vacancy diffusion in the orthorhombic lattice, and for LSF40, to oxygen-vacancy diffusion in the cubic lattice (dashed extrapolation in Fig. 7.6b). It is seen that, for dataset C,[292] the agreement is excellent for both compositions; for dataset D[30] there is good agreement in terms of activation enthalpies, but some differences in terms of absolute values; and for dataset E[389] there are larger deviations—it seems to be an outlier. These conclusions are also evident in the summary of activation enthalpies for oxygen-vacancy migration given in Fig. 7.8.

Table 7.1 Activation enthalpies of oxygen-vacancy migration ΔH_{mig} in LSF, obtained from molecular dynamics simulations.

Composition	ΔH_{mig}^{cub} / eV	ΔH_{mig}^{orth} / eV
LSF10	0.60 ± 0.01	0.88 ± 0.02
LSF40	0.71 ± 0.01	0.90 ± 0.04

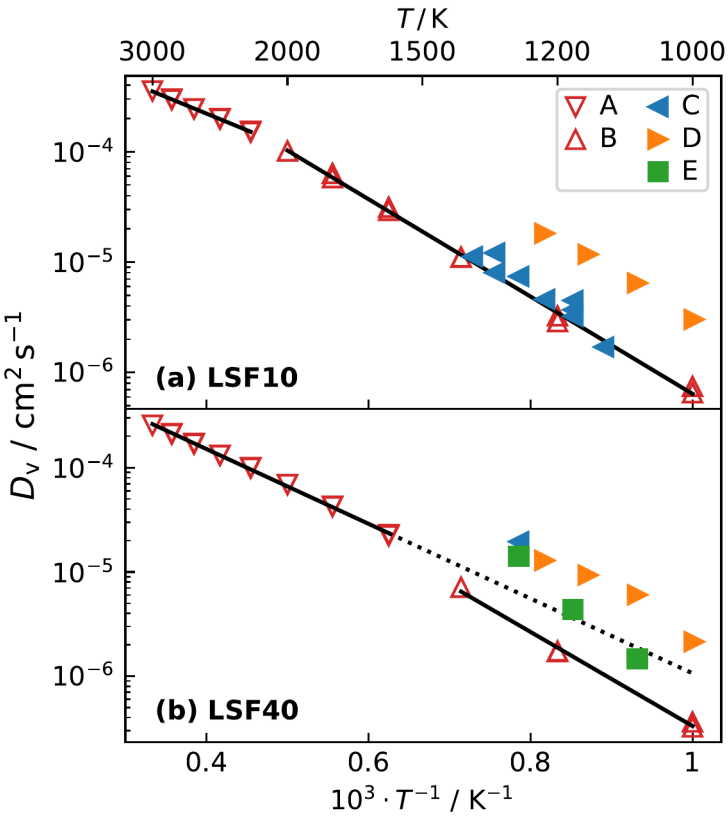


Figure 7.6 Oxygen-vacancy diffusion coefficients D_v as a function of inverse temperature for (a) LSF10 and (b) LSF40: A, this work (orthorhombic); B, this work (cubic); C,[292]; D,[30]; E,[389]. The high-temperature simulation data and the linear extrapolation represent diffusion in cubic LSF, whereas low-temperature data refer to orthorhombic LSF. The transition temperature in LSF40 is overestimated by the empirical potentials, hence, the linear extrapolation of the cubic data is given as a guide to the eye. Errors in the diffusion coefficients, calculated with the expression of USLER *et al.*,[197] are smaller than the symbol size. Fig. 7.7 compares simulations with different oxygen vacancy concentrations.

7.3.2 Polycrystalline LSF

Chemical Analysis

The chemical compositions of the grain-boundary and bulk regions were analysed according to the protocols outlined in Sec. 7.2.4 for the polycrystalline cells after MD runs (i.e. only oxygen vacancies were allowed to re-distribute) and after MMC+MD runs (i.e. Sr'_{La} and $v^{\bullet\bullet}_{O}$ were re-distributed at $T = 2000$ K in the MMC calculation; cations were not mobile in the subsequent MD simulations, but $v^{\bullet\bullet}_{O}$ were).

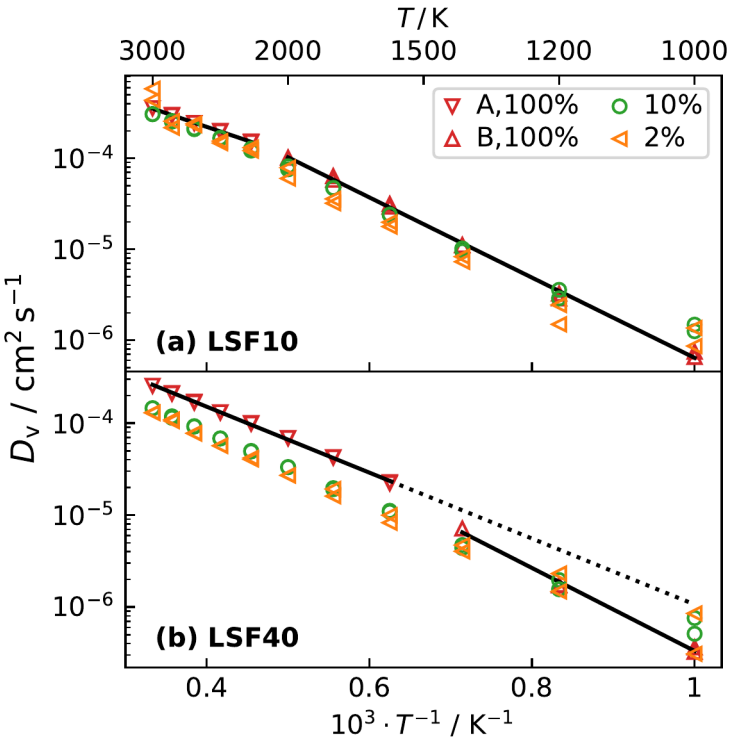


Figure 7.7 Oxygen-vacancy diffusion coefficients D_v as a function of inverse temperature for (a) LSF10 and (b) LSF40: A, this work (orthorhombic); B, this work (cubic); C, oxygen vacancy concentration reduced to 10 %; D, oxygen vacancy concentration reduced to 2 %.

Case I: Only $v_O^{\bullet\bullet}$ Equilibrate

Although a system with a uniform distribution of acceptors does not correspond to ceramic samples sintered at high temperatures, this set of data allows some important points to be made. Fig. 7.9 shows that the Sr'_{La} fraction, averaged over the cells with 2, 5 or 10 boundaries, remains close to the initial values. This essentially confirms the method, since there are no possibilities for cations to move, no cation vacancies were introduced into the cell, and cation-vacancy formation is characterised by prohibitively high energies, so that no cation defects form during the MD simulation. Small deviations from the nominal values indicate the limits of the method, with higher deviations for the more highly substituted LSF40 systems (cf. Fig. 7.3). In contrast, the oxygen sublattice does equilibrate during the MD run, and the $v_O^{\bullet\bullet}$ concentration is found to be higher in the grain-boundary regions than in the bulk regions, indicating a segregation of the vacancies to the grain boundaries. By increasing the Sr content from LSF10 to LSF40, the relative accumulation is less substantial, while the absolute change is similar (e.g., $\approx$ 1 % for 2-grain cells).

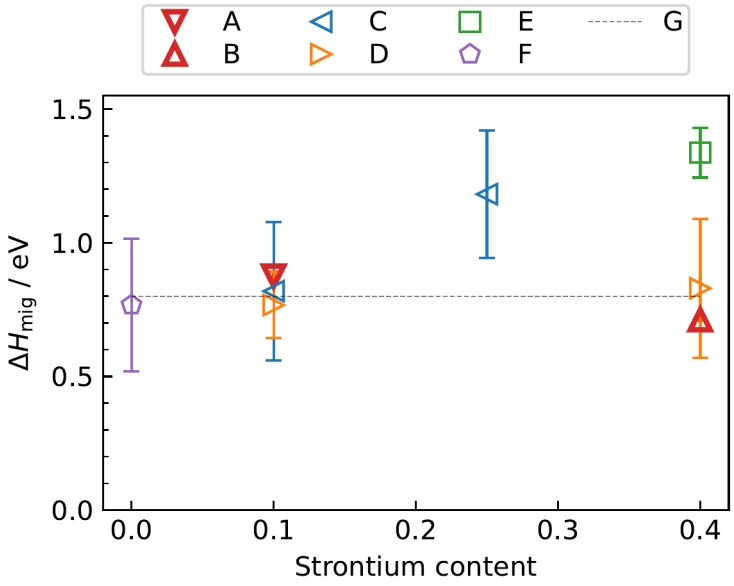


Figure 7.8 Activation enthalpy of oxygen-vacancy diffusion in $La_{1-x}Sr_xFeO_{3-\delta}$ as a function of strontium content x: A, this work (orthorhombic); B, this work (cubic); C,[292]; D,[30]; E,[389]; F,[386]; G,[394]. Note that the phase transitions are temperature dependent and thus not all experimental data points always correspond to the same phase.

Case II: Sr'_{La} Equilibrated at High T, $v_O^{\bullet\bullet}$ at All T

In order to capture the Sr'_{La} distribution after a high-temperature sintering step, MMC simulations as described in Sec. 7.2.3 were performed, swapping Sr'_{La} and $La^{\times}_{La}$ as well as $O^{\times}_{O}$ and $v_O^{\bullet\bullet}$ with MMC temperatures in the range of $1000 \leq T/\mathrm{K} \leq 2000$. The strong decrease in the system's energy to a constant value is shown in Fig. S3.

When structures obtained from MMC calculations with different MMC temperatures were compared, little to no difference in grain-boundary compositions was found. Since the MMC swapping temperature evidently does not have a substantial influence on the results (see also Fig. S4), only the cells that were subject to MMC swapping at the highest T are used.

The compositional analysis of the equilibrated simulation cells is shown in Fig. 7.10. The Sr content and the oxygen-vacancy content in the grain-boundary regions increase strongly, decreasing drastically in the bulk regions. The effects are so pronounced that the bulk of LSF10 has essentially neither Sr'_{La} nor $v_O^{\bullet\bullet}$ left. The drastic decreases are due to the rather small grain sizes in the simulation cells, which result in much higher ratios of grain-boundary volume (see Fig. 7.3) to bulk volume than in a typical ceramic sample.

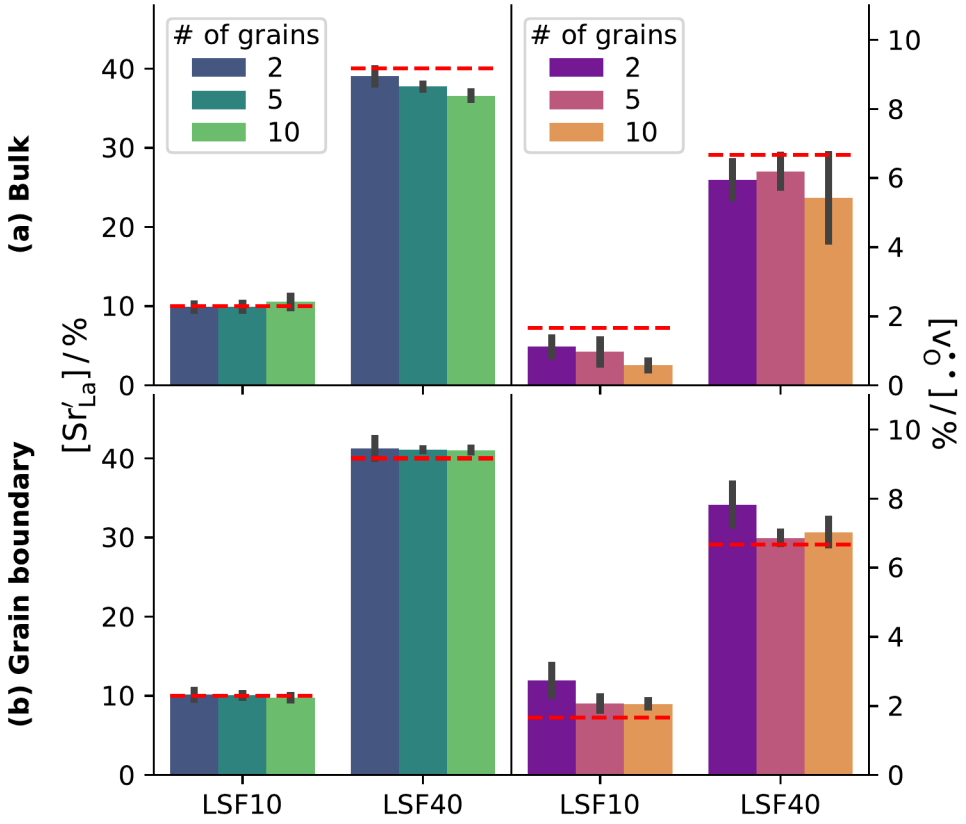


Figure 7.9 *A*-site fraction of Sr (determined directly) and oxygen-vacancy site fraction (determined indirectly from cation-to-anion-ratio) after equilibration of the structures at 2000 K: (a) bulk and (b) grain-boundary region. Grain boundary and bulk regions were identified with the Adaptive Common Neighbour Analysis. The red horizontal lines indicate the expected values. The oxygen plots show accumulation of oxygen vacancies at the grain boundary. Error bars refer to the standard deviation.

7.3.3 Oxygen Diffusion in Polycrystalline Cells

For the present analysis of diffusion data, it should be borne in mind that the diffusion coefficients D_{O}^{*} obtained for polycrystalline cells refer to an effective diffusivity, i.e., some average of diffusion in the bulk phase and along and across grain boundaries. Depending on the relative rates of these three processes, a variety of scenarios are possible. For example, if diffusion along boundaries is faster than in the bulk and diffusion across boundaries is not hindered, then an increase in the effective diffusion coefficient would be expected. This is not the only scenario, however, that may give rise to higher D_{O}^{*}, so that care must be taken when drawing conclusions from effective diffusion data.

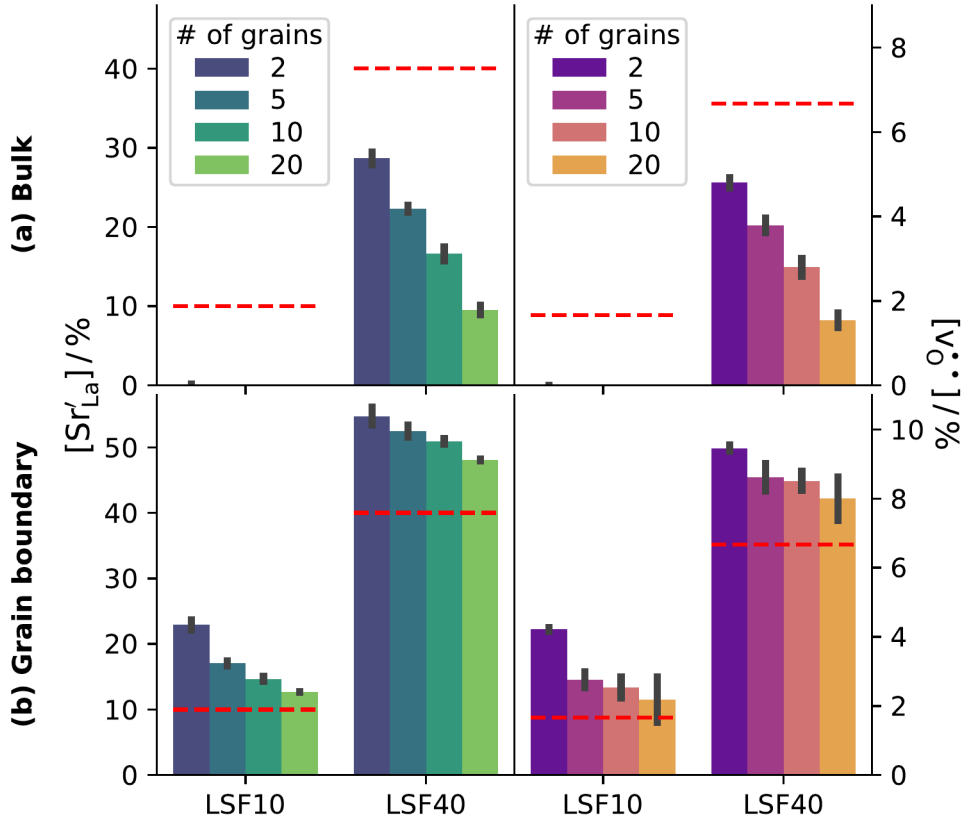


Figure 7.10 *A*-site fraction of Sr and oxygen vacancy fraction (both determined directly) after MMC ion swapping at 2000 K in LSF: (a) bulk region and (b) grain-boundary region. Grain-boundary and bulk regions were identified with the Adaptive Common Neighbour Analysis. The horizontal lines indicate the expected values. All plots show accumulation of oxygen vacancies at the grain boundary. By increasing the Sr content from LSF10 to LSF40, a saturation effect is observed, i.e. the accumulation is less significant. Error bars refer to the standard deviation.

Oxide ions can be sorted, at the beginning of an MD run, into those in grain-boundary regions and those in the bulk regions (see Sec. 7.2.4). From the respective $\langle r_O^2 \rangle$, it may be tempting to calculate tracer diffusion coefficients for the two regions. If, however, oxide ions leave their initial region during the course of the MD run and diffuse most of the time in the other region, they still count as belonging to the initial region. Calculated diffusion coefficients are therefore not necessarily representative of the regions to which they are attributed. In order to avoid such problems, the analysis was restricted to effective diffusion coefficients.

Case I: Only $v_O^{\bullet\bullet}$ Equilibrate

After thermal equilibration at 2000 K for 2 ns, each structure was subject to a 0.5 ns equilibration period followed by a 0.5 ns production run at the target temperature. Tracer diffusion data are plotted in Fig. 7.11.

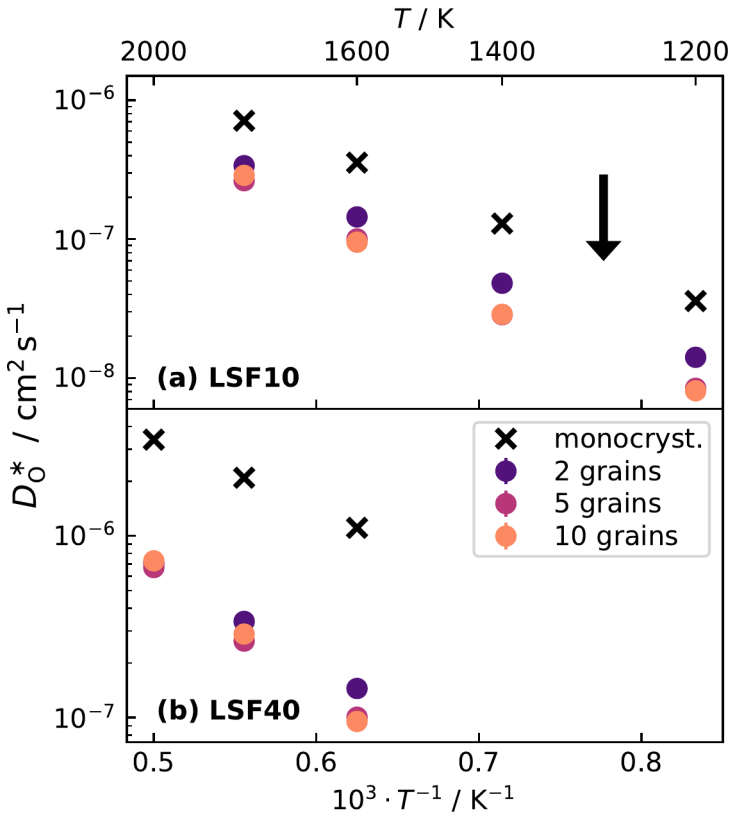


Figure 7.11 Oxygen tracer diffusion coefficients for grain-boundary cells relative to bulk cells for a homogeneous distribution of Sr: (a) orthorhombic LSF10 and (b) cubic LSF40. The arrow indicates a decrease in D_O^* with increasing grain-boundary density. Data for LSF10 at 1000 K is omitted from the plot due to high uncertainties.

Over the entire temperature range, oxygen diffusion is slower in the polycrystalline cells than in the monocrystalline cells. Moreover, as the total number of grains (and thus the density of grain boundaries) increases, the diffusivities decrease. This decrease indicates that grain boundaries hinder oxygen diffusion. In order to explain this behaviour, it is required, in the grain-boundary regions, that there are fewer oxygen vacancies, or that the oxygen vacancies have a lower diffusivity, or some combination thereof. In fact, the chemical analysis of Fig. 7.9 revealed that the concentration of oxygen vacancies is increased at the grain boundaries, leading to the conclusion that D_V^{gb} has to be much lower than D_V^b, at least for a random distribution of Sr. The boundaries evidently act as

a structural perturbation as far as oxygen-vacancy diffusion is concerned, and it could be argued tentatively that this arises from the lower symmetry of the grain-boundary regions relative to that of the bulk phase (cf. Sec. 7.3.1).

Case II: Sr'_{La} Equilibrated at High T, $v_O^{\bullet\bullet}$ at All T

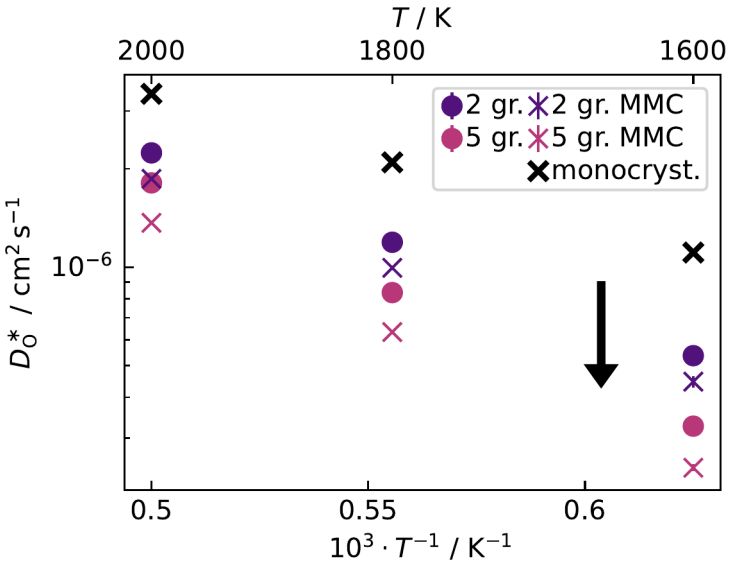


Figure 7.12 Oxygen tracer diffusion coefficients in cubic LSF40. The arrow indicates a decrease in D_O^* with increasing grain-boundary density. Cells subjected to MMC minimisation exhibit lower D_O^* values, indicating a deleterious effect from increasing Sr concentrations at the grain boundaries.

In Fig. 7.12, oxygen tracer diffusion coefficients in polycrystalline LSF40 are compared with and without prior MMC runs, i.e., equilibrium distributions of Sr'_{La} versus homogeneous distributions. Systems subjected to MMC minimisation exhibited lower values of D_O^*, indicating that higher Sr'_{La} at the grain boundaries has a detrimental effect on oxygen transport. Similar behaviour was observed for LSF10 (see Fig. 7.13).

Since the grain-boundary regions in the cation-equilibrated cells are even richer in oxygen vacancies (see Fig. 7.10) than in the homogeneous cell (see Fig. 7.9), it is evident that the oxygen-vacancy diffusivity is diminished by the presence of Sr'_{La}. Indeed, the same behaviour is observed for the bulk phase: monocrystalline simulation cells of LSF display decreasing oxygen-vacancy diffusivity with increasing Sr substitution level (see Fig. 7.14).

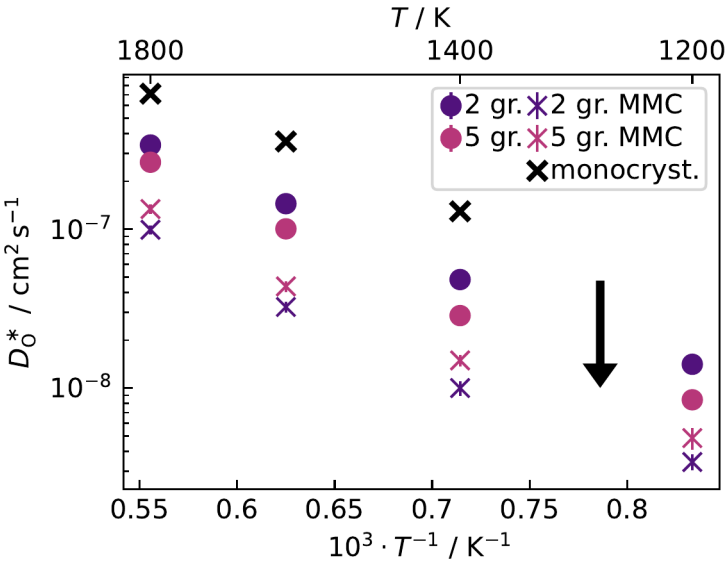


Figure 7.13 Oxygen tracer diffusion coefficients in LSF10. The corresponding data for LSF40 is shown in Fig. 7.12.

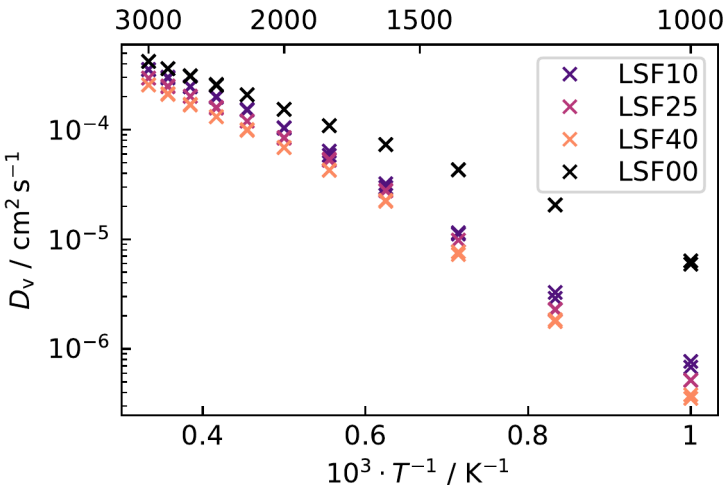


Figure 7.14 Oxygen-vacancy diffusion coefficients D_v as a function of inverse temperature for different Sr'_{La} concentrations.

Case III: Lower $v_O^{\bullet\bullet}$ Concentration

In the two previous sections, it was shown that (i) the grain boundaries themselves do not give rise to faster grain-boundary diffusion of oxygen and (ii) that increased amounts of Sr at the grain boundaries lead to a decrease rather than an increase in oxygen diffusivity. This is not consistent, however, with experiment. One significant difference between simulation and experiment is that the simulation cells have a constant concentration of vacancies (that exactly charge compensates the Sr substituent), whereas the experimental samples have variable oxygen-vacancy concentrations (corresponding to constant oxygen partial pressure). In particular, experimental samples undergo oxidation at lower temperatures, and at lower temperatures faster grain-boundary diffusion of oxygen is observed.[31,382] To mimic sample oxidation in the simulation cells, the number of oxygen vacancies was lowered (and the Fe valence increased), while the other simulation parameters were kept constant. Specifically, two new sets of calculations were carried out in which the concentrations of oxygen vacancies were only 10 % or 2 % of the original values. The excess charge was compensated by modifying the Fe^{3+} charge uniformly (LSF10: to $Fe^{3.09+}$ or $Fe^{3.098+}$, LSF40: to $Fe^{3.36+}$ or $Fe^{3.392+}$). Both single crystals and polycrystals were considered, in order to ascertain the differences displayed by the polycrystalline cells relative to the correct reference values (i.e. single-crystal cells). To reproduce the experimental situation as closely as possible, the Sr'_{La} distribution obtained from MMC calculations with the full oxygen-vacancy amount was kept and only the number of oxygen vacancies was reduced, since the Sr'_{La} distribution that develops at sintering temperatures will not change at the low temperatures of sample oxidation.

Oxygen diffusivities obtained from MD simulations are given in Fig. 7.15. In single-crystal cells, tracer diffusion coefficients decrease, relative to the 100 % case, by about one order of magnitude for 10 % and another half an order of magnitude for 2 %, as expected for the relevant decreases in the oxygen-vacancy concentrations. The decreases are not, however, exactly a factor of 10 and a further factor of 5, since not only are there major changes in the oxygen-vacancy concentrations, but also minor changes in the oxygen-vacancy diffusivities, which can be attributed to increases in Fe valence or increases in oxide-ion concentration (cf. Fig. 7.7).

In contrast, this behaviour is not seen for the polycrystalline cells on going from 100 % of the Sr'_{La}-balancing vacancies to 10 % or 2 % vacancies. In LSF40, the variation in isothermal diffusion coefficient with grain-boundary density is now reversed. An increase in grain-boundary density leads to an increase of D^*_O, indicating that faster grain-boundary diffusion is observed when the bulk concentration of oxygen vacancies is low. For LSF10, two effects are observed that are not present

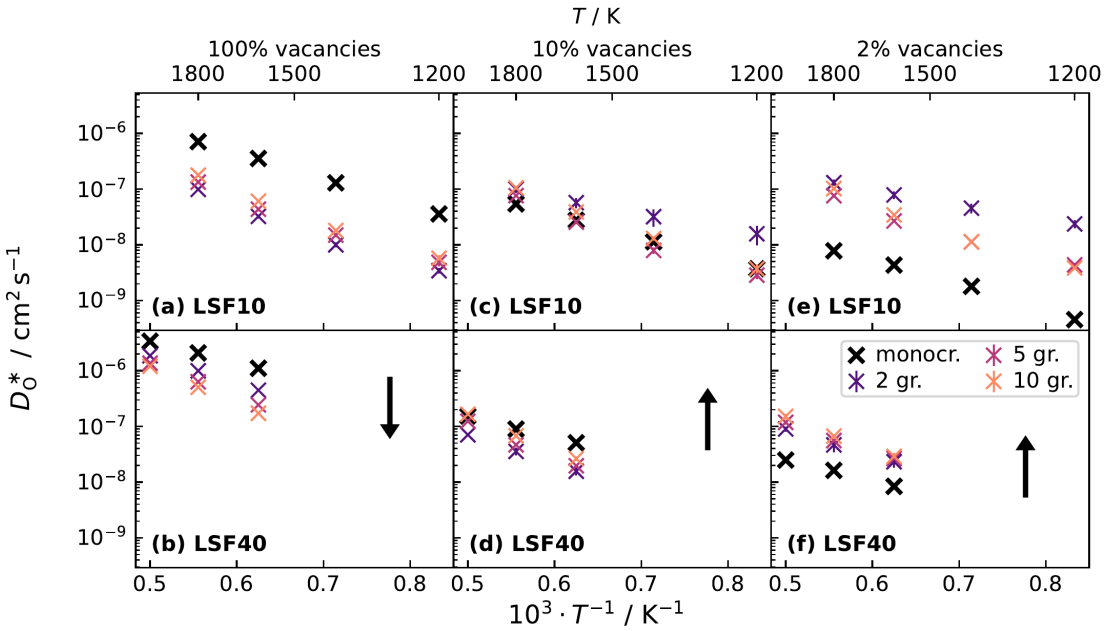


Figure 7.15 Comparison of diffusion coefficients obtained from calculations with (a) 1.7 % (LSF10) and (c) 6.7 % (LSF40) oxygen vacancies versus calculations with only (b) 0.17 % (LSF10), (d) 0.67 % (LSF40), (e) 0.033 % (LSF10) and (f) 0.13 % (LSF40) oxygen vacancies. In both cases, structures underwent MMC swapping at 2000 K with the full oxygen vacancy concentration, and the Sr'_{La} distribution was kept frozen in for the other two oxygen vacancy concentrations. The arrows indicate the changes in D_O^* with increasing grain-boundary density.

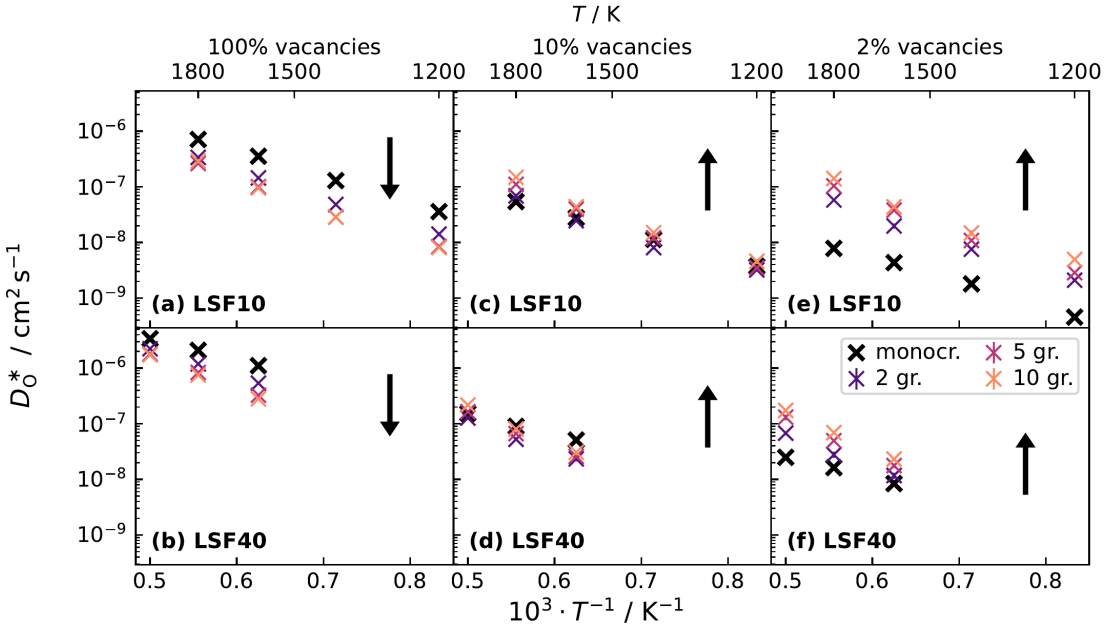


Figure 7.16 Comparison of diffusion coefficients obtained from calculations with (a) 1.7 % (LSF10) and (c) 6.7 % (LSF40) oxygen vacancies versus calculations with only (b) 0.17 % (LSF10), (d) 0.67 % (LSF40), (e) 0.033 % (LSF10) and (f) 0.13 % (LSF40) oxygen vacancies. The Sr'_{La} distribution is homogenous. The arrows indicate the changes in D_O^* with increasing grain-boundary density.

in LSF40. First, the reversal of the variation in isothermal diffusion coefficient with grain-boundary density is present at the full vacancy concentration, rather than only at lower vacancy concentration as for LSF40. This is a consequence of oxygen vacancies being almost fully depleted from the bulk regions after the MMC runs (see Fig. 7.10); thus, the reversal occurs already at the highest vacancy concentration. Second, in the cases 10 % and 2 % vacancies, the cells with 2 grains deviate from the trend by showing higher-than-expected tracer diffusion coefficients. From trajectories of the molecular dynamics run, bulk transport in regions far away from the grain boundaries was identified. While only very few oxygen vacancies are available there (most are present at the grain boundaries), high diffusivities are exhibited as these regions are nominally free of Sr; thus, the lower activation enthalpy (0.52 eV vs. 0.6 eV) and higher oxygen diffusivity of lanthanum ferrite is sampled (cf. Fig. 7.14).

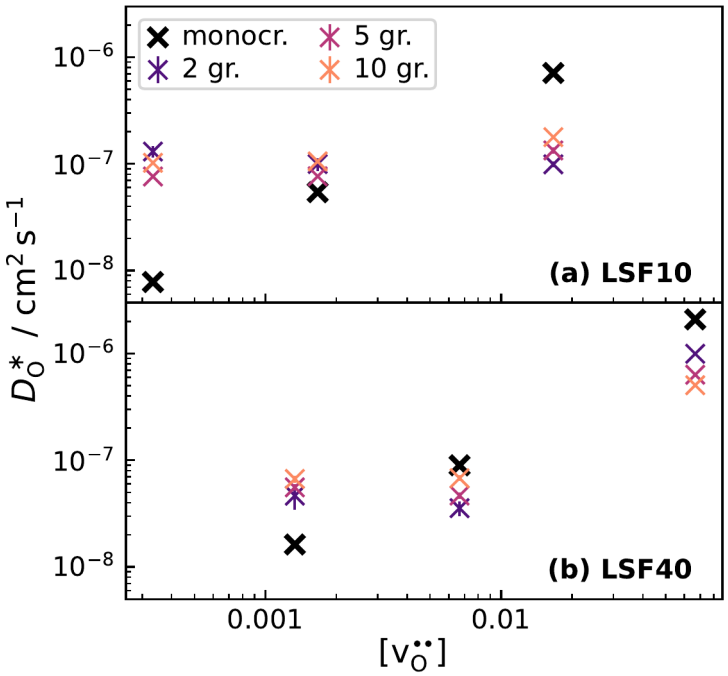


Figure 7.17 Oxygen tracer diffusion coefficients in polycrystalline LSF at $T = 1800$ K, extracted from Fig. 7.15, as a function of $[v_O^{\bullet\bullet}]$.

Lastly, the extent to which the general behaviour observed in Fig. 7.15 is due to increased Sr'_{La} at the grain boundaries was investigated. To this end, an additional set of simulations was carried out with a homogeneous Sr'_{La} distribution. The results are shown in Fig. 7.16. The D_O^* values in LSF40 are mostly unchanged due to the smaller relative changes in Sr'_{La} content in grain boundary regions (see Fig. 7.10), confirming that increased Sr'_{La} accumulation does not play a significant role in the observed behaviour. In LSF10, however, the two effects mentioned above are not observed, i.e. the reversal of the variation in isothermal diffusion coefficient with grain-boundary density is

not present in case (a) with a full vacancy concentration, and the cells with 2 grains do not deviate from the trend.

To emphasise the main result, Fig. 7.17 shows oxygen tracer diffusion coefficients calculated for $T = 1800\,\mathrm{K}$ versus oxygen-vacancy concentration for both compositions. In these double-logarithmic plots, D^{*}_{O} for the monocrystalline cells decreases, as expected, almost linearly with $[\mathrm{v}^{\bullet\bullet}_{\mathrm{O}}]$. D^{*}_{O} for the polycrystalline cells, however, is essentially constant for LSF10 for all $[\mathrm{v}^{\bullet\bullet}_{\mathrm{O}}]$ and for LSF40 at the two lowest $[\mathrm{v}^{\bullet\bullet}_{\mathrm{O}}]$. This suggests that $[\mathrm{v}^{\bullet\bullet}_{\mathrm{O}}]$ within the grain-boundary regions in these simulations is more or less invariant of the bulk level. The plots also emphasise the need to regard short-circuit diffusion as faster, rather than fast. For LSF10, the rate of oxygen diffusion in the polycrystalline cells hardly changes. What does change is its relation to the diffusion rate in the bulk value. One last point is that care must be exercised in interpreting such data. The bulk composition in the monocrystalline cells is not the bulk composition in the polycrystalline cells, owing to the small grain size and the strong $[\mathrm{Sr}'_{\mathrm{La}}]$ segregation to the grain boundaries.

7.4 Discussion

The main result of this computational investigation is that faster grain-boundary diffusion of oxygen in polycrystalline LSF materials is only observed when bulk diffusion of oxygen is relatively slow. This agrees very well with experimental studies[31,382] of oxygen diffusion in polycrystalline LSCF6482, in which faster grain-boundary diffusion was detected at low temperatures, where bulk diffusion is substantially diminished on account of sample oxidation.

Looking beyond the (La,Ba,Sr)(Fe,Co)$\mathrm{O}_{3-\delta}$ system, it is found that the main result also agrees well with the observation of faster grain-boundary diffusion of oxygen in the (La,Sr)$\mathrm{MnO}_{3+\delta}$ perovskites.[411–414] Compared with (La,Ba,Sr)(Fe,Co)$\mathrm{O}_{3-\delta}$ perovskites, (La,Sr)$\mathrm{MnO}_{3+\delta}$ is an oxygen hyperstoichiometric material, with the excess oxygen arising from the presence of cation vacancies. These defects depress the concentration of oxygen vacancies through a Schottky equilibrium,[415–420] and they also diminish the oxygen-vacancy diffusivity.[279] As a consequence, bulk diffusion of oxygen in (La,Sr)$\mathrm{MnO}_{3+\delta}$ is orders of magnitude lower than in (La,Ba,Sr)(Fe,Co)$\mathrm{O}_{3-\delta}$ compositions, and faster grain-boundary diffusion of oxygen is observed, not just at lower temperatures, but also at much higher temperatures.

Of the defining questions in the Introduction (Sec. 7.1), one remains unanswered. It concerns the possible presence and role of space-charge zones. On the one hand, the activation enthalpies measured experimentally for bulk and grain-boundary diffusion in LSCF6482[382] (and also for grain boundaries[411] and dislocations[414] in (La,Sr)$MnO_{3+\delta}$) are the same within experimental error. This behaviour is consistent with faster diffusion along space-charge zones at the grain boundaries.[385,421] On the other hand, the MD simulations yield activation enthalpies of diffusion that are higher for the polycrystals than for the single crystals (see Fig. S5). This is consistent with the idea that the boundaries constitute structural perturbations, for which the activation enthalpy of migration is higher than in the bulk. And faster diffusion then arises from the higher concentration of oxygen vacancies. (A lower activation enthalpy of oxygen diffusion in $LaMnO_3$ has also been predicted from DFT calculations,[384] but these predictions do not take cation vacancies into account.) It is, however, questionable if space-charge zones were rendered properly in the simulations, since the bulk phases often were completely devoid of defects, and space-charge zones are regions of modified bulk defect concentrations. The chemical analysis of Sec. 7.2.4 is unable to provide any information, since it is not sufficiently sensitive to small local deviations in charge neutrality. It is concluded that the simulations reproduce the experimental results qualitatively, but quantitative agreement requires a new, extensive set of simulations. In particular, simulations with much larger grains are required, so that bulk defect concentrations are recovered within the bulk phase. It is estimated that simulation cells with at least 10^6 ions are necessary. And in these cells, given the importance of the degree of oxygen nonstoichiometry, experimental values of $\delta(T)$ should be used.

7.5 Concluding Remarks

In this chapter, polycrystalline (La,Sr)$FeO_{3-\delta}$ was investigated by means of molecular dynamics simulations with the aim of improving the understanding of the role of grain boundaries in oxygen transport. The major findings are as follows:

- Owing to the complexity of polycrystalline simulation cells, extraction of information about the grain-boundary composition is not straightforward. A compositional analysis protocol was developed to differentiate between bulk and grain-boundary regions and to quantify acceptor-substituent and oxygen-vacancy concentrations in the respective regions.

- Oxygen tracer diffusion coefficients in stoichiometric polycrystalline cells are lower than in

the corresponding monocrystalline cells, and they decrease with increasing grain-boundary density, confirming a blocking effect of grain boundaries.

- The increased concentration of the acceptor substituent Sr'_{La} at the grain boundaries (as a consequence of high-T annealing) was found to have a detrimental effect on oxygen transport, as it further decreases the oxygen-vacancy diffusivity.

- The observed low-temperature behaviour is reproduced by the simulations when the oxygen-vacancy concentration is reduced from fully compensating the acceptor substituent to a much lower level, for which bulk diffusion is drastically diminished. In this case, the grain boundaries remain oxygen-vacancy rich and thus are the only place where oxygen-vacancy diffusion can occur. Caution is required in transferring all results to experiments, however, because of the extremely small grain size in the simulation cells.

8 Conclusions

The aim of this thesis was to investigate ion transport in ion-conducting perovskite materials, with a focus on the influence of structural, compositional, and external factors on ionic conductivity. With atomic-scale simulations, mechanisms of ion transport were studied in detail, and the results were compared with experimental findings and theoretical predictions.

Chapter 4: Best practices for MD simulations of ion diffusion in solids The first part of the thesis systematically addressed the critical aspects and best practices for conducting molecular dynamics (MD) simulations of ion diffusion in solids, in particular the reliability and interpretation of simulation results. While MD simulations are a powerful tool for probing ion transport mechanisms at the atomic scale, the accuracy and significance of the results depend on careful attention to simulation setup, statistical analysis, and data interpretation.

A key outcome is the importance of rigorous analysis to ensure that the observables correspond to an equilibrium distribution of microstates. This includes equilibration not only of thermodynamic variables, but also of the distribution of mobile ions, especially in systems with multiple energetically similar configurations. The Marginal Standard Error Rule (MSER) was identified as a robust, automated method for determining equilibration time, but visual inspection remains essential to confirm true equilibrium, particularly for complex or disordered systems.

Fluctuations in thermodynamic quantities, far from being artifacts, are intrinsic to simulations of finite systems and provide a means to validate simulation setups and force fields by comparison with experimental data. It was shown that these fluctuations can be related to material constants, but many data points (i.e. timesteps) are needed to obtain reliable estimates.

A significant finding concerns the necessity of ensuring that diffusion coefficients are extracted

from the true diffusive regime. The analysis shows that at lower temperatures or short simulation times, systems may not reach this regime, leading to unreliable diffusion coefficients and activation energies. The results emphasize that simulation times must be adapted to temperature and system specifics, and that data outside the diffusive regime should be excluded from further analysis.

The impact of simulation cell size and ensemble choice was systematically evaluated. It was shown that small supercells can introduce significant statistical and systematic errors in both diffusion coefficients and activation energies, and that neglecting thermal expansion by fixing the lattice volume can lead to substantial underestimation of diffusion coefficients and incorrect ARRHENIUS fit parameters. Simulations must therefore be performed with sufficiently large cells and at volumes appropriate for the target temperature, either by NpT equilibration or by explicit adjustment using thermal expansion data.

A central methodological advance discussed is the proper estimation of uncertainties in diffusion coefficients. There are serious concerns regarding the common practice of using regression errors from linear fits, as this approach underestimates the true uncertainty due to autocorrelation in the data. Instead, closed-form expressions and Bayesian approaches are recommended for robust uncertainty quantification, which is especially crucial when extrapolating diffusion coefficients to lower temperatures. The analysis reveals that uncertainties can grow rapidly upon extrapolation, often spanning orders of magnitude, emphasizing the need for careful statistical treatment.

The correct procedures for fitting ARRHENIUS-type expressions to diffusion data are clarified. It is shown that non-linear weighted least-squares fitting yields unbiased estimates of activation energies and pre-exponential factors, particularly when the number of observed diffusion events is low and uncertainties are heteroscedastic. Linear fits or unweighted approaches can introduce systematic biases, especially for cell sizes and simulation times that are, by necessity, used in typical *ab initio* MD studies with limited statistics.

Finally, the conversion of tracer diffusion coefficients to ionic conductivities is discussed, with an emphasis on the role of the HAVEN ratio and the limitations of common assumptions. Alternative methods for directly computing conductivity from MD simulations are outlined, such as using the ONSAGER coefficient or field-driven simulations, and the importance of consistent thermodynamic and statistical frameworks is highlighted.

Chapter 5: Substitution of Ba by Ca in BSCF5582 In the first materials-related chapter, the chemical composition of a fast oxide ion conductor was modified in order to enhance its stability. To this end, the structural and oxygen transport properties of the Ca-substituted perovskite $Ca_{0.5}Sr_{0.5}Co_{0.8}Fe_{0.2}O_{3-\delta}$ (CSCF5582) were investigated. The emphasis was on evaluating whether CSCF5582 could serve as a chemically more stable alternative to BSCF5582 while maintaining comparably high oxygen-vacancy diffusion rates.

First, the ability of two well-established Ca^{2+}–O^{2-} potential sets to describe the high-temperature cubic phases was assessed. Simulations initialised with orthorhombic symmetry revealed that CSCF5582 becomes cubic above $T = 1100\,\mathrm{K}$, regardless of which potential set was used. Although the predicted phase transition temperature may be overestimated due to limitations inherent in MD simulations, this result suggests that cubic symmetry (a prerequisite for high oxygen diffusion in many perovskite-type oxides) might be accessible under realistic operating conditions. Furthermore, the reduced lattice parameter observed in CSCF5582 compared to BSCF5582 is consistent with the smaller ionic radius of Ca^{2+}.

Further MD simulations were conducted to calculate oxygen tracer diffusion coefficients, D^*_O, in both BSCF5582 and CSCF5582 in their cubic phases at constant nonstoichiometry $\delta = 0.5$. The reliability of the computed diffusion coefficients for BSCF5582 was validated by comparison with a previous simulation study, with good agreement observed over a wide temperature range. However, the new results revealed that previous simulations likely overestimated diffusion at low temperatures due to insufficient equilibration. The present work employed significantly longer equilibration times, often in the nanosecond range, as well as additional Monte Carlo-based oxygen-vacancy swapping to address the shortcomings of previous simulations.

An interesting (and somewhat unexpected) result was that oxygen-vacancy diffusion coefficients for CSCF5582 closely match those of BSCF5582 across the entire temperature range studied. This agreement was observed for both Ca^{2+}–O^{2-} potential sets, despite the structural distortion expected from the smaller *A*-site cation. Although a definitive conclusion regarding the symmetry of CSCF5582 at application-relevant temperatures remains pending, these results imply that Ca substitution does not impair oxygen diffusion, at least in the cubic phase.

To assess the reasonableness of these results, MD-derived lattice expansion and diffusion data for BSCF5582 were compared with multiple experimental datasets. The calculated thermal expansion coefficient α agreed very well with experimentally measured values in the regime where chemical

expansion is negligible. Similarly, tracer diffusion coefficients, corrected for experimental oxygen nonstoichiometry, compared favourably with several experimental datasets. Notably, the MD results aligned with a subset of literature data characterised by higher activation enthalpies ($\Delta H_{\mathrm{mig}} \approx$ 1.0 eV). This suggests that the simulations capture the intrinsic bulk diffusion mechanism, rather than fast diffusion along pores or grain boundaries, which dominate some other studies with significantly lower activation energies.

The convergence of CSCF5582 and BSCF5582 diffusion coefficients, despite their different lattice constants and cation sizes, highlights the complex nature of ion migration in perovskites. Apparently, various contributing factors (such as lattice distortion, ion size, and local bonding environments) combine in such a way that similar diffusion rates are observed in both materials.

Besides the material-specific findings, a noteworthy methodological aspect emerged: the importance of oxygen sublattice equilibration. The initial random distributions of oxygen and vacancies were far from equilibrium, as shown by significant changes in coordination numbers during Monte Carlo sampling. These deviations from equilibrium resulted in long equilibration times during MD, especially at lower temperatures, and emphasize the need for enhanced sampling techniques when simulating oxygen transport.

Chapter 6: Transition-Metal Exsolution from Perovskite Oxides Next, the importance of atmospheric conditions was addressed, specifically in the context of metal exsolution from perovskite oxides. A unified thermodynamic and kinetic model was proposed, addressing three critical and previously unresolved questions: why only the substituent transition-metal cation exsolves and not the host *B*-site cation, how exsolution can proceed so rapidly at relatively low temperatures, and why perovskite oxides are particularly suitable host materials. Hybrid DFT calculations, including charge-transition levels, reaction energies, and migration barriers, were carried out for Ni in $SrTiO_3$, a widely studied model system.

A key result is the prediction of charge-transition levels that allow Ni to be reduced to neutral species within the perovskite lattice, but only when Ni resides in interstitial positions and forms associates with oxygen vacancies, and possibly strontium vacancies. Substitutional Ni on either the *A*-site or *B*-site remains positively charged, even under reducing conditions. Once reduced, neutral interstitial Ni species (Ni_i^0) are thermodynamically unstable in the lattice and are energetically driven to be expelled as metallic Ni. This provides the thermodynamic rationale for exsolution and

constitutes the core of the new model: exsolution begins with valence-state changes inside the host lattice, not at the surface.

The thermodynamic driving force for exsolution was quantified by proposing an overall exsolution reaction that includes Ni reduction, SCHOTTKY disorder reversal, and the formation of metal particles at the surface. The calculated reaction energy, obtained for typical exsolution conditions ($T = 1000\,\mathrm{K}$, $p_{\mathrm{O}_2} = 10^{-20}\,\mathrm{bar}$), was found to be strongly negative ($\Delta_{\mathrm{exsoln}}E = -2.33\,\mathrm{eV}$), indicating a highly favourable process. In contrast, existing alternative models neglecting SCHOTTKY reversal or considering only NiO reduction yield strongly positive reaction energies, showing the importance of taking into account the solid solution and changes in the host crystal. A thermodynamic map of the exsolution threshold in (T, p_{O_2}) space further confirms that exsolution is thermodynamically favourable at moderate temperatures under sufficiently reducing conditions, and explains the experimental observation of a critical oxygen-vacancy concentration.

In order to investigate kinetics, migration barriers were computed for relevant cationic and interstitial species. Vacancy-mediated migration of substitutional Ni on the B-site was found to have an effective barrier of 3.40 eV when assisted by an adjacent v_{Sr}. In contrast, the interstitial neutral species $\mathrm{Ni}_{\mathrm{i}}^{0}$ can migrate with a much lower barrier of 1.44 eV as part of a $\mathrm{Ni}_{\mathrm{i}}^{0}\mathrm{v}_{\mathrm{O}}$ associate. This low barrier explains the surprisingly fast exsolution kinetics, as this migration pathway avoids the need for sluggish cation vacancy transport. The initial step of displacing Ni from a Ti site to an interstitial position, facilitated by v_{O} and v_{Sr}, was found to be energetically accessible, though not barrierless.

This kinetic framework also accounts for the observed sluggish re-incorporation of Ni under oxidising conditions: it requires diffusion of charged substitutional species via high-barrier pathways. Furthermore, socket formation can occur rapidly at defect-rich locations without requiring long-range cation migration, since expelled Ni can diffuse to surface nucleation sites while maintaining host lattice integrity.

Finally, several key material characteristics were identified that may explain why perovskites are uniquely suited for exsolution: their ability to accommodate oxygen nonstoichiometry and cation vacancies, their favourable band structures for charge transitions, and their capacity to host mobile interstitial transition-metal species in multiple charge states. Other oxide classes, such as fluorites and spinels, lack one or more of these properties, potentially explaining their poorer performance. However, further systematic studies, especially in the experimental realm, are needed to confirm these hypotheses.

Chapter 7: Oxygen Grain-Boundary Diffusion in LSF Lastly, oxygen transport in polycrystalline (La,Sr)$FeO_{3-\delta}$ (LSF) was investigated, in order to elucidate the role of temperature and structural disorder on oxygen diffusion. The simulations revealed that, contrary to some expectations, grain boundaries do not inherently facilitate faster oxygen diffusion compared to the bulk lattice. Instead, grain boundaries act as structural perturbations that generally hinder oxygen transport, as evidenced by the observed decrease in effective oxygen tracer diffusion coefficients with increasing grain-boundary density. This blocking effect is robust across different grain sizes and compositions, and is further exacerbated when strontium segregates to the grain boundaries following high-temperature annealing.

A significant finding is the strong tendency for both strontium and oxygen vacancies to accumulate at grain boundaries after high-temperature annealing, leading to pronounced compositional inhomogeneities between grain-boundary and bulk regions. While the accumulation of oxygen vacancies at grain boundaries might intuitively be expected to enhance local diffusivity, the simulations demonstrate that the presence of strontium at the boundaries actually reduces the oxygen-vacancy mobility, resulting in a net decrease in oxygen transport rates. This effect is consistent with the observed trend in monocrystalline (single crystal) cells, where increasing strontium content leads to lower oxygen-vacancy diffusivity.

The simulations also clarify the conditions under which faster grain-boundary diffusion of oxygen can be observed. When the overall oxygen-vacancy concentration is reduced (to mimic the effect of sample oxidation at lower temperatures), the bulk becomes depleted of mobile oxygen vacancies, while the grain boundaries retain a relatively high vacancy concentration. Under these circumstances, the grain boundaries become the dominant pathways for oxygen transport, and the effective diffusivity in polycrystalline samples can exceed that of the bulk. This scenario aligns well with experimental observations in related perovskite systems, where enhanced grain-boundary diffusion is detected at low temperatures or under oxidising conditions that reduce bulk vacancy concentrations.

The compositional analysis protocol developed for these simulations, which employs structural identification methods to distinguish bulk and grain-boundary regions, proved essential for quantifying local defect concentrations and understanding their impact on transport properties. It highlights the importance of considering both structural and chemical heterogeneity in polycrystalline materials, especially when interpreting macroscopic diffusion measurements.

Overall, the findings show how the interplay between defect chemistry, cation segregation, and structural disorder at grain boundaries critically determines the oxygen transport properties of these perovskite oxides. Enhanced grain-boundary diffusion is not an intrinsic property of the boundaries themselves, but rather emerges when bulk diffusion is suppressed and the boundaries remain defect-rich. These results provide a framework for rationalising experimental trends across different perovskite compositions and processing conditions, and emphasize the need for careful control of defect distributions and grain-boundary chemistry in the design of materials for solid oxide fuel cells and related applications. The results also suggest that further progress in modelling grain-boundary phenomena will require simulations with larger grains and more realistic defect equilibria, to bridge the gap between atomistic models and experimental systems.

In summary, this thesis has advanced the understanding of ion transport in perovskite materials by systematically examining how structural, compositional, and external factors influence ionic conductivity in three distinct contexts: the effect of chemical composition on oxygen diffusion, the thermodynamics and kinetics of transition-metal exsolution, and the impact of grain boundaries on oxygen transport at different temperatures. The findings highlight the necessity of a holistic approach to ion transport phenomena, as these processes are often interconnected and shaped by multiple factors simultaneously.

9 Bibliography

[1] A. Bonkowski, C. Perkampus, R. A. De Souza, *J. Mater. Chem. A* **2023**, *11*, 10231–10262 (cit. on pp. C, 79).

[2] A. Bonkowski, J. A. Kilner, R. A. De Souza, *RSC Appl. Interfaces* **2024**, *1*, 699–710 (cit. on pp. C, 56, 105).

[3] A. Bonkowski, M. J. Wolf, J. Wu, S. C. Parker, A. Klein, R. A. De Souza, *J. Am. Chem. Soc.* **2024**, *146*, 23012–23021 (cit. on pp. C, 89).

[4] H. Mehrer, *Diffusion in Solids*, (Eds.: M. Cardona, P. Fulde, K. Von Klitzing, H.-J. Queisser, R. Merlin, H. Störmer), Springer Berlin Heidelberg, Berlin, Heidelberg, **2007** (cit. on pp. 7, 11, 13, 19).

[5] J. Maier, *Physical Chemistry of Ionic Materials: Ions and Electrons in Solids*, Wiley, Chichester, England Hoboken, NJ, **2005** (cit. on p. 7).

[6] R. Dronskowski, *Computational Chemistry of Solid State Materials: A Guide for Materials Scientists, Chemists, Physicists and others*, 1st ed., Wiley, **2005** (cit. on pp. 7, 21, 35, 37).

[7] A. R. West, *Solid state chemistry and its applications*, Second edition, student edition, Wiley, Chichester, West Sussex, **2014** (cit. on pp. 7, 11).

[8] In *Perovskites*, Wiley, Chichester, UK, **2016**, pp. 1–41 (cit. on pp. 7, 14).

[9] F. Kröger, H. Vink in *Solid State Physics*, *Vol. 3*, Elsevier, **1956**, pp. 307–435 (cit. on pp. 9, 92).

[10] T. Norby, *J. Korean Ceram. Soc.* **2010**, *47*, 19–25 (cit. on pp. 9, 92).

[11] P. Lejcek, *Grain Boundary Segregation in Metals*, Springer, Berlin, Heidelberg, **2010** (cit. on pp. 10, 11).

[12] L. G. Harrison, *Trans. Faraday Soc.* **1961**, *57*, 1191 (cit. on p. 11).

[13] A. Fick, *Ann. Phys.* **1855**, *170*, 59–86 (cit. on p. 12).

[14] A. Einstein, *Ann. Phys.* **1905**, *322*, 549–560 (cit. on pp. 12, 73).

[15] M. von Smoluchowski, *Ann. Phys.* **1906**, *326*, 756–780 (cit. on pp. 12, 73).

[16] R. A. De Souza, *Phys. Chem. Chem. Phys.* **2006**, *8*, 890 (cit. on p. 14).

[17] E. A. Katz, *Helv. Chim. Acta* **2020**, *103*, e2000061 (cit. on p. 14).

[18] J. Schmidt, J. Shi, P. Borlido, L. Chen, S. Botti, M. A. L. Marques, *Chem. Mater.* **2017**, *29*, 5090–5103 (cit. on p. 14).

[19] H. D. Megaw, J. Barber, *Crystal structures: a working approach*, Saunders, Philadelphia, Pa., **1973** (cit. on p. 15).

[20] V. M. Goldschmidt, *Naturwissenschaften* **1926**, *14*, 477–485 (cit. on pp. 15, 80).

[21] M. W. Lufaso, P. M. Woodward, *Acta Crystallogr. Sect. B: Struct. Sci.* **2001**, *57*, 725–738 (cit. on p. 15).

[22] C. J. Bartel, C. Sutton, B. R. Goldsmith, R. Ouyang, C. B. Musgrave, L. M. Ghiringhelli, M. Scheffler, *Sci. Adv.* **2019**, *5*, eaav0693 (cit. on p. 15).

[23] M. Johnsson, P. Lemmens in *Handbook of Magnetism and Advanced Magnetic Materials*, (Eds.: H. Kronmüller, S. Parkin), Wiley, Chichester, UK, **2007**, hmm411 (cit. on p. 15).

[24] R. E. Schaak, T. E. Mallouk, *Chem. Mater.* **2002**, *14*, 1455–1471 (cit. on p. 16).

[25] T. T. Mayeshiba, D. D. Morgan, *Solid State Ion.* **2016**, *296*, 71–77 (cit. on p. 16).

[26] W. Li, J. Sunarso, Y. Yang, Y. Chen, C. Ge, W. Wang, Y. Guo, R. Ran, W. Zhou, *Energy Rev.* **2024**, *3*, 100085 (cit. on p. 16).

[27] R. A. De Souza, *J. Mater. Chem. A* **2017**, *5*, 20334–20350 (cit. on pp. 16, 105).

[28] P. C. Bowes, J. N. Baker, D. L. Irving, *J. Am. Ceram. Soc.* **2020**, *103*, 1156–1173 (cit. on pp. 17, 94).

[29] J. Lane, *Solid State Ion.* **1999**, *121*, 201–208 (cit. on p. 17).

[30] J. E. ten Elshof, M. H. R. Lankhorst, H. J. M. Bouwmeester, *J. Electrochem. Soc.* **1997**, *144*, 1060–1067 (cit. on pp. 17, 113, 114, 116).

[31] S. J. Benson, R. J. Chanter, J. A. Kilner in Proceedings of the Third International Symposium on Ionic and Mixed Conducting Ceramics, Paris. France, **1997** (cit. on pp. 17, 105, 122, 125).

[32] S. Arrhenius, *Z. Phys. Chem.* **1889**, *4U*, 226–248 (cit. on p. 19).

[33] H. Eyring, *J. Chem. Phys.* **1935**, *3*, 107–115 (cit. on pp. 19, 44).

[34] M. G. Evans, M. Polanyi, *Trans. Faraday Soc.* **1935**, *31*, 875 (cit. on p. 19).

[35] D. Frenkel, B. Smit, *Understanding Molecular Simulation: From Algorithms to Applications*, 2nd ed, Academic press, San Diego, **2002** (cit. on pp. 21, 29, 58).

[36] C. J. Cramer, *Essentials of Computational Chemistry: Theories and Models*, 2nd ed., Wiley, Chichester, **2004** (cit. on pp. 21, 46).

[37] M. P. Allen, D. J. Tildesley, *Computer Simulation of Liquids*, 2nd ed., Oxford University Press, Oxford, **2017** (cit. on pp. 21, 26, 27, 29, 52, 58, 59).

[38] W. Koch, M. C. Holthausen, *A Chemist's Guide to Density Functional Theory*, 1st ed., Wiley, **2001** (cit. on pp. 21, 34).

[39] *Histoire de l'Academie royale des sciences*, (Ed.: A. r. d. s. Paris), De l'imprimerie royale, Paris, **1788** (cit. on p. 22).

[40] J. E. Jones, *Proc. R. Soc. Lond. A* **1924**, *106*, 463–477 (cit. on p. 23).

[41] J. E. Jones, *Proc. R. Soc. Lond. A* **1924**, *106*, 441–462 (cit. on p. 23).

[42] R. A. Buckingham, *Proc. R. Soc. Lond. A* **1938**, *168*, 264–283 (cit. on p. 23).

[43] P. M. Morse, *Phys. Rev.* **1929**, *34*, 57–64 (cit. on p. 23).

[44] J. Behler, M. Parrinello, *Phys. Rev. Lett.* **2007**, *98*, 146401 (cit. on p. 24).

[45] L. Verlet, *Phys. Rev.* **1967**, *159*, 98–103 (cit. on pp. 24, 48).

[46] W. C. Swope, H. C. Andersen, P. H. Berens, K. R. Wilson, *J. Chem. Phys.* **1982**, *76*, 637–649 (cit. on pp. 24, 28).

[47] J. Koettgen, T. Zacherle, S. Grieshammer, M. Martin, *Phys. Chem. Chem. Phys.* **2017**, *19*, 9957–9973 (cit. on pp. 26, 62).

[48] A. P. Thompson, S. J. Plimpton, W. Mattson, *J. Chem. Phys.* **2009**, *131*, 154107 (cit. on p. 28).

[49] F. Bamer, F. Ebrahem, B. Markert, B. Stamm, *Arch. Comput. Methods Eng.* **2023**, *30*, 2105–2180 (cit. on pp. 28, 29).

[50] R. Clausius, *Lond. Edinb. Dublin Philos. Mag. J. Sci.* **1870**, *40*, 122–127 (cit. on p. 28).

[51] D. H. Tsai, *J. Chem. Phys.* **1979**, *70*, 1375–1382 (cit. on p. 28).

[52] L. Woodcock, *Chem. Phys. Lett.* **1971**, *10*, 257–261 (cit. on pp. 29, 30).

[53] S. Nosé, *J. Chem. Phys.* **1984**, *81*, 511–519 (cit. on pp. 29, 31, 48).

[54] W. G. Hoover, *Phys. Rev. A* **1985**, *31*, 1695–1697 (cit. on pp. 29, 31, 48).

[55] G. J. Martyna, M. L. Klein, M. Tuckerman, *J. Chem. Phys.* **1992**, *97*, 2635–2643 (cit. on pp. 29, 31).

[56] P. H. Hünenberger in *Advanced Computer Simulation*, *Vol. 173*, (Eds.: A. Abe, J.-F. Joanny, A.-C. Albertsson, R. Duncan, H.-H. Kausch, S. Kobayashi, K. Dušek, K.-S. Lee, W. De Jeu, L. Leibler, O. Nuyken, T. E. Long, E. Terentjev, B. Voit, I. Manners, G. Wegner, M. Möller, C. Dr. Holm, K. Prof. Dr. Kremer), Series Title: Advances in Polymer Science, Springer Berlin Heidelberg, Berlin, Heidelberg, **2005**, pp. 105–149 (cit. on p. 29).

[57] H. C. Andersen, *J. Chem. Phys.* **1980**, *72*, 2384–2393 (cit. on p. 30).

[58] T. Schneider, E. Stoll, *Phys. Rev. B* **1978**, *17*, 1302–1322 (cit. on p. 30).

[59] H. J. C. Berendsen, J. P. M. Postma, W. F. Van Gunsteren, A. DiNola, J. R. Haak, *J. Chem. Phys.* **1984**, *81*, 3684–3690 (cit. on p. 30).

[60] T. Morishita, *J. Chem. Phys.* **2000**, *113*, 2976–2982 (cit. on p. 30).

[61] S. C. Harvey, R. K.-Z. Tan, T. E. Cheatham, *J. Comput. Chem.* **1998**, *19*, 726–740 (cit. on p. 30).

[62] E. Braun, S. M. Moosavi, B. Smit, *J. Chem. Theory Comput.* **2018**, *14*, 5262–5272 (cit. on p. 30).

[63] M. Born, R. Oppenheimer, *Ann. Phys.* **1927**, *389*, 457–484 (cit. on p. 31).

[64] M. Born, *Z. Physik* **1926**, *37*, 863–867 (cit. on p. 32).

[65] H. J. Monkhorst, J. D. Pack, *Phys. Rev. B* **1976**, *13*, 5188–5192 (cit. on p. 33).

[66] D. R. Hartree, *Math. Proc. Camb. Phil. Soc.* **1928**, *24*, 111–132 (cit. on p. 33).

[67] V. Fock, *Z. Physik* **1930**, *61*, 126–148 (cit. on p. 33).

[68] J. W. S. Baron Rayleigh, *The Theory of Sound.* Macmillan and Co., London, **1877** (cit. on p. 34).

[69] W. Ritz, *J. Reine Angew. Math.* **1909**, *1909*, 1–61 (cit. on p. 34).

[70] L. H. Thomas, *Math. Proc. Camb. Phil. Soc.* **1927**, *23*, 542–548 (cit. on p. 34).

[71] E. Fermi, *Z. Physik* **1928**, *48*, 73–79 (cit. on p. 34).

[72] W. Kohn, L. J. Sham, *Phys. Rev.* **1965**, *140*, A1133–A1138 (cit. on pp. 34, 36).

[73] P. Hohenberg, W. Kohn, *Phys. Rev.* **1964**, *136*, B864–B871 (cit. on p. 34).

[74] W. Kohn, *Rev. Mod. Phys.* **1999**, *71*, 1253–1266 (cit. on p. 34).

[75] M. Levy, *Proc. Natl. Acad. Sci. U.S.A.* **1979**, *76*, 6062–6065 (cit. on p. 36).

[76] M. G. Medvedev, I. S. Bushmarinov, J. Sun, J. P. Perdew, K. A. Lyssenko, *Science* **2017**, *355*, 49–52 (cit. on p. 36).

[77] J. P. Perdew in AIP Conference Proceedings, *Vol. 577*, ISSN: 0094243X, AIP, Antwerp (Belgium), **2001**, pp. 1–20 (cit. on p. 36).

[78] J. P. Perdew, A. Zunger, *Phys. Rev. B* **1981**, *23*, 5048–5079 (cit. on p. 36).

[79] D. C. Langreth, M. J. Mehl, *Phys. Rev. B* **1983**, *28*, 1809–1834 (cit. on p. 36).

[80] D. C. Langreth, M. J. Mehl, *Phys. Rev. B* **1984**, *29*, 2310–2310 (cit. on p. 36).

[81] A. D. Becke, *Phys. Rev. A* **1988**, *38*, 3098–3100 (cit. on p. 36).

[82] J. P. Perdew, J. A. Chevary, S. H. Vosko, K. A. Jackson, M. R. Pederson, D. J. Singh, C. Fiolhais, *Phys. Rev. B* **1992**, *46*, 6671–6687 (cit. on p. 36).

[83] J. P. Perdew, *Phys. Rev. Lett.* **1985**, *55*, 2370–2370 (cit. on p. 37).

[84] J. P. Perdew, *Phys. Rev. Lett.* **1985**, *55*, 1665–1668 (cit. on p. 37).

[85] J. P. Perdew, S. Kurth, A. Zupan, P. Blaha, *Phys. Rev. Lett.* **1999**, *82*, 2544–2547 (cit. on p. 37).

[86] J. P. Perdew, S. Kurth, A. Zupan, P. Blaha, *Phys. Rev. Lett.* **1999**, *82*, 5179–5179 (cit. on p. 37).

[87] J. Tao, J. P. Perdew, V. N. Staroverov, G. E. Scuseria, *Phys. Rev. Lett.* **2003**, *91*, 146401 (cit. on p. 37).

[88] A. D. Becke, *J. Chem. Phys.* **1993**, *98*, 1372–1377 (cit. on p. 37).

[89] A. D. Becke, *J. Chem. Phys.* **1993**, *98*, 5648–5652 (cit. on pp. 37, 39).

[90] P. Haas, F. Tran, P. Blaha, *Phys. Rev. B* **2009**, *79*, 085104 (cit. on p. 37).

[91] P. Haas, F. Tran, P. Blaha, *Phys. Rev. B* **2009**, *79*, 209902 (cit. on p. 37).

[92] L. He, F. Liu, G. Hautier, M. J. T. Oliveira, M. A. L. Marques, F. D. Vila, J. J. Rehr, G.-M. Rignanese, A. Zhou, *Phys. Rev. B* **2014**, *89*, 064305 (cit. on p. 37).

[93] J. P. Perdew, K. Burke, M. Ernzerhof, *Phys. Rev. Lett.* **1996**, *77*, 3865–3868 (cit. on pp. 37, 48).

[94] J. P. Perdew, K. Burke, M. Ernzerhof, *Phys. Rev. Lett.* **1997**, *78*, 1396–1396 (cit. on pp. 37, 48).

[95] J. P. Perdew, A. Ruzsinszky, G. I. Csonka, O. A. Vydrov, G. E. Scuseria, L. A. Constantin, X. Zhou, K. Burke, *Phys. Rev. Lett.* **2008**, *100*, 136406 (cit. on p. 37).

[96] J. P. Perdew, A. Ruzsinszky, G. I. Csonka, O. A. Vydrov, G. E. Scuseria, L. A. Constantin, X. Zhou, K. Burke, *Phys. Rev. Lett.* **2009**, *102*, 039902 (cit. on p. 37).

[97] G.-X. Zhang, A. M. Reilly, A. Tkatchenko, M. Scheffler, *New J. Phys.* **2018**, *20*, 063020 (cit. on p. 37).

[98] J. Sun, A. Ruzsinszky, J. P. Perdew, *Phys. Rev. Lett.* **2015**, *115*, 036402 (cit. on p. 38).

[99] Y. Hinuma, H. Hayashi, Y. Kumagai, I. Tanaka, F. Oba, *Phys. Rev. B* **2017**, *96*, 094102 (cit. on p. 38).

[100] G. Sai Gautam, E. A. Carter, *Phys. Rev. Materials* **2018**, *2*, 095401 (cit. on p. 38).

[101] R. Devi, B. Singh, P. Canepa, G. Sai Gautam, *npj Comput. Mater.* **2022**, *8*, 160 (cit. on p. 38).

[102] S. Swathilakshmi, R. Devi, G. S. Gautam, Performance of the r^{2}SCAN functional in transition metal oxides, en, arXiv:2301.00535 [cond-mat], **2023** (cit. on p. 38).

[103] A. P. Bartók, J. R. Yates, *J. Chem. Phys.* **2019**, *150*, 161101 (cit. on p. 38).

[104] J. W. Furness, A. D. Kaplan, J. Ning, J. P. Perdew, J. Sun, *J. Phys. Chem. Lett.* **2020**, *11*, 8208–8215 (cit. on p. 38).

[105] J. W. Furness, A. D. Kaplan, J. Ning, J. P. Perdew, J. Sun, *J. Phys. Chem. Lett.* **2020**, *11*, 9248–9248 (cit. on p. 38).

[106] J. W. Furness, A. D. Kaplan, J. Ning, J. P. Perdew, J. Sun, *J. Chem. Phys.* **2022**, *156*, 034109 (cit. on p. 38).

[107] R. Kingsbury, A. S. Gupta, C. J. Bartel, J. M. Munro, S. Dwaraknath, M. Horton, K. A. Persson, *Phys. Rev. Materials* **2022**, *6*, 013801 (cit. on p. 38).

[108] A. J. Cohen, P. Mori-Sánchez, W. Yang, *Phys. Rev. B* **2008**, *77*, 115123 (cit. on p. 38).

[109] J. P. Perdew, M. Ernzerhof, K. Burke, *J. Chem. Phys.* **1996**, *105*, 9982–9985 (cit. on p. 38).

[110] C. Adamo, V. Barone, *J. Chem. Phys.* **1999**, *110*, 6158–6170 (cit. on p. 38).

[111] J. Heyd, G. E. Scuseria, *J. Chem. Phys.* **2004**, *121*, 1187–1192 (cit. on p. 38).

[112] J. Jaramillo, G. E. Scuseria, M. Ernzerhof, *J. Chem. Phys.* **2003**, *118*, 1068–1073 (cit. on p. 39).

[113] J. Heyd, G. E. Scuseria, M. Ernzerhof, *J. Chem. Phys.* **2003**, *118*, 8207–8215 (cit. on pp. 39, 48, 92).

[114] J. Heyd, G. E. Scuseria, M. Ernzerhof, *J. Chem. Phys.* **2006**, *124*, 219906 (cit. on pp. 39, 48, 92).

[115] A. V. Krukau, O. A. Vydrov, A. F. Izmaylov, G. E. Scuseria, *J. Chem. Phys.* **2006**, *125*, 224106 (cit. on pp. 39, 48, 92).

[116] C. Lee, W. Yang, R. G. Parr, *Phys. Rev. B* **1988**, *37*, 785–789 (cit. on p. 39).

[117] S. H. Vosko, L. Wilk, M. Nusair, *Can. J. Phys.* **1980**, *58*, 1200–1211 (cit. on p. 39).

[118] P. J. Stephens, F. J. Devlin, C. F. Chabalowski, M. J. Frisch, *J. Phys. Chem.* **1994**, *98*, 11623–11627 (cit. on p. 39).

[119] O. A. Vydrov, J. Heyd, A. V. Krukau, G. E. Scuseria, *J. Chem. Phys.* **2006**, *125*, 074106 (cit. on p. 39).

[120] V. I. Anisimov, J. Zaanen, O. K. Andersen, *Phys. Rev. B* **1991**, *44*, 943–954 (cit. on p. 39).

[121] A. K. McMahan, R. M. Martin, S. Satpathy, *Phys. Rev. B* **1988**, *38*, 6650–6666 (cit. on p. 39).

[122] M. S. Hybertsen, M. Schlüter, N. E. Christensen, *Phys. Rev. B* **1989**, *39*, 9028–9041 (cit. on p. 39).

[123] I. A. Nekrasov, M. A. Korotin, V. I. Anisimov, Coulomb interaction in oxygen \textit{p}-shell in LDA+U method and its influence on calculated spectral and magnetic properties of transition metal oxides, arXiv:cond-mat/0009107, **2000** (cit. on p. 39).

[124] A. I. Liechtenstein, V. I. Anisimov, J. Zaanen, *Phys. Rev. B* **1995**, *52*, R5467–R5470 (cit. on p. 39).

[125] S. L. Dudarev, G. A. Botton, S. Y. Savrasov, C. J. Humphreys, A. P. Sutton, *Phys. Rev. B* **1998**, *57*, 1505–1509 (cit. on p. 39).

[126] M. Cococcioni, S. de Gironcoli, *Phys. Rev. B* **2005**, *71*, 035105 (cit. on p. 40).

[127] L. Wang, T. Maxisch, G. Ceder, *Phys. Rev. B* **2006**, *73*, 195107 (cit. on pp. 40, 50, 92).

[128] P. E. Blöchl, *Phys. Rev. B* **1994**, *50*, 17953–17979 (cit. on pp. 41, 48).

[129] A. Walsh, *npj Comput. Mater.* **2021**, *7*, 72 (cit. on p. 42).

[130] M. Leslie, N. J. Gillan, *J. Phys. C: Solid State Phys.* **1985**, *18*, 973–982 (cit. on p. 42).

[131] G. Makov, M. C. Payne, *Phys. Rev. B* **1995**, *51*, 4014–4022 (cit. on p. 42).

[132] S. Lany, A. Zunger, *Modelling Simul. Mater. Sci. Eng.* **2009**, *17*, 084002 (cit. on p. 42).

[133] C. Freysoldt, J. Neugebauer, C. G. Van de Walle, *Phys. Rev. Lett.* **2009**, *102*, 016402 (cit. on pp. 42, 49, 92).

[134] Y. Kumagai, F. Oba, *Phys. Rev. B* **2014**, *89*, 195205 (cit. on p. 42).

[135] G. Henkelman, B. P. Uberuaga, H. Jónsson, *J. Chem. Phys.* **2000**, *113*, 9901–9904 (cit. on pp. 43, 44, 49, 92).

[136] G. Henkelman, H. Jónsson, *J. Chem. Phys.* **2000**, *113*, 9978–9985 (cit. on pp. 43, 44, 49, 92).

[137] G. H. Vineyard, *J. Phys. Chem. Solids* **1957**, *3*, 121–127 (cit. on p. 44).

[138] K. Binder, *Adv. Mater.* **1992**, *4*, 540–547 (cit. on p. 44).

[139] N. Metropolis, A. W. Rosenbluth, M. N. Rosenbluth, A. H. Teller, E. Teller, *J. Chem. Phys.* **1953**, *21*, 1087–1092 (cit. on pp. 45, 48, 56, 108).

[140] W. K. Hastings, *Biometrika* **1970**, *57*, 97–109 (cit. on p. 46).

[141] S. P. Ong, W. D. Richards, A. Jain, G. Hautier, M. Kocher, S. Cholia, D. Gunter, V. L. Chevrier, K. A. Persson, G. Ceder, *Comput. Mater. Sci.* **2013**, *68*, 314–319 (cit. on p. 47).

[142] S. Bahn, K. Jacobsen, *Comput. Sci. Eng.* **2002**, *4*, 56–66 (cit. on p. 47).

[143] A. Hjorth Larsen, J. Jørgen Mortensen, J. Blomqvist, I. E. Castelli, R. Christensen, M. Dułak, J. Friis, M. N. Groves, B. Hammer, C. Hargus, E. D. Hermes, P. C. Jennings, P. Bjerre Jensen, J. Kermode, J. R. Kitchin, E. Leonhard Kolsbjerg, J. Kubal, K. Kaasbjerg, S. Lysgaard, J. Bergmann Maronsson, T. Maxson, T. Olsen, L. Pastewka, A. Peterson, C. Rostgaard, J. Schiøtz, O. Schütt, M. Strange, K. S. Thygesen, T. Vegge, L. Vilhelmsen, M. Walter, Z. Zeng, K. W. Jacobsen, *J. Phys.: Condens. Matter* **2017**, *29*, 273002 (cit. on p. 47).

[144] P. Hirel, *Comput. Phys. Commun.* **2015**, *197*, 212–219 (cit. on pp. 47, 107).

[145] K. Momma, F. Izumi, *J. Appl. Crystallogr.* **2008**, *41*, 653–658 (cit. on p. 47).

[146] A. Stukowski, *Modelling Simul. Mater. Sci. Eng.* **2010**, *18*, 015012 (cit. on pp. 47, 109).

[147] S. Plimpton, *J. Comput. Phys.* **1995**, *117*, 1–19 (cit. on pp. 47, 48).

[148] A. P. Thompson, H. M. Aktulga, R. Berger, D. S. Bolintineanu, W. M. Brown, P. S. Crozier, P. J. in 't Veld, A. Kohlmeyer, S. G. Moore, T. D. Nguyen, R. Shan, M. J. Stevens, J. Tranchida, C. Trott, S. J. Plimpton, *Comput. Phys. Commun.* **2022**, *271*, 108171 (cit. on pp. 47, 48).

[149] J. D. Gale, *Faraday Trans.* **1997**, *93*, 629–637 (cit. on p. 47).

[150] J. D. Gale, A. L. Rohl, *Mol. Simul.* **2003**, *29*, 291–341 (cit. on p. 47).

[151] J. D. Gale, *J. Phys. Chem. B* **1998**, *102*, 5423–5431 (cit. on p. 47).

[152] J. D. Gale, *Z. Kristallogr. Cryst. Mater.* **2005**, *220*, 552–554 (cit. on p. 47).

[153] G. Kresse, J. Hafner, *Phys. Rev. B* **1994**, *49*, 14251–14269 (cit. on pp. 47, 92).

[154] G. Kresse, J. Furthmüller, *Comput. Mater. Sci.* **1996**, *6*, 15–50 (cit. on pp. 47, 92).

[155] G. Kresse, J. Furthmüller, *Phys. Rev. B* **1996**, *54*, 11169–11186 (cit. on pp. 47, 92).

[156] G. Kresse, D. Joubert, *Phys. Rev. B* **1999**, *59*, 1758–1775 (cit. on p. 47).

[157] C. Freysoldt, sxdefectalign, **2022** (cit. on pp. 47, 49).

[158] G. Henkelman, A. Arnaldsson, H. Jónsson, *Comput. Mater. Sci.* **2006**, *36*, 354–360 (cit. on p. 47).

[159] T. A. Manz, N. G. Limas, *RSC Adv.* **2016**, *6*, 47771–47801 (cit. on p. 47).

[160] N. G. Limas, T. A. Manz, *RSC Adv.* **2016**, *6*, 45727–45747 (cit. on p. 47).

[161] G. Balducci, J. Kašpar, P. Fornasiero, M. Graziani, M. S. Islam, J. D. Gale, *J. Phys. Chem. B* **1997**, *101*, 1750–1753 (cit. on pp. 48, 54, 161).

[162] A. R. Genreith-Schriever, R. A. De Souza, *Phys. Rev. B* **2016**, *94*, 224304 (cit. on pp. 48, 54, 75).

[163] C. Fisher, M. Yoshiya, Y. Iwamoto, J. Ishii, M. Asanuma, K. Yabuta, *Solid State Ion.* **2007**, *177*, 3425–3431 (cit. on pp. 48, 51, 161).

[164] H. Shiiba, C. L. Bishop, M. J. D. Rushton, M. Nakayama, M. Nogami, J. A. Kilner, R. W. Grimes, *J. Mater. Chem. A* **2013**, *1*, 10345 (cit. on pp. 48, 81, 82).

[165] M. Islam, M. Cherry, C. Catlow, *J. Solid State Chem.* **1996**, *124*, 230–237 (cit. on pp. 48, 106, 161).

[166] M. Cherry, M. Islam, C. Catlow, *J. Solid State Chem.* **1995**, *118*, 125–132 (cit. on pp. 48, 161).

[167] A. Jones, M. S. Islam, *J. Phys. Chem. C* **2008**, *112*, 4455–4462 (cit. on pp. 48, 106).

[168] R. Wahl, D. Vogtenhuber, G. Kresse, *Phys. Rev. B* **2008**, *78*, 104116 (cit. on p. 48).

[169] F. El-Mellouhi, E. N. Brothers, M. J. Lucero, G. E. Scuseria, *Phys. Rev. B* **2011**, *84*, 115122 (cit. on p. 48).

[170] D. Gryaznov, E. Blokhin, A. Sorokine, E. A. Kotomin, R. A. Evarestov, A. Bussmann-Holder, J. Maier, *J. Phys. Chem. C* **2013**, *117*, 13776–13784 (cit. on pp. 48, 50).

[171] F. Viñes, O. Lamiel-García, K. Chul Ko, J. Yong Lee, F. Illas, *J. Comput. Chem.* **2017**, *38*, 781–789 (cit. on p. 48).

[172] K. van Benthem, C. Elsässer, R. H. French, *J. Appl. Phys.* **2001**, *90*, 6156–6164 (cit. on pp. 48, 93).

[173] D. J. Kok, K. Irmscher, M. Naumann, C. Guguschev, Z. Galazka, R. Uecker, *Phys. Status Solidi A* **2015**, *212*, 1880–1887 (cit. on pp. 48, 93).

[174] R. A. De Souza, D. Kemp, M. J. Wolf, A. H. H. Ramadan, *J. Phys. Chem. Lett.* **2022**, 11363–11368 (cit. on p. 49).

[175] V. L. Chevrier, S. P. Ong, R. Armiento, M. K. Y. Chan, G. Ceder, *Phys. Rev. B* **2010**, *82*, 075122 (cit. on pp. 50, 92).

[176] K. Binder, J. Horbach, W. Kob, W. Paul, F. Varnik, *J. Phys.: Condens. Matter* **2004**, *16*, S429–S453 (cit. on p. 51).

[177] H. Jobic, D. N. Theodorou, *Microporous Mesoporous Mater.* **2007**, *102*, 21–50 (cit. on p. 51).

[178] J. Wang, T. Hou, *J. Comput. Chem.* **2011**, *32*, 3505–3519 (cit. on p. 51).

[179] T. D. De La Rubia, *Annu. Rev. Mater. Sci.* **1996**, *26*, 613–649 (cit. on p. 51).

[180] A. V. Korchuganov, V. M. Chernov, K. P. Zolnikov, D. S. Kryzhevich, S. G. Psakhie, *Inorg. Mater. Appl. Res.* **2016**, *7*, 648–657 (cit. on p. 51).

[181] R. Darkins, D. M. Duffy, *Comput. Mater. Sci.* **2018**, *147*, 145–153 (cit. on p. 51).

[182] Z. Yan, R. Liu, B. Liu, Y. Shao, M. Liu, *Energies* **2023**, *16*, 1176 (cit. on p. 51).

[183] D. Poulikakos, S. Maruyama, *Microscale Thermophys. Eng.* **2003**, *7*, 181–206 (cit. on p. 51).

[184] A. McGaughey, M. Kaviany in *Advances in Heat Transfer*, *Vol. 39*, Elsevier, **2006**, pp. 169–255 (cit. on p. 51).

[185] E. A. Algaer, F. Müller-Plathe, *Soft Mater.* **2012**, *10*, 42–80 (cit. on p. 51).

[186] F. H. Stillinger, T. A. Weber, R. A. LaViolette, *J. Chem. Phys.* **1986**, *85*, 6460–6469 (cit. on p. 51).

[187] B. J. Garrison, *Chem. Soc. Rev.* **1992**, *21*, 155 (cit. on p. 51).

[188] A. Warshel, *Acc. Chem. Res.* **2002**, *35*, 385–395 (cit. on p. 51).

[189] A. Chroneos, B. Yildiz, A. Tarancón, D. Parfitt, J. A. Kilner, *Energy Environ. Sci.* **2011**, *4*, 2774 (cit. on p. 51).

[190] K. N. Grew, W. K. Chiu, *J. Power Sources* **2012**, *199*, 1–13 (cit. on p. 51).

[191] K. T. Butler, J. M. Frost, J. M. Skelton, K. L. Svane, A. Walsh, *Chem. Soc. Rev.* **2016**, *45*, 6138–6146 (cit. on p. 51).

[192] A. Marin-Laflèche, M. Haefele, L. Scalfi, A. Coretti, T. Dufils, G. Jeanmairet, S. Reed, A. Serva, R. Berthin, C. Bacon, S. Bonella, B. Rotenberg, P. Madden, M. Salanne, *J. Open Source Softw.* **2020**, *5*, 2373 (cit. on p. 51).

[193] J. Savioli, G. W. Watson, *Curr. Opin. Electrochem.* **2020**, *21*, 14–21 (cit. on p. 51).

[194] A. Mahmood, A. Irfan, J.-L. Wang, *J. Mater. Chem. A* **2022**, *10*, 4170–4180 (cit. on p. 51).

[195] N. Yao, X. Chen, Z.-H. Fu, Q. Zhang, *Chem. Rev.* **2022**, *122*, 10970–11021 (cit. on p. 51).

[196] G. Ciccotti, C. Dellago, M. Ferrario, E. R. Hernández, M. E. Tuckerman, *Eur. Phys. J. B* **2022**, *95*, 3 (cit. on p. 52).

[197] A. L. Usler, D. Kemp, A. Bonkowski, R. A. De Souza, *J. Comput. Chem.* **2023**, *44*, 1347–1359 (cit. on pp. 52, 66–68, 71, 82, 111, 112, 114).

[198] A. R. McCluskey, S. W. Coles, B. J. Morgan, *J. Chem. Theory Comput.* **2024**, *21*, 79–87 (cit. on pp. 52, 67).

[199] S. Beschnitt, R. A. De Souza, *Solid State Ion.* **2017**, *305*, 23–29 (cit. on p. 54).

[200] S. P. Waldow, R. A. De Souza, *J. Phys. Energy* **2020**, *2*, 024001 (cit. on p. 54).

[201] A. R. Genreith-Schriever, J. P. Parras, H. J. Heelweg, R. A. De Souza, *ChemElectroChem* **2020**, *7*, 4718–4723 (cit. on p. 54).

[202] C. A. Becker, F. Tavazza, Z. T. Trautt, R. A. Buarque De Macedo, *Curr. Opin. Solid State Mater. Sci.* **2013**, *17*, 277–283 (cit. on p. 54).

[203] J. A. Harrison, J. D. Schall, S. Maskey, P. T. Mikulski, M. T. Knippenberg, B. H. Morrow, *Appl. Phys. Rev.* **2018**, *5*, 031104 (cit. on p. 54).

[204] S. P. Waldow, R. A. De Souza, *ACS Appl. Mater. Interfaces* **2016**, *8*, 12246–12256 (cit. on pp. 54, 102).

[205] J. Kaub, J. Kler, S. C. Parker, R. A. De Souza, *Phys. Chem. Chem. Phys.* **2020**, *22*, 5413–5417 (cit. on p. 54).

[206] H. J. Heelweg, R. A. De Souza, *Phys. Rev. Materials* **2021**, *5*, 013804 (cit. on pp. 54, 100, 108).

[207] E. Robens, R. Rauschen, J. Kaub, J. P. Parras, D. Kemp, C. L. Freeman, R. A. De Souza, *J. Mater. Chem. A* **2022**, *10*, 2388–2397 (cit. on pp. 54, 80, 87, 102, 113).

[208] R. W. Conway, *Manag. Sci.* **1963**, *10*, 47–61 (cit. on p. 55).

[209] G. S. Fishman, *Oper. Res.* **1972**, *20*, 785–790 (cit. on p. 55).

[210] A. V. Gafarian, C. J. Ancker, T. Morisaku, *Nav. Res. Logist.* **1978**, *25*, 511–529 (cit. on p. 55).

[211] J. R. Wilson, A. A. B. Pritsker, *Simulation* **1978**, *31*, 55–58 (cit. on p. 55).

[212] M. Snell, L. Schruben, *IIE Trans.* **1985**, *17*, 354–363 (cit. on p. 55).

[213] K. White, M. Cobb, S. Spratt in 2000 Winter Simulation Conference Proceedings (Cat. No.00CH37165), *Vol. 1*, IEEE, Orlando, FL, USA, **2000**, pp. 755–760 (cit. on p. 55).

[214] K. Hoad, S. Robinson, R. Davies, *J. Oper. Res. Soc.* **2010**, *61*, 1389–1403 (cit. on p. 55).

[215] R. Pasupathy, B. Schmeiser in Proceedings of the 2010 Winter Simulation Conference, IEEE, Baltimore, MD, USA, **2010**, pp. 184–197 (cit. on p. 55).

[216] R. J. Wang, P. W. Glynn, *ACM Trans. Model. Comput. Simul.* **2017**, *27*, 1–30 (cit. on p. 55).

[217] F. Clark, D. J. Cole, J. Michel, *J. Chem. Theory Comput.* **2025**, *21*, 88–101 (cit. on p. 55).

[218] M. A. McClarnon, MA thesis, University of Virginia, **1990** (cit. on p. 55).

[219] K. White, M. Minnox in Proceedings of IEEE International Conference on Systems, Man and Cybernetics, *Vol. 1*, IEEE, San Antonio, TX, USA, **1994**, pp. 215–220 (cit. on p. 55).

[220] K. White in 1995 IEEE International Conference on Systems, Man and Cybernetics. Intelligent Systems for the 21st Century, *Vol. 1*, IEEE, Vancouver, BC, Canada, **1995**, pp. 206–211 (cit. on p. 55).

[221] K. P. White, *Simulation* **1997**, *69*, 323–334 (cit. on p. 55).

[222] F. L. Oliveira, B. Luan, P. M. Esteves, M. Steiner, R. Neumann Barros Ferreira, *J. Chem. Theory Comput.* **2024**, *20*, 8559–8568 (cit. on pp. 56, 57).

[223] J. A. Dawson, P. Canepa, M. J. Clarke, T. Famprikis, D. Ghosh, M. S. Islam, *Chem. Mater.* **2019**, *31*, 5296–5304 (cit. on pp. 56, 109).

[224] A. R. Symington, M. Molinari, J. A. Dawson, J. M. Statham, J. Purton, P. Canepa, S. C. Parker, *J. Mater. Chem. A* **2021**, 6487–6498 (cit. on p. 56).

[225] D. Kemp, A. Tarancón, R. A. De Souza, *Phys. Chem. Chem. Phys.* **2022**, *24*, 12926–12936 (cit. on pp. 56, 75).

[226] S. Duane, A. Kennedy, B. J. Pendleton, D. Roweth, *Phys. Lett. B* **1987**, *195*, 216–222 (cit. on p. 58).

[227] J. A. Purton, J. D. Blundy, J. A. Purton, M. B. Taylor, G. D. Barrera, N. L. Allan, *Chem. Commun.* **1998**, 627–628 (cit. on p. 58).

[228] J. A. Purton, G. D. Barrera, N. L. Allan, J. D. Blundy, *J. Phys. Chem. B* **1998**, *102*, 5202–5207 (cit. on p. 58).

[229] E. C. Neyts, A. Bogaerts, *Theor. Chem. Acc.* **2013**, *132*, 1320 (cit. on p. 58).

[230] A. R. Symington, J. Purton, J. Statham, M. Molinari, M. S. Islam, S. C. Parker, *J. Mater. Chem. A* **2020**, *8*, 19603–19611 (cit. on p. 58).

[231] J. Hickman, Y. Mishin, *Phys. Rev. B* **2016**, *94*, 184311 (cit. on p. 58).

[232] T. L. Hill, *An Introduction to Statistical Thermodynamics*, unabridged, corr. republ. of the 2. printing of the work Reading, Mass. : Addison-Wesley, 1960, Dover Publ, New York, **1998** (cit. on p. 59).

[233] E. F. Westrum, A. F. Beale, *J. Phys. Chem.* **1961**, *65*, 353–355 (cit. on p. 60).

[234] M. Ricken, J. Nölting, I. Riess, *J. Solid State Chem.* **1984**, *54*, 89–99 (cit. on p. 60).

[235] H. Zhu, C. Yang, Q. Li, Y. Ren, J. C. Neuefeind, L. Gu, H. Liu, L. Fan, J. Chen, J. Deng, N. Wang, J. Hong, X. Xing, *Nat. Commun.* **2018**, *9*, 5063 (cit. on p. 60).

[236] G. Neilsen, P. F. Rosen, M. S. Dickson, M. Popovic, J. Schliesser, L. D. Hansen, A. Navrotsky, B. F. Woodfield, *Acta Mater.* **2020**, *188*, 740–744 (cit. on p. 60).

[237] A. Nakajima, A. Yoshihara, M. Ishigame, *Phys. Rev. B* **1994**, *50*, 13297–13307 (cit. on p. 60).

[238] L. Gerward, J. Staun Olsen, L. Petit, G. Vaitheeswaran, V. Kanchana, A. Svane, *J. Alloys Compd.* **2005**, *400*, 56–61 (cit. on p. 60).

[239] S. J. Duclos, Y. K. Vohra, A. L. Ruoff, A. Jayaraman, G. P. Espinosa, *Phys. Rev. B* **1988**, *38*, 7755–7758 (cit. on p. 60).

[240] L. Gerward, J. S. Olsen, *Powder Diffr.* **1993**, *8*, 127–129 (cit. on p. 60).

[241] R. Metzler, J. Klafter, *Phys. Rep.* **2000**, *339*, 1–77 (cit. on p. 60).

[242] M. Schie, M. P. Müller, M. Salinga, R. Waser, R. A. De Souza, *J. Chem. Phys.* **2017**, *146*, 094508 (cit. on p. 62).

[243] T. J. A. M. Smolders, A. B. Walker, M. J. Wolf, *J. Phys. Chem. Lett.* **2021**, *12*, 5169–5177 (cit. on p. 62).

[244] J. Hinterberg, T. Zacherle, R. A. De Souza, *Phys. Rev. Lett.* **2013**, *110*, 205901 (cit. on p. 63).

[245] Z. Deng, Z. Zhu, I.-H. Chu, S. P. Ong, *Chem. Mater.* **2017**, *29*, 281–288 (cit. on p. 67).

[246] C. L. Perrin, *J. Chem. Educ.* **2017**, *94*, 669–672 (cit. on p. 68).

[247] A. R. McCluskey, *J. Chem. Educ.* **2023**, *100*, 4174–4176 (cit. on p. 68).

[248] O. Abril-Pla, V. Andreani, C. Carroll, L. Dong, C. J. Fonnesbeck, M. Kochurov, R. Kumar, J. Lao, C. C. Luhmann, O. A. Martin, M. Osthege, R. Vieira, T. Wiecki, R. Zinkov, *PeerJ Comput. Sci.* **2023**, *9*, e1516 (cit. on p. 72).

[249] A. McCluskey, T. Snow, *J. Open Source Softw.* **2020**, *5*, 2214 (cit. on pp. 72, 73).

[250] D. Kester, M. Mueller, *Astron. Comput.* **2021**, *37*, 100503 (cit. on p. 72).

[251] A. D. Le Claire in Physical Chemistry - An Advanced Treatise, Academic Press, New York, **1970** (cit. on p. 73).

[252] G. Murch, *Solid State Ion.* **1982**, *7*, 177–198 (cit. on p. 73).

[253] G. E. Murch, *Philos. Mag. A* **1982**, *45*, 685–692 (cit. on p. 74).

[254] A. R. Allnatt, *J. Phys. C: Solid State Phys.* **1982**, *15*, 5605–5613 (cit. on p. 75).

[255] A. R. Allnatt, E. L. Allnatt, *Philos. Mag. A* **1984**, *49*, 625–635 (cit. on p. 75).

[256] S. Grieshammer, I. V. Belova, G. E. Murch, *Acta Mater.* **2021**, *210*, 116802 (cit. on p. 75).

[257] D. Kemp, R. A. De Souza, *Phys. Rev. Materials* **2021**, *5*, 105401 (cit. on p. 75).

[258] M. S. Abdallah, M. Youssef, *Phys. Rev. Materials* **2021**, *5*, 114606 (cit. on p. 76).

[259] Z. Shao, W. Yang, Y. Cong, H. Dong, J. Tong, G. Xiong, *J. Membr. Sci.* **2000**, *172*, 177–188 (cit. on p. 79).

[260] S. Baumann, J. Serra, M. Lobera, S. Escolástico, F. Schulze-Küppers, W. Meulenberg, *J. Membr. Sci.* **2011**, *377*, 198–205 (cit. on p. 79).

[261] Z. Shao, S. M. Haile, *Nature* **2004**, *431*, 170–173 (cit. on p. 79).

[262] J. Zhang, S. Ricote, P. V. Hendriksen, Y. Chen, *Adv. Funct. Mater.* **2022**, *32*, 2111205 (cit. on p. 79).

[263] W. Zhang, B. Yu, J. Xu, *Int. J. Hydrogen Energy* **2012**, *37*, 837–842 (cit. on p. 79).

[264] S. McIntosh, J. F. Vente, W. G. Haije, D. H. A. Blank, H. J. M. Bouwmeester, *Chem. Mater.* **2006**, *18*, 2187–2193 (cit. on p. 79).

[265] D. N. Mueller, R. A. De Souza, H.-I. Yoo, M. Martin, *Chem. Mater.* **2012**, *24*, 269–274 (cit. on pp. 79, 85).

[266] H. Kruidhof, H. Bouwmeester, R. Vdoorn, A. Burggraaf, *Solid State Ion.* **1993**, *63-65*, 816–822 (cit. on p. 79).

[267] S. Svarcova, *Solid State Ion.* **2008**, *178*, 1787–1791 (cit. on p. 79).

[268] D. N. Mueller, R. A. De Souza, T. E. Weirich, D. Roehrens, J. Mayer, M. Martin, *Phys. Chem. Chem. Phys.* **2010**, *12*, 10320 (cit. on p. 79).

[269] M. Kuklja, Y. Mastrikov, B. Jansang, E. Kotomin, *Solid State Ion.* **2013**, *230*, 21–26 (cit. on p. 79).

[270] F. Wang, T. Nakamura, K. Yashiro, J. Mizusaki, K. Amezawa, *Phys. Chem. Chem. Phys.* **2014**, *16*, 7307 (cit. on p. 79).

[271] A. Yan, V. Maragou, A. Arico, M. Cheng, P. Tsiakaras, *Appl. Catal. B* **2007**, *76*, 320–327 (cit. on p. 80).

[272] E. Bucher, A. Egger, G. B. Caraman, W. Sitte, *J. Electrochem. Soc.* **2008**, *155*, B1218 (cit. on p. 80).

[273] M. Schulz, R. Kriegel, A. Kämpfer, *J. Membr. Sci.* **2011**, *378*, 10–17 (cit. on p. 80).

[274] R. Søndenå, S. Stølen, P. Ravindran, T. Grande, N. L. Allan, *Phys. Rev. B* **2007**, *75*, 184105 (cit. on p. 80).

[275] J. F. Vente, S. McIntosh, W. G. Haije, H. J. M. Bouwmeester, *J. Solid State Electrochem.* **2006**, *10*, 581–588 (cit. on p. 80).

[276] W. Zhou, R. Ran, Z. Shao, *J. Power Sources* **2009**, *192*, 231–246 (cit. on p. 80).

[277] G. C. Mather, M. S. Islam, F. M. Figueiredo, *Adv. Funct. Mater.* **2007**, *17*, 905–912 (cit. on pp. 80, 83, 161).

[278] G. V. Lewis, C. Catlow, *J. Phys. C: Solid State Phys.* **1985**, *18*, 1149 (cit. on pp. 80, 83, 161).

[279] J. M. Börgers, R. A. De Souza, *Phys. Chem. Chem. Phys.* **2020**, *22*, 14329–14339 (cit. on pp. 80, 125).

[280] H. Wang, C. Tablet, A. Feldhoff, J. Caro, *J. Membr. Sci.* **2005**, *262*, 20–26 (cit. on p. 84).

[281] Q. Zhu, T. Jin, Y. Wang, *Solid State Ion.* **2006**, *177*, 1199–1204 (cit. on pp. 84, 85).

[282] B. Huang, J. Malzbender, R. Steinbrech, L. Singheiser, *J. Membr. Sci.* **2010**, *359*, 80–85 (cit. on pp. 84, 85).

[283] R. Kriegel, R. Kircheisen, J. Töpfer, *Solid State Ion.* **2010**, *181*, 64–70 (cit. on pp. 84, 85).

[284] M.-B. Choi, S.-Y. Jeon, H.-N. Im, E. Wachsman, S.-J. Song, *J. Electrochem. Soc.* **2011**, *159*, P23–P28 (cit. on pp. 84–86).

[285] U. Pippardt, J. Böer, C. Bollert, A. Hoffmann, M. Heidenreich, R. Kriegel, M. Schulz, A. Simon, *J. Ceram. Sci. Tech.* **2014**, *5*, 309–316 (cit. on pp. 84, 85).

[286] T. Itoh, S. Shirasaki, Y. Fujie, N. Kitamura, Y. Idemoto, K. Osaka, H. Ofuchi, S. Hirayama, T. Honma, I. Hirosawa, *J. Alloys Compd.* **2010**, *491*, 527–535 (cit. on p. 85).

[287] A. Berenov, A. Atkinson, J. Kilner, M. Ananyev, V. Eremin, N. Porotnikova, A. Farlenkov, E. Kurumchin, H. Bouwmeester, E. Bucher, W. Sitte, *Solid State Ion.* **2014**, *268*, 102–109 (cit. on pp. 85, 86).

[288] E. Bucher, A. Egger, P. Ried, W. Sitte, P. Holtappels, *Solid State Ion.* **2008**, *179*, 1032–1035 (cit. on pp. 85, 86).

[289] D. Chen, Z. Shao, *Int. J. Hydrogen Energy* **2011**, *36*, 6948–6956 (cit. on pp. 85, 86).

[290] V. A. Eremin, M. V. Ananyev, H. J. M. Bouwmeester, E. K. Kurumchin, C.-Y. Yoo, *Phys. Chem. Chem. Phys.* **2020**, *22*, 10158–10169 (cit. on pp. 85, 86).

[291] L. Wang, R. Merkle, J. Maier, T. Acartürk, U. Starke, *Appl. Phys. Lett.* **2009**, *94*, 071908 (cit. on pp. 85, 86).

[292] T. Ishigaki, S. Yamauchi, K. Kishio, J. Mizusaki, K. Fueki, *J. Solid State Chem.* **1988**, *73*, 179–187 (cit. on pp. 85, 106, 112–114, 116).

[293] E. Kotomin, Y. A. Mastrikov, M. Kuklja, R. Merkle, A. Roytburd, J. Maier, *Solid State Ion.* **2011**, *188*, 1–5 (cit. on p. 87).

[294] D. Neagu, G. Tsekouras, D. N. Miller, H. Ménard, J. T. S. Irvine, *Nature Chem.* **2013**, *5*, 916–923 (cit. on pp. 89–91, 98).

[295] D. Neagu, T.-S. Oh, D. N. Miller, H. Ménard, S. M. Bukhari, S. R. Gamble, R. J. Gorte, J. M. Vohs, J. T. Irvine, *Nat. Commun.* **2015**, *6*, 8120 (cit. on pp. 89, 91, 97, 99).

[296] O. Kwon, S. Sengodan, K. Kim, G. Kim, H. Y. Jeong, J. Shin, Y.-W. Ju, J. W. Han, G. Kim, *Nat. Commun.* **2017**, *8*, 15967 (cit. on pp. 89, 90).

[297] O. Kwon, S. Joo, S. Choi, S. Sengodan, G. Kim, *J. Phys. Energy* **2020**, *2*, 032001 (cit. on pp. 89, 90).

[298] K. Kim, C. Lim, J. W. Han, *Korean J. Chem. Eng.* **2020**, *37*, 1295–1305 (cit. on pp. 89, 90).

[299] J. Zhang, M.-R. Gao, J.-L. Luo, *Chem. Mater.* **2020**, *32*, 5424–5441 (cit. on pp. 89, 90).

[300] J. H. Kim, J. K. Kim, J. Liu, A. Curcio, J.-S. Jang, I.-D. Kim, F. Ciucci, W. Jung, *ACS Nano* **2021**, *15*, 81–110 (cit. on pp. 89, 90, 92).

[301] H. Jeong, Y. H. Kim, B.-R. Won, H. Jeon, C.-h. Park, J.-h. Myung, *Chem. Mater.* **2023**, *35*, 3745–3764 (cit. on pp. 89, 90).

[302] J. Mei, T. Liao, Z. Sun, *Mater. Today Energy* **2023**, *31*, 101216 (cit. on pp. 89, 90).

[303] T. Ruh, D. Berkovec, F. Schrenk, C. Rameshan, *Chem. Commun.* **2023**, *59*, 3948–3956 (cit. on pp. 89, 90, 92).

[304] Z. Sun, C. Hao, S. Toan, R. Zhang, H. Li, Y. Wu, H. Liu, Z. Sun, *J. Mater. Chem. A* **2023**, 17961–17976 (cit. on pp. 89, 90).

[305] D. Neagu, J. T. S. Irvine, *Chem. Mater.* **2010**, *22*, 5042–5053 (cit. on pp. 89, 91).

[306] G. Tsekouras, D. Neagu, J. T. S. Irvine, *Energy Environ. Sci.* **2013**, *6*, 256–266 (cit. on pp. 89, 90).

[307] H. Han, Y. Xing, B. Park, D. I. Bazhanov, Y. Jin, J. T. S. Irvine, J. Lee, S. H. Oh, *Nat. Commun.* **2022**, *13*, 6682 (cit. on p. 90).

[308] Y. Gao, D. Chen, M. Saccoccio, Z. Lu, F. Ciucci, *Nano Energy* **2016**, *27*, 499–508 (cit. on pp. 90, 98).

[309] Y. H. Kim, H. Jeong, B.-R. Won, H. Jeon, C.-h. Park, D. Park, Y. Kim, S. Lee, J.-h. Myung, *Nano-Micro Lett.* **2024**, *16*, 33 (cit. on pp. 90, 98).

[310] I. Hamada, A. Uozumi, Y. Morikawa, A. Yanase, H. Katayama-Yoshida, *J. Am. Chem. Soc.* **2011**, *133*, 18506–18509 (cit. on p. 90).

[311] Y. Gao, Z. Lu, T. L. You, J. Wang, L. Xie, J. He, F. Ciucci, *J. Phys. Chem. Lett.* **2018**, *9*, 3772–3778 (cit. on p. 90).

[312] K. Kousi, D. Neagu, L. Bekris, E. I. Papaioannou, I. S. Metcalfe, *Angew. Chem. Int. Ed.* **2020**, *59*, 2510–2519 (cit. on p. 90).

[313] D. Neagu, V. Kyriakou, I.-L. Roiban, M. Aouine, C. Tang, A. Caravaca, K. Kousi, I. Schreur-Piet, I. S. Metcalfe, P. Vernoux, M. C. M. Van De Sanden, M. N. Tsampas, *ACS Nano* **2019**, *13*, 12996–13005 (cit. on p. 91).

[314] K. Gömann, G. Borchardt, M. Schulz, A. Gömann, W. Maus-Friedrichs, B. Lesage, O. Kaïtasov, S. Hoffmann-Eifert, T. Schneller, *Phys. Chem. Chem. Phys.* **2005**, *7*, 2053–2060 (cit. on pp. 91, 100, 101).

[315] U. N. Gries, M. Kessel, F. V. E. Hensling, R. Dittmann, M. Martin, R. A. De Souza, *Phys. Rev. Materials* **2020**, *4*, 123404 (cit. on pp. 91, 92, 100, 101).

[316] M. P. Zahler, S. M. Kraschewski, H. Störmer, D. Gerthsen, M. Bäurer, W. Rheinheimer, *J. Eur. Ceram. Soc.* **2023**, *43*, 1613–1624 (cit. on p. 91).

[317] T. Zhu, H. Troiani, L. V. Mogni, M. Santaya, M. Han, S. A. Barnett, *J. Power Sources* **2019**, *439*, 227077 (cit. on pp. 91, 99).

[318] M. L. Weber, Y. J. Sohn, R. Dittmann, R. Waser, N. H. Menzler, O. Guillon, C. Lenser, S. Nemšák, F. Gunkel, *J. Mater. Chem. A* **2023**, *11*, 17718–17727 (cit. on p. 91).

[319] M. Santaya, C. E. Jiménez, H. E. Troiani, E. A. Carbonio, M. D. Arce, L. M. Toscani, R. Garcia-Diez, R. G. Wilks, A. Knop-Gericke, M. Bär, L. V. Mogni, *J. Mater. Chem. A* **2022**, *10*, 15554–15568 (cit. on pp. 91, 102).

[320] K. Kousi, C. Tang, I. S. Metcalfe, D. Neagu, *Small* **2021**, *17*, 2006479 (cit. on pp. 91, 103).

[321] D. Neagu, J. T. S. Irvine, J. Wang, B. Yildiz, A. K. Opitz, J. Fleig, Y. Wang, J. Liu, L. Shen, F. Ciucci, B. A. Rosen, Y. Xiao, K. Xie, G. Yang, Z. Shao, Y. Zhang, J. Reinke, T. A. Schmauss, S. A. Barnett, R. Maring, V. Kyriakou, U. Mushtaq, M. N. Tsampas, Y. Kim, R. O'Hayre, A. J. Carrillo, T. Ruh, L. Lindenthal, F. Schrenk, C. Rameshan, E. I. Papaioannou, K. Kousi, I. S. Metcalfe, X. Xu, G. Liu, *J. Phys. Energy* **2023**, *5*, 031501 (cit. on p. 92).

[322] B. Koo, K. Kim, J. K. Kim, H. Kwon, J. W. Han, W. Jung, *Joule* **2018**, *2*, 1476–1499 (cit. on p. 92).

[323] K. Szot, W. Speier, U. Breuer, R. Meyer, J. Szade, R. Waser, *Surf. Sci.* **2000**, *460*, 112–128 (cit. on p. 92).

[324] D. J. Keeble, S. Wicklein, R. Dittmann, L. Ravelli, R. A. Mackie, W. Egger, *Phys. Rev. Lett.* **2010**, *105*, 226102 (cit. on p. 92).

[325] H. Schraknepper, C. Bäumer, R. Dittmann, R. A. De Souza, *Phys. Chem. Chem. Phys.* **2015**, *17*, 1060–1069 (cit. on p. 92).

[326] J. Fierro, *J. Catal.* **1985**, *93*, 83–91 (cit. on p. 92).

[327] G. Kresse, J. Hafner, *Phys. Rev. B* **1993**, *47*, 558–561 (cit. on p. 92).

[328] R. De Souza, G. Harrington, *Nat. Mater.* **2023**, *22*, 794–797 (cit. on p. 92).

[329] R. A. De Souza, D. N. Mueller, *Nat. Mater.* **2021**, *20*, 443–446 (cit. on p. 92).

[330] K. Blazey, O. Schirmer, W. Berlinger, K. Müller, *Solid State Commun.* **1975**, *16*, 589–592 (cit. on p. 93).

[331] B. A. Wechsler, M. B. Klein, *J. Opt. Soc. Am. B* **1988**, *5*, 1711 (cit. on p. 93).

[332] E. Possenriede, O. F. Schirmer, H. J. Donnerberg, G. Godefroy, A. Maillard, *Ferroelectrics* **1989**, *92*, 245–252 (cit. on p. 93).

[333] E. Possenriede, P. Jacobs, H. Kröse, O. F. Schirmer, *Appl. Phys. A* **1992**, *55*, 73–81 (cit. on p. 93).

[334] T. Bieger, J. Maier, R. Waser, *Ber. Bunsen-Ges. Phys. Chem.* **1993**, *97*, 1098–1104 (cit. on p. 93).

[335] R. Scharfschwerdt, O. Schirmer, H. Hesse, D. Rytz, *Appl. Phys. B: Lasers Opt.* **1999**, *68*, 807–812 (cit. on p. 93).

[336] J. Dashdorj, M. E. Zvanut, L. J. Stanley, *J. Appl. Phys.* **2010**, *107*, 083513 (cit. on p. 93).

[337] I. Suzuki, L. Gura, A. Klein, *Phys. Chem. Chem. Phys.* **2019**, *21*, 6238–6246 (cit. on p. 93).

[338] K. A. Müller, W. Berlinger, R. S. Rubins, *Phys. Rev.* **1969**, *186*, 361–371 (cit. on pp. 93–95).

[339] G. Blasse, P. De Korte, A. Mackor, *J. Inorg. Nucl. Chem.* **1981**, *43*, 1499–1503 (cit. on p. 93).

[340] K. H. Kim, K. H. Yoon, J. S. Choi, *J. Phys. Chem. Solids* **1985**, *46*, 1061–1066 (cit. on p. 93).

[341] R. Waser, *J. Am. Ceram. Soc.* **1991**, *74*, 1934–1940 (cit. on p. 93).

[342] R. Hagenbeck, R. Waser, *J. Appl. Phys.* **1998**, *83*, 2083–2092 (cit. on pp. 93, 95).

[343] I. A. Sluchinskaya, A. I. Lebedev, A. Erko, *Phys. Solid State* **2014**, *56*, 449–455 (cit. on pp. 93, 95).

[344] A. I. Lebedev, I. A. Sluchinskaya, *Ferroelectrics* **2016**, *501*, 1–8 (cit. on p. 93).

[345] A. Klein, K. Albe, N. Bein, O. Clemens, K. A. Creutz, P. Erhart, M. Frericks, E. Ghorbani, J. P. Hofmann, B. Huang, B. Kaiser, U. Kolb, J. Koruza, C. Kübel, K. N. S. Lohaus, J. Rödel, J. Rohrer, W. Rheinheimer, R. A. De Souza, V. Streibel, A. Weidenkaff, M. Widenmeyer, B.-X. Xu, H. Zhang, *J. Electroceram.* **2023**, *51*, 147–177 (cit. on pp. 93, 95).

[346] D. M. Long, B. Cai, J. N. Baker, P. C. Bowes, T. J. Bayer, J.-J. Wang, R. Wang, L.-Q. Chen, C. A. Randall, D. L. Irving, E. C. Dickey, *J. Am. Ceram. Soc.* **2019**, *102*, 3567–3577 (cit. on p. 93).

[347] J. M. Polfus, M.-L. Fontaine, A. Thøgersen, M. Riktor, T. Norby, R. Bredesen, *J. Mater. Chem. A* **2016**, *4*, 8105–8112 (cit. on pp. 93, 94).

[348] T. Zacherle, A. Schriever, R. A. De Souza, M. Martin, *Phys. Rev. B* **2013**, *87*, 134104 (cit. on p. 95).

[349] M. P. Mueller, F. Gunkel, S. Hoffmann-Eifert, R. A. De Souza, *J. Appl. Phys.* **2021**, *129*, 025104 (cit. on p. 95).

[350] R. Merkle, J. Maier, *Angew. Chem. Int. Ed.* **2008**, *47*, 3874–3894 (cit. on p. 95).

[351] K. Schindler, D. Schmeisser, U. Vohrer, H. Wiemhöfer, W. Göpel, *Sens. Actuators* **1989**, *17*, 555–568 (cit. on p. 95).

[352] G. M. Choi, H. L. Tuller, *J. Am. Ceram. Soc.* **1988**, *71*, 201–205 (cit. on p. 96).

[353] R. Moos, K. H. Hardtl, *J. Am. Ceram. Soc.* **1997**, *80*, 2549–2562 (cit. on p. 96).

[354] F. Horikiri, N. Iizawa, L. Han, K. Sato, K. Yashiro, T. Kawada, J. Mizusaki, *Solid State Ion.* **2008**, *179*, 2335–2344 (cit. on p. 96).

[355] R. A. De Souza, F. Gunkel, S. Hoffmann-Eifert, R. Dittmann, *Phys. Rev. B* **2014**, *89*, 241401 (cit. on p. 96).

[356] T. Tanaka, K. Matsunaga, Y. Ikuhara, T. Yamamoto, *Phys. Rev. B* **2003**, *68*, 205213 (cit. on p. 96).

[357] B. Liu, V. R. Cooper, H. Xu, H. Xiao, Y. Zhang, W. J. Weber, *Phys. Chem. Chem. Phys.* **2014**, *16*, 15590–15596 (cit. on p. 96).

[358] M. J. Akhtar, Z.-U.-N. Akhtar, R. A. Jackson, C. R. A. Catlow, *J. Am. Ceram. Soc.* **1995**, *78*, 421–428 (cit. on p. 96).

[359] J. Crawford, P. Jacobs, *J. Solid State Chem.* **1999**, *144*, 423–429 (cit. on p. 96).

[360] C. R. A. Catlow, Z. X. Guo, M. Miskufova, S. A. Shevlin, A. G. H. Smith, A. A. Sokol, A. Walsh, D. J. Wilson, S. M. Woodley, *Phil. Trans. R. Soc. A.* **2010**, *368*, 3379–3456 (cit. on p. 96).

[361] D. R. Stull, H. Prophet, JANAF thermochemical tables, second edition, en, tech. rep. NBS NSRDS 37, Edition: 0, National Bureau of Standards, Gaithersburg, MD, **1971**, NBS NSRDS 37 (cit. on p. 97).

[362] S.-K. Otto, K. Kousi, D. Neagu, L. Bekris, J. Janek, I. S. Metcalfe, *ACS Appl. Energy Mater.* **2019**, *2*, 7288–7298 (cit. on p. 100).

[363] E. Vera, V. Trillaud, J. Metaouaa, M. Aouine, A. Boreave, L. Burel, I.-L. Roiban, P. Steyer, P. Vernoux, *ACS Appl. Mater. Interfaces* **2024**, *16*, 7219–7231 (cit. on p. 100).

[364] R. Meyer, R. Waser, J. Helmbold, G. Borchardt, *Phys. Rev. Lett.* **2003**, *90*, 105901 (cit. on p. 100).

[365] A. Walsh, C. R. A. Catlow, A. G. H. Smith, A. A. Sokol, S. M. Woodley, *Phys. Rev. B* **2011**, *83*, 220301 (cit. on p. 100).

[366] T. Mizoguchi, N. Takahashi, H.-S. Lee, *Appl. Phys. Lett.* **2011**, *98*, 091909 (cit. on p. 100).

[367] R. A. De Souza, M. S. Islam, E. Ivers-Tiffée, *J. Mater. Chem.* **1999**, *9*, 1621–1627 (cit. on p. 100).

[368] D. B. Schwarz, H. U. Anderson, *J. Electrochem. Soc.* **1975**, *122*, 707–710 (cit. on p. 102).

[369] A. Hackmann, O. Kanert, *Radiat. Eff. Defects Solids* **1991**, *119-121*, 651–656 (cit. on p. 102).

[370] F. Cordero, *Phys. Rev. B* **2007**, *76*, 172106 (cit. on p. 102).

[371] R. A. De Souza, V. Metlenko, D. Park, T. E. Weirich, *Phys. Rev. B* **2012**, *85*, 174109 (cit. on p. 102).

[372] M. Schie, R. Waser, R. A. De Souza, *J. Phys. Chem. C* **2014**, *118*, 15185–15192 (cit. on p. 102).

[373] O. Yamamoto, *Solid State Ion.* **1987**, *22*, 241–246 (cit. on p. 105).

[374] B. Steele, *J. Power Sources* **1994**, *49*, 1–14 (cit. on p. 105).

[375] J. C. Boivin, G. Mairesse, *Chem. Mater.* **1998**, *10*, 2870–2888 (cit. on p. 105).

[376] J. Kilner, *Solid State Ion.* **2000**, *129*, 13–23 (cit. on p. 105).

[377] T. Norby, *J. Mater. Chem.* **2001**, *11*, 11–18 (cit. on p. 105).

[378] J. B. Goodenough, *Annu. Rev. Mater. Res.* **2003**, *33*, 91–128 (cit. on p. 105).

[379] E. V. Tsipis, V. V. Kharton, *J. Solid State Electrochem.* **2008**, *12*, 1367–1391 (cit. on p. 105).

[380] A. Orera, P. R. Slater, *Chem. Mater.* **2010**, *22*, 675–690 (cit. on p. 105).

[381] J. A. Kilner, M. Burriel, *Annu. Rev. Mater. Res.* **2014**, *44*, 365–393 (cit. on p. 105).

[382] V. Thoréton, M. Niania, J. Druce, H. Tellez, J. A. Kilner, *J. Electrochem. Soc.* **2022**, *169*, 044513 (cit. on pp. 105, 122, 125, 126).

[383] V. Metlenko, A. H. H. Ramadan, F. Gunkel, H. Du, H. Schraknepper, S. Hoffmann-Eifert, R. Dittmann, R. Waser, R. A. De Souza, *Nanoscale* **2014**, *6*, 12864–12876 (cit. on p. 105).

[384] J. M. Polfus, B. Yildiz, H. L. Tuller, *Phys. Chem. Chem. Phys.* **2018**, *20*, 19142–19150 (cit. on pp. 106, 126).

[385] J. P. Parras, G. Feldmann, R. A. De Souza, *J. Am. Ceram. Soc.* **2021**, *104*, 5946–5954 (cit. on pp. 106, 126).

[386] T. Ishigaki, S. Yamauchi, J. Mizusaki, K. Fueki, H. Naito, T. Adachi, *J. Solid State Chem.* **1984**, *55*, 50–53 (cit. on pp. 106, 116).

[387] J. Mizusaki, I. Yasuda, J.-i. Shimoyama, S. Yamauchi, K. Fueki, *J. Electrochem. Soc.* **1993**, *140*, 467–471 (cit. on p. 106).

[388] D. Bayraktar, S. Diethelm, P. Holtappels, T. Graule, J. Van herle, *J. Solid State Electrochem.* **2006**, *10*, 589–596 (cit. on p. 106).

[389] M. Søgaard, P. Vang Hendriksen, M. Mogensen, *J. Solid State Chem.* **2007**, *180*, 1489–1503 (cit. on pp. 106, 113, 114, 116).

[390] H. Kishimoto, N. Sakai, T. Horita, K. Yamaji, M. Brito, H. Yokokawa, *Solid State Ion.* **2007**, *178*, 1317–1325 (cit. on p. 106).

[391] I. Wærnhus, T. Grande, K. Wiik, *Top. Catal.* **2011**, *54*, 1009–1015 (cit. on p. 106).

[392] A. M. Ritzmann, A. B. Muñoz-García, M. Pavone, J. A. Keith, E. A. Carter, *Chem. Mater.* **2013**, *25*, 3011–3019 (cit. on p. 106).

[393] A. M. Ritzmann, A. B. Muñoz-García, M. Pavone, J. A. Keith, E. A. Carter, *MRS Commun.* **2013**, *3*, 161–166 (cit. on p. 106).

[394] Y. A. Mastrikov, R. Merkle, E. A. Kotomin, M. M. Kuklja, J. Maier, *Phys. Chem. Chem. Phys.* **2013**, *15*, 911–918 (cit. on pp. 106, 116).

[395] F. H. Taylor, J. Buckeridge, C. R. A. Catlow, *Chem. Mater.* **2016**, *28*, 8210–8220 (cit. on p. 106).

[396] J. A. Santana, J. T. Krogel, P. R. C. Kent, F. A. Reboredo, *J. Chem. Phys.* **2017**, *147*, 034701 (cit. on p. 106).

[397] T. Das, J. D. Nicholas, Y. Qi, *ECS Trans.* **2017**, *78*, 2807–2814 (cit. on p. 106).

[398] T. Das, J. D. Nicholas, Y. Qi, *Phys. Chem. Chem. Phys.* **2020**, *22*, 9723–9733 (cit. on pp. 106, 111).

[399] Y.-S. Zheng, M. Zhang, Q. Li, Y.-A. Zhu, Z.-J. Sui, D. Chen, X.-G. Zhou, *J. Phys. Chem. C* **2019**, *123*, 275–290 (cit. on p. 106).

[400] H. Zhang, A. H. H. Ramadan, R. A. De Souza, *J. Mater. Chem. A* **2018**, *6*, 9116–9123 (cit. on p. 108).

[401] M. Wagih, C. A. Schuh, *Acta Mater.* **2019**, *181*, 228–237 (cit. on p. 108).

[402] J. A. Purton, *Phys. Chem. Chem. Phys.* **2019**, *21*, 9802–9809 (cit. on p. 108).

[403] K. Govers, M. Verwerft, *J. Nucl. Mater.* **2013**, *438*, 134–143 (cit. on p. 109).

[404] J. D. Honeycutt, H. C. Andersen, *J. Phys. Chem.* **1987**, *91*, 4950–4963 (cit. on p. 109).

[405] D. Faken, H. Jónsson, *Comput. Mater. Sci.* **1994**, *2*, 279–286 (cit. on p. 109).

[406] A. Stukowski, *Modelling Simul. Mater. Sci. Eng.* **2012**, *20*, 045021 (cit. on p. 109).

[407] P. M. Larsen, S. Schmidt, J. Schiøtz, *Modelling Simul. Mater. Sci. Eng.* **2016**, *24*, 055007 (cit. on p. 109).

[408] A. Bonkowski, agility, **2025** (cit. on p. 111).

[409] S. M. Selbach, J. R. Tolchard, A. Fossdal, T. Grande, *J. Solid State Chem.* **2012**, *196*, 249–254 (cit. on p. 111).

[410] A. Fossdal, M. Menon, I. Waernhus, K. Wiik, M.-A. Einarsrud, T. Grande, *J. Am. Ceram. Soc.* **2005**, *87*, 1952–1958 (cit. on pp. 111, 112).

[411] R. De Souza, J. Kilner, J. Walker, *Mater. Lett.* **2000**, *43*, 43–52 (cit. on pp. 125, 126).

[412] E. Navickas, T. M. Huber, Y. Chen, W. Hetaba, G. Holzlechner, G. Rupp, M. Stöger-Pollach, G. Friedbacher, H. Hutter, B. Yildiz, J. Fleig, *Phys. Chem. Chem. Phys.* **2015**, *17*, 7659–7669 (cit. on p. 125).

[413] A. M. Saranya, D. Pla, A. Morata, A. Cavallaro, J. Canales-Vázquez, J. A. Kilner, M. Burriel, A. Tarancón, *Adv. Energy Mater.* **2015**, *5*, 1500377 (cit. on p. 125).

[414] J. M. Börgers, J. Kler, K. Ran, E. Larenz, T. E. Weirich, R. Dittmann, R. A. De Souza, *Adv. Funct. Mater.* **2021**, 2105647 (cit. on pp. 125, 126).

[415] B. Tofield, W. Scott, *J. Solid State Chem.* **1974**, *10*, 183–194 (cit. on p. 125).

[416] J. Mizusaki, H. Tagawa, K. Naraya, T. Sasamoto, *Solid State Ion.* **1991**, *49*, 111–118 (cit. on p. 125).

[417] J. Mizusaki, N. Mori, H. Takai, Y. Yonemura, H. Minamiue, H. Tagawa, M. Dokiya, H. Inaba, K. Naraya, T. Sasamoto, T. Hashimoto, *Solid State Ion.* **2000**, *129*, 163–177 (cit. on p. 125).

[418] F. W. Poulsen, *Solid State Ion.* **2000**, *129*, 145–162 (cit. on p. 125).

[419] D. S. Mebane, Y. Liu, M. Liu, *Solid State Ion.* **2008**, *178*, 1950–1957 (cit. on p. 125).

[420] Y.-L. Lee, D. Morgan, *Phys. Chem. Chem. Phys.* **2012**, *14*, 290–302 (cit. on p. 125).

[421] J. P. Parras, R. A. De Souza, *Acta Mater.* **2020**, *195*, 383–391 (cit. on p. 126).

[422] M. T. Buscaglia, V. Buscaglia, M. Viviani, P. Nanni, *J. Am. Ceram. Soc.* **2004**, *84*, 376–384 (cit. on p. 161).

Appendix

Table S1 BUCKINGHAM type potential parameters used for the simulations in chapter 4.

Interaction	A_{ij} / eV	ρ_{ij} / Å	C_{ij} / eV Å^6	source
Ce^{4+}–O^{2-}	1986.83	0.35107	20.4	[161]
O^{2-}–O^{2-}	22764.3	0.1490	27.89	[165, 166]

Table S2 BUCKINGHAM type potential parameters used for the simulations in chapter 5.

Interaction	A_{ij} / eV	ρ_{ij} / Å	C_{ij} / eV Å^6	source
Ca^{2+}–O^{2-} (I)	1340.18	0.3214	0.0	[166, 277]
Ca^{2+}–O^{2-} (II)	1090.4	0.3437	0.0	[278]
Ba^{2+}–O^{2-}	1214.4	0.3522	0.0	[163, 422]
Sr^{2+}–O^{2-}	774.2	0.3538	0.0	[165]
Co^{3+}–O^{2-}	1329.82	0.3087	0.0	[165, 166]
Fe^{3+}–O^{2-}	1156.36	0.3299	0.0	[166]
O^{2-}–O^{2-}	22764.3	0.1490	43.0	[165, 166]

Table S3 BUCKINGHAM type potential parameters used for the simulations in chapter 7.

Interaction	A_{ij} / eV	ρ_{ij} / Å	C_{ij} / eV Å^6	source
La^{3+}–O^{2-}	1516.3	0.3525	0.0	[165]
Sr^{2+}–O^{2-}	774.2	0.3538	0.0	[165]
Fe^{3+}–O^{2-}	1156.36	0.3299	0.0	[166]
O^{2-}–O^{2-}	22764.3	0.1490	43.0	[165]

A: Best Practices for Molecular Dynamics Simulations of Ion Diffusion in Solids

Evaluation of the Arrhenius fit

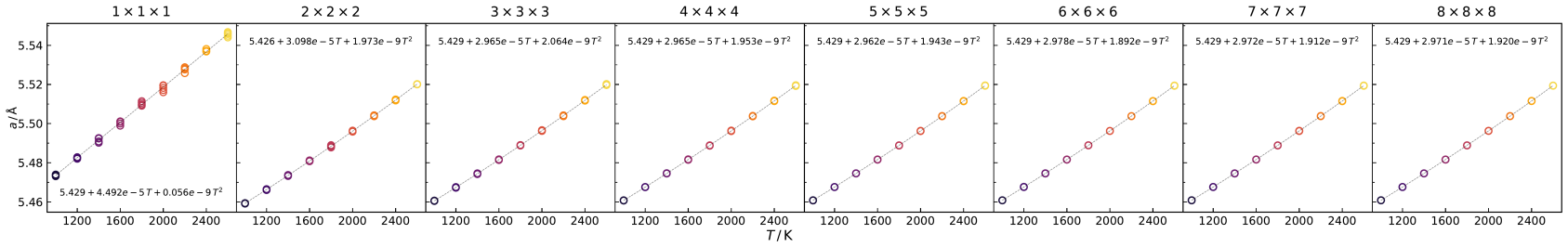


Figure S1 The lattice parameter a as a function of temperature for $CeO_{2-\delta}$ with different cell sizes and one oxygen vacancy. Five random seeds were used for each temperature.

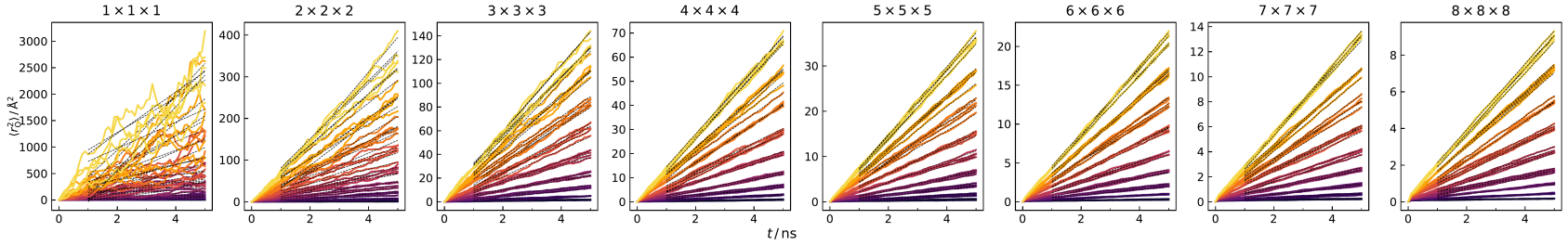


Figure S2 The mean squared displacement of oxygen in $CeO_{2-\delta}$ as a function of time for different temperatures and cell sizes. The data was fitted to a linear function, starting at $t = 1$ ns, to obtain the diffusion coefficient.

B: Oxygen grain-boundary diffusion in LSF

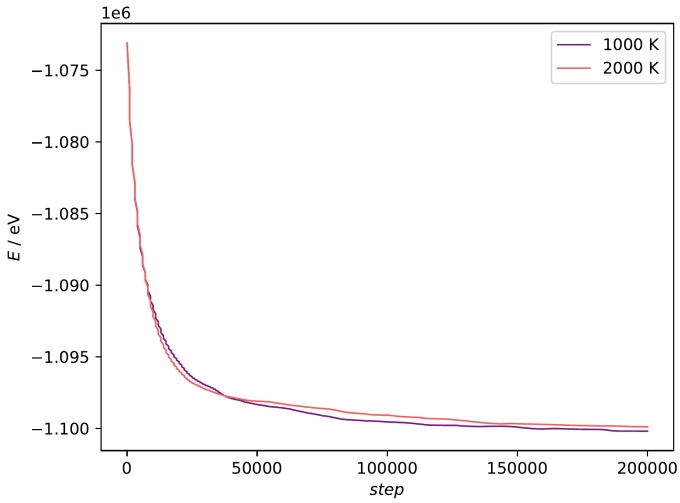


Figure S3 Total energy of a representative polycrystalline cell (LSF10, 20 grains) during MMC swapping.

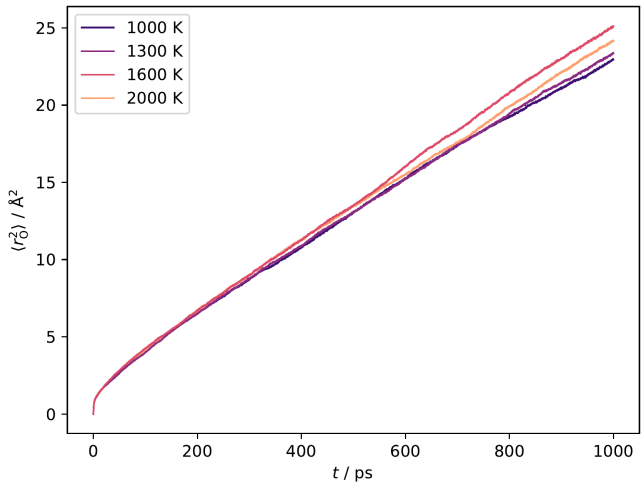


Figure S4 Mean-squared displacement of oxygen ions $\langle r_O^2 \rangle$ obtained as a function of time from equilibration MD simulations of a polycrystalline LSF10 cell at 2000 K with 2 grains after MMC swapping at different temperatures.

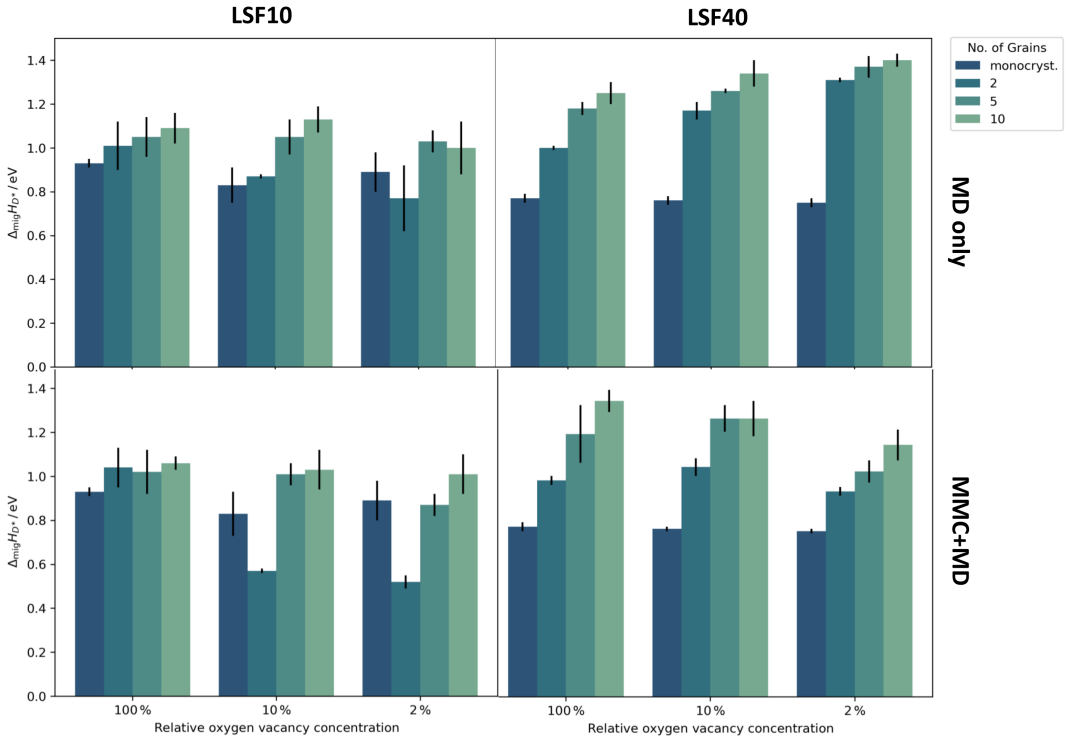


Figure S5 Activation enthalpies of oxygen diffusion in LSF10 and LSF40, obtained from diffusion coefficients in Fig. 7.15 and 7.16. For LSF10 structures with low oxygen vacancy concentrations and 2 grains, the activation enthalpy of LFO is sampled (see Fig. 7.14) due to a nominally Sr free bulk and a few oxygen vacancies in the bulk regions.

List of Tables

3.1 Overview of different types of exchange-correlation functionals. 37
3.2 Pseudopotentials used in the calculations. 49

6.1 Activation energies of migration for B-site cations in $SrTiO_3$ along $\langle 100 \rangle$, in the presence of v_{Sr}. 101

7.1 Activation enthalpies of oxygen-vacancy migration ΔH_{mig} in LSF, obtained from molecular dynamics simulations. 113

S1 BUCKINGHAM type potential parameters used for the simulations in chapter 4. . . 161
S2 BUCKINGHAM type potential parameters used for the simulations in chapter 5. . . 161
S3 BUCKINGHAM type potential parameters used for the simulations in chapter 7. . . 161

List of Figures

2.1 Schematic depiction of defects in a binary compound. The atoms are represented by circles of different colours and size. The square box represents a vacancy Shown are (a) vacancies, (b) interstitials, (c) substitutional defects, and (d) antisite defects. . . 8

2.2 Schematic depiction of the different mechanisms of ion migration in a binary compound. The ions are represented by circles of different colours and size. The arrows indicate the direction in which the ions have migrated. The square box represents an existing vacancy. Shown are the mechanisms for (a) vacancy diffusion, (b) interstitial diffusion, and (c) interstitialcy diffusion. 13

4.1 Equilibration of $CeO_{2-\delta}$ at $T = 2000\,\mathrm{K}$ and $p = 0\,\mathrm{bar}$ using the MSER method. E_{pot} and V normalised per unit cell. Minima of MSER determined using `pyMSER`[222] . 56

4.2 Temperature T, total energy E, pressure p, and volume V in a simulation of $Ca_{0.5}Sr_{0.5}Co_{0.8}Fe_{0.2}O_{2.5}$ at $T_{\mathrm{target}} = 900\,\mathrm{K}$ and $p_{\mathrm{target}} = 0$ during the first 10 ns of the simulation. Energy and volume are normalised per unit cell. Much longer simulation times are required for their equilibration (as determined with `pyMSER`[222]), and even in the supposedly equilibrated region, a slow decrease in both of these quantities is still observed. 57

4.3 Temperature T, energy E, pressure p, and volume V in a simulation of oxygen-deficient CeO_2 at $T_{\mathrm{target}} = 2000\,\mathrm{K}$ and $p_{\mathrm{target}} = 0$ during the first 100 ps of the simulation (the equilibration period for each variable is shown in grey); left: as a function of time, right: relative frequency (grey equilibration period excluded) of the values with normal distribution fit (dotted red line) and fit parameters. 61

4.4 Mean square displacement of oxide ions in oxygen-deficient CeO_2 at $800 \leq T/\mathrm{K} \leq 2600$ (a) on a linear scale, (b) on a double-logarithmic scale, where dotted lines indicate $\alpha = 1$. The colour gradient indicates the temperature. 62

4.5 Vacancy diffusion coefficients and migration barrier of oxygen in ceria as a function of temperature for a system with 13814 oxygen ions and 10 oxygen vacancies (six random seeds). The lattice parameter was fixed at $a = 5.4286$ Å. As a comparison, the vacancy diffusion coefficients for simulations at equilibrium volume are shown as a red solid line. 63

4.6 Average pressure as a function of temperature for the same simulation as in Fig. 4.5. With increasing temperature, the pressure increases, indicating the suppression of the volume expansion. 64

4.7 Migration barriers and effective attempt frequencies obtained from non-linear WLS fits of oxygen diffusion in ceria. Vertical lines indicate the large-cell values as obtained from a $12 \times 12 \times 12$ supercell with 10 vacancies. Bars represent median values. 65

4.8 Migration barriers obtained from linear and non-linear OLS and WLS fits of randomly generated data points for the temperature range $600 \leq T\,/\,\mathrm{K} \leq 1400$. The obtained activation energies are normalised to the true value. 69

4.9 Migration barriers and entropy terms obtained from linear and non-linear OLS and WLS fits of oxygen diffusion in ceria. Vertical lines indicate the large-cell values as obtained from a $12 \times 12 \times 12$ supercell with 10 vacancies. Bars represent median values. 70

4.10 The distribution of the prefactor D_0 (left), the activation energy ΔH (middle), and the diffusion coefficient D at 300 K (right) for oxygen diffusion in $CeO_{2-\delta}$. The data were obtained from a BAYESian non-linear fit to the ARRHENIUS equation for one random seed per temperature. The corresponding ARRHENIUS plot is shown in Fig. 4.11. 72

4.11 ARRHENIUS plot of the diffusion coefficient of oxygen in $CeO_{2-\delta}$. The data was obtained from a BAYESian non-linear fit to the ARRHENIUS equation for one random seed per temperature. The errorbars were calculated with Eq. (4.11). The red lines represent 0.8% of the whole data set. Fitted using the `uravu` package[249]. 73

4.12 Corner plot of the prefactor D_v^0 and the activation energy ΔH_v for oxygen diffusion in $CeO_{2-\delta}$. The data was obtained from a BAYESian non-linear fit to the ARRHENIUS equation for one random seed per temperature. See Fig. 4.11 for the corresponding ARRHENIUS plot. 74

5.1 Pseudocubic lattice parameters in CSCF5582, starting from orthorhombic CSCF5582, shown for two different potential sets with their standard deviation as error bars. For comparison, the cubic lattice parameters of BSCF5582 are given, where simulations were initialised from the cubic structure. The lattice parameter of CSCF5582 is smaller than that of BSCF5582 due to the smaller cation radius of Ca^{2+} relative to Ba^{2+}. 81

5.2 Oxygen tracer diffusion coefficients versus inverse temperature for cubic $Ba_{0.5}Sr_{0.5}Co_{0.8}Fe_{0.2}O_{2.5}$ (circles) and cubic $Ca_{0.5}Sr_{0.5}Co_{0.8}Fe_{0.2}O_{2.5}$ (squares), obtained from MD simulations. Also plotted are literature data from MD simulations reported by SHIIBA *et al.*[164] . 82

5.3 Oxygen tracer diffusion coefficients versus inverse temperature for cubic $Ba_{0.5}Sr_{0.5}Co_{0.8}Fe_{0.2}O_{2.5}$, obtained from MD simulations, with and without preceding MMC simulations. . . 83

5.4 Lattice expansion of BSCF5582. A (MD, this work, linear fit), B,[280] C,[281] D,[282] E,[283] F,[284] G.[285] 84

5.5 Comparison of oxygen tracer diffusion coefficients obtained for $Ba_{0.5}Sr_{0.5}Co_{0.8}Fe_{0.2}O_{3-\delta}$. MD data obtained in this work were corrected for experimental nonstoichiometry (see text). A (MD, this work), B and C,[287] D,[288] E,[289] F,[290] G,[291] H.[284] Line J [$\Delta H_{\mathrm{mig}} = (0.92 \pm 0.11)$ eV] and line K ($\Delta H_{\mathrm{mig}} = (0.43 \pm 0.04)$ eV) are fits to the two groups of data (see text). 86

6.1 Schematic illustration of the preparation and exsolution processes. A transition-metal oxide is incorporated into a perovskite host lattice at high temperatures under oxidising conditions. Subsequently, it is exsolved at much lower temperatures under reducing conditions. 91

6.2 Thermodynamic charge-transition levels of different Ni-containing defects in $SrTiO_3$ obtained from hybrid DFT calculations. The six defects are divided into three groups that refer to *B* -site, *A* -site, and interstice occupation respectively. The blue region indicates the valence band; the orange region, the conduction band. †The $(Ni_i^{z+}v_O v_{Sr})$ associate refers to a different configuration, in which the Ni^{2+} ion is displaced from the octahedral interstice towards the *A* -site vacancy. 94

6.3 Thermodynamic prediction of conditions necessary for the exsolution of Ni from $SrTiO_3$ based on the reaction energy for the overall exsolution reaction, Eq. (6.3). The dotted line refers to $\Delta_{\mathrm{exsoln}}E = 0$; the area above and to the right corresponds to a negative reaction energy and thus to conditions under which exsolution can take place (in the absence of kinetic hindrance). Interface-specific energies are not included (see text); dilute-solution thermodynamics are assumed. 99

7.1 Polycrystalline simulation cells generated and used in this chapter. Different grains are indicated with different colours. $\bar{V}$ is the average grain volume; $\bar{d}$ is the average grain diameter (assuming spherical grains). 107

7.2 Polycrystalline cell with 10 grains (see Fig. 7.1c) after equilibration at 1800 K. Shown are only the cations (i.e. La, Sr, and Fe). The colour coding refers to the structure type identified by common-neighbour analysis of the cation sub-lattice, as implemented in the `ovito` package.[146] Blue ions are identified as bcc structured (and hence as bulk ions or grain core), whereas red ions do not have a bbc type coordination (grain boundary ions). 109

7.3 Average grain boundary fractions (cations only) for the initial structures. As the cells were subject to MD simulation, the fractions increased slightly. The fractions are higher for LSF40 than LSF10 due to the higher structural perturbation induced by the higher substitution fraction (see text). Error bars refer to the standard deviation. 110

7.4 Pseudocubic cell parameters a (purple squares), b (magenta triangles), and c (orange circles) obtained for LSF10 and LSF40 from MD simulations as a function of temperature T. At each temperature, two simulations with different random $\mathrm{Sr}'_{\mathrm{La}}$ distributions and different initial kinetic-energy distributions were carried out. The phase transitions from orthorhombic ($a \neq b \neq c$) to cubic ($a = b = c$) are indicated with black lines; the grey line indicates the experimental transition temperature for LSF40.[410] 112

7.5 Mean-squared displacement of oxygen ions $\langle r_{\mathrm{O}}^2 \rangle$ obtained as a function of time from MD simulations of LSF10, $n_{\mathrm{v}} = 1.66\,\%$. Results are shown for various temperatures $1000 < T\mathrm{K} < 3000$; at each temperature, two simulations with different random initial kinetic energy distributions were carried out. 113

7.6 Oxygen-vacancy diffusion coefficients D_{v} as a function of inverse temperature for (a) LSF10 and (b) LSF40: A, this work (orthorhombic); B, this work (cubic); C,[292]; D,[30]; E,[389]. The high-temperature simulation data and the linear extrapolation represent diffusion in cubic LSF, whereas low-temperature data refer to orthorhombic LSF. The transition temperature in LSF40 is overestimated by the empirical potentials, hence, the linear extrapolation of the cubic data is given as a guide to the eye. Errors in the diffusion coefficients, calculated with the expression of Usler *et al.*,[197] are smaller than the symbol size. Fig. 7.7 compares simulations with different oxygen vacancy concentrations. 114

7.7 Oxygen-vacancy diffusion coefficients D_v as a function of inverse temperature for (a) LSF10 and (b) LSF40: A, this work (orthorhombic); B, this work (cubic); C, oxygen vacancy concentration reduced to 10 %; D, oxygen vacancy concentration reduced to 2 %. 115

7.8 Activation enthalpy of oxygen-vacancy diffusion in $La_{1-x}Sr_xFeO_{3-\delta}$ as a function of strontium content x: A, this work (orthorhombic); B, this work (cubic); C,[292]; D,[30]; E,[389]; F,[386]; G,[394]. Note that the phase transitions are temperature dependent and thus not all experimental data points always correspond to the same phase. 116

7.9 *A*-site fraction of Sr (determined directly) and oxygen-vacancy site fraction (determined indirectly from cation-to-anion-ratio) after equilibration of the structures at 2000 K: (a) bulk and (b) grain-boundary region. Grain boundary and bulk regions were identified with the Adaptive Common Neighbour Analysis. The red horizontal lines indicate the expected values. The oxygen plots show accumulation of oxygen vacancies at the grain boundary. Error bars refer to the standard deviation. 117

7.10 *A*-site fraction of Sr and oxygen vacancy fraction (both determined directly) after MMC ion swapping at 2000 K in LSF: (a) bulk region and (b) grain-boundary region. Grain-boundary and bulk regions were identified with the Adaptive Common Neighbour Analysis. The horizontal lines indicate the expected values. All plots show accumulation of oxygen vacancies at the grain boundary. By increasing the Sr content from LSF10 to LSF40, a saturation effect is observed, i.e. the accumulation is less significant. Error bars refer to the standard deviation. 118

7.11 Oxygen tracer diffusion coefficients for grain-boundary cells relative to bulk cells for a homogeneous distribution of Sr: (a) orthorhombic LSF10 and (b) cubic LSF40. The arrow indicates a decrease in D_O^* with increasing grain-boundary density. Data for LSF10 at 1000 K is omitted from the plot due to high uncertainties. 119

7.12 Oxygen tracer diffusion coefficients in cubic LSF40. The arrow indicates a decrease in D_O^* with increasing grain-boundary density. Cells subjected to MMC minimisation exhibit lower D_O^* values, indicating a deleterious effect from increasing Sr concentrations at the grain boundaries. 120

7.13 Oxygen tracer diffusion coefficients in LSF10. The corresponding data for LSF40 is shown in Fig. 7.12. 121

7.14 Oxygen-vacancy diffusion coefficients D_v as a function of inverse temperature for different Sr'_{La} concentrations. 121

7.15 Comparison of diffusion coefficients obtained from calculations with (a) 1.7 % (LSF10) and (c) 6.7 % (LSF40) oxygen vacancies versus calculations with only (b) 0.17 % (LSF10), (d) 0.67 % (LSF40), (e) 0.033 % (LSF10) and (f) 0.13 % (LSF40) oxygen vacancies. In both cases, structures underwent MMC swapping at 2000 K with the full oxygen vacancy concentration, and the Sr'_{La} distribution was kept frozen in for the other two oxygen vacancy concentrations. The arrows indicate the changes in D^*_O with increasing grain-boundary density. 123
7.16 Comparison of diffusion coefficients obtained from calculations with (a) 1.7 % (LSF10) and (c) 6.7 % (LSF40) oxygen vacancies versus calculations with only (b) 0.17 % (LSF10), (d) 0.67 % (LSF40), (e) 0.033 % (LSF10) and (f) 0.13 % (LSF40) oxygen vacancies. The Sr'_{La} distribution is homogenous. The arrows indicate the changes in D^*_O with increasing grain-boundary density. 123
7.17 Oxygen tracer diffusion coefficients in polycrystalline LSF at $T = 1800$ K, extracted from Fig. 7.15, as a function of $[v^{\bullet\bullet}_O]$. 124

S1 The lattice parameter a as a function of temperature for $CeO_{2-\delta}$ with different cell sizes and one oxygen vacancy. Five random seeds were used for each temperature. 162
S2 The mean squared displacement of oxygen in $CeO_{2-\delta}$ as a function of time for different temperatures and cell sizes. The data was fitted to a linear function, starting at $t = 1$ ns, to obtain the diffusion coefficient. 162
S3 Total energy of a representative polycrystalline cell (LSF10, 20 grains) during MMC swapping. 163
S4 Mean-squared displacement of oxygen ions $\langle r^2_O \rangle$ obtained as a function of time from equilibration MD simulations of a polycrystalline LSF10 cell at 2000 K with 2 grains after MMC swapping at different temperatures. 164
S5 Activation enthalpies of oxygen diffusion in LSF10 and LSF40, obtained from diffusion coefficients in Fig. 7.15 and 7.16. For LSF10 structures with low oxygen vacancy concentrations and 2 grains, the activation enthalpy of LFO is sampled (see Fig. 7.14) due to a nominally Sr free bulk and a few oxygen vacancies in the bulk regions. . . 164